

DIRECTION OF ARRIVAL ESTIMATION USING ANTENNA ARRAYS

by

Rias Muhamed

Thesis submitted to the Faculty of the
Virginia Polytechnic Institute and State University
in partial fulfillment of the requirements for the degree of

MASTER OF SCIENCE

in

Electrical Engineering

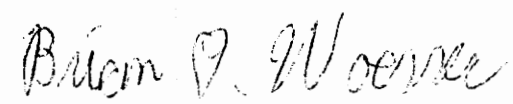
APPROVED:



Dr. Theodore S. Rappaport, Chairman



Dr. Jeffrey H. Reed



Dr. Brian D. Woerner

January 1996

Blacksburg, Virginia

Keywords: Direction of Arrival, DOA, Adaptive Arrays

L.D
5655
V855
1996
M843
C.R

Abstract

DIRECTION-OF-ARRIVAL ESTIMATION USING ANTENNA ARRAYS

by

Rias Muhamed

Theodore S. Rappaport, Chairman

Bradley Department of Electrical Engineering

ABSTRACT

The objective of this thesis is to design, build and evaluate a direction-of-arrival measurement system using an antenna array operating at 2050 MHz. The first phase of the project is an extensive study of various high resolution DOA estimation algorithms. The algorithms studied include subspace-based techniques such as the MUSIC (MULTiple Signal Classification) and ESPRIT (Estimation of Signal Parameters via Rotational Invariance) algorithm, and the integrated approaches which combine property restoral-based techniques such as the Iterative Least Squares Projection-based Constant Modulus Algorithm (ILSP-CMA) with subspace-based techniques. All these algorithms were simulated in MATLAB and their performance under different conditions were tested and compared. In the second phase of the project a six element uniformly spaced linear array receiver was built. Three Ariel DSP-96 boards based on the Motorola DSP96002 are used to simultaneously sample, collect, and store data from each of the array elements. The data collected by the DSP boards are processed off-line to estimate the directions of arrival. Several experiments are conducted to test the functioning of the system under various conditions, and demonstrate the performance of different algorithms. Results of these experiments are also presented in this thesis.

Acknowledgments

I would like to thank my academic advisor, Dr. Theodore S. Rappaport, for the invaluable support, guidance and encouragement he has provided over the past two years. I thank my committee members, Dr. Jeffrey H. Reed and Dr. Brain D. Woerner, for carefully reviewing my thesis report and providing useful suggestions.

I am grateful to Joe Liberti for his help and guidance during the course of this research. I sincerely appreciate the time and effort he had spent in getting me up to speed on this project. I also thank Tom Beidka for his valuable advice and suggestions.

This project could not have been completed without the help of several students at MPRG. Mansoor Ahmed modeled the measurement site in the site specific propagation prediction tool. Keith Blankenship and Bill Newhall provided the power delay profiles taken at the measurement site. Zhigang Rong, Mansoor Ahmed, Francis Dominique, Paul Petrus, Nitin Mangalvade, Kevin Saldanha, and Anil Doradla assisted me during the measurement campaign. I wish to thank each one of them for the help they provided.

I wish to thank Francis Dominique and Paul Petrus for providing several ideas and suggestions throughout the course of this work.

I would like to thank Prab Koushik for providing the necessary support for my computational demands.

I would like to thank the Advanced Research Project Agency's (ARPA) Global Mobile (GLOMO), the Office of the National Drug Control Policy (ONDCP), and the MPRG industrial affiliates for providing financial support for this work.

Most of all, I would like to thank my parents and family without whose continuous and immeasurable support I could not have completed my degree.

Contents

1. Introduction	1
1.1 Motivation	1
1.2 Objective and Outline of Thesis	2
2. Adaptive Arrays - Background Theory	5
2.1 Fundamentals of Antenna Arrays	5
2.1.1 Uniformly Spaced Linear Array	11
2.1.2 Spatial Signature	12
2.2 Beamforming and Spatial filtering	14
2.3 Wideband Arrays	16
2.4 Adaptive Arrays	18
2.5 The LMS Algorithm	21
2.6 Property Restoral Algorithms	24
2.6.1 The Constant Modulus Algorithm	24
2.6.2 Spectral Coherence Restoral Algorithm	27
2.7 Summary	28
3. Overview of Direction of Arrival Estimation Algorithms	29
3.1 Introduction	29
3.2 Conventional Methods for DOA Estimation	30
3.2.1 Delay-and-Sum Method	30
3.2.2 Capon's Minimum Variance Method	32
3.3 Subspace Methods for DOA Estimation	35
3.3.1 The MUSIC Algorithm	35
3.3.2 Improvements to the MUSIC Algorithm	41
3.3.3 The ESPRIT Algorithm	44
3.4 Maximum Likelihood Techniques	49
3.5 DOA Estimation under Coherent Signal Conditions	54
3.5.1 Spatial Smoothing Techniques	55
3.5.2 Multidimensional MUSIC	58
3.6 The Iterative Least-Squares Projection Based CMA	59
3.7 The Integrated Approach to DOA Estimation	61
3.8 Detection of Number of Sources	64
3.8.1 The SH, MDL and AIC Criteria	65
3.8.2 Order Estimation Using Transformed Gershgorin Radii	67
3.9 Summary	71

4. Simulation Based Performance Comparison of DOA Estimation Algorithms	72	
4.1	Introduction.....	72
4.2	Resolution and Sensitivity to Calibration of MUSIC type algorithms.	73
4.3	Performance Comparison of DOA Estimation Algorithms	77
4.4	Performance of Source Order Estimation Algorithms	94
4.5	Conclusion	99
5. Description of the DOA Measurement System	100	
5.1	Introduction.....	100
5.2	Antenna Array and RF front-end	102
5.3	Sampling and Data Collection	103
5.3.1	Configuring Multiple DSP-96 boards for Synchronous Sampling	105
5.4	RF Chain Phase Calibration	108
5.5	Receiver Sensitivity and Dynamic Range.....	110
5.6	Processing for DOA Estimation	112
6. DOA Measurement Experiments and Results.....	116	
6.1	Introduction.....	116
6.2	Description of the DOA Measurements	116
6.2.1	Measurements with a Single Transmitter Antenna.....	119
6.2.2	Measurements With Multiple Transmitter Antennas Fed From Uncorrelated Sources	120
6.2.3	Measurements With Multiple Transmitter Antennas Fed From a Single Source	126
6.3	Sources of Error in DOA Estimation	130
6.4	Results of the Simulation Based Study.....	137
6.5	Conclusion	146
7. Conclusion and Future Work	146	
7.1	Conclusion	146
7.2	Future Work	148
Appendix 1 List of Abbreviations	148	
References	149	
Programs	155	

List of Figure

Figure 2.1: Illustration of an array with antenna elements located at arbitrary locations in space..	6
Figure 2.2: Illustration of a plane wave incident on a linear equispaced array. The dotted lines represent the phase fronts of the incident wave.....	11
Figure 2.3: Direct and multipath signals from multiple sources impinging on a receiver antenna array.	12
Figure 2.4: A narrowband beamformer whose output is a complex weighted sum of the spatially sampled input data.....	15
Figure 2.5: Illustration of a wideband array with a transversal filter attached to each antenna element.	17
Figure 2.6: Illustration of a simple adaptive array.....	19
Figure 2.7: An example of a two dimensional quadratic performance surface.	20
Figure 3.1: Illustration of the classical beamforming structure.	30
Figure 3.2: Comparison of resolution performance of delay-and-sum method and Capon's minimum variance method. Two signals of equal power at an SNR of 20 dB arrive at a 6-element uniformly spaced array with an interelement spacing equal to half a wavelength at angles 90 and 100 degrees respectively.....	34
Figure 3.3: Comparison of MUSIC and Capon's minimum variance method. Two signals of equal power at an SNR of 20 dB arrive at a 6-element uniformly spaced array with an interelement spacing equal to half a wavelength at angles 90 and 95 degrees respectively.40	
Figure 3.4: Illustration of ESPRIT array geometry [Roy90].....	45
Figure 3.5: Comparison of MUSIC with and without forward/backward averaging in coherent multipath. Three coherent signals of equal power at an SNR of 20 dB arrive at a 6-	

element uniformly spaced array with an interelement spacing equal to half a wavelength at angles 60, 90 and 120 degrees respectively.....57

Figure 3.6: Example of spatial spectrum estimated using ILSP-CMA for spatial signature estimation, followed by MUSIC with forward backward averaging. The six element array is able to resolve 24 direct and multipath components and associate each component to the appropriate signal (user).....64

Figure 4.1: Resolution performance of MUSIC and the integrated ILSP-CMA with MUSIC approaches. The resolution is plotted here as the angle Dq such that two equal powered signals impinging on the six element uniformly spaced linear array at 90 and $90 + Dq$ respectively were consistently resolved. Resolution is plotted as function of both SNR and number of samples of data used for DOA estimation, for the case of both coherent and uncorrelated signals. For the coherent cases, forward/conjugate backward averaging was used 74

Figure 4.2: Sensitivity of the MUSIC spectrum to spacing errors. Four noncoherent signals arrive at angles 10,30,50,70 degrees, respectively, on a six element uniform linear array with half wavelength interelement spacing. This figure illustrates how the MUSIC spectrum becomes corrupted due to imperfections in constructing the array. The first figure is without any spacing errors, and the subsequent ones are with +/- 1, 2, and 5 percent spacing errors respectively.76

Figure 4.3: Performance of various DOA estimation algorithms. RMS error in DOA estimation is plotted as a function of number of samples of data used to estimate the DOA. In all simulations, two uncorrelated (non-coherent) signals with equal power are incident on a six element uniform linear array at 90 and 95 degrees, respectively, at a 20dB SNR. The RMS error is averaged over 200 repeated DOA estimation trials.79

Figure 4.4: RMS Error in DOA Estimation as a function of number of samples. Simulation parameters same as Figure 4.3, except that the SNR here is only 5 dB.79

Figure 4.5: Performance of various DOA estimation algorithms. RMS error in DOA estimation is plotted as a function of signal-to-noise ratio. In all simulations, 50 samples of two uncorrelated (non-coherent) signals with equal power incident on a six element uniform linear array at 90 and 95 degrees respectively are used for DOA estimation. The RMS error is averaged over 200 repeated DOA estimation trials.80

Figure 4.6: Simulation parameters same as in Figure 4.5 with the two sources being coherent.80

Figure 4.7: Performance of various DOA estimation algorithms. RMS error in DOA estimation is plotted as a function of number of samples of data used to estimate DOA. In all simulations, two coherent signals with equal power are incident on a six element uniform linear array at 90 and 95 degrees respectively, at a 20dB SNR. The RMS error is averaged over 200 repeated DOA estimation trials. All subspace based algorithms are used along

with forward/backward averaging.	81
Figure 4.8: RMS Error in DOA Estimation as a function of number of samples. Simulation parameters same as figure 4.7, except that the SNR is 5 dB.	81
Figure 4.9: RMS Error in DOA estimation as a function of the angle of arrival. A single sinusoidal tone signal is incident on a six element uniformly spaced linear array at 20 dB SNR. 500 samples of data is used for each DOA estimation and the rms error is obtained by averaging over 200 repeated trials.	83
Figure 4.10: RMS Error in DOA estimation as a function of angle of arrival. Simulation parameters same as in Figure 4.9, except that forward/backward averaging (spatial smoothing) is used.	84
Figure 4.11: RMS error in DOA estimation as a function of angle of separation (D_q) and number of sources for TLS-ESPRIT and the integrated ILSP-CMA with TLS-ESPRIT algorithms. All sources are assumed to be uncorrelated (non-coherent) and at the same power level with an SNR = 20 dB. The estimations are made using 500 samples of data and the rms error is computed by averaging over 200 repeated trials. The top figure shows the case where the incident signals arrive at $10, 10+\Delta\theta, 10+2\Delta\theta$, and $10+3\Delta\theta$ degrees, and the bottom figure shows the case where the incident signals arrive at $30, 30+\Delta\theta, 30+2\Delta\theta$ and $30+3\Delta\theta$ degrees.	85
Figure 4.12: RMS error in DOA estimation as a function of the angle of separation between adjacent signals. The top figure shows the case where the incident signals arrive at $60, 60+\Delta\theta, 60+2\Delta\theta$, and $60+3\Delta\theta$ degrees, and the bottom figure shows the case where the incident signals arrive at $90, 90+\Delta\theta, 90+2\Delta\theta$ and $90+3\Delta\theta$ degrees.	86
Figure 4.13: RMS error in DOA estimation as a function of the angle of separation between adjacent signals and the number of signals. Simulation parameters are the same as used in Figure 4.11, except that the signals are perfectly correlated as would be the case in a coherent multipath environment. Forward/backward averaging is used to decorrelate the coherent signals.	87
Figure 4.14: RMS error in DOA estimation as a function of angle of separation between adjacent signals and the number of signals. Simulation parameters are the same as used in Figure 4.12, except that the signals are perfectly correlated as would be the case in a coherent multipath environment. Forward/backward averaging is used to decorrelate the coherent signals.	88
Figure 4.15: RMS error in DOA estimation as a function of the difference in power between the uncorrelated (non-coherent) signals. All the sources except the first one is assumed to be at the same power level. The estimations are made using 500 samples of data and the rms error is computed by averaging over 200 repeated computations.	90
Figure 4.16: RMS error in DOA estimation as a function of the difference in power between the incident coherent signals. All the sources except the first one is assumed to be at	

the same power level.....	91
Figure 4.17: RMS error in DOA estimation as a function of angle of arrival for different spacing errors. Spacing errors were simulated by perturbing the location of the sensors. All the sources incident on the array are uncorrelated with one another. The estimations were made using 500 samples of data and the rms error was computed by averaging over 200 repeated trials.....	92
Figure 4.18: RMS error in DOA estimation as a function of the angle of arrival for different spacing errors for the case of coherent (perfectly correlated) signals incident on the array. Spatial smoothing through forward/backward averaging is used to decorrelate the signals. The estimations are made using 500 samples of data and the rms error is computed by averaging over 200 repeated computations.....	93
Figure 4.19: Comparison of MDL,AIC, GMDL, GAIC detection for a six element uniform linear array with equal powered uncorrelated sources incident 10 degrees apart from each other with the first source at 90 degrees, second source at 100 degrees, and so on. The probability of detection error computed as a relative frequency over 200 trials is plotted as a function of the number of samples used in the detection scheme. The signal-to-noise ratio was 10 dB.....	95
Figure 4.20: Comparison of MDL,AIC, GMDL, GAIC detection for a six element uniform linear array with uncorrelated sources incident 10 degrees apart from each other with the first source at 90 degrees, second source at 100 degrees, and so on. The probability of detection error computed as a relative frequency over 200 trials is plotted as a function of the signal-to-noise ratio. 100 samples of the input data was used to estimate the DOA. . .	96
Figure 4.21: Comparison of the modified MDL,AIC detection for a six element uniform linear array with coherent sources of equal power incident 10 degrees apart from each other with the first source at 90 degrees, second source at 100 degrees, and so on. The probability of detection error computed as a relative frequency over 200 trials is plotted as a function of number of samples of data used. The input signal-to-noise ratio was 10 dB. . .	97
Figure 4.22: Comparison of MDL,AIC detection for a six element uniform linear array with coherent sources incident 10 degrees apart from each other with the first source at 90 degrees, second source at 100 degrees, and so on. The probability of detection error computed as a relative frequency over 200 trials is plotted as a function of the signal-to-noise ratio. . .	98
Figure 5.1: A block diagram of the DOA measurement system.	101
Figure 5.2: Photograph of the six element uniformly spaced linear array receiver used for DOA measurements.	102
Figure 5.3: Flowchart illustrating the frame synchronization process	106
Figure 5.4: Hardware setup for the RF chain phase calibration	109

Figure 5.5: Flowchart illustrating the off-line processing steps	113
Figure 5.6: Flowchart illustrating the TLS-ESPRIT algorithm for DOA estimation	114
Figure 5.7: Flow chart illustrating the integrated ILSP-CMA with TLS-ESPRIT algorithm for DOA estimation.....	115
Figure 6.1: DOA Measurement Results - RMS Error in DOA Estimation as a function of the angle of arrival. RMS error is computed as the absolute difference between the estimated and actual angle of arrival	120
Figure 6.2: Illustration of a the DOA measurement setup with three uncorrelated signals being transmitted at different angles with respect to the receiver array location.	121
Figure 6.3: DOA Measurement Results - RMS Error in DOA estimation as a function of angle of separation between the two uncorrelated sources. The first signal arrives at 10 degrees and the second signal arrives at $10 + \Delta\theta$ degrees.....	122
Figure 6.4: DOA Measurement Results - RMS Error in DOA estimation as a function of angle of separation between the two uncorrelated signals. The first signal arrives at 30 degrees and the second signal arrives at $30 + \Delta\theta$ degrees.....	123
Figure 6.5: DOA Measurement Results - RMS Error in DOA estimation as a function of angle of separation between adjacent uncorrelated signals. The first signal arrives at 30 degrees, the second signal arrives at $30 + \Delta\theta$ degrees and the third signal arrives at $30 + 2\Delta\theta$ degrees.	123
Figure 6.6: DOA Measurement Results - RMS Error in DOA estimation as a function of angle of separation between the two uncorrelated signals. The first signal arrives at 60 degrees and the second signal arrives at $60 + \Delta\theta$ degrees.	124
Figure 6.7: DOA Measurement Results - RMS Error in DOA estimation as a function of angle of separation between adjacent uncorrelated signals. The first signal arrives at 60 degrees, the second signal arrives at $60 + \Delta\theta$ degrees, and the third signal arrives at $60 + 2\Delta\theta$ degrees.	124
Figure 6.8: DOA Measurement Results - RMS Error in DOA estimation as a function of angle of separation between the two uncorrelated signals. The first signal arrives at 90 degrees and the second signal arrives at $90 + \Delta\theta$ degrees.	125
Figure 6.9: DOA Measurement Results - RMS Error in DOA estimation as a function of angle of separation between adjacent uncorrelated signals. The first signal arrives at 90 degrees, the second signal arrives at $90 + \Delta\theta$ degrees, and the third signal arrives at $90 + 2\Delta\theta$ degrees.	125
Figure 6.10: Illustration of a the DOA measurement setup with three correlated (fully coherent) signals being transmitted at different angles with respect to the receiver array location.....	127

Figure 6.11: DOA Measurement Results - RMS Error in DOA estimation as a function of angle of separation between the two fully correlated (coherent) signals. The first signal arrives at 30 degrees and the second signal arrives at $30+\Delta\theta$ degrees.....	128
Figure 6.12: DOA Measurement Results - RMS Error in DOA estimation as a function of angle of separation between the two fully correlated (coherent) signals. The first signal arrives at 60 degrees and the second signal arrives at $60+\Delta\theta$ degrees.....	128
Figure 6.13: DOA Measurement Results - RMS Error in DOA estimation as a function of angle of separation between the two fully correlated (coherent) signals. The first signal arrives at 60 degrees, the second signal arrives at $60+\Delta\theta$ degrees, and the third signal arrives at $60+2\Delta\theta$ degrees.	129
Figure 6.14: DOA Measurement Results - RMS Error in DOA estimation as a function of angle of separation between the two fully correlated (coherent) signals. The first signal arrives at 90 degrees and the second signal arrives at $90+\Delta\theta$ degrees.	129
Figure 6.15: DOA Measurement Results - RMS Error in DOA estimation as a function of angle of separation between the two fully correlated (coherent) signals. The first signal arrives at 90 degrees, the second signal arrives at $90+\Delta\theta$ degrees, and the third signal arrives at $90+2\Delta\theta$ degrees.	130
Figure 6.16: Figure showing sample power delay profiles corresponding to two transmitter locations. The first profile was obtained when the transmitter was located at 20 degrees with respect to the receiver, and the subsequent ones were measured when it was located at 120, 90, and 150 degrees respectively.	134
Figure 6.17: Figure showing the single bounce multipath rays incident on the array when a single transmitter antenna is located at 20 degrees with respect to the receiver array axis. Using ray tracing it was found that for all transmitter locations, there were at least three multipath components that were about 15 to 20 dB below the line-of-sight component.	136
Figure 6.18: Simulation Results - Figure illustrates the RMS error in estimating the DOA of a single source under RF chain phase errors, sensor location errors, and multipath in channel.	137
Figure 6.19: Simulation Results -Figure illustrates the RMS error in estimating the DOA of two uncorrelated signals arriving at 10 and $10+\Delta\theta$ degrees respectively, under RF chain phase errors, sensor location errors, and multipath in channel.	138
Figure 6.20: Simulation Results - Figure illustrates the RMS error in estimating the DOA of two uncorrelated signals arriving at 30 and $30+\Delta\theta$ degrees respectively, under RF chain phase errors, sensor location errors, and multipath in channel.....	140
Figure 6.21: Simulation Results - Figure illustrates the RMS error in estimating the DOA of three uncorrelated signals arriving at 30, $30+\Delta\theta$, and $30+2\Delta\theta$ degrees respectively, under RF chain phase errors, sensor location errors, and multipath in channel.....	140

- Figure 6.22:** Simulation Results - Figure illustrates the RMS error in estimating the DOA of two uncorrelated signals arriving at 60 and $60+\Delta\theta$ degrees respectively, under RF chain phase errors, sensor location errors, and multipath in channel.141
- Figure 6.23:** Simulation Results - Figure illustrates the RMS error in estimating the DOA of three uncorrelated signals arriving at 60 , $60+\Delta\theta$, and $60+2\Delta\theta$ degrees respectively, under RF chain phase errors, sensor location errors, and multipath in channel.141
- Figure 6.24:** Simulation Results - Figure illustrates the RMS error in estimating the DOA of two uncorrelated signals arriving at 90 and $90+\Delta\theta$ degrees respectively, under RF chain phase errors, sensor location errors, and multipath in channel.142
- Figure 6.25:** Simulation Results -Figure illustrates the RMS error in estimating the DOA of three uncorrelated signals arriving at 90 , $90+\Delta\theta$, and $90+2\Delta\theta$ degrees respectively, under RF chain phase errors, sensor location errors, and multipath in channel.142
- Figure 6.26:** Simulation Results -Figure illustrates the RMS error in estimating the DOA of two coherent signals arriving at 30 and $30+\Delta\theta$ degrees respectively, under RF chain phase errors, sensor location errors, and multipath in channel.143
- Figure 6.27:** Simulation Results -Figure illustrates the RMS error in estimating the DOA of two coherent signals arriving at 60 and $60+\Delta\theta$ degrees respectively, under RF chain phase errors, sensor location errors, and multipath in channel.144
- Figure 6.28:** Simulation Results -Figure illustrates the RMS error in estimating the DOA of three coherent signals arriving at 60 , $60+\Delta\theta$, and $60+2\Delta\theta$ degrees respectively, under RF chain phase errors, sensor location errors, and multipath in channel.144
- Figure 6.29:** Simulation Results -Figure illustrates the RMS error in estimating the DOA of two coherent signals arriving at 90 and $90+\Delta\theta$ degrees respectively, under RF chain phase errors, sensor location errors, and multipath in channel.145
- Figure 6.30:** Simulation Results -Figure illustrates the RMS error in estimating the DOA of three coherent signals arriving at 90 , $90+\Delta\theta$, and $90+2\Delta\theta$ degrees respectively, under RF chain phase errors, sensor location errors, and multipath in channel.145

Chapter 1

Introduction

1.1 Motivation

Direction of arrival (DOA) estimation or *direction finding* has been an active area of research for a long time. Historically, direction finding techniques have found application in the field of radar, sonar, electronic surveillance and seismic exploration. In radar applications, they are useful for air traffic control and target acquisition[Hay85]. Intelligence agencies use them for covert location of transmitters and signal interception. Direction finding also finds application in position location and tracking systems.

More recently, direction of arrival estimation has become important in mobile radio communications [Mat89]. For example, it is useful in determining the multipath structure of radio channels. Channel models incorporate the angle of arrival statistics along with the time of arrival statistics to more accurately characterize multipath radio channels [Lib96]. Such characterization is especially important in analyzing communication systems which employ some form of spatial filtering using sectorized directional antennas, switched beam antennas, or adaptive antennas[Lib95].

Estimation of angle of arrival of multiple signals and their multipath components is important in systems employing adaptive antenna arrays for signal extraction in interference environments. Adaptive antenna systems are capable of automatically forming beams in the directions of the desired signal and steering nulls in the direction of the interfering signals. Direction finding techniques can be used to estimate the directions of the desired and interfering signals, so that they can be separated using appropriate spatial filtering. DOA based beamforming techniques are particularly suited for wireless communication systems which utilize different frequencies for uplink and downlink transmissions. Due to the difference in frequencies, the beamforming weights for the smart uplinks cannot be directly mapped to the downlink. However, since the directions of arrival of a signal does not change as rapidly as the spatial signature of the signal does, DOA based beamforming offers some advantages over spatial signature based beamforming [Big95][Xu94C].

With the FCC mandating that the Enhanced 911 (E-911) services, which include location identification, be made available to mobile users, there is a great deal of research interest in developing reliable position location techniques [Bla94]. One technique which offers great promise is that based on direction finding algorithms [Ken95][TR45].

1.2 Objective and Outline of Thesis

The aim of this project is to build a direction-of-arrival measurement system using an antenna array operating in the 2050 MHz band and verify the performance of some high resolution DOA estimation algorithms.

The first phase of the project is an extensive study of various high resolution DOA estimation algorithms. The algorithms studied include subspace-based techniques such as the MUSIC (MULTiple Signal Classification) and ESPRIT (Estimation of Signal Parameters via Rotational Invariance) algorithms, and the integrated approaches which combine property restoral-based techniques such as the Iterative Least Squares Projection-based Con-

stant Modulus Algorithm (ILSP-CMA) with the subspace-based techniques. All these algorithms were simulated in MATLAB and their performance under different conditions were tested and compared. These algorithms were evaluated for their accuracy in DOA estimation, ability to resolve closely spaced signals, performance under various angle spread and power spread, and performance under coherent signal conditions.

In the second phase of the project a six element uniformly spaced linear array receiver was built. Three Ariel DSP-96 boards based on the Motorola DSP96002 are used to simultaneously sample, collect, and store data from each of the array elements. The data collected by the DSP boards are processed off-line to estimate the directions of arrival. Several experiments are conducted to test the functioning of the system under various conditions, and demonstrate the performance of different algorithms. The results of these experiments are presented in this thesis.

This thesis is organized as follows. Chapter 2 introduces the fundamentals of antenna arrays, and some basic terminology and notations. It also provides an overview of some adaptive algorithms. Chapter 3 provides a detailed survey of various direction-of-arrival estimation algorithms. The algorithms detailed include the conventional beamforming type of algorithms, the high resolution subspace based algorithms, maximum likelihood algorithms, and the integrated approaches which combine property restoral techniques with the subspace based techniques. Spatial smoothing techniques that are necessary for direction finding in coherent multipath are also described. Chapter 3 also provides a brief survey of source order estimation algorithms.

Chapter 4 presents the results of various simulations that were conducted to evaluate the performance of various direction-of-arrival and source order estimation algorithms. A detailed comparison of the performance of these algorithms under different conditions is made in this chapter.

Chapter 5 provides a detailed description of the hardware and software developed for direction-of-arrival measurements at 2050 MHz. Chapter 6 describes the experiments conducted to perform direction-of-arrival measurements, and presents the results of the measurements. Chapter 6 also presents a simulation based study of the effect of various errors in DOA estimation.

A brief summary and conclusion is provided in Chapter 7 along with some suggestions for future work.

Chapter 2

Antenna Arrays - Background Theory

2.1 Fundamentals of Antenna Arrays

An *array antenna* or an *array* is a configuration of multiple antenna elements arranged and interconnected in space to obtain a directional radiation pattern. Arrays built using small antenna elements achieve the same level of performance as that of a single large antenna, by trading the electrical problems of feeding for mechanical simplicity. It is possible, using arrays, to electronically scan the main beam and/or place nulls in any direction by changing the phase of the exciting currents in each of the antenna elements. An array which does this is called a *phased array* [Stu81].

Arrays can be constructed in various types of geometric configurations. A *linear array* is the most elementary form of arrangement in which the centers of the elements of the array are aligned along a straight line. A *planar array* is one in which the centers of the array elements lie on a single plane. Planar arrays could be circular, rectangular or arbitrarily shaped. Arrays whose element locations conform to a given nonplanar surface are called *conformal arrays*.

The radiation pattern of an array is determined by the radiation pattern of the individual

elements, their orientation and relative positions in space, and the amplitude and phase of the feeding currents. If each element of the array is an isotropic point source, then the radiation pattern of the array will depend solely on the geometry and feeding current of the array, and the radiation pattern so obtained is called the *array factor*. If each of the elements of the array are similar but non-isotropic, by the principle of *pattern multiplication*, the radiation pattern can be computed as a product of the array factor and the individual element pattern [Stu81].

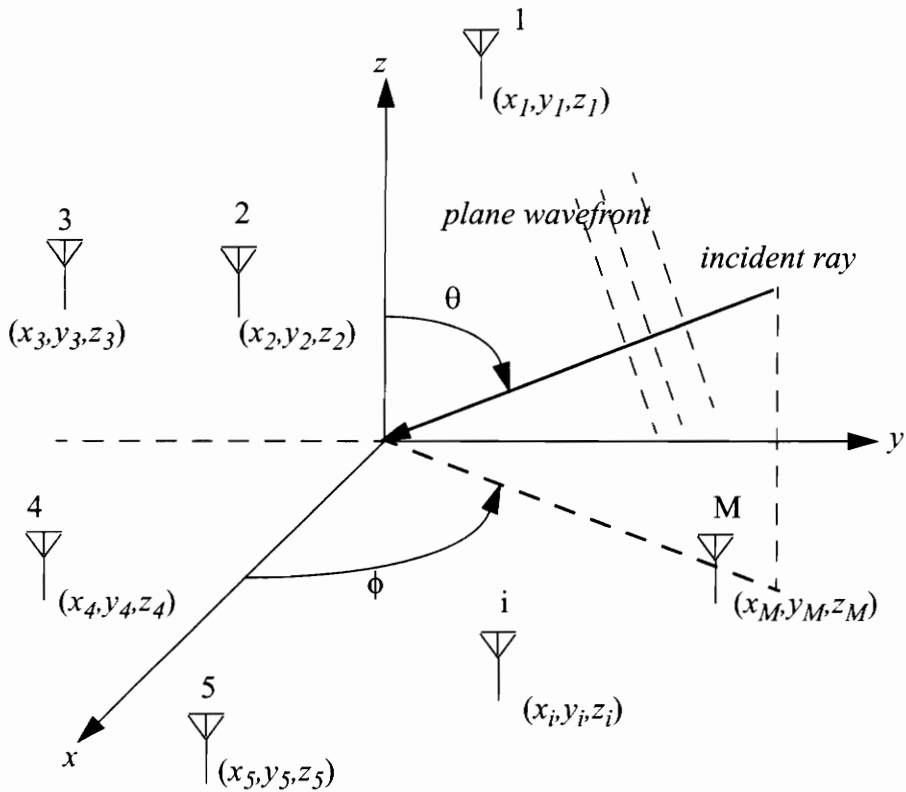


Figure 2.1: Illustration of an array with antenna elements located at arbitrary locations in space.

Figure 2.1 shows an array of M elements distributed arbitrarily in space. Consider a narrowband signal $\tilde{s}(t)$ having a frequency ω_0 , and arriving at an angle θ and ϕ with respect to the z -axis and x -axis, respectively. The narrowband signal may be expressed as

$$\tilde{s}(t) = u(t)\cos(\omega_0 t + v(t)) \quad (2.1)$$

where $u(t)$ and $v(t)$ are slowly varying functions of time that define the amplitude and phase, respectively, of $\tilde{s}(t)$. In the array context, slowly varying implies that the amplitude and phase variations as functions of spatial position for fixed t are negligible over the extent of the array. That is, the approximation

$$\tilde{s}(t - \tau) \approx u(t)\cos\{\omega_0(t - \tau) + v(t)\} \quad (2.2)$$

is valid for the all time τ required by the signal to travel over the extent of the array. It is convenient to express the narrowband signal in complex envelope representation, in which $\tilde{s}(t) = Re\{s(t)\}$, where

$$s(t) = u(t)\exp\{-j[\omega_0 t + v(t)]\} \quad (2.3)$$

Assuming that the propagation medium does not significantly effect the signal as it propagates from one end to the array to the other, the signal received at one sensor differs from that of the other only by a delay. As seen from Figure 2.1, the delay depends on the relative position of the sensors and on the angle of arrival. If we take the origin of the rectangular coordinate system as the reference location, and the i th antenna element to be located at (x_i, y_i, z_i) , the delay τ_i of the signal at the i th sensor relative to the signal at the reference location can be expressed as

$$\tau_i = \frac{[x_i \sin \theta \cos \phi + y_i \sin \theta \sin \phi + z_i \cos \theta]}{c} \quad (2.4)$$

where c is the velocity of light. However, since the signal is a narrowband complex signal (analytic signal), the effect of the propagation delay τ_i is simply a phase shift $\zeta_i = -\omega_0 \tau_i$, i.e.,

$$s(t - \tau_i) = s(t)\exp(j\zeta_i) = s(t)\exp(-j\omega_0 \tau_i) \quad (2.5)$$

where the phase shift ζ_i is given by [Col69]

$$\begin{aligned}\zeta_i &= \frac{\omega}{c}(x_i \sin \theta \cos \phi + y_i \sin \theta \sin \phi + z_i \cos \theta) \\ &= \frac{2\pi}{\lambda}(x_i \sin \theta \cos \phi + y_i \sin \theta \sin \phi + z_i \cos \theta)\end{aligned}\quad (2.6)$$

and λ is the wavelength of the incident signal. Now, if the signal received at sensor (antenna element) locations $1, 2, \dots, M$ are designated x_1, x_2, \dots, x_M respectively, the analytic signal received at the array can be expressed in vector form as

$$\mathbf{x}(t) = \begin{bmatrix} x_1(t) \\ x_2(t) \\ \dots \\ x_M(t) \end{bmatrix} = \begin{bmatrix} e^{j\zeta_1} \\ e^{j\zeta_2} \\ \dots \\ e^{j\zeta_M} \end{bmatrix} s(t) \quad (2.7)$$

The vector $\mathbf{x}(t)$ is often referred to as the array *input data vector* or the *illumination vector*. In equation (2.7) the phase shifts are assumed to be solely due to the spatial separation between the array elements. In a more general sense, the array elements will themselves have a directional and frequency dependent response. This can be modeled by applying differing gains and phases to the elements of the vector in (2.7). If the direction and frequency dependent gain and phase of the i th antenna element is denoted by $g_i(\omega, \theta, \phi)$, the analytic signal at the array output can be expressed as

$$\mathbf{x}(t) = \begin{bmatrix} x_1(t) \\ x_2(t) \\ \dots \\ x_M(t) \end{bmatrix} = \begin{bmatrix} g_1(\omega, \theta, \phi) e^{j\zeta_1(\omega, \theta, \phi)} \\ g_2(\omega, \theta, \phi) e^{j\zeta_2(\omega, \theta, \phi)} \\ \dots \\ g_M(\omega, \theta, \phi) e^{j\zeta_M(\omega, \theta, \phi)} \end{bmatrix} = \mathbf{a}(\omega, \theta, \phi) s(t) \quad (2.8)$$

where the vector

$$\begin{aligned}
 \mathbf{a}(\omega, \theta, \phi) &= \begin{bmatrix} g_1(\omega, \theta, \phi)e^{j\zeta_1(\omega, \theta, \phi)} \\ g_2(\omega, \theta, \phi)e^{j\zeta_2(\omega, \theta, \phi)} \\ \dots \\ g_M(\omega, \theta, \phi)e^{j\zeta_M(\omega, \theta, \phi)} \end{bmatrix} \\
 &= \begin{bmatrix} g_1(\omega, \theta, \Phi)e^{j\frac{\omega}{c}(x_1 \sin \theta \cos \phi + y_1 \sin \theta \sin \phi + z_1 \cos \theta)} \\ g_2(\omega, \theta, \Phi)e^{j\frac{\omega}{c}(x_2 \sin \theta \cos \phi + y_2 \sin \theta \sin \phi + z_2 \cos \theta)} \\ \dots \\ g_M(\omega, \theta, \Phi)e^{j\frac{\omega}{c}(x_M \sin \theta \cos \phi + y_M \sin \theta \sin \phi + z_M \cos \theta)} \end{bmatrix} \tag{2.9}
 \end{aligned}$$

is called the *steering vector*. Equation (2.9) represents the general form of the *steering vector* for an array. As seen from (2.9), the steering vector (also called *direction vector*, *array vector* or *aperture vector*) is a function of the individual element response, the array geometry, signal frequency, and the angle-of-arrival. The collection of array vectors for all angles (θ, ϕ) and frequencies ω is referred to as the *array manifold*. (Some authors in the literature refer to the individual steering vectors themselves as the array manifold). Though for many simple arrays the array manifold can be computed analytically, in practice, the array manifold is measured as point source responses of the array at various angles and frequencies. This process of obtaining the array manifold is called *array calibration*.

If the frequency band of interest is sufficiently narrow, the steering vector $\mathbf{a}(\omega, \theta, \phi)$ is approximately constant with respect to ω over the band of interest for all angles (θ, ϕ) . This condition is satisfied, if the sensor characteristics do not vary significantly across this bandwidth. Such an array is called a *narrowband array*. In most of the discussion that follows, the array is assumed to be narrowband unless specified otherwise, and for

simplicity the steering vectors of narrowband arrays are denoted by $\mathbf{a}(\theta, \phi)$ with the frequency dependence dropped.

The input data model of equation (2.8) can be extended to the more general case of multiple signals and interference impinging on the array by decomposing the input signal in the frequency domain and using linear supersposition.

$$\mathbf{x}(\omega) = \sum_{i=1}^D \mathbf{a}(\omega, \theta_i, \phi_i) s_i(\omega) + \mathbf{n}(\omega) \quad (2.10)$$

Using matrix notation, this can be represented as

$$\mathbf{x}(\omega) = \begin{bmatrix} & \\ \mathbf{a}(\omega, \theta_1, \phi_1) & \dots & \mathbf{a}(\omega, \theta_D, \phi_D) \end{bmatrix} \begin{bmatrix} s_1(\omega) \\ \dots \\ s_D(\omega) \end{bmatrix} + \mathbf{n}(\omega) \quad (2.11)$$

or

$$\mathbf{x}(\omega) = \mathbf{A}(\omega, \Theta, \Phi) \mathbf{s}(\omega) + \mathbf{n}(\omega) \quad (2.12)$$

where D signals $s_1(\omega), \dots, s_D(\omega)$ arrive from angles $(\theta_1, \phi_1), \dots, (\theta_D, \phi_D)$ respectively and $\mathbf{n}(\omega)$ represents the interference and noise components. If the frequency band of interest is sufficiently narrow to categorize the array as a narrowband array, the dependence on ω can be dropped and the array data can be modeled in the time domain as the analytic signal

$$\mathbf{x}(t) = \sum_{i=1}^D \mathbf{a}(\theta_i, \phi_i) s_i(t) + \mathbf{n}(t) \quad (2.13)$$

which can be written using matrix notation as,

$$\mathbf{x}(t) = \mathbf{A}(\Theta) \mathbf{s}(t) + \mathbf{n}(t) \quad (2.14)$$

Equation (2.14) represents the most commonly used *narrowband input data model* for analyzing data obtained from an antenna array.

2.1.1 Uniformly Spaced Linear Array

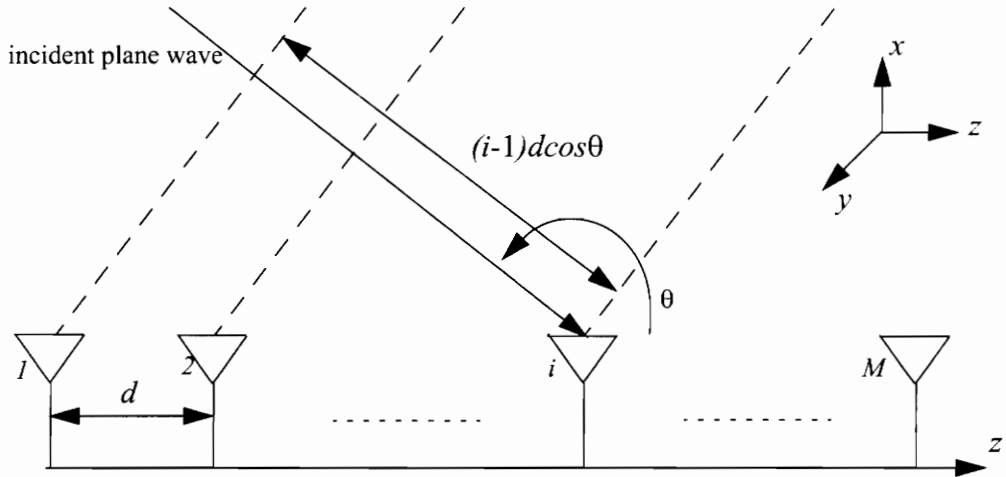


Figure 2.2: Illustration of a plane wave incident on a linear equispaced array. The dotted lines represent the phase fronts of the incident wave.

For the case of the uniformly spaced linear array lying along the z -axis as shown in Figure 2.2, the steering vector can be computed by simplifying equation (2.9) as follows. Let the first antenna element be located at the reference location, i.e $(x_1, y_1, z_1) = (0, 0, 0)$. The incoming plane wave at element 2 travels a distance longer by an amount equal to $d\cos\theta$ with respect to the wave arriving at the first element, and hence arrives later. Using (2.6), the corresponding phase lag of the plane wave arriving at element 2 with respect to that at element 1 is $\zeta_2 = \beta d \cos\theta$, where β is the phase propagation factor given by $2\pi/\lambda$. By the same argument, $\zeta_3 = \beta 2d \cos\theta$, $\zeta_4 = \beta 3d \cos\theta$, and so on. Hence, using equation (2.9) the steering vector for the uniformly spaced linear array comprising of isotropic antenna elements can be written as

$$\mathbf{a}(\theta) = \begin{bmatrix} 1 \\ e^{j\beta d \cos\theta} \\ \dots \\ e^{j\beta(M-1)d \cos\theta} \end{bmatrix} \quad (2.15)$$

Note that for the case of the linear array, the steering vector is independent of the elevation angle ϕ . Further, the steering vector of the uniformly spaced linear array of isotropic elements is a Vandermonde vector (vector having the form $\begin{bmatrix} 1 & \lambda & \lambda^2 & \lambda^3 & \dots & \lambda^M \end{bmatrix}^T$), and this fact is exploited by many array-based direction of arrival estimation algorithms.

2.1.2 Spatial Signature

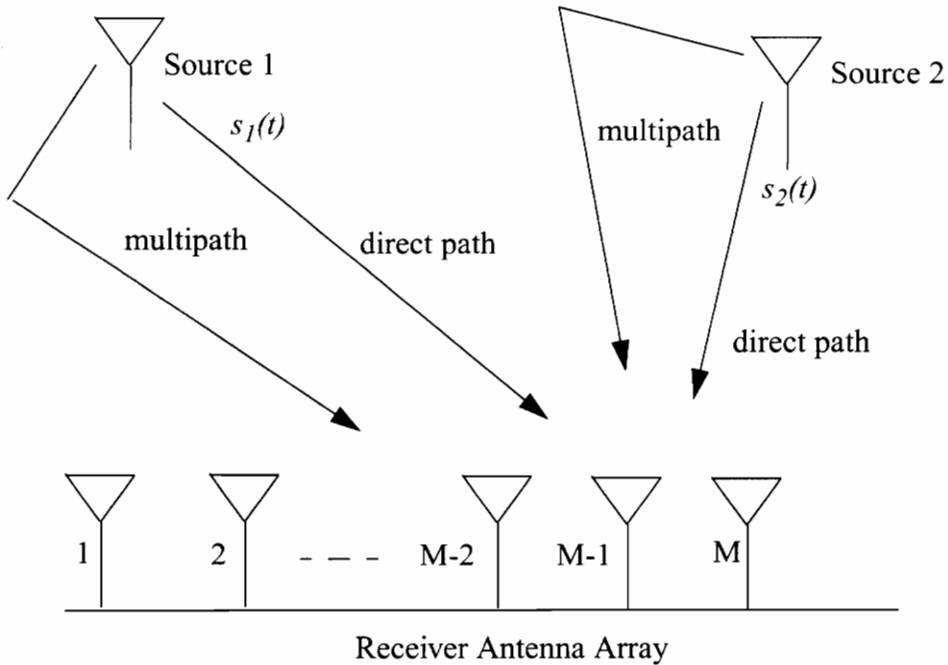


Figure 2.3: Direct and multipath signals from multiple sources impinging on a receiver antenna array.

Consider an M -element antenna array receiving signals from users located at different positions. The signals impinging on the array may contain both direct path and multipath components of multiple sources, and each of these components may be from different directions of arrival. Following the narrowband data model discussed in section 2.1, the array input data vector corresponding to one source, say the k th source, may be written as

$$\mathbf{x}_k = \mathbf{a}(\theta_1)s_k + \sum_{l=2}^{N_{mp}} c_l \mathbf{a}(\theta_l)s_k = \mathbf{a}_{ss,k}s_k \quad (2.16)$$

where $N_{mp}-1$ is the total number of multipath signals (excluding direct path), c_l is the amplitude and phase difference between the l th multipath and the direct path, $\mathbf{a}(\theta)$ is the array steering vector corresponding to the angle of arrival θ , and s_k is the first (line-of-sight) component of the signal from the k th source. The vector $\mathbf{a}_{ss,k}$ defined by

$$\mathbf{a}_{ss,k} = \mathbf{a}(\theta_1) + \sum_{l=2}^{N_{mp}} c_l \mathbf{a}(\theta_l) \quad (2.17)$$

is called the *spatial signature* of the signal s_k . Note that the above model assumes that all the multipath components arrive within a time window which is much less than the inverse bandwidth of the signal so that the multipath components differ only in phase shift, and not in delay. This of course follows directly from the narrowband assumption.

Now, if there are D sources present, then the array input data vector can be expressed as

$$\mathbf{x}(k) = \sum_{i=1}^D \mathbf{a}_{ss,i}(k)s_i(k) + \mathbf{n}(k) \quad (2.18)$$

or equivalently,

$$\mathbf{X}(k) = \mathbf{A}(\Theta)\mathbf{s}(k) + \mathbf{n}(k) \quad (2.19)$$

where $\mathbf{A}(\Theta)$ is the *spatial signature matrix* and $\mathbf{s}(k)$ is the $D \times 1$ signal vector comprising of signals from D different sources.

The correlation between the signals impinging on the array has a significant effect on the performance of algorithms used to process the received signal. For example, many direction-of-arrival estimation algorithms will fail completely when there are two or more signals that are fully correlated. The correlation coefficient may be used to quantify the degree of correlation between signals. Two zero mean signals s_i and s_j are said to be *uncorrelated* or *noncoherent* if their *correlation coefficient* defined by

$$\rho = \frac{E[s_i s_j]}{\sqrt{E[s_i^2] E[s_j^2]}} \quad (2.20)$$

is equal to zero, and *fully correlated* or *coherent* if $|\rho| = 1$, with values of $|\rho|$ in between zero and unity indicating partial correlation (Assuming ergodicity, the expectation operation may be replaced by a time averaging operation in the above definition). For example, multipath signals which are attenuated and phase shifted versions of one another are coherent signals, and signals from two different users are in general uncorrelated.

2.2 Beamforming and Spatial filtering

An antenna array essentially provides a means of *sampling* the received signal *in space*. By processing the sampled signals, it is possible to estimate the parameters of the signal such as the direction-of-arrival, and also achieve spatial discrimination through filtering. The techniques employed for parameter estimation and spatial filtering have a lot in common.

Analogous to performing filtering on a set of data sampled in time to obtain a specific frequency response, it is possible to process the spatially sampled data to obtain a desired spatial response through a process called *spatial filtering*. Through spatial filtering it is possible to separate a desired signal from interference even if they occupy the same frequency band at the same time, as long as they are spatially separated. A processor used in conjunction with an array of sensors to obtain some form of spatial filtering is called a *beamformer*. Typically a beamformer linearly combines the spatially sampled data from each sensor to obtain a scalar output in the same manner that an FIR filter linearly combines temporally sampled data [Van88].

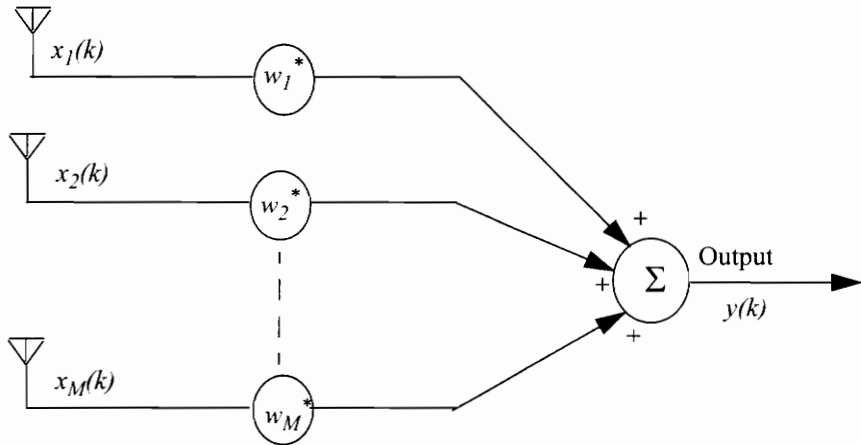


Figure 2.4: A narrowband beamformer whose output is a complex weighted sum of the spatially sampled input data.

Figure 2.4 shows a linear combiner beamformer which is typically used to process narrowband signals. As shown in Figure 2.4, the output of each element is multiplied by a complex factor called the element *weights*. The weights associated with all the elements are collectively represented as the *weight vector*.

$$\mathbf{w} = [w_1, w_2, \dots, w_M]^T \quad (2.21)$$

Note that the weights are represented as complex conjugates of the elements of the weight vector, and for the sake of consistency this notation shall be adhered to throughout this document. Also note that throughout this document lowercase bold letters represent vectors, and uppercase bold letters represent matrices. Superscripts *, T, and H represent conjugate, transpose, and hermitian transpose (conjugate transpose) respectively.

In practice, the weights are built using attenuators and phase shifters at the RF front-end or IF, or as complex multiplying factors in baseband using digital processing. The output of the beamformer can be expressed as

$$y(k) = \sum_{i=1}^M w_i^* x_i(k) \quad (2.22)$$

or in matrix notation as

$$y(k) = \mathbf{w}^H \mathbf{x}(k) \quad (2.23)$$

By appropriately choosing the weight vector, the output of the array can be adjusted to discriminate between spatially separate signals. The resulting radiation pattern of the array is directly related to the weight vector and is given by

$$F(\theta, \phi, \omega) = |\mathbf{w}^H \mathbf{a}(\theta, \phi, \omega)| \quad (2.24)$$

If the array used in a narrowband M -element uniformly spaced linear array with an interelement spacing d , using (2.24) and (2.15) and assuming isotropic elements, the radiation pattern of the beamformer can be expressed as

$$F(\theta) = \left| \sum_{i=1}^M w_i^* e^{j\beta(i-1)d \cos \theta} \right| \quad (2.25)$$

As clearly seen from equations (2.24) and (2.25), the radiation pattern of the array can be adjusted by appropriately selecting the weight vector. Hence it is possible to form beams or steer nulls in any required direction by appropriately adjusting the complex weight vector.

2.3 Wideband Arrays

When only a narrowband of frequencies are of interest an array can be steered by simple phase shifting operations. Therefore, in narrowband arrays, the weights are made up of simple attenuators and phase shifters. However, when signals of significant frequency extent (wideband signals) are of interest, simple phase shifting will not suffice. Instead physical delay is required to accommodate the wide band of frequencies. Hence wideband systems need to sample the incoming wave in both space and time. Thus the wideband system requires spatio-temporal sampling and the processing of a large number of samples from each sensor, and as a result is more complex. Temporal sampling can be achieved by means of a tapped delay line in each antenna element [Gri83].

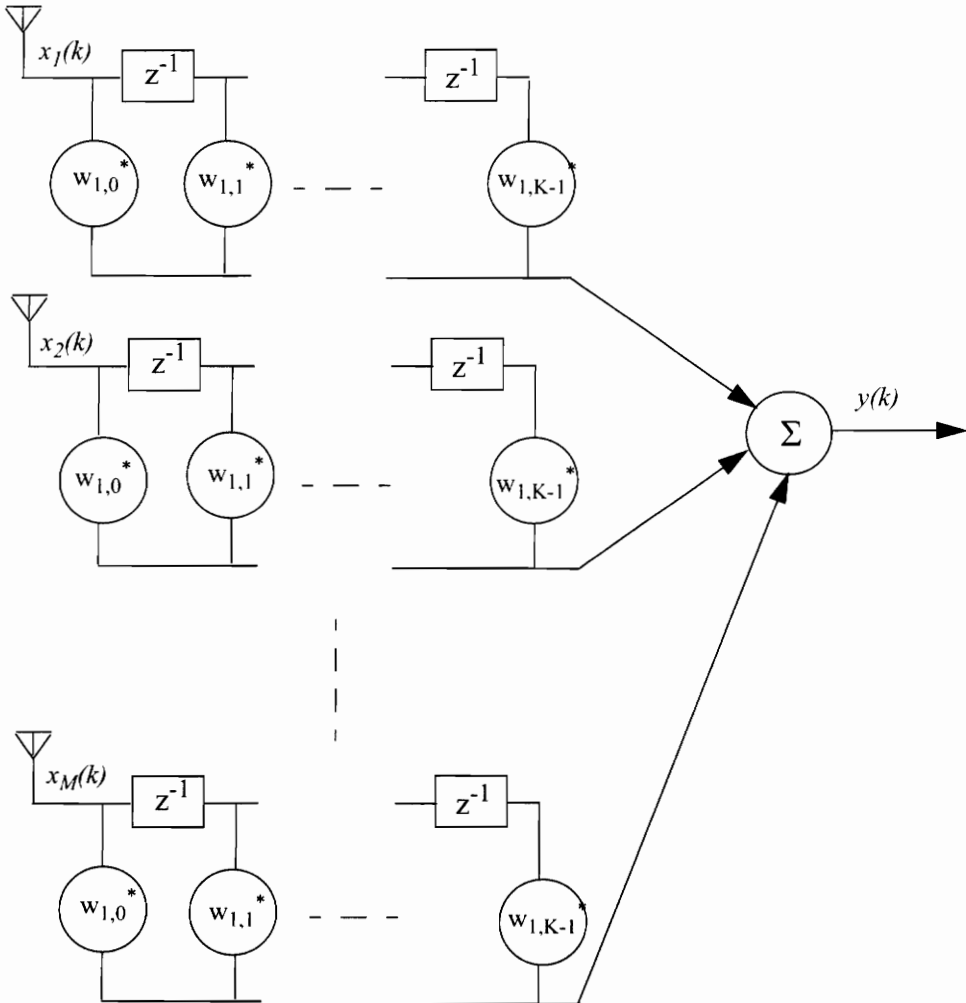


Figure 2.5: Illustration of a wideband array with a transversal filter attached to each antenna element.

Figure 2.5 shows an example of a wideband antenna array with a tapped delay line attached to each antenna element. The output of the array can be expressed as [Van88]

$$y(k) = \sum_{i=1}^{M-1} \sum_{p=0}^{K-1} w_{i,p}^* x_i(k-p) \quad (2.26)$$

where \$K-1\$ is the number of taps in the transversal filter. Consistent with the notation used in the narrowband case, the output of the wideband array can equivalently be expressed as

$$y(k) = \mathbf{w}^H \mathbf{x}(k) \quad (2.27)$$

where \mathbf{w} and $\mathbf{x}(k)$ are of dimension $1 \times KM$ and given by

$$\mathbf{w} = [w_{1,0}, w_{1,1}, \dots, w_{1,K-1}, \dots, w_{M,0}, w_{M,1}, w_{M,K-1}]^T \quad (2.28)$$

and

$$\mathbf{x}(k) = [x_{1,0}(k), \dots, x_{M,K-1}(k), \dots, x_{M,0}(k), \dots, x_{M,K-1}(k)] \quad (2.29)$$

2.4 Adaptive Arrays

An *adaptive array* is a system in which the radiation pattern of the array is adjusted continually to meet a certain performance criterion. Some of the most frequently used performance criteria are: minimum mean squared error (MSE), maximum signal-to-noise and interference ratio (SNIR), maximum likelihood (ML), minimum noise variance, minimum output power, maximum gain, etc. [Nic88]. Adaptive arrays are particularly suited for applications where the statistics of the signals and interference change continuously and are not known in advance. An adaptive array consists of an array of sensor elements whose weights are controlled by an adaptive processor which performs the optimization based on computations performed on the incoming signal.

An adaptive array as shown in Figure 2.6 is an example of an adaptive signal processing system [Wid89]. An M element array can be considered as a multiple input system, where at the k th sampling instant

$$\mathbf{x}_k = [x_{1k} \ x_{2k} \ \dots \ x_{Mk}]^T \quad (2.30)$$

is the array *input vector* or the array *illumination vector*, and

$$\mathbf{w}_k = [w_{1k} \ w_{2k} \ \dots \ w_{Mk}]^T \quad (2.31)$$

is the *weight vector*. Here the first subscript refers to the sensor number and the second subscript refers to the time index. Using this notation, the array output can now be written

as

$$y_k = \mathbf{x}_k^H \mathbf{w}_k = \mathbf{w}_k^H \mathbf{x}_k \quad (2.32)$$

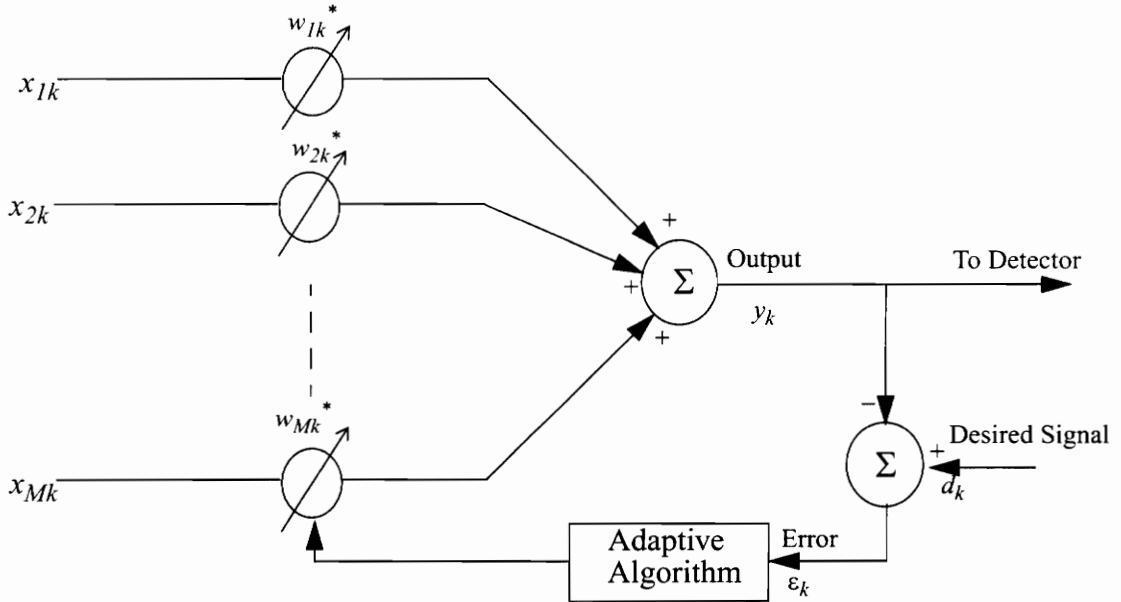


Figure 2.6: Illustration of a simple adaptive array

As illustrated in Figure 2.6, the weight vectors are computed by an adaptive algorithm. In general, the adaptive algorithm works to minimize a *cost function* which is set up to achieve a certain performance criterion. For the particular array shown in Figure 2.6 the weight vector computation depend on the output signal as well as a known “desired response” at the receiver. During the adaptation process a feedback system adjusts the weight vector such that the output, y_k , agrees as closely as possible with the desired response, d_k . This is done by computing the error signal, which is the difference between the output and the desired response, and adjusting the weight vector to minimize the mean squared error signal.

The mean square error in the adaptive system shown in Figure 2.6 is given by

$$MSE = E[\varepsilon_k^2] = E[d_k^2] + \mathbf{w}^H \mathbf{R}_{xx} \mathbf{w} - 2 \mathbf{r}_{xd}^H \mathbf{w} \quad (2.33)$$

From equation (2.33) it is clearly seen that the mean square error is a quadratic function of the weight vector \mathbf{w} . Figure 2.7 shows a typical two-dimensional mean square error function. The bowl shaped surface, called the *performance surface*, formed here is a paraboloid (a hyperparaboloid if there are more than two weights). With a quadratic performance surface there is only a single global minimum; no local minima exists. The goal of adaptive algorithms is to find the optimal weight vector \mathbf{w}_{opt} which corresponds to this minima.

The weight vector \mathbf{w}_{opt} which minimizes the mean squared error is given by the Wiener-Hopf solution [Wid89].

$$\mathbf{w}_{opt} = \mathbf{R}_{xx}^{-1} \mathbf{r}_{xd} \quad (2.34)$$

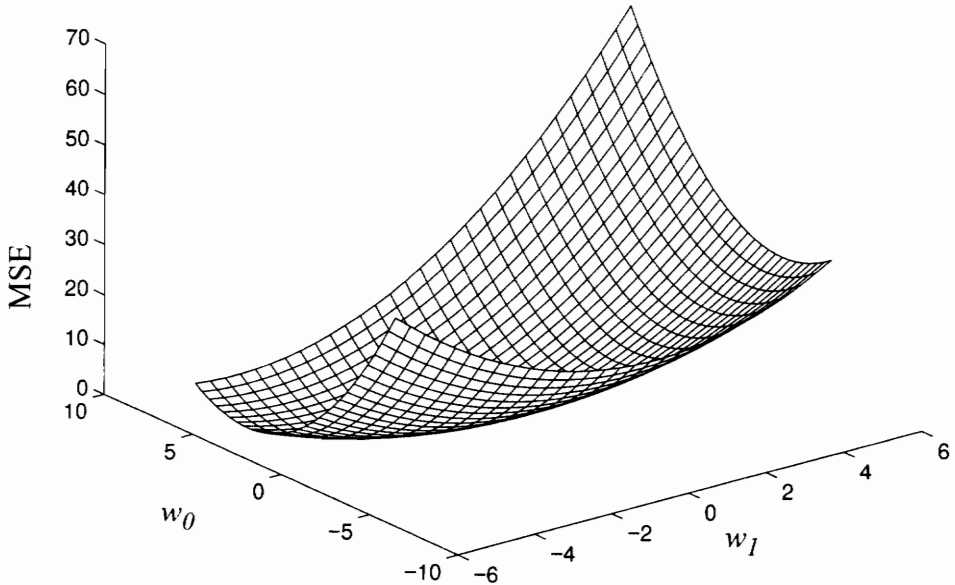


Figure 2.7: An example of a two dimensional quadratic performance surface

where \mathbf{R}_{xx} is the input correlation or covariance matrix, and \mathbf{r}_{xd} is the cross correlation

matrix between the input and the desired response. That is,

$$\mathbf{R}_{xx} = E[\mathbf{x}_k \mathbf{x}_k^H] = E \begin{bmatrix} x_{1k}^2 & x_{1k}^* x_{2k} & \dots & x_{1k}^* x_{Mk} \\ x_{2k}^* x_{1k} & x_{2k}^2 & \dots & x_{2k}^* x_{Mk} \\ \vdots & \vdots & \ddots & \vdots \\ x_{Mk}^* x_{1k} & x_{Mk}^* x_{2k} & \dots & x_{Mk}^2 \end{bmatrix} \quad (2.35)$$

$$\mathbf{r}_{xd} = E[d_k^* \mathbf{x}_k] = E[d_k^* x_{1k} \ d_k^* x_{2k} \ \dots \ d_k^* x_{Mk}]^T \quad (2.36)$$

\mathbf{R}_{xx} and \mathbf{r}_{xd} are in practice computed as time averages using samples collected over an observation period. If the input data is stationary, the adaptive array only needs to acquire enough data to make an adequate estimate of \mathbf{R}_{xx} and \mathbf{r}_{xd} . Once \mathbf{R}_{xx} and \mathbf{r}_{xd} are known, it is conceptually a simple matter to invert \mathbf{R}_{xx} and compute the optimum weight vector. However, since matrix inversion is a computationally expensive operation, the optimum weight vector is almost never computed this way. Iterative techniques such as the steepest descent and stochastic gradient methods are used instead [Wid89]. The steepest descent method computes the optimum weight vector using the following iterative equation.

$$\mathbf{w}_{k+1} = \mathbf{w}_k + \mu(-\nabla_k) \quad (2.37)$$

where μ is a constant that regulates the step size, and ∇_k is the gradient of the mean square error with respect to the weight vector (the slope of the performance surface). Stochastic gradient methods such as the Least Mean Squares (LMS) algorithm uses the same iterative equation with the true gradient replaced by the instantaneous gradient [Wid67].

2.5 The LMS Algorithm

As seen from section 2.4, the design of an adaptive array involves computing the optimum weight vector \mathbf{w}_{opt} . In order to compute the optimum weight vector it is required to find the minimum of the error performance surface. In most applications of interest, the parameters of the performance surface are not available in advance, and hence need to be estimated by averaging the squared error over a period of time. Various algorithms have

been developed to search the performance surface to locate the optimum weight vector.

Iterative methods of searching the performance surface entail the use of gradient estimates to indicate the direction in which the minimum of the surface lies. The steepest descent method of searching the performance surface has been widely used due to its ease of implementation. In the method of steepest descent, all components of the weight vector are changed in the direction of the negative gradient of the performance surface at each iteration. Moving in the direction of the negative gradient leads toward the minimum as long as the origin lies on one of the principal axes of the surface.

The method of steepest descent can be expressed in the form of the following iterative equation,

$$\mathbf{w}_{k+1} = \mathbf{w}_k + \mu(-\nabla_k) \quad (2.38)$$

where μ is a constant that regulates the step size and has dimensions of reciprocal signal power.

As seen from equation (2.38), the steepest descent method requires the estimation of the gradient of the performance surface. There are various procedures to obtain the gradient estimate. The most general method, called the derivative method, estimates the gradient of the mean square error (MSE) by taking the differences between short term averages of the squared error, ε_k^2 .

The Least Mean Square (LMS) algorithm is based on the method of steepest descent which uses the instantaneous value of ε_k^2 itself as an estimate of the mean square error [Wid67]. Therefore, at each iteration in the adaptation process, the gradient estimate is given by

$$\hat{\nabla}_k = \begin{bmatrix} \frac{\partial \varepsilon_k^2}{\partial w_0} \\ \vdots \\ \frac{\partial \varepsilon_k^2}{\partial w_{N-1}} \end{bmatrix} = 2\varepsilon_k \begin{bmatrix} \frac{\partial \varepsilon_k}{\partial w_0} \\ \vdots \\ \frac{\partial \varepsilon_k}{\partial w_{N-1}} \end{bmatrix} = -2\varepsilon_k \mathbf{x}_k \quad (2.39)$$

The derivatives of ε_k with respect to the weights follow directly from

$$\varepsilon_k = d_k - y_k = d_k - \mathbf{x}_k^H \mathbf{w} = d_k - \mathbf{w}^H \mathbf{x}_k \quad (2.40)$$

Using this estimate of the gradient, the LMS algorithm can be obtained from equation (2.38) as

$$\mathbf{w}_{k+1} = \mathbf{w}_k - \mu \hat{\nabla}_k = \mathbf{w}_k + 2\mu \varepsilon_k \mathbf{w}_k \quad (2.41)$$

Since it is based on a simple estimate of gradient, the LMS algorithm can be implemented without squaring, averaging, or differentiation, as would be required by the derivative methods. The greatest appeal of the LMS algorithms is its computational simplicity. However, since the gradient estimates are obtained without averaging, there would be a significant amount of noise in the estimate. The noise is attenuated with time by the adaptation process which acts as a low pass filter.

It can be shown that as the number of iterations increases without limit, the expected value of the weight vector computed by the LMS algorithm converges to the optimum Wiener-Hopf solution. Convergence to the optimum solution is ensured only if step size parameter μ is defined such that [Wid67]

$$|1 + 2\mu \lambda_{max}| < 1 \quad (2.42)$$

or

$$\frac{-1}{\lambda_{max}} < \mu < 0 \quad (2.43)$$

where λ_{max} is the maximum eigen value of the input covariance matrix \mathbf{R}_{xx} .

2.6 Property Restoral Algorithms

The computation of the weight vector using the techniques described so far require that the desired signal be known at the receiver. This entails an overhead in the form of training sequences or pilot signals. A relatively new class of algorithms referred to as *property restoral algorithms* or *blind algorithms* which do not require training, has been proposed and studied extensively. These algorithms are designed to exploit the fact that most signals used in communication systems, have known modulation properties that can be used to adapt the receiver processor. The properties commonly exploited include the constant envelope property of FM, PM, and FSK type of signals, finite alphabet property of digital signals, cyclostationarity of digital modulation signals, etc. The basic idea behind property restoral-based approaches is to find a weight vector \mathbf{w} such that the array output $y(k) = \mathbf{w}^H \mathbf{x}(k)$ has the desired property. Property restoral based methods can be used for signal extraction as well as parameter estimation.

2.6.1 The Constant Modulus Algorithm

The constant modulus algorithm was introduced as an adaptive filtering technique for correcting multipath and interference-induced degradations in constant envelope waveforms such as FM and QPSK signals [Tre83]. Since its inception, the CMA algorithm has been readily applied for spatial filtering as well [Goo86]. This algorithm is based on the premise that multipath and additive interference causes unwanted amplitude modulation on the transmitted signal, and hence destroys its constant envelope property. Therefore, by sensing the received signal envelope variations, it is possible to build an adaptive filter which will remove the channel-induced envelope variations and restore the constant modulus property of the signal, thereby removing the interference components from the desired signal. This is achieved by developing an algorithm to minimize a cost function which penalizes envelope variations.

The CMA cost function J has the general form

$$J = E[(\|y(k)\|^p - \delta^p)^q] \quad (2.44)$$

where p and q are positive integers, and $\delta > 0$ is the desired nominal level of the received signal envelope. Usually, δ is set to unity, and p and q take on values of one or two. The algorithm is generally referred to be of a “p-q” form such as “1-1”, “1-2”, “2-1”, and “2-2”.

A simple gradient search algorithm can be used to minimize the CMA cost function J . The method of steepest descent as given in equation (2.37) may be applied to obtain the following algorithm.

$$\mathbf{w}(k+1) = \mathbf{w}(k) - \mu \nabla J_k \quad (2.45)$$

For the case of $p = 2$, $q = 1$, $d = 1$, it can be shown that ∇J with respect to the weight vector \mathbf{w} is given by [Tre83]

$$\begin{aligned} \nabla J &= \frac{1}{2} E\{[|y(k)|^2 - 1] \nabla [\mathbf{w}^H \mathbf{x} \mathbf{x}^H \mathbf{w}]\} \\ &= E\{[|y(k)|^2 - 1] \mathbf{x}(k) \mathbf{x}^H(k) \mathbf{w}^*\} \\ &= E\{[|y(k)|^2 - 1] y^*(k) \mathbf{x}(k)\} \end{aligned} \quad (2.46)$$

Removing the expectation operation from (2.46) gives the instantaneous gradient estimate. Substituting the instantaneous gradient estimate in (2.45) the steepest descent CMA algorithm is obtained as

$$\mathbf{w}(k+1) = \mathbf{w}(k) - \mu \{[|y(k)|^2 - 1] y^*(k) \mathbf{x}(k)\} \quad (2.47)$$

By defining an error term

$$\varepsilon(k) = \{|y(k)|^2 - 1\} y(k) \quad (2.48)$$

equation (2.47) can be compactly expressed as

$$\mathbf{w}(k+1) = \mathbf{w}(k) - \mu \varepsilon^*(k) \mathbf{x}(k) \quad (2.49)$$

The 2-1 form of CMA as described above closely resembles the complex version of the

LMS algorithm. The only actual difference between the LMS algorithm and this version of CMA is that instead of using an externally applied reference signal to compute the error signal, the *a priori* knowledge that $y(k)$ would be unit modulus in the absence of multipath and interference is used to compute the error signal.

The other forms of the CMA algorithm corresponding to different values of p and q can be similarly derived. The resulting weight update equations are summarized below [Lar83].

$$\text{"1-1"} \quad \mathbf{w}(k+1) = \mathbf{w}(k) - \mu \mathbf{x}(k) \frac{\mathbf{y}^*(k)}{\|\mathbf{y}(k)\|} \operatorname{sgn}(\|\mathbf{y}(k)\| - \delta) \quad (2.50)$$

$$\text{"2-1"} \quad \mathbf{w}(k+1) = \mathbf{w}(k) - 2\mu \mathbf{x}(k) \mathbf{y}^*(k) \operatorname{sgn}(\|\mathbf{y}(k)\|^2 - \delta^2) \quad (2.51)$$

$$\text{"1-2"} \quad \mathbf{w}(k+1) = \mathbf{w}(k) - 2\mu \mathbf{x}(k) \frac{\mathbf{y}^*(k)}{\|\mathbf{y}(k)\|} (\|\mathbf{y}(k)\| - \delta) \quad (2.52)$$

$$\text{"2-2"} \quad \mathbf{w}(k+1) = \mathbf{w}(k) - 4\mu \mathbf{x}(k) \mathbf{y}^*(k) (\|\mathbf{y}(k)\|^2 - \delta^2) \quad (2.53)$$

Ever since its inception, the CMA algorithm has been studied in great detail [Lar83][Lar85][Tre85A][Tre85B][Kik94]. Due to the non-quadratic nature of the CMA cost function its convergence properties are not as intuitive as that of the LMS type algorithms. Existence of troughs in the cost function can cause the convergence to be extremely slow giving an appearance of a false solution. The convergence behavior of CMA under various conditions has been studied by [Lar83], [Age88], and [Tre85A].

The convergence of CMA can be significantly improved by pre-multiplying the input vector $\mathbf{x}(k)$ by the inverse of the input correlation matrix $\mathbf{R}_{xx} = E[\mathbf{x}\mathbf{x}^H]$. This has the effect of orthogonalizing the input correlation function. The resulting algorithm is called the orthogonalized CMA (O-CMA), and can be summarized as follows [Goo86]:

$$\mathbf{w}(k+1) = \mathbf{w}(k) + \mu \mathbf{R}_{xx}^{-1}(k+1) \mathbf{e}^*(k) \mathbf{x}(k) \quad (2.54)$$

where

$$\mathbf{R}_{xx}^{-1}(k+1) = \frac{\mathbf{R}_{xx}^{-1}(k)}{1-\alpha} - \frac{1}{1-\alpha} \left[\frac{\alpha \mathbf{R}_{xx}^{-1}(k) \mathbf{x}^H(k) \mathbf{R}_{xx}^{-1}(k)}{(1-\alpha) + \alpha \mathbf{x}^H(k) \mathbf{R}_{xx}^{-1}(k) \mathbf{x}(k)} \right] \quad (2.55)$$

Various other modifications to the CMA algorithm have been proposed to speed up the convergence rate, and to enable capture of multiple signals. Real arithmetic implementations of CMA and extensions of CMA to non-constant known modulus signals have also been studied by [Tre84], [Tre85B], and [Lun88]. Some of the improved CMA algorithms include techniques such as the Least-Squares CMA, Multitarget CMA [Age89a], Multistage CMA [Shy94][Sub89], and the Iterative Least Squares Projection-Based CMA [Tal94][Par95]. The Iterative Least Squares Projection Based CMA is discussed Chapter 3.

2.6.2 Spectral Coherence Restoral Algorithm

Most communication signals exhibit a property called *cyclostationarity* which can be exploited to achieve blind adaptive beamforming and improve the performance of signal parameter estimation algorithms. Cyclostationarity is a term used to describe the repetitive or cyclic nature of the statistics associated with communication signals. Periodicities in the second order statistics of a signal leads to the existence of a correlation between the random fluctuations of different frequency components. This property is called *spectral coherence*. A signal $s(t)$ is said to exhibit spectral correlation if it is correlated with a frequency shifted version of itself. That is, if the *cyclic autocorrelation function*, defined by [Gar91][Gar94]

$$R_{ss}^\alpha(\tau) = \langle s\left(t + \frac{\tau}{2}\right) \left\{ s\left(t - \frac{\tau}{2}\right) e^{j2\pi\alpha t} \right\}^* \rangle_\infty \quad (2.56)$$

is not identically zero for some cycle frequency α and some delay parameter τ . Most communication signals exhibit non-zero spectral correlation at one or more cycle frequencies (the doubled carrier frequency or the baud rate or chip rate, etc.), and are said to be *cyclostationary* [Gar87A][Gar87B]. The Fourier transform of the cyclic

autocorrelation function called the *cyclic spectral density*, and defined by

$$S_{ss}^{\alpha}(f) = \int_{-\infty}^{\infty} R_{ss}^{\alpha}(\tau) e^{-j2\pi f\tau} d\tau \quad (2.57)$$

provides a clear measure of both the location and degree of spectral correlation in a cyclostationary signal.

Various cost functions based on the cyclic autocorrelation function and the cyclic spectral density were developed by Agee [Age89b], and the class of algorithms which are based on these cost functions are called the Spectral COherence REstoral (SCORE) algorithms.

2.7 Summary

In this chapter we introduced the basic concepts and terminology related to antenna arrays and direction of arrival estimation. A brief overview of adaptive arrays and algorithms was also presented. In the next chapter, we will present algorithms specifically for direction-of-arrival estimation.

Chapter 3

Overview of Direction of Arrival Estimation Algorithms

3.1 Introduction

This chapter provides a detailed survey of the various methods available for estimation of angle of arrival of a radio signal using an antenna array. The array-based direction-of-arrival (DOA) estimation techniques considered here can be broadly divided into four different types: *conventional techniques*, *subspace based techniques*, *maximum likelihood techniques* and the *integrated techniques* which combine property restoral techniques with subspace based techniques. Conventional methods are based on classical beamforming techniques and require a large number of elements to achieve high resolution. Subspace based methods are high resolution sub-optimal techniques which exploit the eigen structure of the input data matrix. Maximum likelihood techniques are optimal techniques which can perform well even under low signal-to-noise ratio conditions, but are in general computationally very intensive. The integrated approach use property restoral based techniques to separate multiple signals and estimate their spatial signatures from which their directions of arrival can be determined using subspace techniques.

3.2 Conventional Methods for DOA Estimation

Conventional methods for direction-of-arrival estimation are based on the concepts of beamforming and null-steering, and do not exploit the nature of the model of the received signal vector $\mathbf{x}(k)$ or the statistical model of the signals and noise. Given the knowledge of the array manifold, an array can be steered electronically just as a fixed antenna can be steered mechanically. Conventional techniques used for DOA estimation consists of electronically steering beams in all possible directions, and looking for peaks in the output power [Sch93]. The conventional methods discussed here are the delay-and-sum method (classical beamformer) and the Capon's minimum variance method.

3.2.1 Delay-and-Sum Method

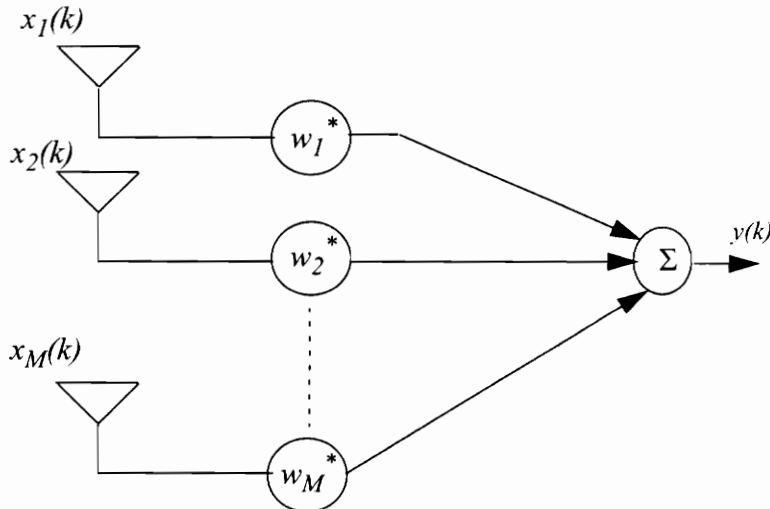


Figure 3.1: Illustration of the classical beamforming structure

The delay and sum method, also referred to as the classical beamformer method or Fourier method, is one of the simplest techniques for DOA estimation. Figure 3.1 shows the classical narrowband beamformer structure, where the output signal $y(k)$ is given by a

linearly weighted sum of the sensor element outputs. That is,

$$y(k) = \mathbf{w}^H \mathbf{x}(k) \quad (3.1)$$

The total output power of the conventional beamformer can be expressed as

$$P_{cbf} = E[|y(k)|^2] = E[|\mathbf{w}^H \mathbf{x}(k)|^2] = \mathbf{w}^H E[\mathbf{x}(k) \mathbf{x}^H(k)] \mathbf{w} = \mathbf{w}^H \mathbf{R}_{xx} \mathbf{w} \quad (3.2)$$

where \mathbf{R}_{xx} is the autocorrelation matrix of the array input data as defined in (1.34). Equation (3.2) plays a central role in all the conventional DOA estimation algorithms. The autocorrelation matrix \mathbf{R}_{xx} contains useful information about both the array response vectors and the signals themselves, and it is possible to estimate signal parameters by careful interpretation of \mathbf{R}_{xx} .

Consider a signal $s(k)$ impinging on the array at an angle θ_0 . Following the narrowband input data model discussed in section 2.1, the power at the beamformer output can be expressed as

$$\begin{aligned} P_{cbf}(\theta_0) &= E[|\mathbf{w}^H \mathbf{x}(k)|^2] = E[|\mathbf{w}^H (\mathbf{a}(\theta_0)s(k) + \mathbf{n}(k))|^2] \\ &= (|\mathbf{w}^H \mathbf{a}(\theta_0)|^2 (\sigma_s^2 + \sigma_n^2)) \end{aligned} \quad (3.3)$$

where $\mathbf{a}(\theta_0)$ is the steering vector associated with the DOA angle θ_0 , $\mathbf{n}(k)$ is the noise vector at the array input, and $\sigma_s = E[s(k)^2]$ and $\sigma_n = E[n(k)^2]$ are the signal power and noise power respectively. It is clearly seen from (3.3) that the output power is maximized when $\mathbf{w} = \mathbf{a}(\theta_0)$. Therefore, of all the possible weight vectors, the receiver antenna has the highest gain in the direction θ_0 , when $\mathbf{w} = \mathbf{a}(\theta_0)$. This is because $\mathbf{w} = \mathbf{a}(\theta_0)$ aligns the phases of the signal components arriving from θ_0 at the sensors, causing them to add constructively.

In the classical beamforming approach to DOA estimation, the beam is scanned over the angular region of interest in discrete steps by forming weights $\mathbf{w} = \mathbf{a}(\theta)$ for different θ , and the output power is measured. Using equation (3.2), the output power at the classical beamformer as a function of the angle of arrival is given by

$$P_{cbf}(\theta) = \mathbf{w}^H \mathbf{R}_{xx} \mathbf{w} = \mathbf{a}^H(\theta) \mathbf{R}_{xx} \mathbf{a}(\theta) \quad (3.4)$$

Therefore, if we have an estimate of the input autocorrelation matrix, and know the steering vectors $\mathbf{a}(\theta)$ for all θ 's of interest (either through calibration or analytical computation), it is possible to estimate the output power as a function of the angle of arrival θ . The output power as a function of angle of arrival is often termed as the *spatial spectrum*. Clearly, the directions of arrival can be estimated by locating peaks in the spatial spectrum defined in (3.4).

The delay and sum method has many disadvantages. The width of the beam and the height of the sidelobes limit the effectiveness when signals arriving from multiple directions and/or sources are present because the signals over a wide angular region contribute to the measured average power at each look direction. Hence, this technique has poor resolution. Although it is possible to increase the resolution by adding more sensor elements, increasing the number of sensors increases the number of receivers and the amount of storage required for the calibration data, i.e., $\mathbf{a}(\theta)$.

3.2.2 Capon's Minimum Variance Method

The delay-and-sum method works on the premise that pointing the strongest beam in a particular direction yields the best estimate of power arriving in that direction. In other words, all the degrees of freedom available to the array were used in forming a beam in the required look direction. This works fine when there is only one signal present. But, when there are more than one signal present the array output power contains contribution from the desired signal as well as the undesired ones from other directions.

Capon's minimum variance technique [Cap69] attempts to overcome the poor resolution problems associated with the delay-and-sum method. The idea is to use some (not all) of the degrees of freedom to form a beam in the desired look direction while simultaneously

using the remaining degrees of freedom to form nulls in the direction of interfering signals. This technique minimizes the contribution of the undesired interferences by minimizing the output power while maintaining the gain along the look direction to be constant, usually unity. That is,

$$\min_{\mathbf{w}} E[|y(k)|^2] = \min_{\mathbf{w}} \mathbf{w}^H \mathbf{R}_{xx} \mathbf{w} \quad \text{subject to } \mathbf{w}^H \mathbf{a}(\theta_0) = 1 \quad (3.5)$$

The weight vector obtained by solving (3.5) is often called the *minimum variance distortionless response* (MVDR) beamformer weights since, for a particular look direction, it minimizes the variance (average power) of the output signal while passing the signal arriving in the look direction without distortion (unity gain and zero phase shift). Equation (3.5) represents a constraint optimization problem which can be solved using the method of Lagrange multipliers. This approach converts the constraint optimization problem into an unconstrained one, thereby allowing the use of least squares techniques to determine the solution. Using a Lagrange multiplier, the weight vector that solves (3.5) can be shown to be [Hay91]

$$\mathbf{w} = \frac{\mathbf{R}_{xx}^{-1} \mathbf{a}(\theta)}{\mathbf{a}^H(\theta) \mathbf{R}_{xx}^{-1} \mathbf{a}(\theta)} \quad (3.6)$$

Now the output power of the array as a function of the angle of arrival, using the Capon's beamforming method, is given by the Capon's spatial spectrum,

$$P_{Capon}(\theta) = \frac{1}{\mathbf{a}^H(\theta) \mathbf{R}_{xx}^{-1} \mathbf{a}(\theta)} \quad (3.7)$$

By computing and plotting the Capon's spectrum over the whole range of θ , the DOA's can be estimated by locating the peaks in the spectrum.

Although it is not a maximum likelihood (ML) estimator, Capon's method is sometimes referred to as an ML estimator since for any choice of θ , $P_{Capon}(\theta)$ is the maximum likelihood estimate of the power of a signal arriving from the direction θ in the presence of white Gaussian noise having arbitrary spatial characteristics [Cap79].

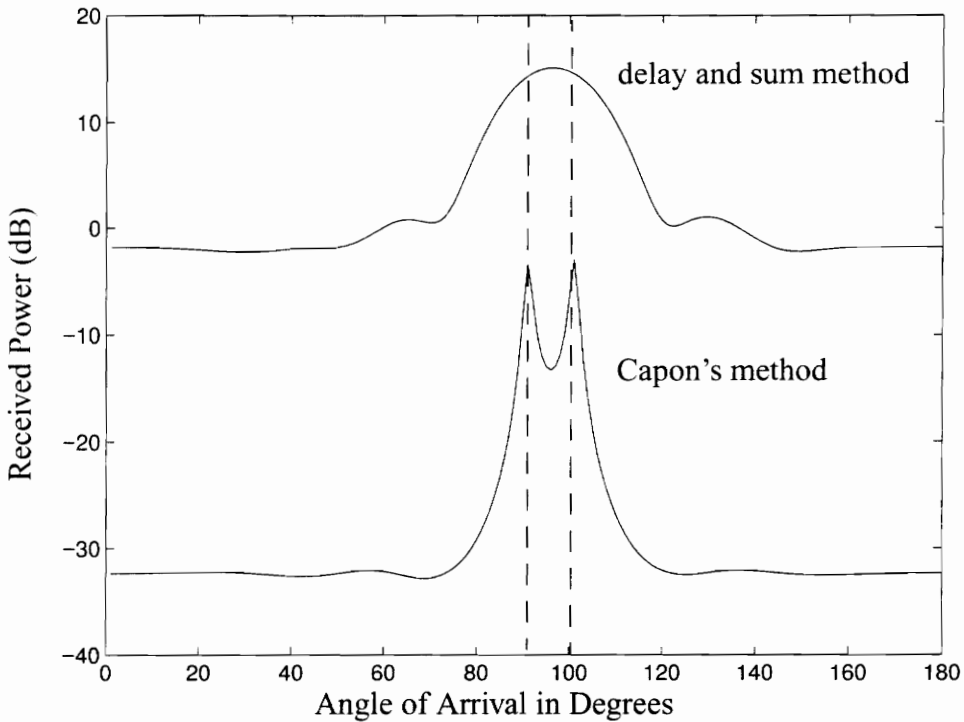


Figure 3.2: Comparison of resolution performance of delay-and-sum method and Capon's minimum variance method. Two signals of equal power at an SNR of 20 dB arrive at a 6-element uniformly spaced array with an interelement spacing equal to half a wavelength at angles 90 and 100 degrees respectively.

Figure 3.2 illustrates the performance improvement obtained by Capon's method over the delay-and-sum method. Computer simulations show that using a six element uniformly spaced linear array with half wavelength interelement spacing, Capon's method is able to distinguish between the two signals arriving at 90 and 100 degrees respectively, while the delay-and-sum method fails to differentiate between the two signals.

Though it provides a better resolution when compared to the delay-and-sum method, Capon's method suffers from many disadvantages. Capon's method fails if other signals that are correlated with the signal of interest are present because it inadvertently uses that correlation to reduce the processor output power without spatially nulling it [Sch93]. In other words, the correlated components may be combined destructively in the process of

minimizing the output power. Also, Capon's method requires the computation of the matrix inverse which can be expensive for large arrays

3.3 Subspace Methods for DOA Estimation

Though many of the classical beamforming based methods such as the Capon's minimum variance method are often successful and widely used, these methods have some fundamental limitations in resolution. Most of these limitations arise due to the fact they do not exploit the structure of the narrowband input data model of the measurements. Schmidt [Sch79] and Bienvenu and Kopp [Bie79] were the first to exploit the structure of a more accurate data model for the case of sensor arrays of arbitrary form. Schmidt derived a complete geometric solution to the DOA estimation problem in the absence of noise, and extended the geometric concepts to obtain a reasonable approximation to the solution in the presence of noise. The technique proposed by Schmidt is called the MUltiple SInal Classification (MUSIC) algorithm, and has been thoroughly investigated since its inception [Bar84][Sto89][Pil89B]. The geometric concepts upon which MUSIC is founded form the basis for a much broader class of *subspace-based* algorithms [Pau93][Joh86]. Apart from MUSIC, the primary contributions to the subspace-based algorithms include the Estimation of Signal Parameters via Rotational Invariance Technique (ESPRIT) proposed by Roy et. al.,[Pau86B][Roy89][Roy90], and the minimum-norm method proposed by Kumaresan and Tufts [Kum83].

3.3.1 The MUSIC Algorithm

The MUSIC algorithm proposed by Schmidt in 1979 [Sch79][Sch86A] is a high resolution multiple signal classification technique based on exploiting the eigen structure of the input covariance matrix. MUSIC is a signal parameter estimation algorithm which provides information about the number of incident signals, direction of arrival (DOA) of each signal, strengths and cross correlations between incident signals, noise power, etc.

While the MUSIC algorithm provides very high resolution, it requires very precise and accurate array calibration. The MUSIC algorithm has also been implemented and its performance experimentally verified [Sch86B].

The development of the MUSIC algorithm was based on a geometric view of the signal parameter estimation problem. Following the narrowband data model discussed in section 1.1, If there are D signals incident on the array, the received input data vector at an M -element array can be expressed as a linear combination of the D incident waveforms and noise. That is,

$$\begin{bmatrix} x_1 \\ \vdots \\ x_M \end{bmatrix} = \begin{bmatrix} \mathbf{a}(\theta_1) & \dots & \mathbf{a}(\theta_D) \end{bmatrix} \begin{bmatrix} s_1 \\ \vdots \\ s_D \end{bmatrix} + \begin{bmatrix} n_1 \\ \vdots \\ n_M \end{bmatrix} \quad (3.8)$$

$$\mathbf{x} = \mathbf{As} + \mathbf{n} \quad (3.9)$$

where $\mathbf{s} = [s_1 \ s_2 \ \dots \ s_D]$ is the vector of incident signals, $\mathbf{n} = [n_1 \ n_2 \ \dots \ n_D]$ is the noise vector, and $\mathbf{a}(\theta_j)$ is the array steering vector corresponding to the direction of arrival of the j th signal. In geometric terms, the received vector \mathbf{x} and the steering vectors $\mathbf{a}(\theta_j)$ can be visualized as vectors in M dimensional space. From (3.8), it is seen that the received vector \mathbf{x} is a particular linear combination of the array steering vectors, with s_1, s_2, \dots, s_D being the coefficients of the combination. In terms of the above data model, the input covariance matrix \mathbf{R}_{xx} can be expressed as

$$\mathbf{R}_{xx} = E[\mathbf{xx}^H] = \mathbf{A}E[\mathbf{ss}^H]\mathbf{A}^H + E[\mathbf{nn}^H] \quad (3.10)$$

$$\mathbf{R}_{xx} = \mathbf{A}\mathbf{R}_{ss}\mathbf{A}^H + \sigma_{Noise}^2 \mathbf{I} \quad (3.11)$$

where \mathbf{R}_{ss} is the *signal correlation matrix* $E[\mathbf{ss}^H]$.

Since \mathbf{A} is comprised of steering vectors which are linearly independent, it has full column rank, and the signal correlation matrix \mathbf{R}_{ss} is non-singular as long as the incident signals are only at most partially correlated.

A full column rank \mathbf{A} and nonsingular \mathbf{R}_{ss} guarantees that, when the number of incident signals D is less than the number of array elements M , the $M \times M$ matrix $\mathbf{A}\mathbf{R}_{ss}\mathbf{A}^H$ is positive semidefinite with rank D . From elementary linear algebra, this implies that $M-D$ of its eigenvalues are zero. If $\lambda_1, \lambda_2, \dots, \lambda_M$ and $\mathbf{v}_1, \mathbf{v}_2, \dots, \mathbf{v}_M$ denote the eigenvalues and eigenvectors, respectively, of \mathbf{R}_{xx} , it is clear from (3.11) that the $M-D$ smallest eigenvalues of \mathbf{R}_{xx} are all equal to σ_{Noise}^2 . That is,

$$\lambda_{D+1} = \lambda_{D+2} = \dots = \lambda_M = \lambda_{min} = \sigma_{Noise}^2 \quad (3.12)$$

In practice, however, when the autocorrelation matrix \mathbf{R}_{xx} is estimated from a finite data sample, all the eigenvalues corresponding to the noise power will not be identical. Instead they will appear as a closely spaced cluster, with the variance of their spread decreasing as the number of samples used to obtain an estimate of \mathbf{R}_{xx} is increased. Once the multiplicity, K , of the smallest eigenvalue is determined, an estimate of the number of signals, \hat{D} , can be obtained from the relation $M = D + K$. Therefore, the estimated number of signals is given by

$$\hat{D} = M - K \quad (3.13)$$

From the definition of eigenvalues and eigenvectors [Gol89], the eigenvectors corresponding to the smallest eigenvalues (non-principle eigenvalues) must satisfy

$$\mathbf{R}_{xx}\mathbf{v}_i = \sigma_{Noise}^2\mathbf{v}_i, \quad i = D + 1, \dots, M \quad (3.14)$$

From (3.11), this means that

$$\mathbf{A}\mathbf{R}_{ss}\mathbf{A}^H\mathbf{v}_i = 0, \quad i = D + 1, \dots, M \quad (3.15)$$

Now since \mathbf{A} is full column rank, and \mathbf{R}_{ss} is non-singular, it follows that

$$\mathbf{A}^H\mathbf{v}_i = 0, \quad i = D + 1, \dots, M \quad (3.16)$$

From (3.16), since the dot product of \mathbf{A}^H and the eigenvectors $\mathbf{v}_{D+1}, \dots, \mathbf{v}_M$ are zero, it implies that the column vectors of \mathbf{A} are perpendicular to those eigenvectors.

$$\{\mathbf{a}(\theta_1), \dots, \mathbf{a}(\theta_D)\} \perp \{\mathbf{v}_{D+1}, \dots, \mathbf{v}_M\} \quad (3.17)$$

In short, the above analysis has shown that the eigenvectors of the covariance matrix \mathbf{R}_{xx} belong to either of the two orthogonal subspaces, called the principal eigen subspace (*signal subspace*) and the non-principal eigen subspace (*noise subspace*). The steering vectors corresponding to the direction of arrivals of signals lie in the signal subspace and are hence orthogonal to the noise subspace. By searching through all possible array steering vectors to find those which are perpendicular to the space spanned by the non-principal eigenvectors, the direction of arrivals θ_i 's can be determined.

The direction of arrival of the multiple incident signals can be estimated by locating the peaks of a MUSIC spatial spectrum given by

$$P_{MUSIC}(\theta) = \frac{1}{\mathbf{a}^H(\theta) \mathbf{V}_N \mathbf{V}_N^H \mathbf{a}(\theta)} \quad (3.18)$$

or

$$P_{MUSIC}(\theta) = \frac{\mathbf{a}^H(\theta) \mathbf{a}(\theta)}{\mathbf{a}^H(\theta) \mathbf{V}_N \mathbf{V}_N^H \mathbf{a}(\theta)} \quad (3.19)$$

where

$$\mathbf{V}_N = \{\mathbf{v}_{D+1}, \dots, \mathbf{v}_M\}. \quad (3.20)$$

Equations (3.18) and (3.19) are two possible measures of the closeness of an element of the array manifold to the signal subspace. The denominator of (3.18) and (3.19) is essentially a scalar measure of the distance between the steering vectors, $\mathbf{a}(\theta)$, in the array manifold, and the estimated noise subspace spanned by the eigenvectors, \mathbf{V}_N . The product $\mathbf{V}_N \mathbf{V}_N^H$ represents the projection matrix on the noise subspace. Orthogonality between $\mathbf{a}(\theta)$ and \mathbf{V}_N will minimize the denominator and hence will give rise to peaks in the MUSIC spectrum defined in (3.18) and (3.19). The \hat{D} largest peaks in the MUSIC spectrum correspond to the directions of arrival of the signals impinging on the array.

Once the directions of arrival θ_i 's are determined from the MUSIC spectrum the signal covariance matrix \mathbf{R}_{ss} can be determined from the following relation [Sch86A].

$$\mathbf{R}_{ss} = (\mathbf{A}^H \mathbf{A})^{-1} \mathbf{A}^H (\mathbf{R}_{xx} - \lambda_{min} \mathbf{I}) \mathbf{A} (\mathbf{A}^H \mathbf{A})^{-1} \quad (3.21)$$

From (3.21), the powers and cross correlations between the various input signals can be readily obtained.

The MUSIC algorithm may be summarized as follows:

Step 1. Collect input samples $\{\mathbf{x}(k), k = 1, \dots, N\}$ and estimate the input covariance matrix

$$\hat{\mathbf{R}}_{xx} = \frac{1}{N} \sum_{k=1}^N \mathbf{x} \mathbf{x}^H \quad (3.22)$$

Step 2. Perform eigen decomposition on $\hat{\mathbf{R}}_{xx}$

$$\hat{\mathbf{R}}_{xx} \mathbf{V} = \mathbf{V} \Lambda \quad (3.23)$$

where $\Lambda = \text{diag}\{\lambda_1, \lambda_2, \dots, \lambda_M\}$, $\lambda_1 \geq \lambda_2 \geq \dots \geq \lambda_M$ are the eigenvalues and $\mathbf{V} = \{\mathbf{v}_1, \mathbf{v}_2, \dots, \mathbf{v}_M\}$ are the corresponding eigenvectors of $\hat{\mathbf{R}}_{xx}$.

Step 3. Estimate the number of signals \hat{D} , from the multiplicity K , of the smallest eigenvalue λ_{min} as

$$\hat{D} = M - K \quad (3.24)$$

Step 4. Compute the MUSIC spectrum

$$\hat{P}_{MUSIC}(\theta) = \frac{\mathbf{a}^H(\theta) \mathbf{a}(\theta)}{\mathbf{a}^H(\theta) \mathbf{V}_N \mathbf{V}_N^H \mathbf{a}(\theta)} \quad (3.25)$$

where $\mathbf{V}_N = \{\mathbf{v}_{\hat{D}+1}, \dots, \mathbf{v}_M\}$

Step 5. Find the \hat{D} largest peaks of $\hat{P}_{MUSIC}(\theta)$ to obtain estimates of the direction-of-arrival.

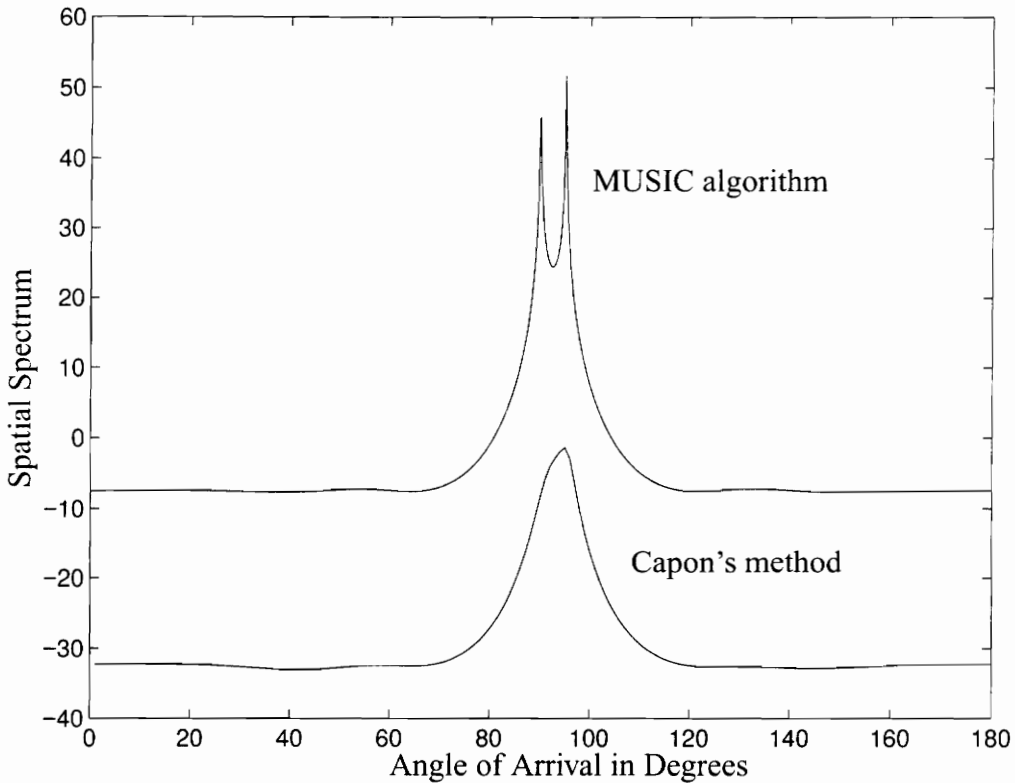


Figure 3.3: Comparison of MUSIC and Capon's minimum variance method. Two signals of equal power at an SNR of 20 dB arrive at a 6-element uniformly spaced array with an interelement spacing equal to half a wavelength at angles 90 and 95 degrees respectively.

Figure 3.3 shows a comparison between the resolution performance of MUSIC and the Capon's minimum variance method. As seen clearly from the plot, MUSIC can resolve closely spaced signals which cannot be detected by Capon's method. Simulation results show that two signals arriving at angles 90 and 95 degrees, respectively, at the input of a 6-element uniformly spaced linear array can be detected by MUSIC, while Capon's minimum variance method fails to differentiate between the two signals.

It should be noted that unlike the conventional methods, the MUSIC spatial spectrum does not estimate the signal power associated with each arrival angle. Instead, when the ensemble average of the array input covariance matrix is known exactly, under uncorrelated and identical noise conditions, the peaks of $P_{MUSIC}(\theta)$ are guaranteed to

correspond to the true angles of arrival. Since these peaks are distinct irrespective of the actual separation between arrival angles, in principle, with perfect array calibration, these estimators can distinguish and resolve arbitrarily closely spaced signals.

3.3.2 Improvements to the MUSIC Algorithm

Various modifications to the MUSIC algorithm have been proposed to increase its resolution performance and decrease the computational complexity. One such improvement is the Root-MUSIC algorithm developed by Barabell [Bar83], which is based on polynomial rooting, and provides higher resolution but is applicable only to a uniform spaced linear array. Another improvement proposed by Barabell uses the properties of the signal space eigenvectors (principal eigenvectors) to define a rational spectrum function with improved resolution capability [Bar83].

CYCLIC MUSIC which exploits the spectral coherence properties of the signal to improve the performance of the conventional MUSIC algorithms has been proposed in [Sch89]. Fast Subspace Decomposition techniques have also been studied to decrease the computational complexity of MUSIC [Xu94B].

Root-MUSIC Algorithm

For the case of a uniformly spaced linear array with interelement spacing d , the m th element of the steering vector $\mathbf{a}(\theta)$ may be expressed as (see (2.15)):

$$a_m(\theta) = \exp\left(j2\pi m\left(\frac{d}{\lambda}\right)\cos\theta\right); \quad m = 1 \dots M \quad (3.26)$$

The MUSIC spectrum given by (3.18) is an all-pole function of the form

$$\begin{aligned} P_{MUSIC}(\theta) &= \frac{1}{\mathbf{a}^H(\theta)\mathbf{V}_N\mathbf{V}_N^H\mathbf{a}(\theta)} \\ &= \frac{1}{\mathbf{a}^H(\theta)\mathbf{C}\mathbf{a}(\theta)} \end{aligned} \quad (3.27)$$

where $\mathbf{C} = \mathbf{V}_N \mathbf{V}_N^H$. Using equation (3.26) the denominator of (3.27) may be written as

$$P_{MUSIC}^{-1}(\theta) = \sum_{m=1}^M \sum_{n=1}^M \exp\left(-j2\pi m\left(\frac{d}{\lambda}\right)\cos\theta\right) C_{mn} \exp\left(-j2\pi n\left(\frac{d}{\lambda}\right)\cos\theta\right) \quad (3.28)$$

where C_{mn} is the entry in the m th row and n th column of \mathbf{C} . Combining the two summations into one, (3.28) can be simplified as

$$P_{MUSIC}^{-1}(\theta) = \sum_{l=-M+1}^{M-1} C_l \exp\left(-j2\pi\left(\frac{d}{\lambda}\right)\cos\theta\right) \quad (3.29)$$

where $C_l = \sum_{m-n=l} C_{mn}$ is the sum of the entries of \mathbf{C} along the l th diagonal.

By defining a polynomial $D(z)$ as follows,

$$D(z) = \sum_{l=-M+1}^{M+1} C_l z^{-l} \quad (3.30)$$

evaluating the MUSIC spectrum $P_{MUSIC}(\theta)$ becomes equivalent to evaluating the polynomial $D(z)$ on the unit circle, and the peaks in the MUSIC spectrum are due to the roots of $D(z)$ lying close to the unit circle. (Ideally (no noise) the poles will lie exactly on the unit circle at locations determined by the angle of arrival). In other words, a pole of $D(z)$ at $z = z_1 = |z_1| \exp(j \arg(z_1))$ will result in a peak in the MUSIC spectrum at

$$\cos\theta = \left(\frac{\lambda}{2\pi d}\right) \arg(z_1) \quad (3.31)$$

Barabell [Bar83] showed through simulations that the ROOT-MUSIC algorithm has better resolution than the spectral MUSIC algorithm, especially at low SNR conditions.

Cyclic MUSIC Algorithm

Cyclic MUSIC is a signal selective direction finding algorithm which exploits the *spectral coherence* of the received signal as well as the *spatial coherence*. By exploiting spectral correlation along with MUSIC, it is possible to resolve signals spaced more closely than the resolution threshold of the array when only one of them is an signal-of-interest (SOI)

[Sch89][Sch94]. Cyclic MUSIC also circumvents the requirement that the total number of signals impinging on the array (including both SOI and interference) be less than the number of sensor elements [Gar88].

Consider an array of M sensors which receives D_α signals which exhibit spectral correlation at a cycle frequency α , and an arbitrary number of interferers that do not exhibit spectral correlation at that particular frequency. Let $s_i(t)$, $i = 1, \dots, D_\alpha$ be the desired signals, and $\mathbf{n}(t)$ the noise and interference vector incident on the array. The received signal vector $\mathbf{x}(t)$ can then be expressed as

$$\begin{aligned}\mathbf{x}(t) &= \sum_{i=1}^{D_\alpha} \mathbf{a}(\theta_i) s_i(t) + \mathbf{n}(t) \\ &= \mathbf{A}\mathbf{s}(t) + \mathbf{n}(t)\end{aligned}\quad (3.32)$$

Since only the desired signals exhibit spectral correlation at α , the cyclic autocorrelation matrix $\mathbf{R}_{xx}^\alpha(\tau)$ of the received signal $\mathbf{x}(t)$ defined as

$$\mathbf{R}_{xx}^\alpha = \langle \mathbf{x}\left(t + \frac{\tau}{2}\right) \left\{ \mathbf{x}\left(t - \frac{\tau}{2}\right) \exp(j2\pi\alpha t) \right\}^H \rangle_\infty \quad (3.33)$$

can be expressed as

$$\mathbf{R}_{xx}^\alpha(\tau) = \mathbf{A}\mathbf{R}_{ss}^\alpha(\tau)\mathbf{A}^H \quad (3.34)$$

where $\mathbf{R}_{ss}^\alpha(\tau)$ is the cyclic autocorrelation matrix of the desired signals, and defined as

$$\mathbf{R}_{ss}^\alpha = \langle \mathbf{s}\left(t + \frac{\tau}{2}\right) \left\{ \mathbf{s}\left(t - \frac{\tau}{2}\right) \exp(j2\pi\alpha t) \right\}^H \rangle_\infty \quad (3.35)$$

where

$$\langle . \rangle_\infty = \lim_{T \rightarrow \infty} \int_{-\frac{T}{2}}^{\frac{T}{2}} (.) dt \quad (3.36)$$

Clearly, the matrix $\mathbf{R}_{xx}^\alpha(\tau)$ has rank D_α . For $D_\alpha < M$, the null space of $\mathbf{R}_{xx}^\alpha(\tau)$ is spanned

by the eigenvectors $\mathbf{V}_{N,\alpha}$ corresponding to its zero eigenvalues,

$$\mathbf{R}_{xx}^\alpha(\tau) \mathbf{V}_{N,\alpha} = 0 \quad (3.37)$$

If the signals are not fully correlated, $\mathbf{R}_{ss}^\alpha(\tau)$ has full rank equal to D_α . Since \mathbf{A} is also full rank, it follows from (3.34) and (3.37), that the null space of $\mathbf{R}_{xx}^\alpha(\tau)$ is orthogonal to the direction vectors of the desired signals. That is,

$$\mathbf{V}_{N,\alpha}^H \mathbf{a}(\theta_i) = 0, \quad i = 1, \dots, D_\alpha \quad (3.38)$$

Using (3.38) as a measure of orthogonality, a cyclic MUSIC spectrum similar to (3.19) can be defined as follows:

$$P_{CYCLIC-MUSIC} = \frac{\mathbf{a}^H(\theta)(\mathbf{a}(\theta))}{\mathbf{a}^H(\theta) \mathbf{V}_{N,\alpha} \mathbf{V}_{N,\alpha}^H \mathbf{a}(\theta)} \quad (3.39)$$

The direction of arrival of the desired signals can be computed by searching through all θ for the D_α highest peaks on $P_{CYCLIC-MUSIC}$.

3.3.3 The ESPRIT Algorithm

The Estimation of Signal Parameters via Rotational Invariance Techniques (ESPRIT) algorithm is another subspace-based DOA estimation technique developed by Roy et. al [Pau86A][Roy89][Roy90]. ESPRIT dramatically reduces the computational and storage requirements of MUSIC, and does not involve an exhaustive search through all possible steering vectors to estimate the direction of arrival. Unlike in MUSIC, ESPRIT does not require that the array manifold vectors be precisely known, and hence the calibration requirements are not stringent. ESPRIT derives its advantages by requiring that the sensor array have a structure that can be decomposed into two equal sized identical subarrays with the corresponding elements of the two subarrays being displaced from one another by a fixed translational (not rotational) distance. That is, the array should possess a displacement (translational) invariance, and the sensors should occur in matched pairs with identical displacement. Fortunately, there are many practical situations where these

conditions are satisfied, such as in the case of a uniform linear array.

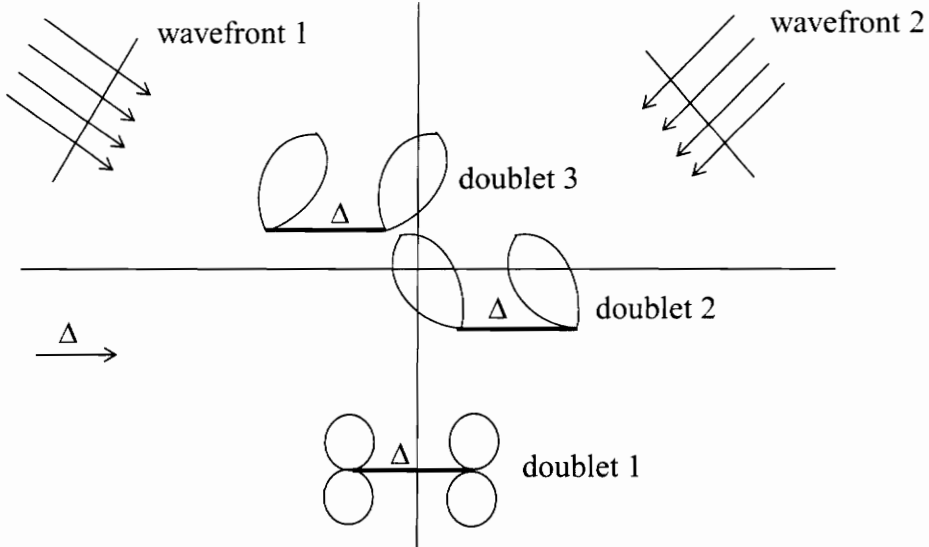


Figure 3.4: Illustration of ESPRIT array geometry [Roy90]

Consider a planar array of arbitrary geometry composed of $m = M/2$ sensor pairs or doublets, as shown in Figure 3.4. (It should be noted that, though in this example the array is assumed to be composed of $M/2$ sensor doublets, it is possible to have M -element arrays like the uniformly spaced linear array to be composed of $M-1$ overlapping doublets). To describe mathematically the effect of the translational invariance of the sensor array, it is convenient to describe the array as being composed of two identical subarrays, X_0 and X_1 , physically displaced (not rotated) from each other by a known displacement (translational) vector Δ . The signals received at the i th doublet can then be expressed as

$$x_{0i}(t) = \sum_{k=1}^D s_k(t) a_i(\theta_k) + n_{0i}(t) \quad (3.40)$$

$$x_{1i}(t) = \sum_{k=1}^D s_k(t) \exp\left[j\omega_0 \Delta \cos\left(\frac{\theta_k}{c}\right)\right] a_i(\theta_k) + n_{1i}(t) \quad (3.41)$$

where θ_k is the direction of arrival of the k th source relative to the direction of the

translational vector Δ , and D is the number of signals incident on the array. Now, using matrix and vector notation, the received signal vector at the two subarrays can be written as follows:

$$\mathbf{x}_0(t) = \mathbf{A}\mathbf{s}(t) + \mathbf{n}_0(t) \quad (3.42)$$

$$\mathbf{x}_1(t) = \mathbf{A}\Phi\mathbf{s}(t) + \mathbf{n}_1(t) \quad (3.43)$$

where Φ is a $D \times D$ diagonal unitary matrix whose diagonal elements represent the phase delays between the doublet sensors for the D signals. The matrix Φ relates the measurements from subarray X_0 to those from subarray X_1 , and is given by

$$\Phi = \text{diag}[\exp(j\gamma_1), \exp(j\gamma_2), \dots, \exp(j\gamma_D)], \quad \text{where } \gamma_k = \frac{\omega_0 \Delta}{c} \cos(\theta_k) \quad (3.44)$$

Though in the complex field, the matrix Φ is a simple scaling operator, it is similar to the real two-dimensional rotation operator. The total array output vector $\mathbf{x}(t)$ can be written as

$$\mathbf{x}(t) = \begin{bmatrix} \mathbf{x}_0(t) \\ \mathbf{x}_1(t) \end{bmatrix} = \bar{\mathbf{A}}\mathbf{s}(t) + \mathbf{n}(t) \quad (3.45)$$

where

$$\bar{\mathbf{A}} = \begin{bmatrix} \mathbf{A} \\ \mathbf{A}\Phi \end{bmatrix} \quad \text{and} \quad \mathbf{n}(t) = \begin{bmatrix} \mathbf{n}_0(t) \\ \mathbf{n}_1(t) \end{bmatrix} \quad (3.46)$$

The basic idea behind ESPRIT is to exploit the rotational invariance of the underlying signal subspace induced by the translational invariance of the sensor array[Roy89]. The relevant signal subspace is the one that contains the outputs from the two subarrays X_0 and X_1 . Simultaneous sampling of the output of the arrays leads to two sets of vectors V_0 and V_1 , that span the same signal subspace.

The signal subspace can be obtained from the knowledge of the input covariance matrix $\mathbf{R}_{xx} = \bar{\mathbf{A}}\mathbf{R}_{ss}\bar{\mathbf{A}}^H + \sigma_{Noise}^2 \mathbf{I}$. If $D \leq m$, the $M-D$ smallest eigenvalues of \mathbf{R}_{xx} are equal to σ_{Noise}^2 . The D eigenvectors V_s corresponding to the D largest eigenvalues satisfy the relation,

$$\text{Range}\{\mathbf{V}_s\} = \text{Range}\{\bar{\mathbf{A}}\} \quad (3.47)$$

Now, since $\text{Range}\{\mathbf{V}_s\} = \text{Range}\{\bar{\mathbf{A}}\}$, there must exist a unique nonsingular \mathbf{T} such that $\mathbf{V}_s = \bar{\mathbf{A}}\mathbf{T}$. Further, the invariance structure of the array allows the decomposition of \mathbf{V}_s into $\mathbf{V}_0 \in \mathbb{C}^{m \times D}$ and $\mathbf{V}_1 \in \mathbb{C}^{m \times D}$ such that $\mathbf{V}_0 = \mathbf{A}\mathbf{T}$ and $\mathbf{V}_1 = \mathbf{A}\Phi\mathbf{T}$. This implies that

$$\text{Range}\{\mathbf{V}_0\} = \text{Range}\{\mathbf{V}_1\} = \text{Range}\{\mathbf{A}\} \quad (3.48)$$

Since \mathbf{V}_0 and \mathbf{V}_1 share a common column space, the rank of $\mathbf{V}_{01} = [\mathbf{V}_0 \mid \mathbf{V}_1]$ is D . This implies that there exists a unique rank- D matrix $\mathbf{F} \in \mathbb{C}^{2D \times D}$, such that

$$0 = [\mathbf{V}_0 \mid \mathbf{V}_1]\mathbf{F} = \mathbf{V}_0\mathbf{F}_0 + \mathbf{V}_1\mathbf{F}_1 = \mathbf{A}\mathbf{T}\mathbf{F}_0 + \mathbf{A}\Phi\mathbf{T}\mathbf{F}_1 \quad (3.49)$$

\mathbf{F} spans the null space of \mathbf{V}_{01} . By defining $\Psi = -\mathbf{F}_0\mathbf{F}_1^{-1}$, (3.49) can be rearranged to obtain

$$\mathbf{A}\mathbf{T}\Psi = \mathbf{A}\Phi\mathbf{T} \quad (3.50)$$

which implies

$$\mathbf{A}\mathbf{T}\Psi\mathbf{T}^{-1} = \mathbf{A}\Phi \quad (3.51)$$

Now, assuming \mathbf{A} to be full rank, which is true as long as the directions of arrival of each signal is distinct, (3.51) implies that

$$\mathbf{T}\Psi = \Phi\mathbf{T} \quad (3.52)$$

From (3.52), it is evident that the eigenvalues of Ψ must be equal to the diagonal elements of Φ , and the columns of \mathbf{T} are the eigenvectors of Ψ . This is the key relationship in the development of ESPRIT. The signal parameters are obtained as nonlinear functions of the eigenvalues of the operator Ψ that maps (rotates) one set of vectors \mathbf{V}_0 that span an m -dimensional signal subspace into another set of vectors \mathbf{V}_1 .

In practice, with only a finite number of noisy measurements available, the condition in equation (3.47) and (3.48) is not satisfied. Hence finding a Ψ such that $\hat{\mathbf{V}}_0\Psi = \hat{\mathbf{V}}_1$ is not possible. Hence it is required to resort to a least squares solution which minimizes the

residual error. Assuming that the set of equations is overdetermined the least squares solution is given by

$$\Psi = (\hat{V}_0^H \hat{V}_0)^{-1} \hat{V}_0^H \hat{V}_1 \quad (3.53)$$

Once Ψ is obtained, its eigenvalues which correspond to the diagonal elements of Φ can be easily computed. Since the diagonal elements of Φ are related to the angle of arrival via equation (3.44), they can then be directly computed.

Since both \hat{V}_0 and \hat{V}_1 are equally noisy, the problem is better solved using the total least squares criterion (TLS). This amounts to replacing the zero matrix in (3.49) by a matrix of errors whose Frobenius norm (i.e., total least squared error) is to be minimized. The TLS ESPRIT algorithm does this, and may be summarized as follows:

Step 1. Obtain an estimate $\hat{\mathbf{R}}_{xx}$ of \mathbf{R}_{xx} from the measurements \mathbf{x} .

Step 2. Perform eigen decomposition on $\hat{\mathbf{R}}_{xx}$, i.e

$$\hat{\mathbf{R}}_{xx} = \mathbf{V} \Lambda \mathbf{V}^H, \quad (3.54)$$

where $\Lambda = \text{diag}\{\lambda_1, \dots, \lambda_M\}$ and $\mathbf{V} = [\mathbf{V}_1, \dots, \mathbf{V}_M]$ are the eigenvalues and eigenvectors respectively.

Step 3. Using the multiplicity, K , of the smallest eigenvalue λ_{min} , estimate the number of signals \hat{D} , as $\hat{D} = M - K$

Step 4. Obtain the signal subspace estimate $\hat{\mathbf{V}}_S = [\hat{\mathbf{V}}_1, \dots, \hat{\mathbf{V}}_{\hat{D}}]$ and decompose it into subarray matrices

$$\hat{\mathbf{V}}_s = \begin{bmatrix} \hat{\mathbf{V}}_0 \\ \hat{\mathbf{V}}_1 \end{bmatrix} \quad (3.55)$$

Step 5. Compute the eigen decomposition ($\lambda_1 > \dots > \lambda_{2\hat{D}}$)

$$\hat{V}_{01}^H \hat{V}_{01} = \begin{bmatrix} \hat{V}_0^H \\ \hat{V}_1^H \end{bmatrix} \begin{bmatrix} \hat{V}_0 & \hat{V}_1 \end{bmatrix} = V \Lambda V^H \quad (3.56)$$

and partition V into $\hat{D} \times \hat{D}$ submatrices,

$$V = \begin{bmatrix} V_{11} & V_{12} \\ V_{21} & V_{22} \end{bmatrix} \quad (3.57)$$

Step 6. Calculate the eigenvalues of $\Psi = -V_{12}V_{22}^{-1}$,

$$\hat{\Phi}_k = \text{eigenvalues of } (-V_{12}V_{22}^{-1}), \quad \forall k = 1, \dots, \hat{D} \quad (3.58)$$

Step 7. Estimate the angle-of-arrival as

$$\hat{\theta}_k = \cos^{-1} \left[c \frac{(\arg(\hat{\Phi}_k))}{\omega_0 \Delta} \right] \quad (3.59)$$

As seen from the above discussion, ESPRIT eliminates the search procedure inherent in most DOA estimation methods. ESPRIT produces the DOA estimates directly in terms of the eigenvalues.

3.4 Maximum Likelihood Techniques

Maximum Likelihood (ML) techniques were one of the first techniques to be investigated for DOA estimation. Since ML techniques were computationally intensive, they were less popular than suboptimal subspace techniques. However, in terms of performance, the ML techniques are superior to the subspace based techniques, especially in low signal-to-noise ratio conditions or when the number of samples is small [Zis88]. Moreover, unlike subspace based techniques, ML based techniques can perform well in coherent signal conditions as well.

To derive the ML estimator, data collected over a block of N snapshots is formulated as

$$\mathbf{X} = \mathbf{A}(\Theta)\mathbf{S} + \mathbf{N} \quad (3.60)$$

where $\mathbf{X} = [\mathbf{x}(1), \dots, \mathbf{x}(N)]$ is the array data input vector matrix of dimension $M \times N$, $\mathbf{A}(\Theta) = [\mathbf{a}(\theta_1), \dots, \mathbf{a}(\theta_D)]$ is the spatial signature matrix of dimension $M \times D$, $\mathbf{S} = [s(1), \dots, s(N)]$ is the signal waveform matrix of dimension $D \times N$, and $\mathbf{N} = [\mathbf{n}(1), \dots, \mathbf{n}(N)]$ is the noise matrix of dimension $M \times N$. In order to estimate the angles of arrival $\theta_1, \dots, \theta_D$ of the D sources, the maximum likelihood estimator makes some assumptions about the signals and noise. First, it is assumed that the number of signals is known or estimated, and is smaller than the number of sensors. Second, every set of D steering vectors are assumed to be linearly independent. The noise component is assumed to be stationary and ergodic complex valued Gaussian process of zero mean and covariance $\sigma^2 \mathbf{I}$, where σ^2 is an unknown scalar and \mathbf{I} is the identity matrix. Finally it is assumed that the noise samples are statistically independent. It should be noted that the ML estimator is meaningful even when the assumptions made about noise do not hold, in which case it coincides with the Least-Squares estimator [Zis88].

The derivation of the ML estimator described here regards the signals to be sample functions of unknown deterministic sequences, rather than random processes. Based on the assumptions made about the nature of noise, the joint probability density function of the sampled data as given by equation (3.60) can be expressed as [Zis88]

$$f(\mathbf{X}) = \prod_{k=1}^N \frac{1}{\pi \det[\sigma^2 \mathbf{I}]} \exp\left(-\frac{1}{\sigma^2} |\mathbf{x}(k) - \mathbf{A}(\Theta)\mathbf{s}(k)|^2\right) \quad (3.61)$$

where $\det[\cdot]$ denotes the determinant. Ignoring the constant terms, the log likelihood function is given by

$$J = -ND\log\sigma^2 - \frac{1}{\sigma^2} \sum_{k=1}^N |\mathbf{x}(k) - \mathbf{A}(\Theta)\mathbf{s}(k)|^2 \quad (3.62)$$

To compute the maximum likelihood estimator, the log likelihood function of (3.62) has to be maximized with respect to the unknown parameters. This yields the following maximization problem:

$$\max_{(\Theta, \mathbf{S})} \left\{ -ND \log \left[\frac{1}{ND} \sum_{k=1}^N |\mathbf{x}(k) - \mathbf{A}(\Theta)\mathbf{s}(k)|^2 \right] \right\} \quad (3.63)$$

The logarithm being a monotonic function, maximizing (3.63) is equivalent to the following minimization problem:

$$\min_{(\Theta, \mathbf{S})} \left\{ \sum_{k=1}^N |\mathbf{x}(k) - \mathbf{A}(\Theta)\mathbf{s}(k)|^2 \right\} \quad (3.64)$$

Fixing Θ and minimizing with respect to \mathbf{S} , yields the well known least squares solution

$$\hat{\mathbf{s}}(k) = (\mathbf{A}^H(\Theta)\mathbf{A}(\Theta))^{-1}\mathbf{A}^H(\Theta)\mathbf{x}(k) \quad (3.65)$$

Substituting (3.65) into (3.64), we obtain

$$\min \sum_{k=1}^N |\mathbf{x}(k) - \mathbf{P}_{\mathbf{A}(\Theta)}\mathbf{x}(k)|^2 \quad (3.66)$$

where $\mathbf{P}_{\mathbf{A}(\Theta)}$ is the projection operator which projects vectors onto the space spanned by the columns of $\mathbf{A}(\Theta)$, and is given by

$$\mathbf{P}_{\mathbf{A}(\Theta)} = \mathbf{A}(\Theta)(\mathbf{A}^H(\Theta)\mathbf{A}(\Theta))^{-1}\mathbf{A}^H(\Theta) \quad (3.67)$$

Therefore, the ML estimate of the directions of arrival $\Theta = \{\theta_1, \dots, \theta_D\}$ is obtained by maximizing the log-likelihood function

$$J(\Theta) = \sum_{k=1}^N |\mathbf{P}_{\mathbf{A}(\Theta)}\mathbf{x}(k)|^2 \quad (3.68)$$

Equation (3.68) can be interpreted in a geometric way such that the ML technique appears as a variant of the subspace based method. Viberg and Otterson [Vib91] presented a generalized framework to highlight the similarities between the various subspace based DOA estimation techniques and the maximum likelihood technique. In geometric terms, it follows from (3.68) that the ML estimator is obtained by searching over the array manifold, of those D steering vectors that form a D -dimensional signal subspace which is closest to the vectors $\{\mathbf{x}(k), k=1, \dots, N\}$, where closeness is measured by the modulus of

the projection of the vectors onto this subspace.

It can be shown that equation (3.68) can be equivalently written as

$$J(\Theta) = \text{trace}[\mathbf{P}_{\mathcal{A}(\Theta)} \hat{\mathbf{R}}_{xx}] \quad (3.69)$$

where $\hat{\mathbf{R}}_{xx}$ is the sample covariance matrix

$$\hat{\mathbf{R}}_{xx} = \frac{1}{N} \sum_{k=1}^N \mathbf{x}(k) \mathbf{x}^H(k) \quad (3.70)$$

The maximization of the log-likelihood function in (3.69) is a nonlinear, multidimensional maximization problem which is computationally very intensive. Many computationally efficient algorithms have been developed to simplify the solution to the maximization problem [Fed88][Zis88][Li93].

The Alternating Projection algorithm developed by Ziskind and Wax [Zis88] is an iterative technique which reduces the maximization problem from a multi-dimensional problem to a one-dimensional problem. The idea is to perform the maximization with respect to a single parameter while holding the remaining parameters fixed. That is, the value of θ_i at the $(n+1)$ th iteration is obtained by solving the following one-dimensional maximization problem:

$$\hat{\theta}_i^{(n+1)} = \arg \max_{\theta_i} \text{trace}[\mathbf{P}_{[\mathcal{A}(\hat{\Theta}_i^{(n)}), a(\theta_i)]} \hat{\mathbf{R}}_{xx}] \quad (3.71)$$

where $\hat{\Theta}_i^{(n)}$ denotes the vector comprising of the direction of arrival angle estimates of all signals other than the one being computed.

$$\hat{\Theta}_i^{(n)} = [\hat{\Theta}_1^{(n)}, \dots, \hat{\Theta}_{i-1}^{(n)}, \hat{\Theta}_{i+1}^{(n)}, \dots, \hat{\Theta}_D^{(n)}] \quad (3.72)$$

Since the log-likelihood function $J(\Theta)$ may have multiple local maximas, proper initialization is critical for global convergence. The initialization procedure suggested by Ziskind and Wax begins by solving the maximization problem for a single source:

$$\hat{\theta}_1^{(0)} = \arg \max_{\theta_1} \text{trace}[\mathbf{P}_{\mathbf{a}(\theta_1)} \hat{\mathbf{R}}_{xx}] \quad (3.73)$$

Using the estimated θ_1, θ_2 is calculated as,

$$\hat{\theta}_2^{(0)} = \arg \max_{\theta_2} \text{trace}[\mathbf{P}_{[\mathbf{a}(\hat{\theta}_1^{(0)}), \mathbf{a}(\theta_2)]} \hat{\mathbf{R}}_{xx}] \quad (3.74)$$

Continuing in this fashion, $\Theta^{(0)} = [\hat{\theta}_1^{(0)} \hat{\theta}_2^{(0)}, \dots, \hat{\theta}_D^{(0)}]$ is computed. After proper initialization, the alternating projection algorithm can be used to maximize the log likelihood function.

Further reduction in computational complexity can be achieved by taking advantage of the properties of the projection matrix [Zis88]. It can be shown that, by using the properties of the projection matrix, (3.71) can be written as

$$\hat{\Theta}_i^{(n+1)} = \arg \max_{\theta_i} \text{trace} \left[\mathbf{P}_{\mathbf{a}(\theta_i)} \hat{\mathbf{R}}_{xx} \right] \quad (3.75)$$

where

$$\mathbf{a}(\theta_i)_{\mathcal{A}(\hat{\Theta}_i^{(n)})} = (\mathbf{I} - \mathbf{P}_{\mathcal{A}(\hat{\Theta}_i^{(n)})}) \mathbf{a}(\theta_i) \quad (3.76)$$

By defining a unit vector,

$$\mathbf{b}(\theta_i, \hat{\Theta}_i^{(n)}) = \frac{\mathbf{a}(\theta_i)_{\mathcal{A}(\hat{\Theta}_i^{(n)})}}{\|\mathbf{a}(\theta_i)_{\mathcal{A}(\hat{\Theta}_i^{(n)})}\|} \quad (3.77)$$

equation (3.75) can be rewritten as

$$\max_{\theta_i} \mathbf{b}^H(\theta_i, \hat{\Theta}_i^{(n)}) \mathbf{R} \mathbf{b}(\theta_i, \hat{\Theta}_i^{(n)}) \quad (3.78)$$

The alternating projection based maximum likelihood estimator algorithm may be summarized as follows:

Step 1: Initialization

$$\hat{\theta}_i^{(0)} = \max_{\theta_i} \mathbf{b}^H(\theta_i, \hat{\Theta}_i^{(0)}) \mathbf{R} \mathbf{b}(\theta_i, \hat{\Theta}_i^{(0)}) \quad , \text{ for } i = 1, \dots, D \quad (3.79)$$

Step2: Main Loop

Until $|\hat{\theta}_i^{(n)} - \hat{\theta}_i^{(n-1)}| < \varepsilon$, do

$$\hat{\theta}_i^{(n)} = \max_{\theta_i} \mathbf{b}^H(\theta_i, \hat{\Theta}_i^{(n)}) \mathbf{R} \mathbf{b}(\theta_i, \hat{\Theta}_i^{(n)}) \quad , \text{ for } i = 1, \dots, D. \quad (3.80)$$

3.5 DOA Estimation under Coherent Signal Conditions

As mentioned in the Section 3.3.1, the MUSIC algorithm works on the premise that the signals impinging on the array are not fully correlated, or coherent. Only under noncoherent conditions does the source covariance matrix \mathbf{R}_{ss} satisfy the full rank condition which is the basis of the MUSIC eigen decomposition. The performance of MUSIC degrades severely in a coherent or highly correlated signal environment as encountered in multipath propagation. Many modifications to the MUSIC algorithm have been proposed to make it work in the presence of coherent signals. Many of these techniques involve modification of the covariance matrix through a preprocessing scheme called *spatial smoothing*. One method of spatial smoothing proposed by Evans et. al [Eva82] and further elaborated by Shan et.al [Sha85] is based on averaging the covariance matrix of identical overlapping arrays. This method requires an array of identical elements built with some form of periodic structure, such as the uniformly spaced linear array. An adaptive spatial smoothing technique was proposed by Takao and Kikuma [Tak87], which is useful for interference cancellation in multipath environments. Another form of spatial smoothing proposed by Haber and Zoltowski [Hab86] involves moving the entire array structure during the time interval in which the covariances are estimated. A similar technique based on moving the array was proposed by Li and Compton [Li94]. Spatial smoothing techniques always impose restrictions of some form or the other on the type and structure of the array. For the general case, coherent signal detection involves employing a multidimensional search through all possible linear combination of steering

vectors to find those orthogonal to the noise subspace [Zol86].

3.5.1 Spatial Smoothing Techniques

The idea behind the spatial smoothing scheme proposed by Evans et. al., [Eva82] is as follows. Let a linear uniform array with M identical sensors be divided into overlapping forward subarrays of size p , such that the sensor elements $\{1, \dots, p\}$ forms the first forward subarray, sensors $\{2, \dots, p+1\}$ forms the second forward subarray, etc. Let $\mathbf{x}_k(t)$, denote the vector of received signals at the k th forward subarray. Based on the notation of equation, (3.9) we can write

$$\mathbf{x}_k^f(t) = \mathbf{A}\mathbf{F}^{(k-1)}\mathbf{s}(t) + \mathbf{n}_k(t) \quad (3.81)$$

where $\mathbf{F}^{(k)}$ denotes the k th power of the diagonal matrix

$$\mathbf{F} = \text{diag} \left\{ \exp \left(-j\omega_0 \left(\frac{d}{c} \cos \theta_1 \right) \right), \dots, \exp \left(-j\omega_0 \frac{d}{c} \cos \theta_D \right) \right\} \quad (3.82)$$

The covariance matrix of the k th forward subarray is therefore given by

$$\mathbf{R}_k^f = \mathbf{A}\mathbf{F}^{(k-1)}\mathbf{R}_{ss}\mathbf{F}^{H(k-1)}\mathbf{A}^H + \sigma_{Noise}^2 \mathbf{I} \quad (3.83)$$

where \mathbf{R}_{ss} is the covariance matrix of the sources.

Based on the above, the forward averaged spatially smoothed covariance matrix \mathbf{R}^f is defined as the sample mean of the subarray covariance matrices:

$$\mathbf{R}^f = \frac{1}{L} \sum_{k=1}^L \mathbf{R}_k^f \quad (3.84)$$

where $L=M-p+1$ is the number of subarrays. Now, substituting (3.83) in (3.84), we obtain

$$\mathbf{R}^f = \mathbf{A} \left(\frac{1}{L} \sum_{k=1}^L \mathbf{F}^{(k-1)} \mathbf{R}_{ss}^f \mathbf{F}^{H(k-1)} \right) \mathbf{A}^H + \sigma_{Noise}^2 \mathbf{I} \quad (3.85)$$

where \mathbf{R}_{ss}^f is the modified covariance matrix of the signals, given by

$$\mathbf{R}_{ss}^f = \frac{1}{L} \sum_{k=1}^L \mathbf{F}^{(k-1)} \mathbf{R}_{ss} \mathbf{F}^{H(k-1)} \quad (3.86)$$

For $L \geq D$, the covariance matrix \mathbf{R}_{ss}^f will be nonsingular regardless of the coherence of the signals [Pil89A].

The price paid for detection of coherent signals using forward averaging spatial smoothing is the reduction in the array aperture. An M element array can only detect $M/2$ coherent signals using MUSIC with forward averaging spatial smoothing as opposed to $M-1$ noncoherent signals that can be detected by conventional MUSIC.

Pillar and Kwon [Pil89A] proved that by making use of a set of forward and conjugate backward subarrays simultaneously, it is possible to detect up to $2M/3$ coherent signals. In this scheme, in addition to splitting the array into overlapping forward subarrays, it is also split into overlapping backward arrays such that the first backward subarray is formed using elements $\{M, M-1, \dots, M-p+1\}$, the second subarray is formed using elements $\{M-1, M-2, \dots, M-p\}$, and so on.

Similar to (3.81), the complex conjugate of the received signal vector at the k th backward subarray can be expressed as

$$\begin{aligned} \mathbf{x}_k^b &= [x_{M-k+1}^*, x_{M-k}^*, \dots, x_{p-k+1}^*]^T \\ &= \mathbf{A}\mathbf{F}^{k-1}(\mathbf{F}^{M-1}\mathbf{s})^* + \mathbf{n}_k^*, \quad (1 \leq k \leq L) \end{aligned} \quad (3.87)$$

where \mathbf{F} is defined in (3.82). The covariance matrix of the k th backward subarray is therefore given by

$$\mathbf{R}_k^b = \mathbf{A}\mathbf{F}^{k-1}\mathbf{R}_{ss}(\mathbf{F}^{k-1})^H\mathbf{A}^H + \sigma_{Noise}^2\mathbf{I} \quad (3.88)$$

where

$$\begin{aligned}\mathbf{R}_{ss} &= \mathbf{F}^{-(M-1)} E[\mathbf{s}^* \mathbf{s}^T] (\mathbf{F}^{-(M-1)})^H \\ &= \mathbf{F}^{-(M-1)} \mathbf{R}_{ss}^* (\mathbf{F}^{-(M-1)})^H\end{aligned}\quad (3.89)$$

Now the spatially smoothed backward subarray matrix \mathbf{R}^b can be defined as

$$\mathbf{R}^b = \frac{1}{L} \sum_{k=1}^L \mathbf{R}_k^b = \mathbf{A} \mathbf{R}_{ss}^b \mathbf{A}^H + \sigma_{Noise}^2 \mathbf{I} \quad (3.90)$$

It can be shown that the backward spatially smoothed covariance matrix \mathbf{R}^b will be of full rank so long as \mathbf{R}_{ss}^b is non-singular, and the non-singularity of \mathbf{R}_{ss}^b is guaranteed whenever $L \geq D$ [Pil89A].

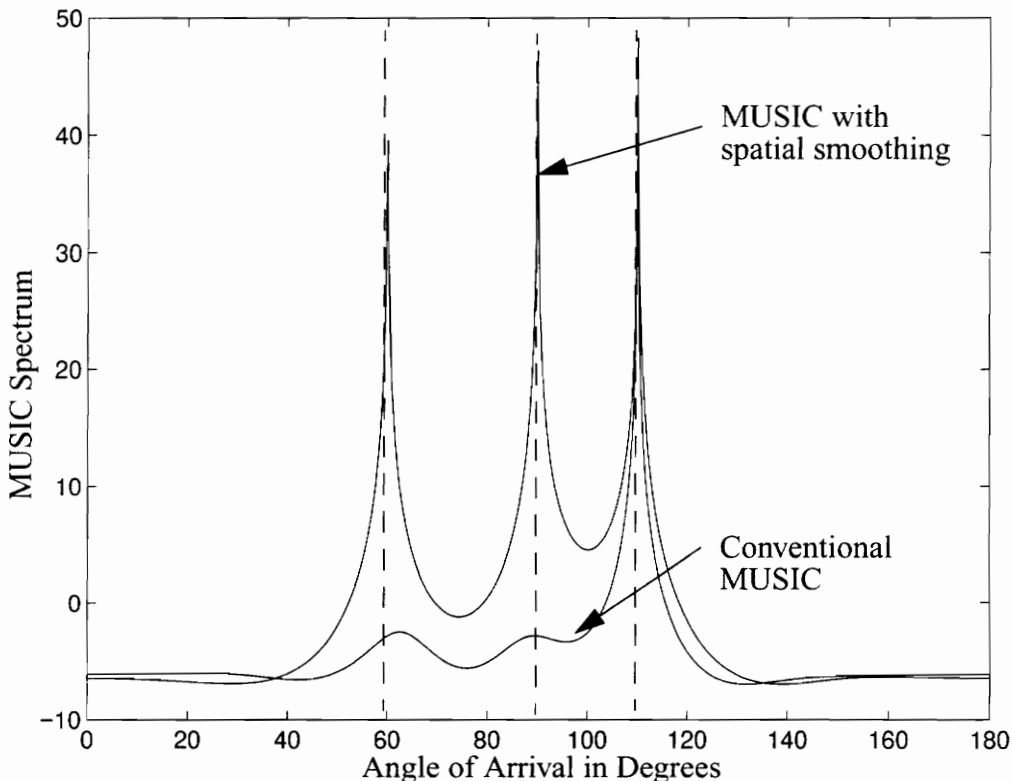


Figure 3.5: Comparison of MUSIC with and without forward/backward averaging in coherent multipath. Three coherent signals of equal power at an SNR of 20 dB arrive at a 6-element uniformly spaced array with an interelement spacing equal to half a wavelength at angles 60, 90 and 120 degrees respectively

Now the forward/conjugate backward smoothed covariance matrix $\tilde{\mathbf{R}}$ is defined as the mean of \mathbf{R}^f and \mathbf{R}^b , i.e,

$$\tilde{\mathbf{R}} = \frac{\mathbf{R}^f + \mathbf{R}^b}{2} \quad (3.91)$$

Using an M element array, applying MUSIC on $\tilde{\mathbf{R}}$, it is possible to detect up to $2M/3$ coherent signals [Pil89A].

Figure 3.5 shows a comparison between conventional MUSIC and MUSIC with forward/backward spatial smoothing in a coherent multipath signal environment. Simulations with three coherent signals impinging on 6-element uniform linear array at 60, 90, and 120 degrees respectively, show that MUSIC fails almost completely, while with spatial smoothing preprocessing scheme all the three multipath signals are detected clearly.

3.5.2 Multidimensional MUSIC

It was stated in section 3.3.1 that in the presence of coherent signals, the signal correlation matrix \mathbf{R}_{ss} becomes singular, and hence violates the premise on which the MUSIC derivation is based on. However if all the coherent signals (typically all multipath components associated with a single source) are grouped together as a single signal the signal correlation matrix can retain its full rank. However, now the direction vector matrix \mathbf{A} will not consist of steering vectors corresponding to distinct directions of arrival. Instead the columns of \mathbf{A} will consist of spatial signatures associated with each source (group of coherent signals). Essentially, we can have \mathbf{R}_{ss} as full rank by applying the data model of equation (1.19) in section 1.1.2. Now the column vectors of \mathbf{A} are linear combinations of one or more steering vectors corresponding to one or more directions of arrival. Once the full rank status of \mathbf{R}_{ss} is maintained, the MUSIC algorithm is valid, and the signal subspace is spanned by the spatial signature vectors

$$\{\mathbf{a}_1, \mathbf{a}_2, \dots, \mathbf{a}_D\} \quad (3.92)$$

which are orthogonal to the noise subspace. Computing the MUSIC spectrum now involves searching through all possible spatial signature vectors to find peaks in the spectrum. Since spatial signatures are linear combinations of steering vectors, this essentially involves a search in an N_{mp} dimensional space, where N_{mp} is the number of components associated with a single source (group). The multi-dimensional MUSIC spectrum is given by:

$$\begin{aligned} & P_{\text{MD-MUSIC}}(\theta_1, \theta_2, \dots, \theta_{N_{mp}}) \\ &= \left\{ \min_{\mathbf{c}} [\mathbf{c}^H \mathbf{a}^H(\theta_1, \theta_2, \dots, \theta_{N_{mp}}) \mathbf{V}_N \mathbf{V}_N^H \mathbf{a}(\theta_1, \theta_2, \dots, \theta_{N_{mp}}) \mathbf{c}] \right\}^{-1} \end{aligned} \quad (3.93)$$

where the vector \mathbf{c} is defined as

$$\mathbf{c} = \left[1, \frac{c_2}{c_1}, \frac{c_3}{c_1}, \dots, \frac{c_{N_{mp}}}{c_1} \right]^T \quad (3.94)$$

As clearly seen from equation (3.93), as the number of multipath components increases, the complexity of the multidimensional search increases exponentially. The computational complexity of MD-MUSIC prohibits its real-time implementation for more than about 2 dimensions.

3.6 The Iterative Least-Squares Projection Based CMA

The Iterative Least Squares Projection Based CMA (ILSP-CMA) is a property restoral based algorithm which can be used to jointly detect the spatial signatures and the waveforms associated with multiple sources incident on a receiver array. The ILSP-CMA is a data-efficient and cost efficient technique which overcomes many of the problems associated with the Multi-target CMA and Multi-stage CMA algorithms[Par95].

Consider an M -element array with signals from D sources incident on it. Over a block of N snapshots, the array output can be expressed as

$$\mathbf{X} = \mathbf{AS} + \mathbf{N} \quad (3.95)$$

where $\mathbf{X} = [\mathbf{x}(1), \dots, \mathbf{x}(N)]$ is the array input data matrix of dimension $M \times N$, $\mathbf{A} = [\mathbf{a}(\theta_1), \dots, \mathbf{a}(\theta_D)]$ is the spatial signature matrix of dimension $M \times D$, $\mathbf{S} = [s(1), \dots, s(N)]$ is the signal waveform matrix of dimension $D \times N$, and $\mathbf{N} = [\mathbf{n}(1), \dots, \mathbf{n}(N)]$ is the noise matrix of dimension $M \times N$. Given this block formulation, the ILSP-CMA algorithm provides a means of jointly estimating the spatial signature matrix \mathbf{A} and the signal waveforms \mathbf{S} , given N snapshots of the array input data matrix \mathbf{X} .

By modeling the unknown signal waveforms as deterministic quantities to be estimated, and assuming that the number of signals are known or has been estimated, the log likelihood function of the array output data is given by [Tal94]

$$J = -\text{constant} - MN \log \sigma_{Noise}^2 - \frac{1}{\sigma_{Noise}^2} \sum_{k=1}^K \|\mathbf{x}(k) - \mathbf{As}(k)\|^2 \quad (3.96)$$

where σ_{Noise}^2 is the noise power. The maximum-likelihood (ML) estimator maximizes J with respect to the unknown spatial signatures \mathbf{A} and $s(k)$, $k = 1, \dots, N$ to yield the following minimization problem [Tal94]

$$\min_{\mathbf{A}, \mathbf{S}} = \|\mathbf{X} - \mathbf{AS}\|_F^2 \quad (3.97)$$

where $\|\cdot\|_F^2$ is the squared Frobenius norm, and the elements of \mathbf{S} are constrained to have a constant modulus. This is a nonlinear separable optimization problem which can be solved in two steps [Gol73].

The ILSP-CMA is an efficient algorithm to solve the minimization problem of (3.97) [Par95]. Let

$$f(\mathbf{A}, \mathbf{S}) = \|\mathbf{X} - \mathbf{AS}\|_F^2 \quad (3.98)$$

be a function of continuous matrix variables \mathbf{A} and \mathbf{S} . Given an initial estimate $\hat{\mathbf{A}}$ of \mathbf{A} , the minimization of $f(\hat{\mathbf{A}}, \mathbf{S})$ with respect to continuous \mathbf{S} is a least squares problem. This is a

separable problem in \mathbf{S} , and the estimate of \mathbf{S} is given by the least squares solution of (3.98), which is given by,

$$\hat{\mathbf{S}} = (\hat{\mathbf{A}}^H \hat{\mathbf{A}})^{-1} \hat{\mathbf{A}}^H \mathbf{X} \quad (3.99)$$

Each element of the solution $\hat{\mathbf{S}}$ is then divided by its absolute value to make each signal unit modulus. That is, each signal is projected onto the unit circle. A better estimate of \mathbf{A} is then obtained by minimizing $f(\mathbf{A}, \hat{\mathbf{S}})$ with respect to \mathbf{A} , keeping $\hat{\mathbf{S}}$ fixed. This is again a least-squares problem and the new estimate of \mathbf{A} is given by the least squares solution,

$$\hat{\mathbf{A}} = \mathbf{X} \hat{\mathbf{S}}^H (\hat{\mathbf{S}} \hat{\mathbf{A}}^H)^{-1} \quad (3.100)$$

Since the first element in each unknown spatial signature is a real value, it can be made equal to unity by dividing the elements of the spatial signature vectors by their first element. This process is continued until $\hat{\mathbf{A}}$ converges.

The ILSP-CMA algorithm may be summarized as follows:

Step 1. Given \mathbf{A}_0 (start with a random \mathbf{A}_0), $n = 0$

Step 2. $n = n+1$

- $\mathbf{S}_n = (\mathbf{A}_{n-1}^H \mathbf{A}_{n-1})^{-1} \mathbf{A}_{n-1}^H \mathbf{X}$
- Project all elements of $[\mathbf{S}_n]$ to the closest values on the unit circle (hard limit)
- $\mathbf{A}_n = \mathbf{X} \mathbf{S}_n^H (\mathbf{S}_n \mathbf{S}_n^H)^{-1}$

Step 3. Divide each column of \mathbf{A}_n by its first element value.

Step 4. Repeat steps 2 and 3 until \mathbf{A}_n and \mathbf{A}_{n-1} are close enough.

3.7 The Integrated Approach to DOA Estimation

In Section 3.6 it was shown how to obtain an estimate of multiple signals and their spatial signatures using the ILSP-CMA algorithm. If a signal has only one component, its spatial

signature is identical to the steering vector corresponding to its direction of arrival. Therefore, if we have an estimate of the spatial signature of a signal with a single component, we can estimate its direction of arrival by observing its spatial signature. The direction of arrival can be estimated by searching through all possible steering vectors, and determining the one closest in two norm to the estimated spatial signature. Mathematically, the direction of arrival θ is given by

$$\theta = \arg \min_{\theta} \|\mathbf{a}(\theta) - \mathbf{a}_{ss}\|_2 \quad (3.101)$$

where $\mathbf{a}(\theta)$ is the steering vector corresponding to direction of arrival θ , and \mathbf{a}_{ss} is the estimated spatial signature.

Xu and Liu proposed a novel technique to estimate the direction of arrivals of the direct and multipath components of a signal from their spatial signature [Xu95]. In subspace based algorithms, in order to determine the directions-of-arrival we had to construct a covariance matrix whose signal subspace is the span of \mathbf{A} . If we have an estimate of the spatial signature matrix \mathbf{A} , we can form a *spatial signature covariance matrix* $\mathbf{R}_{aa} = \mathbf{A}\mathbf{A}^H$ on which the eigen decomposition may equivalently be performed to obtain the directions of arrival. In the presence of coherent signals, it is required to perform forward/backward averaging and form a spatially smoothed spatial signature covariance matrix before eigen decomposition.

If we have the spatial signature estimate of a source, Xu and Liu proposed a technique to estimate the directions of arrival of the various components of the signal [Xu95]. By applying the standard forward/backward spatial smoothing techniques discussed in section 3.5.1 [Pil89A] to the spatial signature vector \mathbf{a}_{ss} , a smoothed spatial signature covariance matrix can be formed as

$$\mathbf{R}_{fb}(K) = \mathbf{R}_f(K) + \mathbf{J}\mathbf{R}_f^*(K)\mathbf{J} \quad (3.102)$$

where \mathbf{J} is the permutation matrix with all zeros except ones in the anti-diagonal elements,

K is the smoothing factor (number of subarrays), and

$$\mathbf{R}_f(K) = \sum_{i=1}^K (\mathbf{a}_{ss}(i:M-K+i)\mathbf{a}_{ss}(i:M-K+1)^H) \quad (3.103)$$

Subspace based algorithms such as MUSIC and ESPRIT can now be applied to this smoothed spatial signature covariance matrix, and up to $2M/3$ DOA's from coherent sources can be estimated. Note that by using ILSP-CMA to estimate M spatial signatures, and applying subspace techniques such as MUSIC or ESPRIT to the smoothed spatial signature covariance matrices of each spatial signature, it is possible to estimate up to $2M^2/3$ DOA's using an M -element array. In a situation where there are multiple cochannel users with each user having multiple components, this technique can determine the directions of arrival of multiple components of multiple users and associate each component to the correct user.

Computer simulations were ran to study the performance of ILSP-CMA for spatial signature estimation along with MUSIC with forward and conjugate backward averaging. Figure 3.6 shows the estimated MUSIC spectrum for the following case: A uniformly spaced linear array with six elements and an interelement spacing of half wavelength was used. For spatial smoothing the array was divided into two overlapping 5-element subarrays. Six uncorrelated signals each with a direct and three multipath components are incident on the array. The multipath components are 10 dB below the line-of-sight component and the signal to noise ratio was 20 dB. The first signal had components arriving at 80, 110, 140 and 170 degrees, the second signal had components at 20, 90, 130, 150 degrees, the third signal had components at 30, 60, 90, 120 degrees, the fourth signal had components at 10, 40, 70, 100 degrees, the fifth signal had components at 45, 75, 105, 135 degrees, and the sixth signal had components at 10, 60, 100, 110 degrees. Figure shows that ILSP-CMA along with forward and conjugate backward averaged MUSIC is able to resolve a total of 24 signal components.

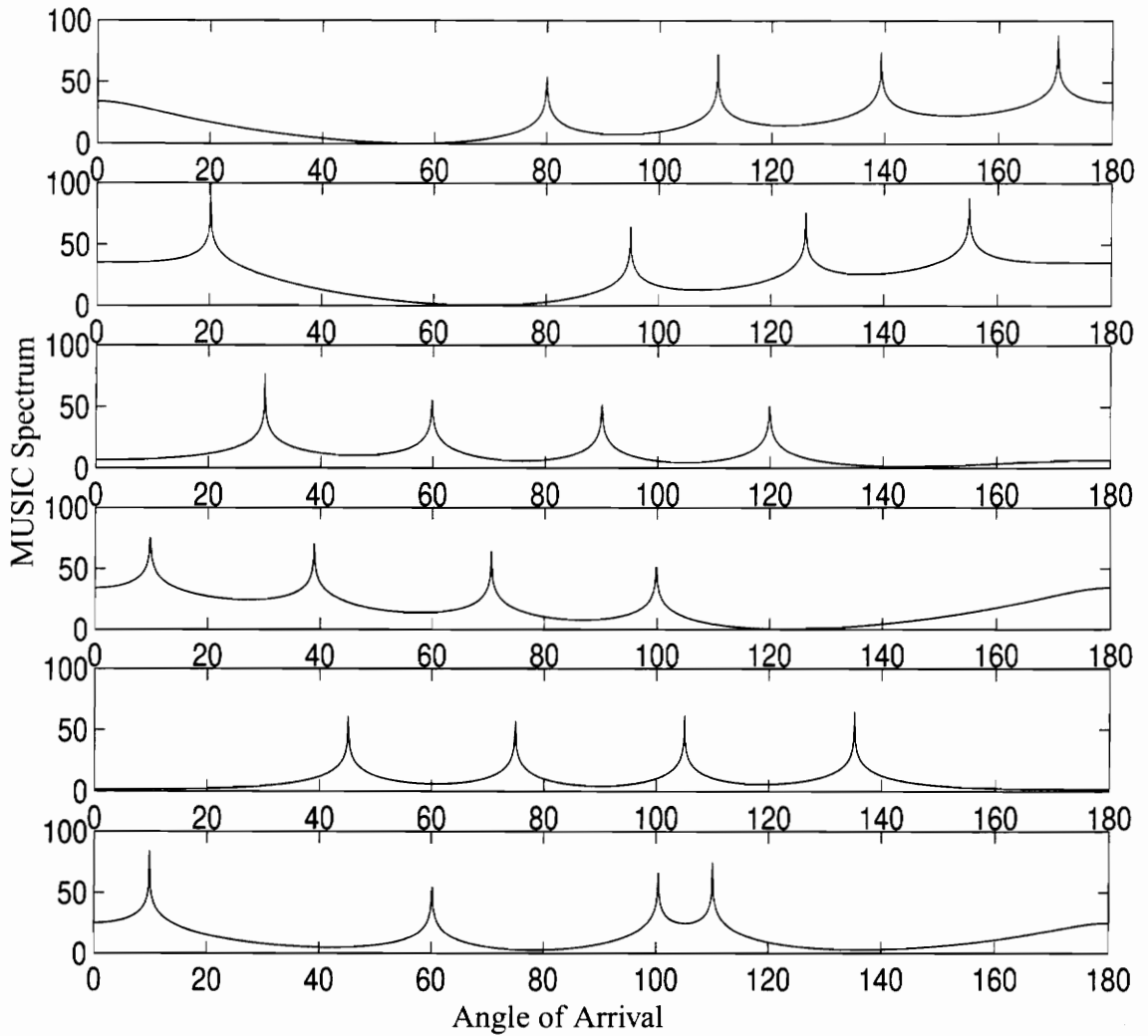


Figure 3.6: Example of spatial spectrum estimated using ILSP-CMA for spatial signature estimation, followed by MUSIC with forward backward averaging. The six element array is able to resolve 24 direct and multipath components and associate each component to the appropriate signal (user).

3.8 Detection of Number of Sources

Most of the DOA estimation algorithms described so far require that the number of sources be known or estimated. Detection of the number of sources impinging on the array

is a key step in most of the superresolution DOA estimation techniques. In the eigen decomposition based techniques, an estimate of the number of sources is obtained from an estimate of the number of repeated smallest eigenvalues. Since in practice the input sample covariance matrix is formed using a finite set of samples, the smallest eigenvalues are not exactly equal. Various statistical methods have been proposed to test for the equality or closeness of eigenvalues, which can be used to estimate the number of sources.

3.8.1 The SH, MDL and AIC Criteria

Anderson [And63] showed that a useful statistic for testing the closeness of eigenvalues is

$$L(d) = -N(M-d)\log \left\{ \frac{\left(\prod_{i=d+1}^M \hat{\lambda}_i \right)^{\frac{1}{(M-d)}}}{\frac{1}{M-d} \sum_{i=d+1}^M \hat{\lambda}_i} \right\} \quad (3.104)$$

where $\hat{\lambda}_i$ is the estimated k th eigenvalue, d is the hypothesized estimate of number of signals, M is the number of elements in the array, and N is the size of the sample data block. In equation (3.104), the closeness of the eigenvalues is measured as the ratio of their geometric mean to their arithmetic mean. By setting up a subjective threshold γ_d , a sequential hypothesis (SH) test can be performed and the first d such that $L(d) < \gamma_d$ can be taken as the estimate \hat{D} of the number of signals D .

While the above sequential hypothesis testing to determine the number of sources is computationally attractive, the need to set up a subjective threshold is a major disadvantage. Wax and Kailath [Wax85] proposed two other detection schemes based on the application of the Akaike information theoretic criteria (AIC) [Aka73] and the Rissanen minimum descriptive length (MDL) criteria [Ris78]. These methods do not require a subjective threshold, and the number of sources is determined as the value for

which the AIC or MDL criteria is minimized.

In the AIC-based approach, the number of signals \hat{D} , is determined as the value of $d \in \{0, 1, \dots, M-1\}$ which minimizes the following criterion

$$AIC(d) = -\log \left\{ \frac{\prod_{i=d+1}^M \lambda_i^{\frac{1}{(M-d)}}}{\frac{1}{M-d} \sum_{i=d+1}^M \lambda_i} \right\}^{(M-d)N} + d(2M-d) \quad (3.105)$$

where λ_i are the eigenvalues of the sample covariance matrix $\hat{\mathbf{R}}_{xx}$, N is the number of snapshots used to compute $\hat{\mathbf{R}}_{xx}$, and M is the number of elements in the array. The first term in equation (3.105) is derived directly from the log-likelihood function, and the second term is the penalty factor added by the AIC criterion.

In the MDL-based approach, the number of signals is determined as the argument which minimizes the following criterion

$$MDL(d) = -\log \left\{ \frac{\prod_{i=d+1}^M \lambda_i^{\frac{1}{(M-d)}}}{\frac{1}{M-d} \sum_{i=d+1}^M \lambda_i} \right\}^{(M-d)N} + \frac{1}{2}d(2M-d)\log N \quad (3.106)$$

Here again, the first term is derived directly from the log-likelihood function, and the second term is the penalty factor added by the MDL criterion. Wax and Kailath [Wax85] showed through simulations that the MDL criterion yields a consistent estimate of the number of signals, and the AIC yields an inconsistent estimate that tends, asymptotically, to overestimate the number of signals.

Xu et. al., [Xu94A] showed that the SH, AIC and MDL procedures cannot be applied directly to situations where spatial smoothing preprocessing is involved. The spatial smoothing preprocessing operation complicates the source order detection process. Xu et.

al., modified the AIC and MDL criterion such that they can be applied correctly to situations where spatial smoothing is performed. Essentially, this leads to a change in the penalty function associated with the AIC and MDL criterion. If the penalty functions (i.e. the second term in equations (3.105) and (3.106)) are denoted $p_{AIC}(d)$ and $p_{MDL}(d)$ respectively, they have to be modified as listed below in Table 2.1 for the various spatial smoothing cases.

Table 2.1: Modified Values of the Penalty function in AIC and MDL Detection Schemes

Spatial Smoothing Type	$p_{AIC}(d)$	$p_{MDL}(d)$
Forward Only	$d(2M - 2d + 1)$	$0.5d(2M - 2d + 1)\log N$
Forward/conjugate Backward	$0.5d(2M - d + 1)$	$0.25d(2M - d + 1)\log N$

3.8.2 Order Estimation Using Transformed Gerschgorin Radii

Wu et.al., [Wu95] proposed a new technique for source order estimation based on the effective use of the Gerschgorin radii of a unitary transformed input covariance matrix. The Gerschgorin theorem on eigenvalues of a matrix provides a method for estimating the location of eigenvalues from the values of the matrix elements. For an $M \times M$ matrix $\mathbf{A} = \{a_{ij}\}$, Gerschgorin proved that all the eigenvalues of the matrix are contained in the union of M disks \mathcal{O}_i , $i = 1, \dots, L$. These disks are centered at a_{ii} and have radii, called the Gerschgorin radii r_i , equal to the sum of the magnitudes of all elements of the i th row vector, excluding the i th element. That is,

$$r_i = \sum_{j=1, j \neq i}^M |a_{ij}| \quad (3.107)$$

In other words, the eigenvalues of a matrix are located within the Gerschgorin disks which represent the collection of points in the complex plane whose distance to a_{ii} is at most r_i . That is, \mathcal{O}_i represents the collection of complex numbers z with the property of

$$r_i \geq |z - a_{ii}| \quad (3.108)$$

Wu et.al., observed that at low signal to noise ratio conditions, the eigenvalues of the input covariance matrix \mathbf{R}_{xx} are spread across a large range and the Gerschgorin disks for the matrix tightly overlap. Through a proper unitary transformation which preserves the eigenvalues, the overlap in the Gerschgorin disks can be reduced and hence be effectively used for source number detection. The idea is to rotate the covariance matrix such that its Gerschgorin disks can be formed into two distinct signal and noise constellations. The source collection with larger Gerschgorin radii will contain exactly M largest signal eigenvalues, and the noise collection with small Gerschgorin radii will contain the remaining noise eigenvalues. That is, a unitary transformation should be chosen such that the noise Gerschgorin disks of the transformed covariance matrix are small and as far away from the signal Gerschgorin disks as possible. Once this is achieved, it is relatively easier to estimate the source order by classification of disks.

In the proposed method, the covariance matrix is first partitioned as follows:

$$\mathbf{R}_{xx} = \begin{bmatrix} r_{11} & r_{12} & \dots & r_{1M} \\ r_{21} & r_{22} & \dots & r_{2M} \\ & \dots & & \\ r_{M1} & r_{M2} & \dots & r_{MM} \end{bmatrix} = \begin{bmatrix} \mathbf{R}_1 & \mathbf{r} \\ \mathbf{r}^H & r_{MM} \end{bmatrix} \quad (3.109)$$

where \mathbf{R}_1 is the leading principal submatrix of \mathbf{R}_{xx} . The reduced covariance matrix \mathbf{R}_1 can also be decomposed by its eigen-structure as

$$\mathbf{R}_1 = \mathbf{U}_1 \mathbf{D}_1 \mathbf{U}_1^H \quad (3.110)$$

where \mathbf{U}_1 is the $M-1 \times M-1$ unitary matrix formed by the eigenvectors of \mathbf{R}_1 as

$$\mathbf{U}_1 = [\mathbf{v}_1' \mathbf{v}_2' \dots \mathbf{v}_D' \dots \mathbf{v}_M'] \quad (3.111)$$

and \mathbf{D}_1 is the diagonal matrix constructed from the corresponding eigenvalues as

$$\mathbf{D}_1 = \text{diag}(\lambda_1' \lambda_2' \dots \lambda_D' \dots \lambda_{M-1}') \quad (3.112)$$

where $\lambda'_1 \geq \lambda'_2 \geq \dots \geq \lambda'_D \geq \dots \geq \lambda'_{M-1}$. If the eigenvalues of the original covariance matrix \mathbf{R}_{xx} are denoted $\lambda_1, \lambda_2, \dots, \lambda_D, \dots, \lambda_M$, it can be shown that the eigenvalues of \mathbf{R}_{xx} and \mathbf{R}_1 satisfy the interlacing property shown as

$$\lambda_1 \geq \lambda'_1 \geq \lambda_2 \geq \lambda'_2 \geq \dots \geq \lambda_D \geq \lambda'_D \geq \dots \geq \lambda_{M-1} \geq \lambda'_{M-1} \geq \lambda_M \quad (3.113)$$

By defining a unitary transformation \mathbf{U}

$$\mathbf{U} = \begin{bmatrix} \mathbf{U}_1 & 0 \\ 0^T & 1 \end{bmatrix} \quad (3.114)$$

the transformed input covariance matrix becomes,

$$\mathbf{Q}_{xx} = \mathbf{U}^H \mathbf{R}_{xx} \mathbf{U} = \begin{bmatrix} \mathbf{U}_1^H \mathbf{R}_{xx} \mathbf{U}_1 & \mathbf{U}_1^H \mathbf{r} \\ \mathbf{r}^H \mathbf{U}_1 & r_{MM} \end{bmatrix} = \begin{bmatrix} \mathbf{D}_1 & \mathbf{U}_1^H \mathbf{r} \\ \mathbf{r}^H \mathbf{U}_1 & r_{MM} \end{bmatrix} \quad (3.115)$$

which can be shown to be equal to [Wu95]

$$\mathbf{Q}_{xx} = \begin{bmatrix} \lambda_1 & 0 & 0 & \dots & 0 & \rho_1 \\ 0 & \lambda'_2 & 0 & \dots & 0 & \rho_2 \\ 0 & 0 & \lambda'_3 & \dots & 0 & \rho_3 \\ \dots & \dots & \dots & \dots & \dots & \dots \\ 0 & 0 & 0 & \dots & \lambda'_{M-1} & \rho_{M-1} \\ \rho_1 & \rho_2 & \rho_3 & \dots & \rho_{M-1} & r_{MM} \end{bmatrix} \quad (3.116)$$

where

$$\rho_i = \mathbf{v}'^H_i \mathbf{r}, \quad i = 1, 2, \dots, M-1 \quad (3.117)$$

The Gerschgorin disks of the transformed covariance matrix \mathbf{Q}_{xx} possess the Gerschgorin radii

$$r_i = |\rho_i| = |\mathbf{v}'^H_i \mathbf{r}| \text{ for } i = 1, 2, \dots, M-1 \quad (3.118)$$

By incorporating the Gerschgorin radii information into the log-likelihood function, Wu et. al. derived a new source order estimator function which they called the Gerschgorin

Likelihood Estimator (GLE). The GLE function is given by [Wu95]

$$GLE(d) \approx -N(M-1-k)\log \left[\frac{\left(\prod_{i=d+1}^{M-1} \lambda_i' \right)^{\frac{1}{M-d-1}}}{\frac{1}{M-d-1} \sum_{i=d+1}^{M-1} \lambda_i'} \right] - N\log \left(r_{MM} - \sum_{i=1}^d \frac{r_i^2}{\lambda_i} \right) \quad (3.119)$$

where N is the number of data snapshots.

By applying the AIC and MDL penalty factors to equation (3.119), two source order estimation functions can be obtained. They are called the Gerschgorin AIC (GAIC) and Gerschgorin MDL (GMDL) criterion respectively, and are given by

$$GAIC(d) \approx -N(M-1-k)\log \left[\frac{\left(\prod_{i=d+1}^{M-1} \lambda_i' \right)^{\frac{1}{M-d-1}}}{\frac{1}{M-d-1} \sum_{i=d+1}^{M-1} \lambda_i'} \right] - N\log \left(r_{MM} - \sum_{i=1}^d \frac{r_i^2}{\lambda_i} \right) + d^2 + d \quad (3.120)$$

$$GMDL(d) \approx -N(M-1-k)\log \left[\frac{\left(\prod_{i=d+1}^{M-1} \lambda_i' \right)^{\frac{1}{M-d-1}}}{\frac{1}{M-d-1} \sum_{i=d+1}^{M-1} \lambda_i'} \right] - N\log \left(r_{MM} - \sum_{i=1}^d \frac{r_i^2}{\lambda_i} \right) + 0.5(d^2 + d)\log N \quad (3.121)$$

The number of sources is determined as the argument which minimizes these functions. It is shown in [Wu95] that the GAIC and GMDL estimators are more consistent than the simple AIC and MDL estimators. Further, since the GAIC and GMDL techniques involves the eigen decomposition of an $M-1 \times M-1$ matrix as against an $M \times M$ matrix required in AIC and MDL techniques, they are computationally more efficient. However, since they are based on a submatrix of \mathbf{R}_{xx} , they can only detect up to $M-2$ sources, as opposed to $M-1$ sources that can be detected using the regular AIC and MDL criteria.

All the source estimators discussed so far are based on the assumptions of Gaussian and spatially white noise. Wu et.al, has also derived modified versions of GAIC and GMDL which they call MGAIC and MGMDL respectively, which yield consistent estimates under non-white noise conditions and when only a few snapshots of data are available.

3.9 Summary

In this chapter, we described various techniques for estimating the direction-of-arrival of radio signals impinging on an antenna array. A survey of algorithms used for DOA estimation was presented. A discussion of the source order estimation algorithms was presented in Section 3.8. Chapter 4 will present a simulation based comparison of some of these algorithms.

Chapter 4

Simulation-Based Performance Comparison of DOA Estimation Algorithms

4.1 Introduction

This chapter presents the results of various simulations conducted to evaluate the performance of some of the direction-of-arrival and source order estimation algorithms described in Chapter 3. All the simulations are run assuming a six element uniformly spaced linear array (ULA) with an interelement spacing of half a wavelength. The operating carrier frequency is assumed to be 2050 MHz. All signals incident on the array are assumed to be narrowband plane waves with the azimuth arrival angle measured counterclockwise with respect to the array axis (see Figure 2.2). Noise at each sensor element is assumed to be additive white Gaussian and uncorrelated with the noise at other sensor elements. Simulations are run for the case of noncoherent as well as coherent signals. Coherent sources are simulated using CW tone signals at the same frequency, and non-coherent signals are simulated using tones at different frequencies. All signals are sampled at a rate of 64 kHz. In all the simulations, the signals are modeled using the baseband complex envelope representation. The narrowband input data model discussed in Section 2.1 and given by equation (2.14) is used throughout all the simulations.

Different DOA estimation algorithms are compared to study their ability to resolve closely spaced signals, ability to resolve coherent multipath signals, and accuracy in DOA estimation. The accuracy in DOA estimation as a function of number of signals, angle of arrival, angular separation between adjacent signals and relative power levels of multiple signals is studied. The DOA estimation errors due to array imperfections (improper spacing between elements) are also studied. The performance of various source order estimation techniques are also determined through simulations. The results of this chapter indicate that the integrated ILSP-CMA with ESPRIT algorithm produces more accurate estimates of the directions of arrival, especially when multiple signals arrive with small angular separation.

4.2 Resolution and Sensitivity to Calibration of MUSIC type algorithms.

To estimate the direction of arrival by computing the MUSIC spatial spectrum (see equation (3.18) and (3.19)), it is required to find the peaks in the spectrum which correspond to the directions of arrival. When signals arrive at closely spaced angles, the MUSIC spectrum will not show distinct peaks corresponding to each signal. Instead, all these signals would appear as one signal with a broader peak. The ability to resolve closely spaced signals depends on the signal to noise ratio at the input of the array and the total number of samples of data (proportional to collect or observation interval) used to compute the MUSIC spectrum. Each sample of data is a complex baseband representation of a snapshot obtained from all the elements of the array.

Figure 4.1 provides a plot of the resolution as a function of number of samples used in the estimation of DOA and the signal-to-noise ratio. With respect to Figure 4.1, the resolution is defined as the angle $\Delta\theta$ such that two equal powered signals impinging on a six element uniformly spaced linear array at 90° and $90^\circ + \Delta\theta$, respectively, are consistently resolved. The signals are deemed to be resolved when there exists distinct peaks in the MUSIC

spectrum corresponding to each of the two signals. The peaks were detected by checking for change of sign of slope (from positive slope to a negative slope) of the MUSIC spectrum curve. As shown in Figure 4.1, the ability of the MUSIC algorithm to resolve closely spaced signals improves with increasing signal to noise ratio and number of samples of data used to compute the MUSIC spectrum. Figure 4.1 shows the resolution performance for the case of both coherent and noncoherent signals impinging on the array.

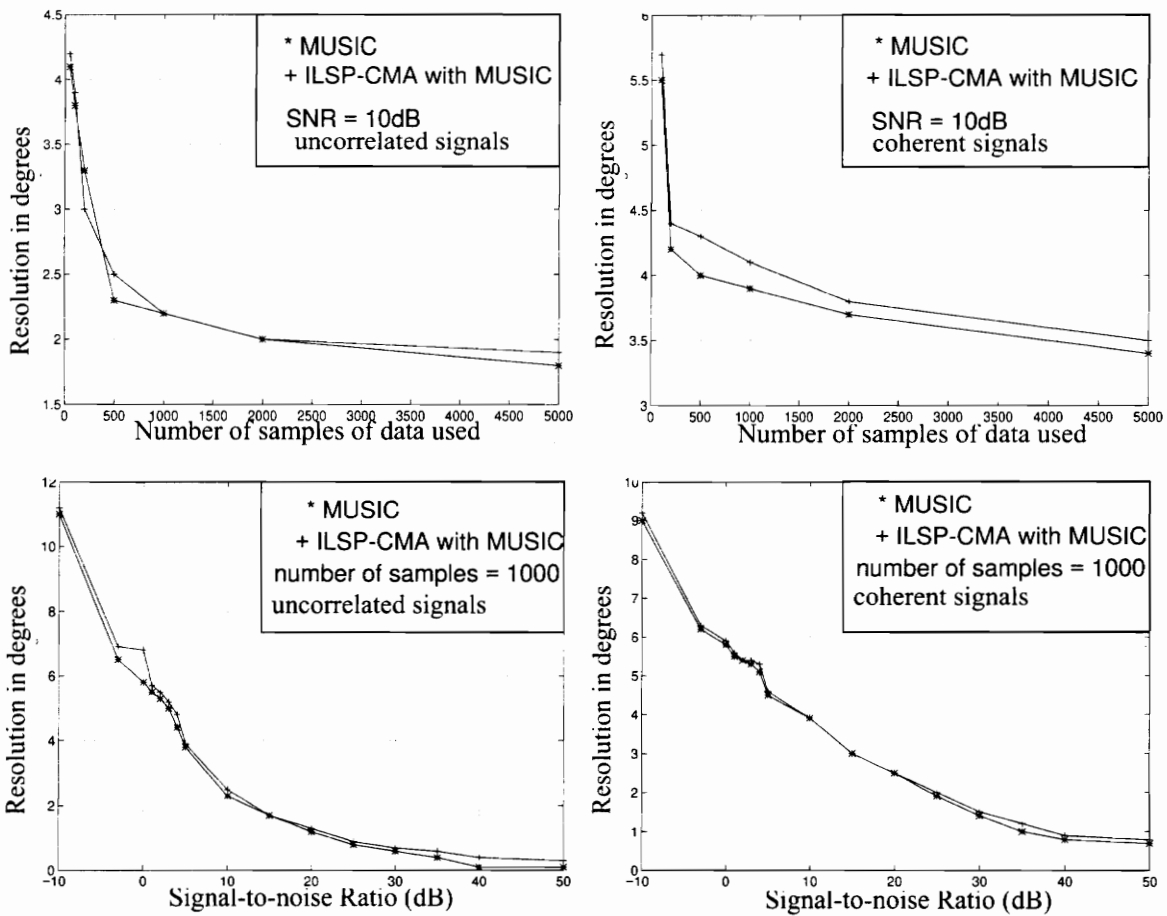


Figure 4.1: Resolution performance of MUSIC and the integrated ILSP-CMA with MUSIC approaches. The resolution is plotted as the angle $\Delta\theta$ such that two equal powered signals impinging on the six element ULA at 90° and $90^\circ + \Delta\theta$ respectively were consistently resolved. Resolution is plotted as function of both SNR and number of samples of data used for DOA estimation, for the case of both coherent and uncorrelated signals. For the coherent cases, forward/conjugate backward averaging was used. (These plots were generated by Program [1])

It should be noted that the resolution shown in Figure 4.1 is measured around an angle-of-arrival of 90 degrees, and that the ability to resolve closely spaced signals varies with the DOA [Sto89][Por88]. Further, the resolution also depends on the number of elements in the array [Sch93]. It is also seen from Figure 4.1 that the resolution of MUSIC is poorer under correlated signal conditions even when spatial smoothing is used [Pil89B]. For the case shown in Figure 4.1, the resolution of the integrated ILSP-CMA with MUSIC (i.e., MUSIC applied to the spatial signature covariance matrix estimated using ILSP-CMA, as discussed in Section 3.7) is almost the same as that of the conventional MUSIC algorithm.

In order to compute the MUSIC spectrum using (3.18) and (3.19), it is required to have the steering vectors, $\mathbf{a}(\theta)$, corresponding to all the angles of arrival. The steering vectors corresponding to different angles of arrival may be computed analytically for a linear array using equation (2.15). However, due to imperfections in the construction of the array, the actual steering vectors will differ from those obtained using (2.15). Therefore, computing the MUSIC spectrum using analytically obtained steering vectors based on the ideal array assumption, will distort the MUSIC spectrum and produce errors in the DOA estimate. One way to overcome this is to actually measure the steering vectors for different angles of arrival and make a calibration table [Sch93]. This requires measuring the array response for different angles of arrival. This may be done by placing a signal source at different known angles in an anechoic chamber to ensure that only a single plane wave at the known incident angle arrives at the array input. Once the steering vectors are measured, the MUSIC spectrum can be computed using the measured steering vectors, instead of relying on the analytically obtained steering vectors. However, errors in calibration measurements will again lead to distortions in the MUSIC spectrum.

Figure 4.2 shows a plot of MUSIC spectrum computed with different array imperfections. Array imperfections were simulated by perturbing the physical location of the six antenna elements of a linear array. That is, instead of placing them all at exactly half wavelength spacing, they were positioned at locations different from their ideal locations by +/- 1, 2,

and 5 percent, and the MUSIC spectrum was computed using the steering vectors corresponding to the ideal, instead of the perturbed, locations. For example, to simulate a 1% error in spacing at a half wavelength of 7.317 cm, the array elements were spaced 7.317 ± 0.07317 cm apart.

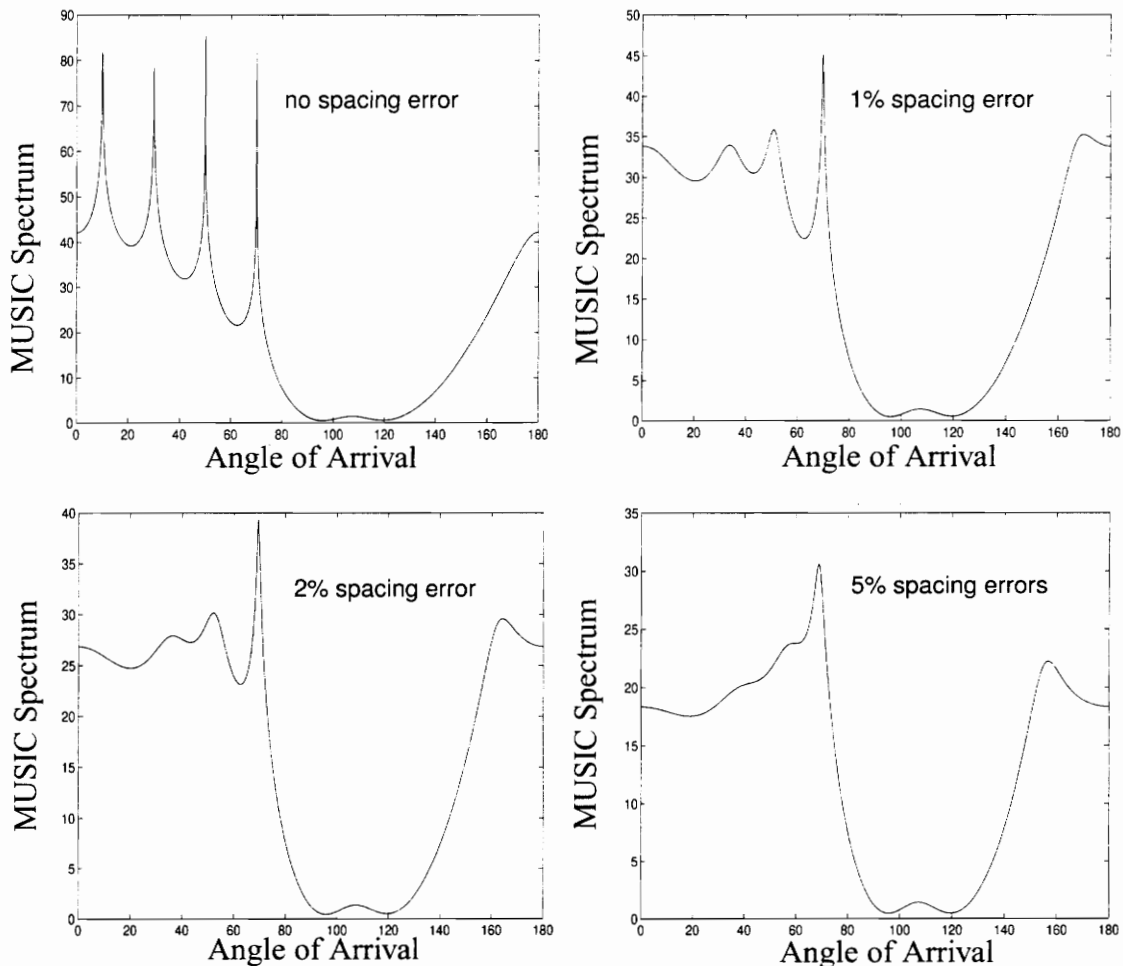


Figure 4.2: Sensitivity of the MUSIC spectrum to spacing errors. Four noncoherent signals arrive at angles 10,30,50,70 degrees, respectively, on a six element uniform linear array with half wavelength interelement spacing. This figure illustrates how the MUSIC spectrum becomes corrupted due to imperfections in constructing the array. The first figure is without any spacing errors, and the subsequent ones are with +/- 1, 2, and 5 percent spacing errors, respectively. (These plots were generated by Program [2])

As clearly seen from Figure 4.2, the MUSIC spectrum is extremely sensitive to errors in element spacings. For the case shown in Figure 4.2, it is seen that even with just one

percent error in spacing, the MUSIC spectrum is considerably distorted. The effect is more significant at angles close to 0 degrees. This implies that to build a DOA measurement system using MUSIC based algorithms, it is required to very accurately calibrate the receiver antenna array and/or build it with very little imperfections.

For an array operating at 2050MHz, a half wavelength spacing is equal to 7.317 cm. At this wavelength, even one millimeter error in interelement spacing corresponds to a 1.36% spacing error which can cause significant distortion in the MUSIC spectrum. As seen in Figure 4.2, the effect of array imperfections is to blunt the peaks in the MUSIC spectrum. Since DOA estimation using MUSIC involves observing the MUSIC spectrum, accurate calibration is a must for MUSIC type algorithms. Array imperfections or calibration errors blunt the peaks of the MUSIC spectrum, since the steering vectors used to compute the spectrum are not fully orthogonal to the noise subspace eigenvectors, as the actual steering vectors would be.

4.3 Performance Comparison of DOA Estimation Algorithms

This section presents simulation results to compare the accuracy of various algorithms in estimating the directions-of-arrival. The DOA estimation algorithms whose performance is evaluated and compared here are the MUSIC algorithm, the ESPRIT algorithm (both the Least Squares and Total Least Squares version), the integrated ILSP-CMA with ML, MUSIC, and ESPRIT algorithms. The root mean square error is used as a metric to compare the performance of these algorithms. The rms error in DOA estimation is computed as the square root of the average squared errors over repeated DOA estimation trials. The rms error (RMSE) in DOA estimation may be defined as

$$RMSE = \sqrt{\frac{1}{K} \sum_{k=1}^K \frac{1}{N} \sum_{n=1}^N (\theta_n - \hat{\theta}_n)^2} \quad (4.1)$$

where,

K = Number of repeated DOA estimation trials over which the error is averaged (unless mentioned otherwise, $K=200$ for all simulations presented here)

N = Number of incident plane waves

θ_n = The actual angle of arrival of the n th plane wave as specified in simulation

$\hat{\theta}_n$ = The angle of arrival of the n th plane wave as estimated by the DOA estimation algorithm

For the simulation results shown in Figures 4.3 to 4.8, two signals at angles 90 and 95 degrees, respectively, are incident on the array. The rms error in DOA estimation is plotted as a function of both signal-to-noise ratio and number of samples of data used to estimate the DOA. Since all simulations are run at a sampling rate of 64000 samples/sec, p samples of data correspond to an observation or collection interval of $p/64000$ seconds. Results are presented for the case of both coherent and noncoherent signals. For coherent signals, forward and conjugate backward averaging was used as a spatial smoothing technique to decorrelate the signals (see Section 3.5.1). For spatial smoothing, the six element array is split into two identical overlapping subarrays of five elements each.

For the four cases of ILSP-CMA with MUSIC, ILSP-CMA with LS-ESPRIT, ILSP-CMA with TLS-ESPRIT and ILSP-CMA with ML, the ILSP-CMA algorithm was used to estimate the spatial signatures corresponding to each source (user). For the case of ILSP-CMA with MUSIC or ESPRIT, a spatial signature covariance matrix was formed using the estimated spatial signatures, and the MUSIC or ESPRIT algorithm was applied on the spatial signature covariance matrix (see Section 3.7). For the case of ILSP-CMA with ML, an exhaustive search through all possible steering vectors (those corresponding to 0 through 180 degrees in steps of 0.1 degrees) were made to find the one closest in 2-norm (squared Euclidean distance) to the estimated spatial signatures (see equation (3.101)). The ILSP-CMA with ML technique is applicable only to the case of uncorrelated signals where the spatial signature of each signal is identical to the steering vector corresponding to its direction of arrival.

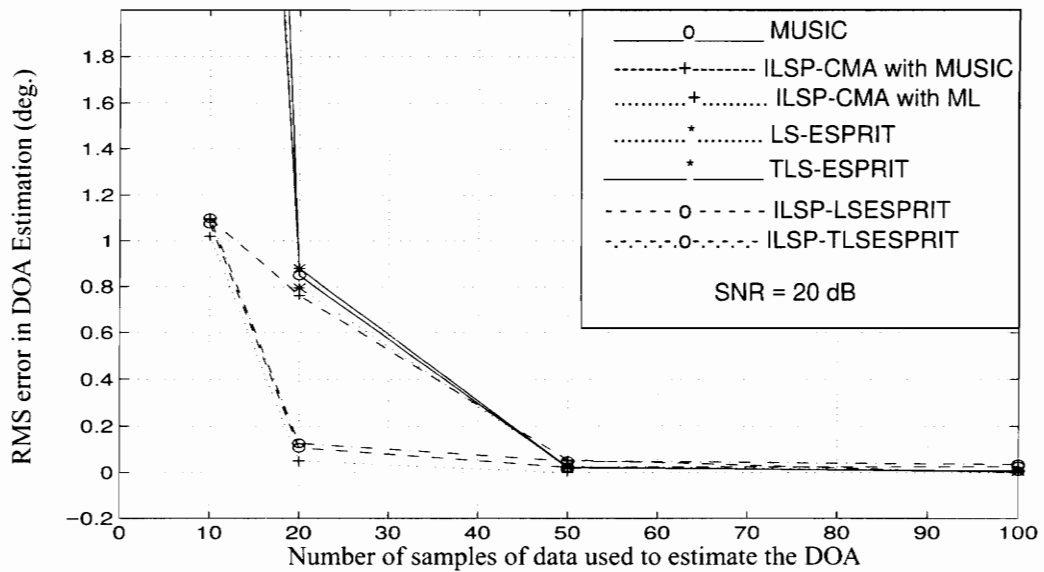


Figure 4.3: Performance of various DOA estimation algorithms. RMS error in DOA estimation is plotted as a function of number of samples of data used to estimate the DOA. In all simulations, two uncorrelated (non-coherent) signals with equal power are incident on a six element uniform linear array at 90 and 95 degrees, respectively, at a 20dB SNR. The RMS error is averaged over 200 repeated DOA estimation trials. (These plots were generated using Programs [3][7][11][15][19][21][25][29])

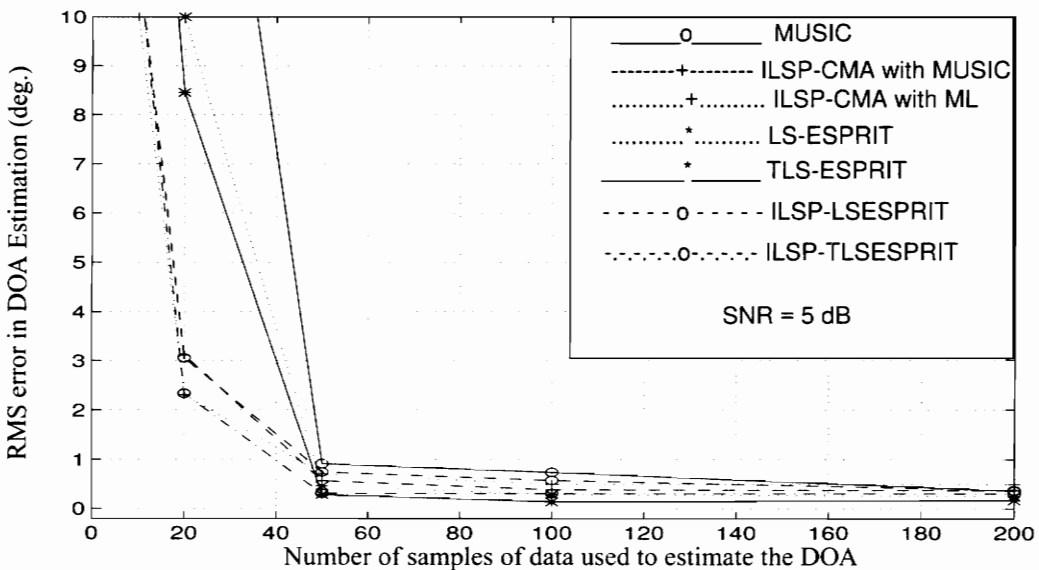


Figure 4.4: RMS Error in DOA Estimation as a function of number of samples. Simulation parameters same as Figure 4.3, except that the SNR here is only 5 dB. (These plots were generated using Programs [3][7][11][15][19][21][25][29])

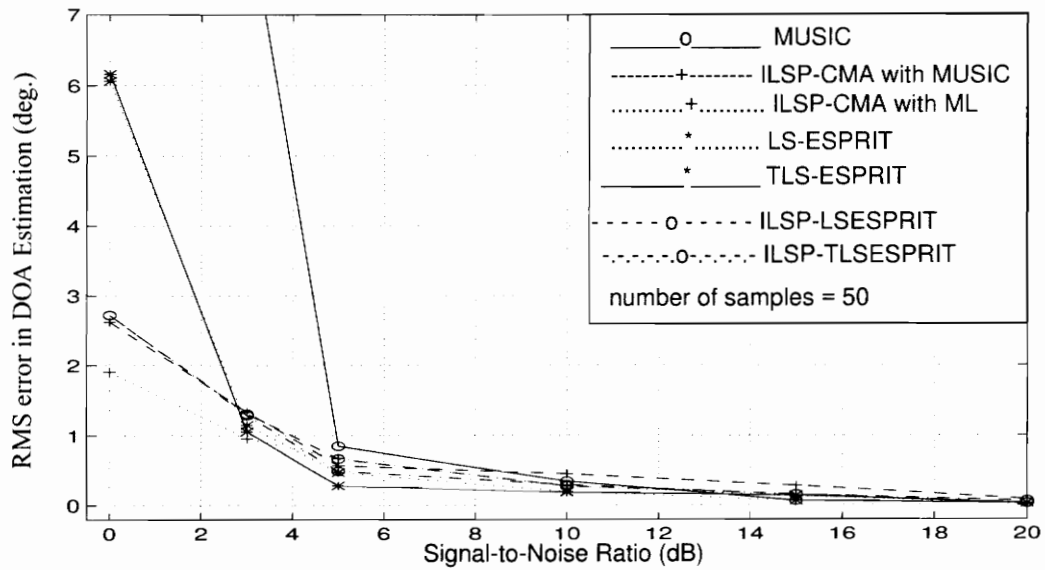


Figure 4.5: Performance of various DOA estimation algorithms. RMS error in DOA estimation is plotted as a function of signal-to-noise ratio. In all simulations, 50 samples of two uncorrelated (non-coherent) signals with equal power incident on a six element uniform linear array at 90 and 95 degrees respectively are used for DOA estimation. The RMS error is averaged over 200 repeated DOA estimation trials. (These plots were generated using Programs [4][8][12][16][20][22][26][30])

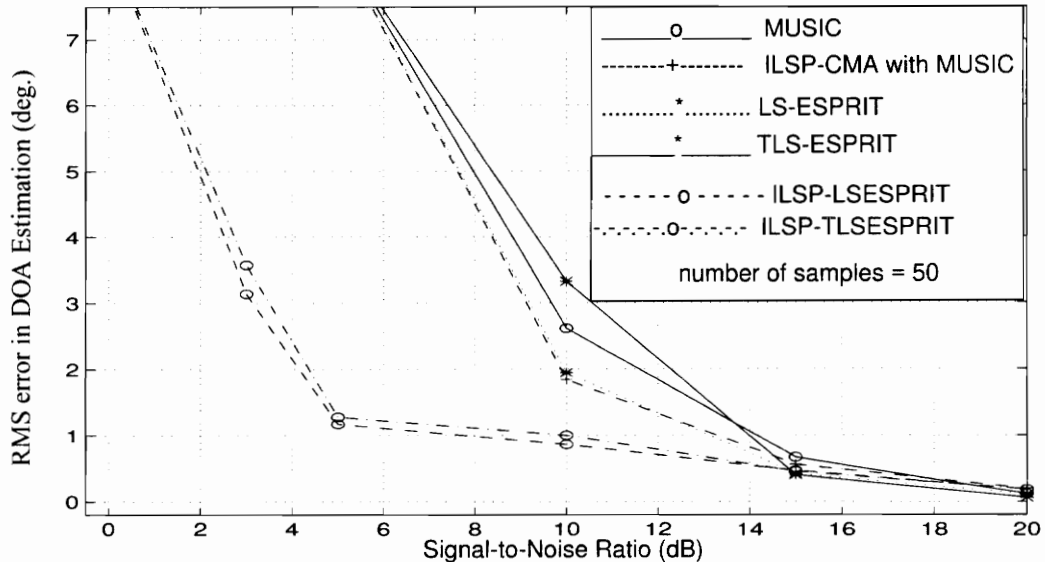


Figure 4.6: Simulation parameters same as in Figure 4.5 with the two sources being coherent. These plots were generated using Programs [6][10][14][18][24][28][30])

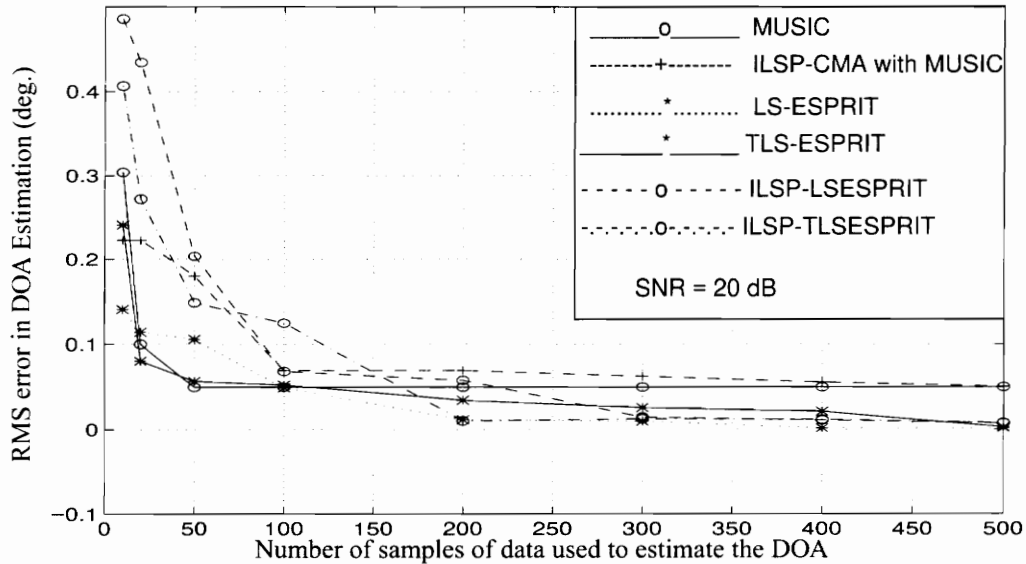


Figure 4.7: Performance of various DOA estimation algorithms. RMS error in DOA estimation is plotted as a function of number of samples of data used to estimate DOA. In all simulations, two coherent signals with equal power are incident on a six element uniform linear array at 90 and 95 degrees respectively, at a 20dB SNR. The RMS error is averaged over 200 repeated DOA estimation trials. All subspace based algorithms are used along with forward/backward averaging. (These plots were generated using Programs [5][9][13][17][23][27][29])

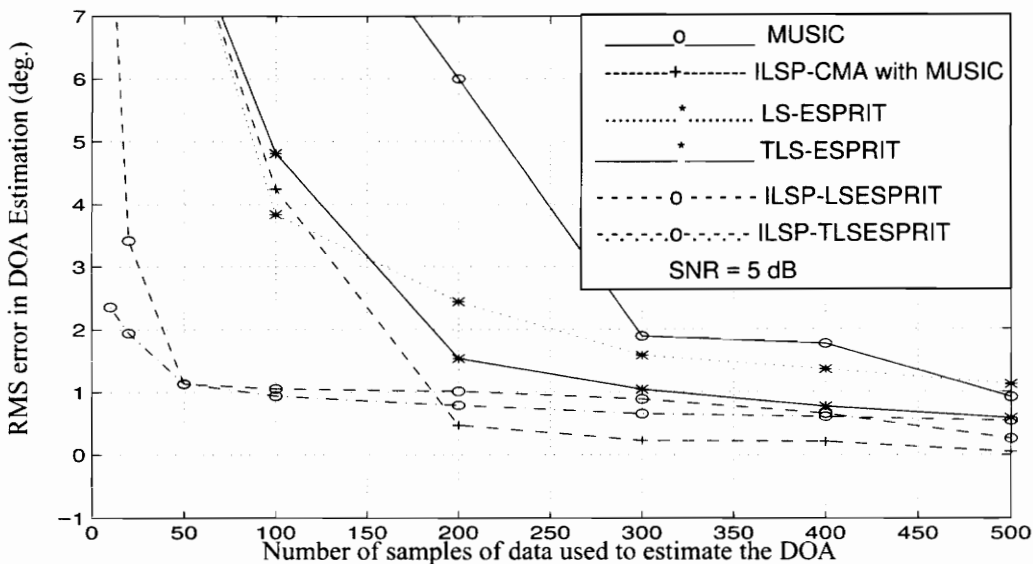


Figure 4.8: RMS Error in DOA Estimation as a function of number of samples. Simulation parameters same as figure 4.7, except that the SNR is 5 dB. (These plots were generated using Programs [5][9][13][17][23][27][29])

As seen from Figures 4.3 to 4.8, all the algorithms perform more or less equally well in high signal-to-noise ratio (20dB or more) and when a large number of data samples (i.e large observation time) is used to compute the DOA estimate. Under low SNR conditions and/or when a smaller number of data samples are used to compute the directions of arrival, it is clearly seen that the integrated approaches perform better than the conventional subspace methods. This is most clearly seen from Figures 4.4, 4.6 and 4.8. In terms of the number of samples required, the improvement in performance of the integrated approach over the conventional subspace methods is larger when the incident signals are uncorrelated. For example, as seen from Figure 4.4, when ILSP-CMA is used along with LS-ESPRIT or TLS-ESPRIT it is possible to resolve uncorrelated signals arriving at 90 and 95 degrees with less than 20 samples, while the LS-ESPRIT and TLS-ESPRIT algorithms by themselves require at least 50 samples. For the case of coherent signals, the improvement in performance of the integrated approach over the conventional subspace techniques is greater at low signal-to-noise ratios. From Figure 4.6, it is seen that with 50 samples of data, the integrated approach can estimate the direction of arrival within an accuracy of about 1 degree at an SNR of 5 dB, while the conventional subspace techniques are able to resolve only when the signal-to-noise ratio is at least 10 dB. It is also seen that between LS-ESPRIT and TLS-ESPRIT, the TLS-ESPRIT performs marginally better than the LS-ESPRIT algorithm, especially at low SNR and/or when a smaller number of data samples are used for the estimation [Ott91]. It is also seen that, though the subspace based techniques are able to resolve coherent multipath through spatial smoothing, the performance of all the algorithms are poorer under coherent signal conditions when compared to their performance under uncorrelated signal conditions.

Since the TLS-ESPRIT algorithm and the integrated ILSP-CMA with TLS-ESPRIT algorithms perform much better than the MUSIC algorithm in terms of DOA estimation error, as well as storage and calibration requirements [Roy89], we shall further study the performance of only these two algorithms.

As stated earlier, for a linear array, the DOA estimation error is also a function of the angle of incidence. Since a linear array is capable of forming sharper beams on broadside than on end-fire, the DOA estimation accuracy is better when the signals arrive from broadside. Figures 4.9 and 4.10 show the rms error in DOA estimation as a function of the angle of arrival for the case of two algorithms: TLS-ESPRIT and the integrated ILSP-CMA with TLS-ESPRIT. As seen clearly from the figures, the error function has a U-shape with the errors peaking at 0 and 180 degrees (end-fire) and having a minima at 90 degrees (broadside). It is also seen that for the case of a single incident signal, the TLS-ESPRIT algorithm produces smaller errors than the integrated ILSP-CMA with TLS-ESPRIT algorithm.

As shown in subsequent plots, the rate at which the error increases as the direction of arrival varies from broad-side to end-fire will also depend on the number of signals, closeness of arrival angles, and relative power levels.

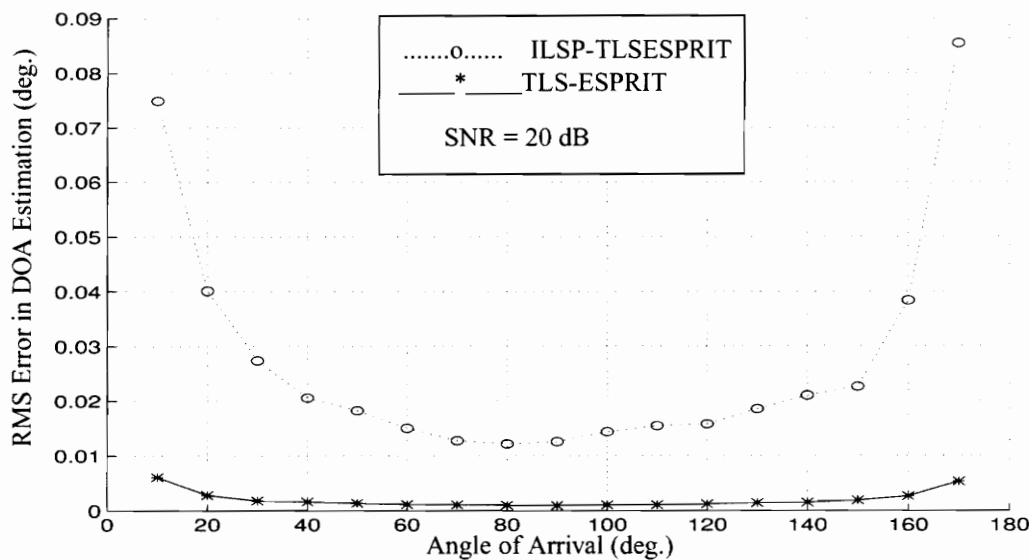


Figure 4.9: RMS Error in DOA estimation as a function of the angle of arrival. A single sinusoidal tone signal is incident on a six element uniformly spaced linear array at 20 dB SNR. 500 samples of data is used for each DOA estimation and the rms error is obtained by averaging over 200 repeated trials. (These plots were generated by Program [31][33][35])

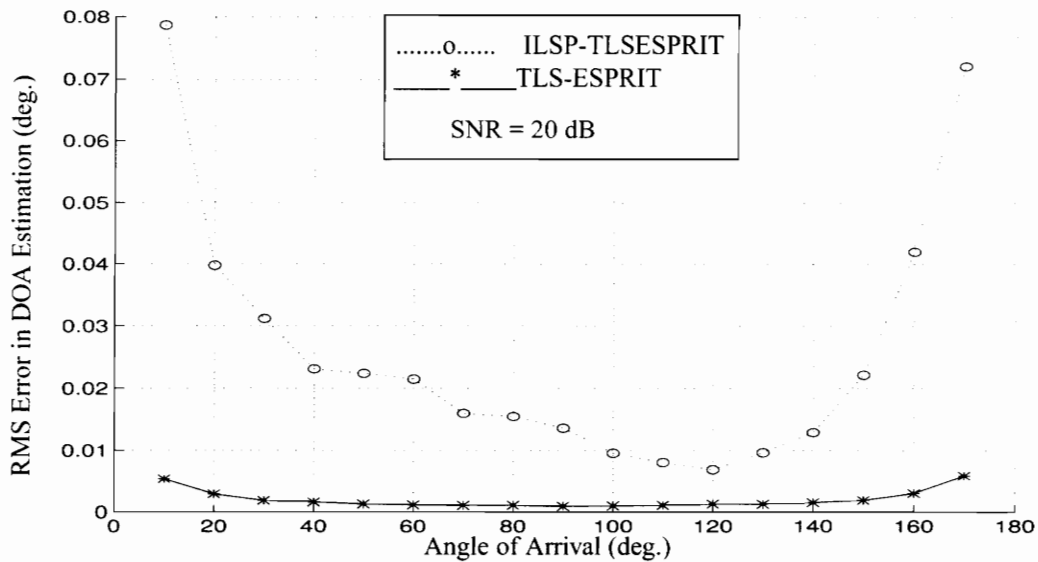


Figure 4.10: RMS Error in DOA estimation as a function of angle of arrival. Simulation parameters same as in Figure 4.9, except that forward/backward averaging (spatial smoothing) is used. (These plots were generated by Programs [32][34][35])

Figures 4.11 to 4.14 show the performance of ESPRIT and ILSP-CMA with ESPRIT algorithms under various angle spread conditions. Multiple uncorrelated signals were simulated with different angular separation and directions of arrival. The first plot in Figure 4.11, shows the performance curve for up to four signals with the signals incident at $10, 10+\Delta\theta, 10+2\Delta\theta$, and $10+3\Delta\theta$ degrees, respectively, where $\Delta\theta$ is the angle of separation in degrees. Subsequent plots in Figures 4.11 and 4.12 show the performance curves for the cases where the first signal arrives at 30, 60, and 90 degrees, respectively. It is clearly seen that there is a rapid degradation in performance as the angle of separation decreases, and this degradation is most pronounced when the incident signals arrive close to end-fire angle (0 degrees). This implies, that it is easier to resolve closely spaced signals coming from the broadside angle than it is for signals coming from the endfire angle.

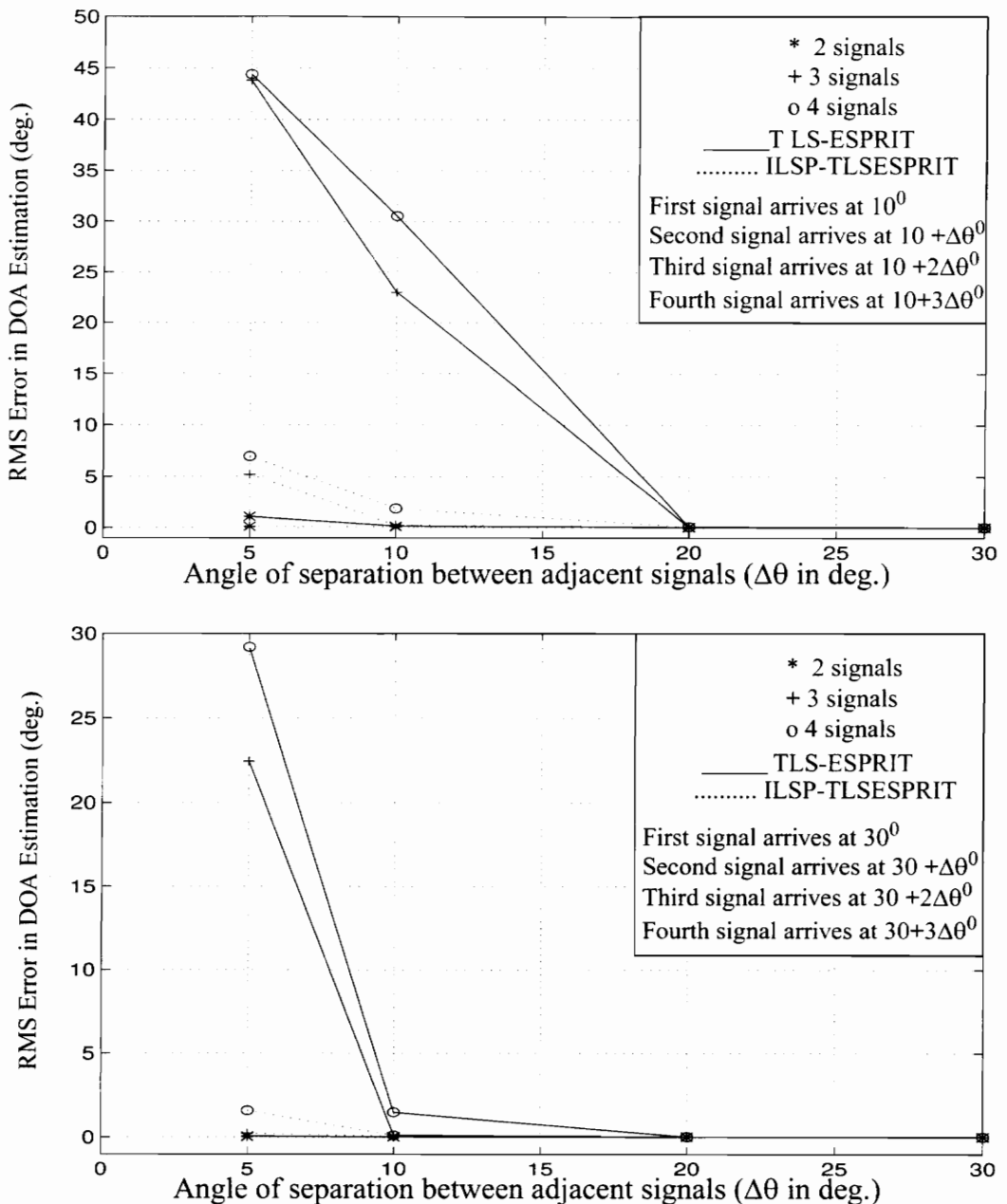


Figure 4.11: RMS error in DOA estimation as a function of angle of separation ($\Delta\theta$) and number of sources for TLS-ESPRIT and the integrated ILSP-CMA with TLS-ESPRIT algorithms. All sources are assumed to be uncorrelated (non-coherent) and at the same power level with an SNR = 20 dB. The estimations are made using 500 samples of data and the rms error is computed by averaging over 200 repeated trials. The top figure shows the case where the incident signals arrive at $10, 10 + \Delta\theta, 10 + 2\Delta\theta, \text{ and } 10 + 3\Delta\theta$ degrees, and the bottom figure shows the case where the incident signals arrive at $30, 30 + \Delta\theta, 30 + 2\Delta\theta \text{ and } 30 + 3\Delta\theta$ degrees. (These plots were generated using Programs [31][33][40])

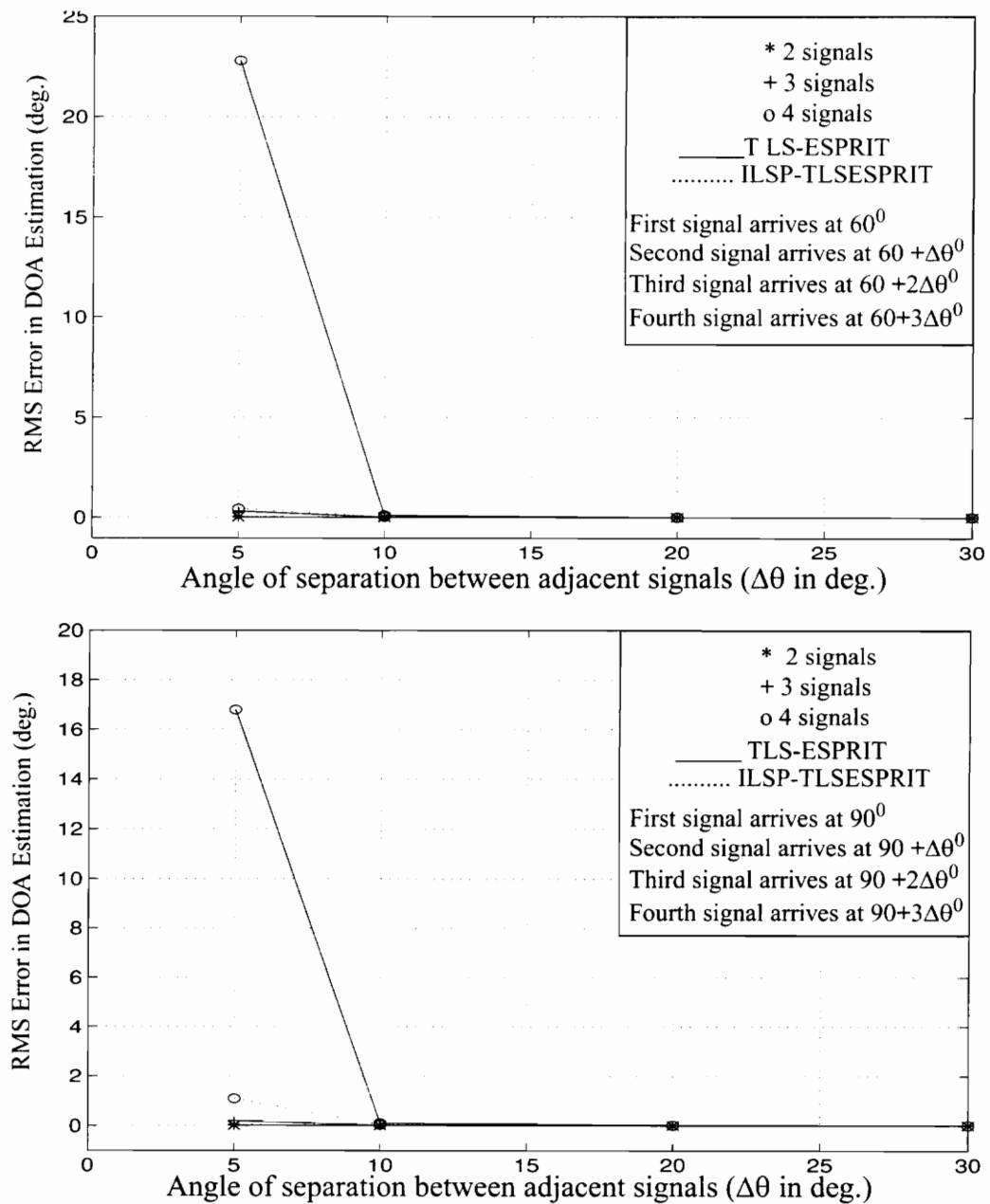


Figure 4.12: RMS error in DOA estimation as a function of the angle of separation between adjacent signals. The top figure shows the case where the incident signals arrive at $60^\circ, 60 + \Delta\theta^\circ, 60 + 2\Delta\theta^\circ$, and $60 + 3\Delta\theta^\circ$ degrees, and the bottom figure shows the case where the incident signals arrive at $90^\circ, 90 + \Delta\theta^\circ, 90 + 2\Delta\theta^\circ$ and $90 + 3\Delta\theta^\circ$ degrees. (These plots were generated using Programs [31][33][40])

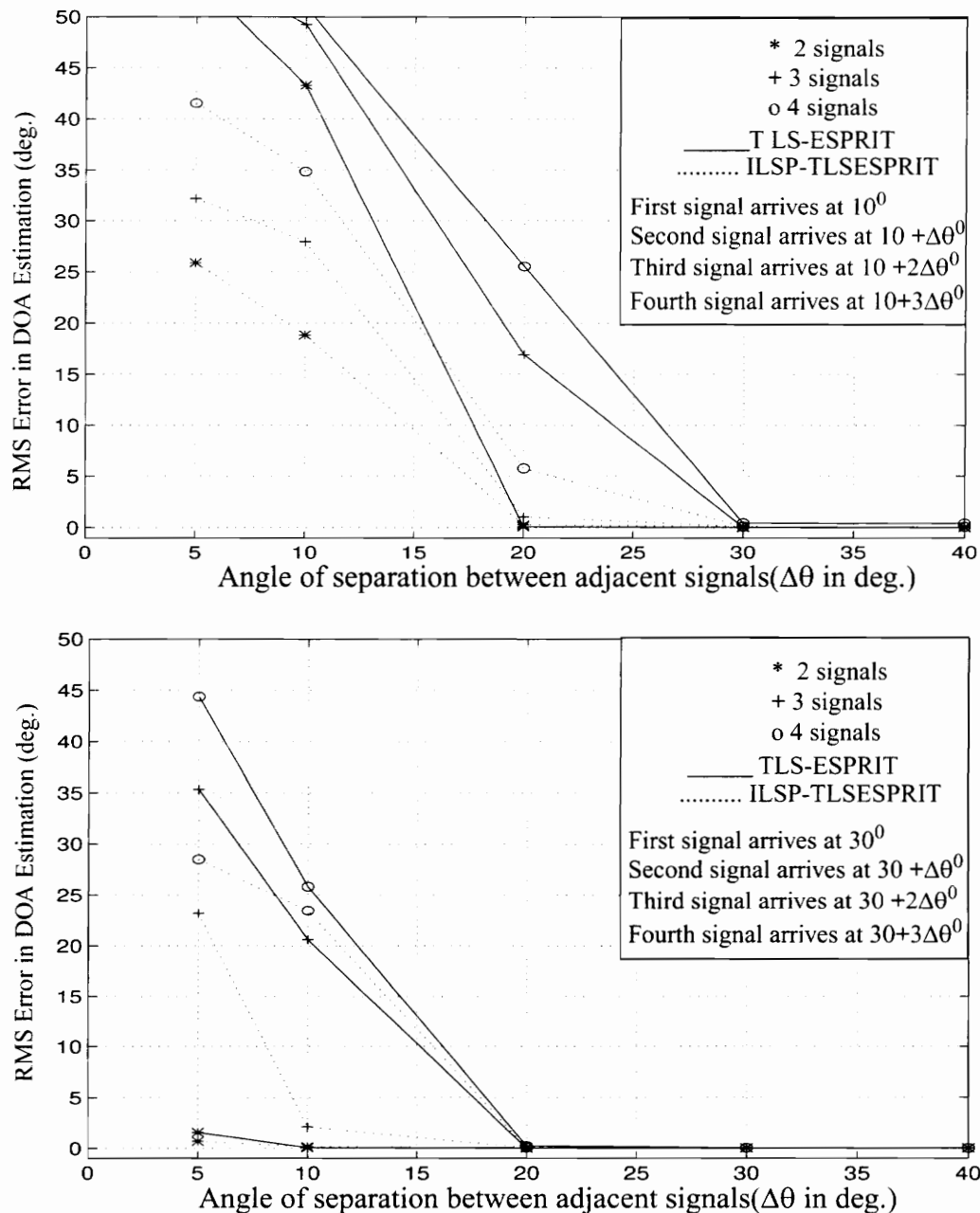


Figure 4.13: RMS error in DOA estimation as a function of the angle of separation between adjacent signals and the number of signals. Simulation parameters are the same as used in Figure 4.11, except that the signals are perfectly correlated as would be the case in a coherent multipath environment. Forward/backward averaging is used to decorrelate the coherent signals. (These plots were generated using Programs [37][39][40])

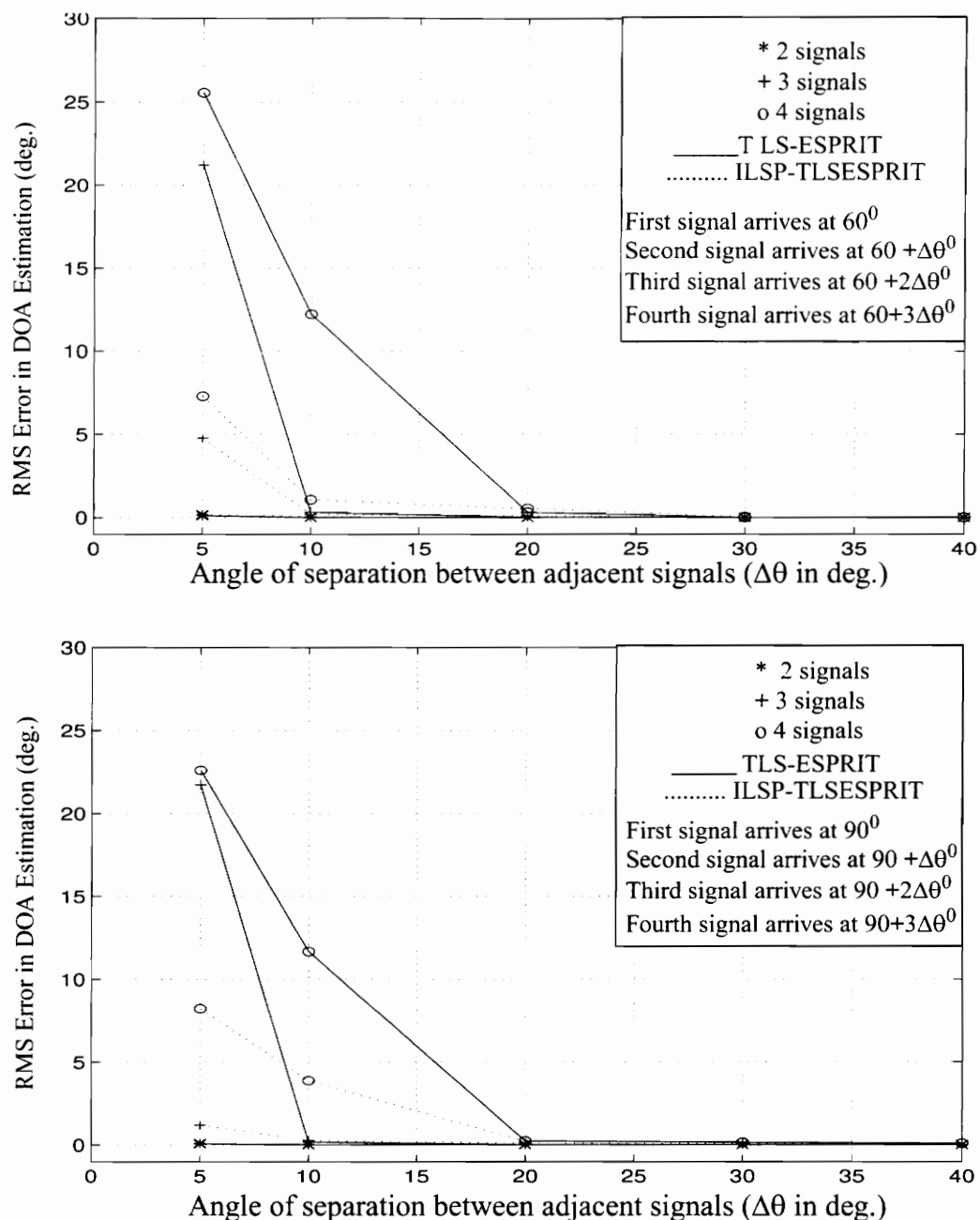


Figure 4.14: RMS error in DOA estimation as a function of angle of separation between adjacent signals and the number of signals. Simulation parameters are the same as used in Figure 4.12, except that the signals are perfectly correlated as would be the case in a coherent multipath environment. Forward/backward averaging is used to decorrelate the coherent signals. (These plots were generated using Programs [37][39][40])

It is seen that the integrated ILSP-CMA with ESPRIT algorithm performs better than the conventional ESPRIT algorithm, and the improvement in performance is most significant when there are multiple uncorrelated signals. The performance improvement over the conventional ESPRIT algorithm increases with increasing number of signals, and decreasing angular separation. Also the improvement is more pronounced at angles closer to end-fire. Using the constant modulus property, the ILSP-CMA algorithm is able to separate multiple users and hence achieves an improvement in performance. Even under coherent signal conditions, the integrated approach outperforms the conventional ESPRIT algorithm when there are a large number of signals arriving at closely spaced angles. Again the improvement in performance of the integrated approach over the conventional subspace approach is more pronounced when there are larger number of signals, and when the signals arrive at an angle of incidence close to end-fire.

It should be noted that at large angular separation, when the number of incident signals are small (two), and the angle of arrival is closer to broadside, the rms error in DOA estimation is very small. Under these conditions, the conventional ESPRIT produces smaller errors than the integrated approach.

Figures 4.15 and 4.16 show the rms error in DOA estimation as a function of the relative power levels of the incident signals for both the TLS-ESPRIT and the integrated ILSP-CMA with TLS-ESPRIT algorithms. They demonstrate how accurately these algorithms can estimate the DOA of weak signals in the presence of a stronger signal. Simulations were performed with the strongest signal arriving at 90 degrees with a power level that is 25 dB above the noise floor, and the power level of the weaker signals were varied from 22 dB to 5 dB above the noise floor. That is, the power difference between the stronger and weaker signals were varied from 3 to 20 dB. The angular separation between adjacent signals were kept at 10 degrees. All of the weaker signals are assumed to be at the same power level and the number of signals are varied from 2 to 4. Figure 4.15 shows the results for the case of uncorrelated (non-coherent) signals and Figure 4.16 shows the results for

the case of correlated (coherent) signals. As seen from Figure 4.15 and 4.16, as the power level of the weaker signals decreases, the rms error in DOA estimation increases. The integrated ILSP-CMA with ESPRIT approach performs better as the number of signals increases, and when the power difference between the signals are large. For the case of less than or equal to three signals, the integrated approach gives larger errors than the conventional ESPRIT algorithm.

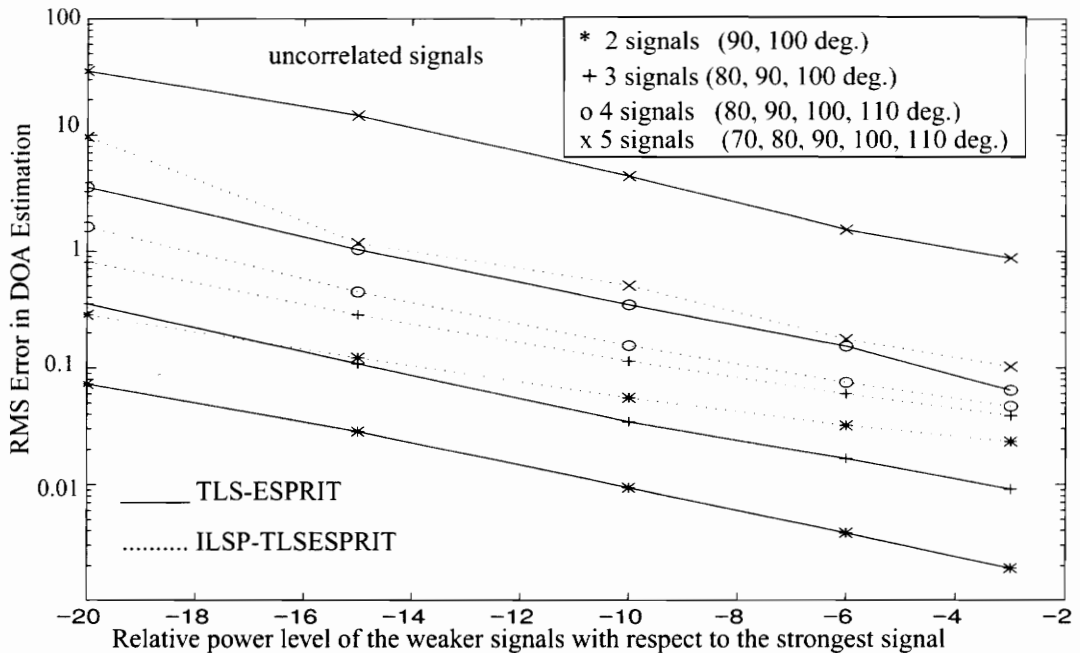


Figure 4.15: RMS error in DOA estimation as a function of the difference in power between the uncorrelated (non-coherent) signals. All the sources except the first one is assumed to be at the same power level. The estimations are made using 500 samples of data and the rms error is computed by averaging over 200 repeated computations. (These plots were generated by Programs [41][43][45])

Figures 4.17 and 4.18 demonstrate the sensitivity of TLS-ESPRIT and the integrated ILSP-CMA with TLS-ESPRIT algorithms to array imperfections. Imperfections were simulated by perturbing the location of the sensor elements from their ideal location by one percent and five percent. Perturbations in antenna element location produce more pronounced errors at the end-fire angles and are less significant at broad-side angles. Both

the integrated and conventional TLS-ESPRIT algorithms are sensitive to array imperfections.

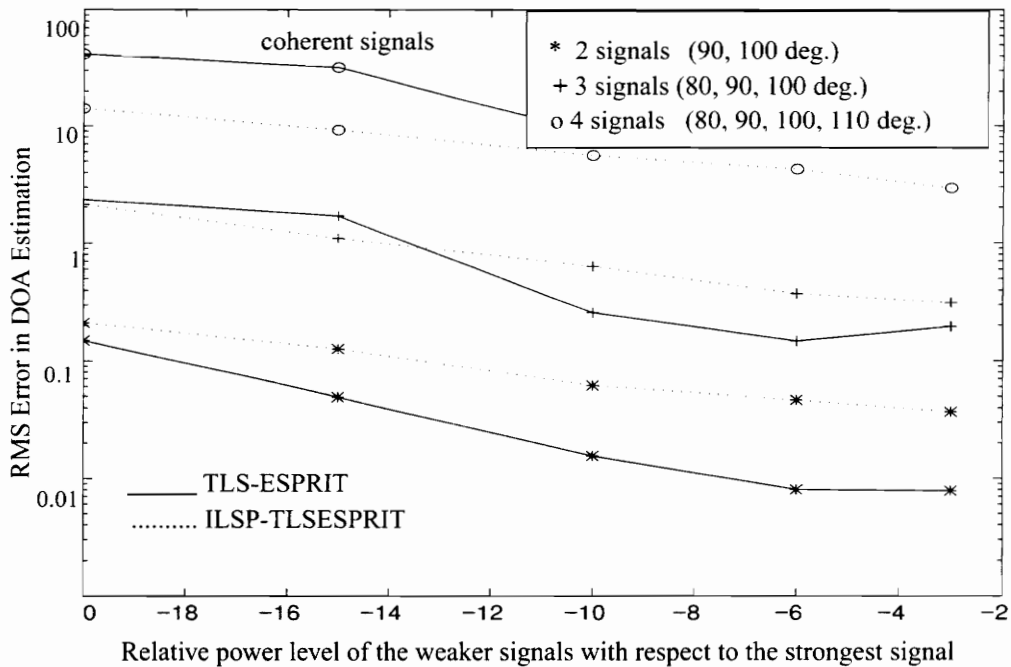


Figure 4.16: RMS error in DOA estimation as a function of the difference in power between the incident coherent signals. All the sources except the first one is assumed to be at the same power level. (These plots were generated by Programs [42][44][45])

Figure 4.17 shows the effect of spacing imperfections for the case of non-coherent incident signals, and Figure 4.18 shows the same for the case of coherent signals. Spacing errors were simulated as discussed in Section 4.2. The simulation set up used to obtain the plots in Figures 4.17 and 4.18 is as follows: Multiple equal power signals are simulated as incident on the array with an SNR of 20 dB. Five hundred (500) samples of data are used to compute the directions-of-arrival. Each signal is separated from its closest neighbor by 20 degrees and the signals arrived at different angles centered around the angle marked on the abscissa. For example, for the case of four signals arriving around 60 degrees, the actual angles of arrival are 30, 50, 70, and 90 degrees, respectively.

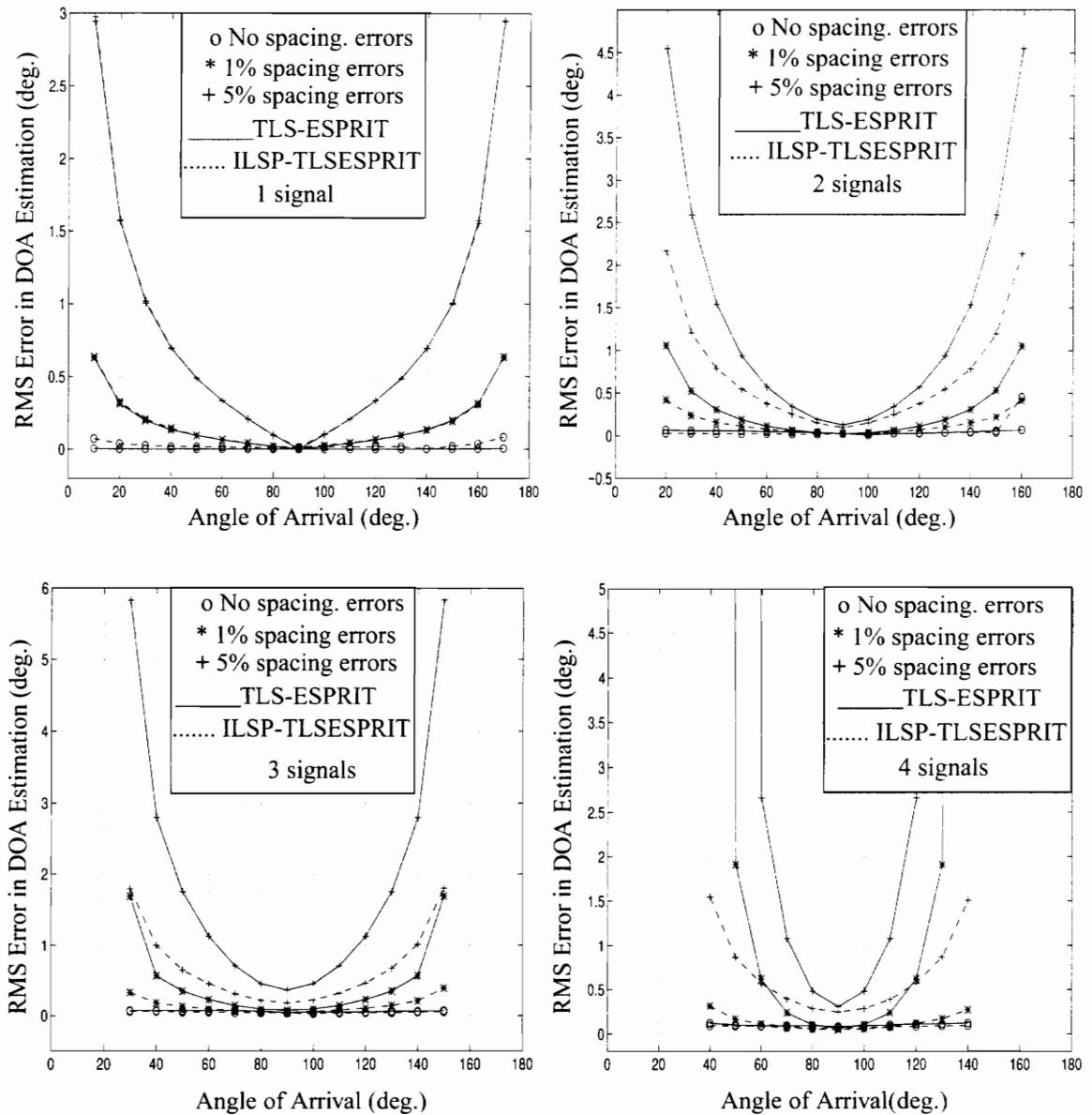


Figure 4.17: RMS error in DOA estimation as a function of angle of arrival for different spacing errors. Spacing errors were simulated by perturbing the location of the sensors. All the sources incident on the array are uncorrelated with one another. The estimations were made using 500 samples of data and the rms error was computed by averaging over 200 repeated trials. (These plots were generated using Programs [46][48][50])

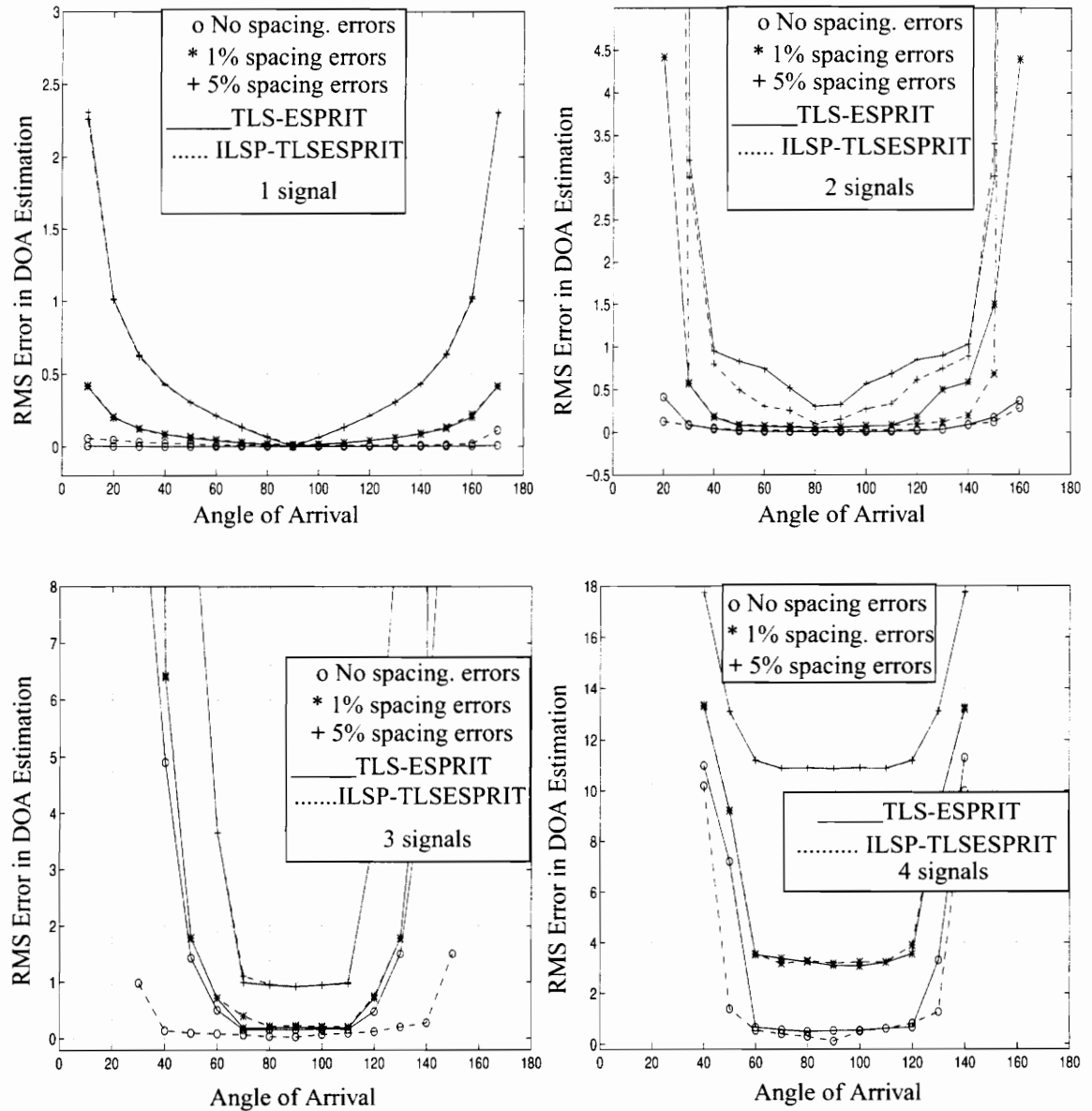


Figure 4.18: RMS error in DOA estimation as a function of the angle of arrival for different spacing errors for the case of coherent (perfectly correlated) signals incident on the array. Spatial smoothing through forward/backward averaging is used to decorrelate the signals. The estimations are made using 500 samples of data and the rms error is computed by averaging over 200 repeated computations. (These plots were generated using Programs [47][49][50])

As seen clearly from Figures 4.17 and 4.18, the DOA estimation error increases rapidly with increasing imperfections. Perturbations in sensor element location cause greater errors on end-fire estimates than on the broadside estimates. Also the errors increase rapidly with increasing number of incident signals. While for estimating the DOA of a single signal, perturbations in the sensor element location do not produce much error, the error grows very rapidly as the number of signals increase. For the case of uncorrelated signals, the integrated approach is more robust to array imperfections than the conventional TLS-ESPRIT algorithm. For the coherent signal case, both the algorithms are equally sensitive. Also, array imperfections cause larger errors in DOA estimation of coherent signals than for non-coherent signals. Though the integrated approach is more robust to array imperfections than the conventional TLS-ESPRIT, to minimize the error in DOA estimation, for both the algorithms, it is required that the array imperfections be kept at a minimum.

4.4 Performance of Source Order Estimation Algorithms

The source order estimation (detection of number of sources) techniques compared here are all based on analyzing the spread of the eigen values of the autocorrelation matrix. The techniques compared are the Maximum Descriptive Length Criterion (MDL), Akaike Information Theoretic Criterion (AIC) [Wax85], and both MDL and AIC modified by incorporating the Gershgorin radii information, i.e, the GMDL and GAIC criteria respectively (see Section 2.7) [Wu95]. Each of these techniques were tested with different number of signals and their detection error probabilities are plotted as function of number of samples and signal-to-noise ratio respectively in Figures 4.19 and 4.20. The detection error probability was computed as the relative frequency of error over 200 Monte Carlo trials. The accuracy of the order estimation algorithms improves with increasing signal-to-noise ratio and number of data samples used.

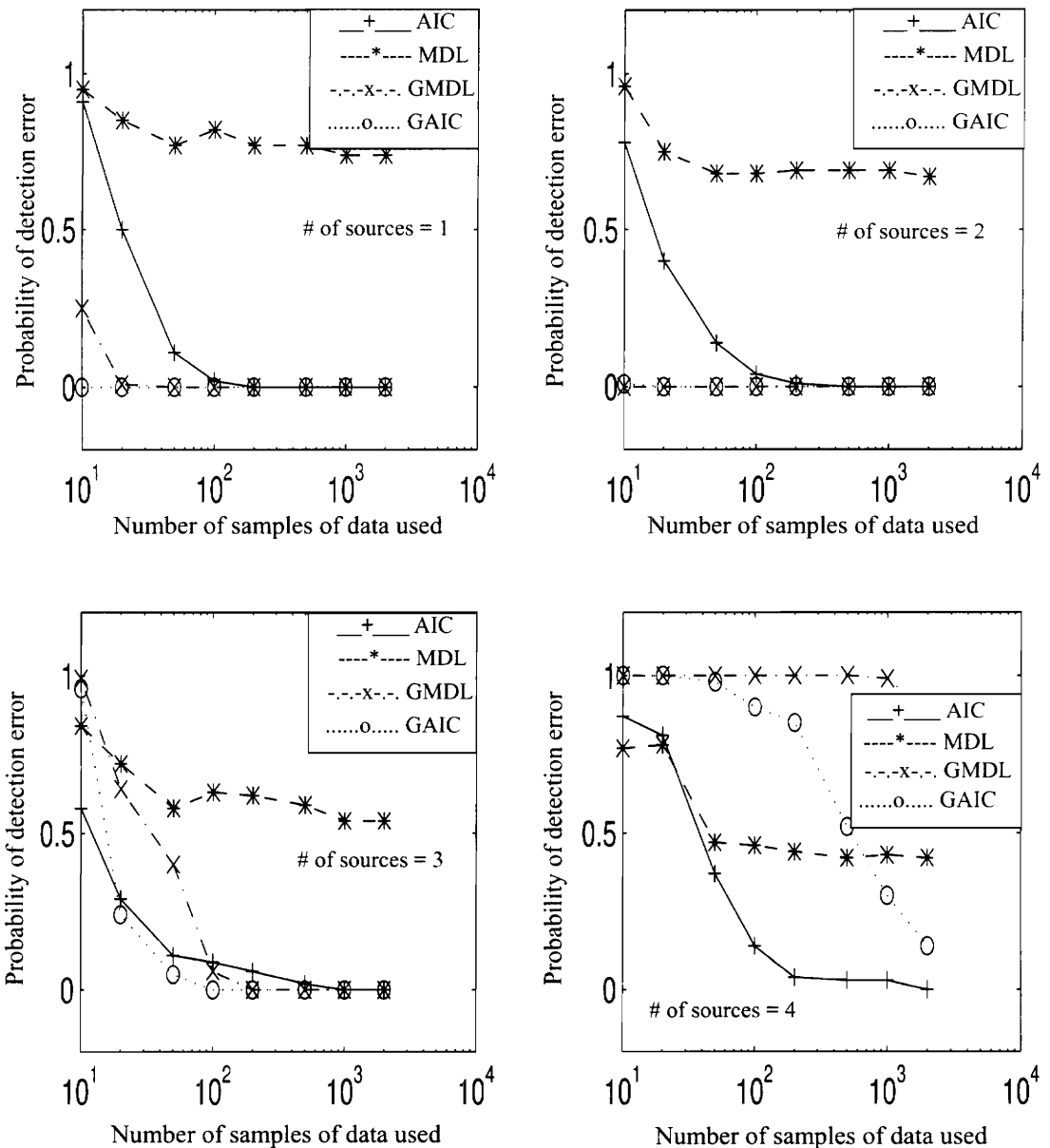


Figure 4.19: Comparison of MDL,AIC, GMDL, GAIC detection for a six element uniform linear array with equal powered uncorrelated sources incident 10 degrees apart from each other with the first source at 90 degrees, second source at 100 degrees, and so on. The probability of detection error computed as a relative frequency over 200 trials is plotted as a function of the number of samples used in the detection scheme. The signal-to-noise ratio was 10 dB. (These plots were generated by Programs [51][52][53][54][63])

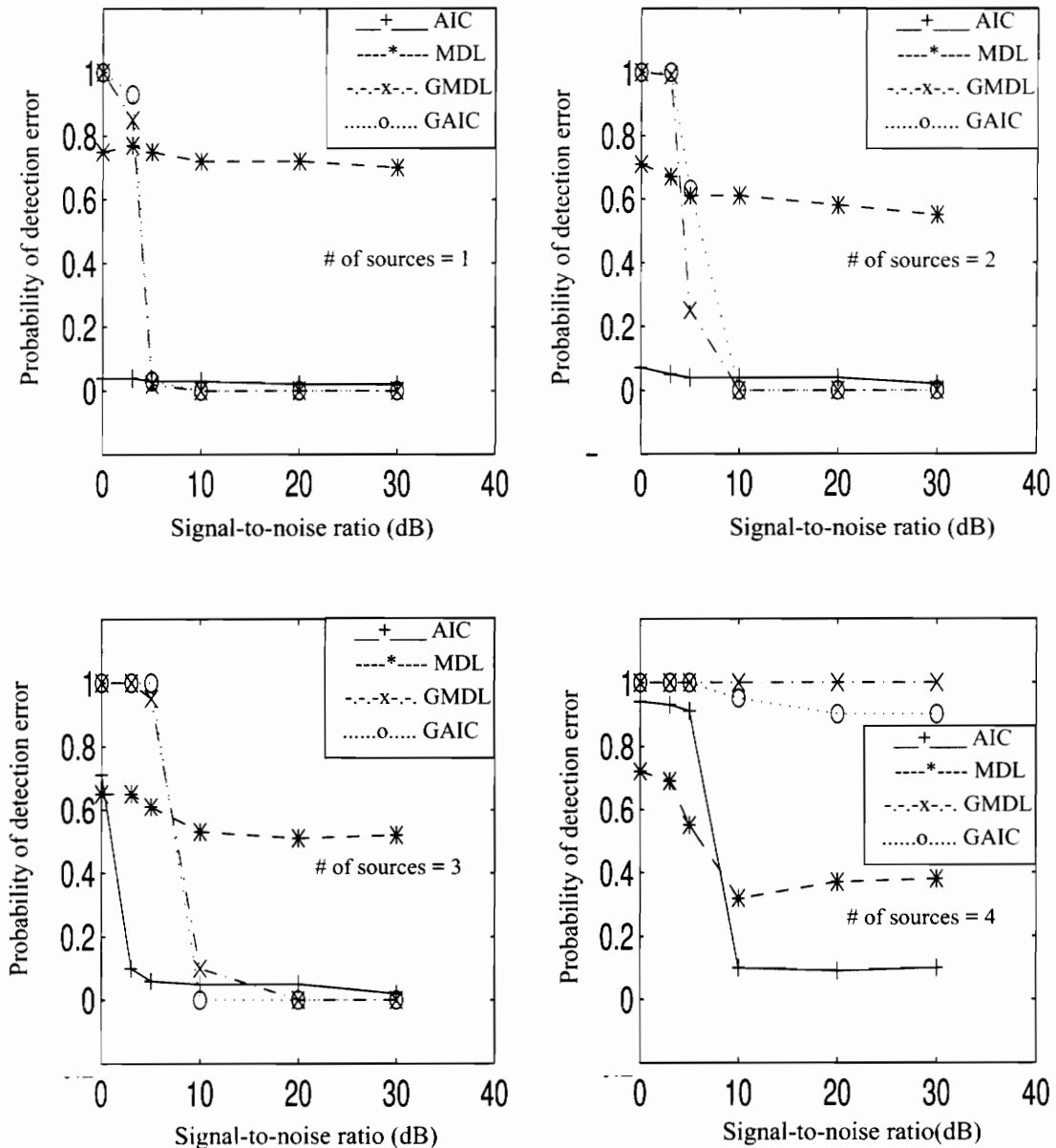


Figure 4.20: Comparison of MDL,AIC, GMDL, GAIC detection for a six element uniform linear array with uncorrelated sources incident 10 degrees apart from each other with the first source at 90 degrees, second source at 100 degrees, and so on. The probability of detection error computed as a relative frequency over 200 trials is plotted as a function of the signal-to-noise ratio. 100 samples of the input data was used to estimate the DOA. (These plots were generated using Programs [55][56][57][58][64])

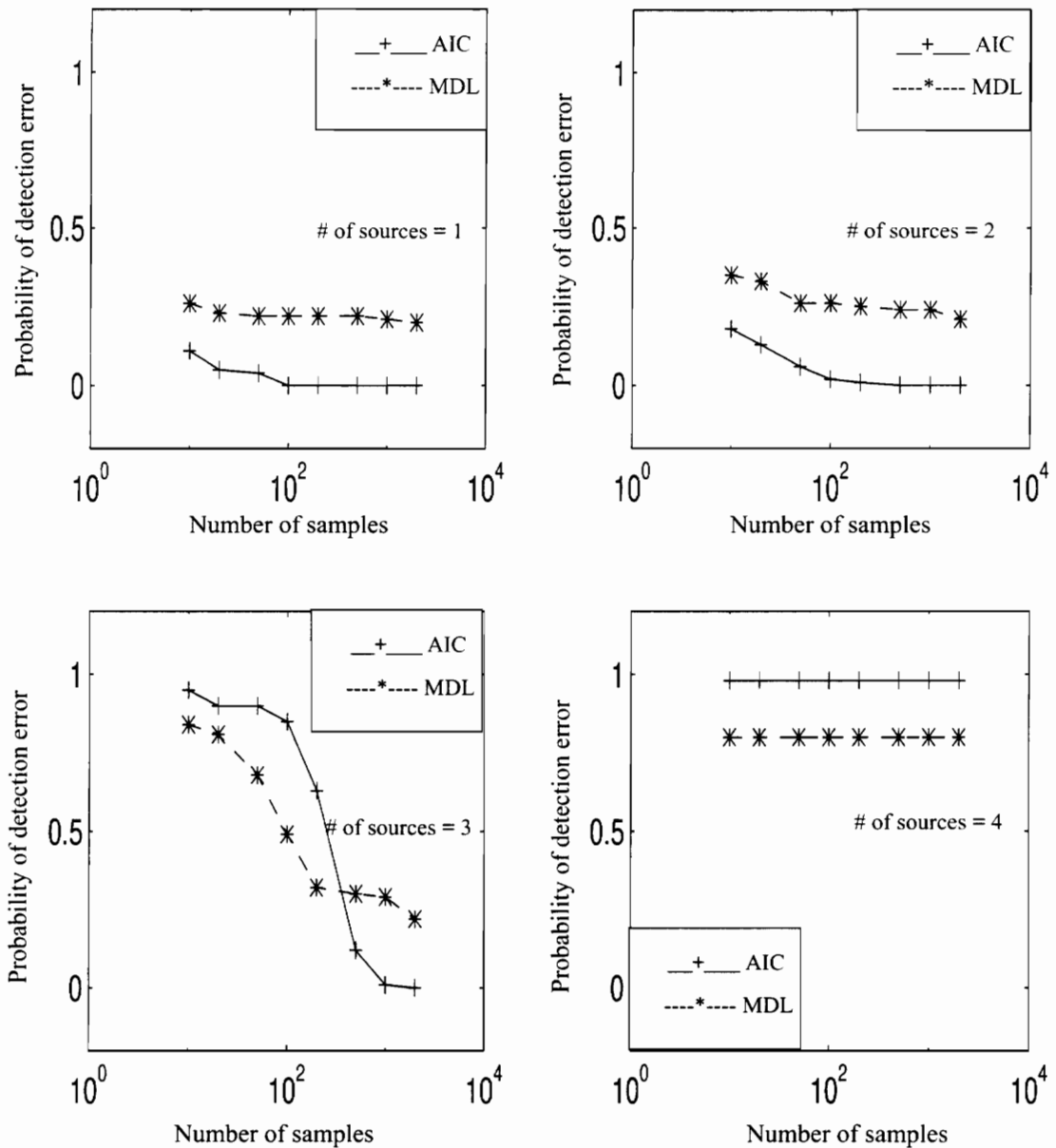


Figure 4.21: Comparison of the modified MDL,AIC detection for a six element uniform linear array with coherent sources of equal power incident 10 degrees apart from each other with the first source at 90 degrees, second source at 100 degrees, and so on. The probability of detection error computed as a relative frequency over 200 trials is plotted as a function of number of samples of data used. The input signal-to-noise ratio was 10 dB. (These plots were generated using Programs [59][60][63])

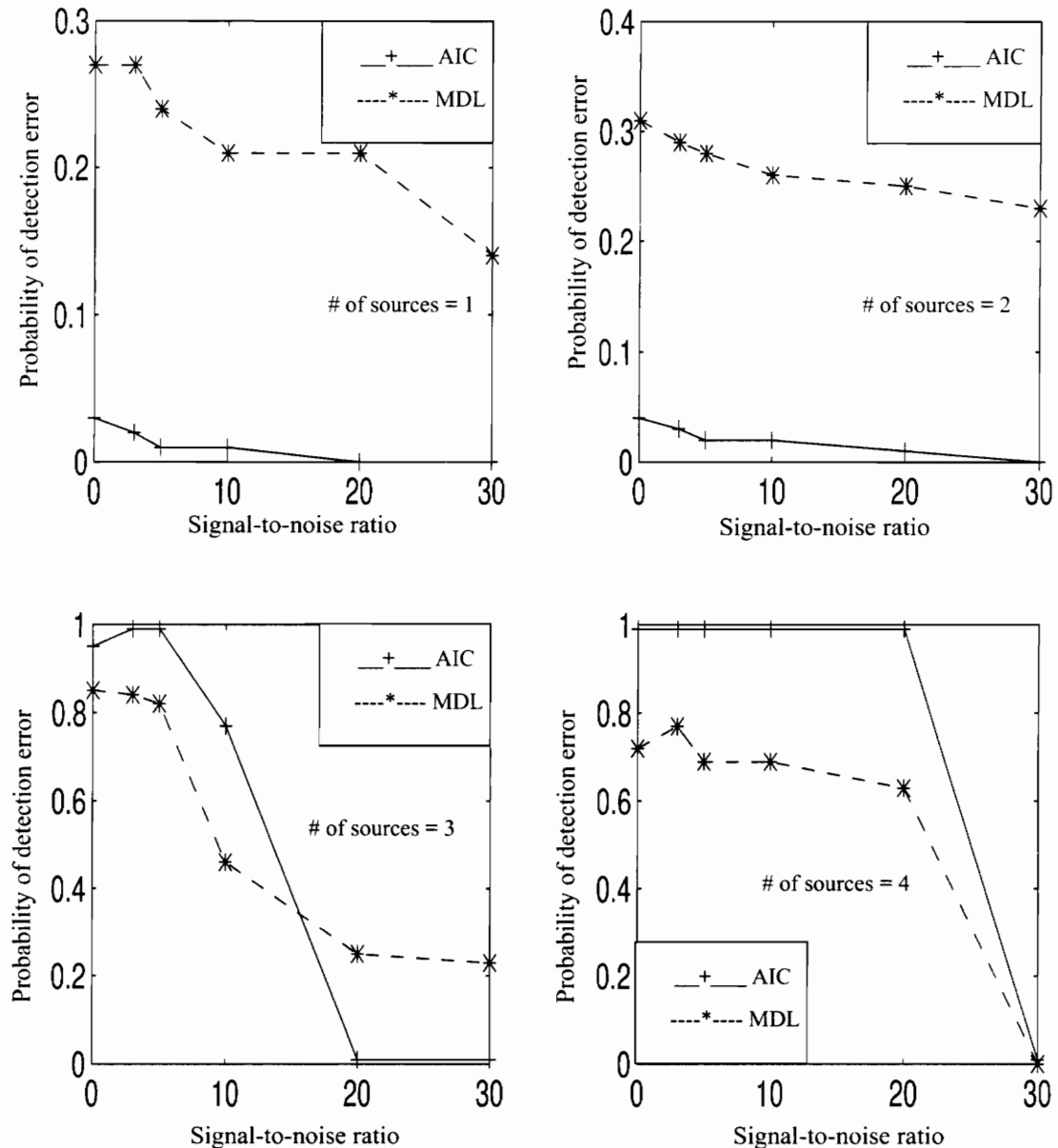


Figure 4.22: Comparison of MDL,AIC detection for a six element uniform linear array with coherent sources incident 10 degrees apart from each other with the first source at 90 degrees, second source at 100 degrees, and so on. The probability of detection error computed as a relative frequency over 200 trials is plotted as a function of the signal-to-noise ratio. (These plots were generated using Programs [61][62][64])

Figures 4.19 to 4.22 show the performance of the order estimation algorithms under the following sample test conditions: All signals incident on the array were at an equal power with the first signal arriving at 90 degrees, the second signal at 100 degrees, the third signal at 110 degrees and the fourth signal at 120 degrees. For the case of the six element linear array for which the performance was evaluated, it is found that the GMDL and GAIC criterion provided more consistent and accurate detection when the number of sources were less than or equal to 3. As can be seen from Figure 4.19 and 4.20, when the number of sources is greater than three, the AIC criterion performs better. Figure 4.19 and 4.20 also shows that the MDL criterion provides highly inconsistent and inaccurate estimates.

For the case of coherent sources the performance of the modified AIC and MDL criterion (see Table 2.1) was compared. Figures 4.21 and 4.22 show that the AIC technique performs better than the MDL technique even under coherent source conditions.

4.5 Conclusion

This chapter presented the results of simulations that compared the performance of various direction-of-arrival and source order estimation algorithms. The simulation results demonstrate that the integrated approach which combines ILSP-CMA with TLS-ESPRIT outperforms the conventional subspace based techniques in most situations. The performance improvement is more significant when multiple signals are incident at closely spaced angles, low signal-to-noise ratio, and when a small number of data samples are used (i.e small collect interval) to estimate the direction of arrival. It is also found that the integrated approach is more robust to imperfections in building the array.

Chapter 5

Description of the DOA Measurement System

5.1 Introduction

In the previous chapters, we presented the background theory and simulation results comparing the performance of different algorithms. In this chapter, we provide a detailed description of the DOA measurement system developed to test the performance of different algorithms. Both the hardware and software developed for performing direction of arrival measurements are detailed in this chapter. The hardware consists of a six element antenna array, three Ariel DSP-96 boards, and an IBM compatible PC which is used to interface with the DSP-96 and store the sampled data collected from the six channels. The system is a narrowband array operating at 2050 MHz.

A block diagram and a photograph of the DOA measurement system is shown in Figure 5.1 and 5.2 respectively. The DOA measurement system may be divided into three sections. The first section described in Section 5.2 consists of the antenna array and the RF front end. The second section does the sampling and data collection, and is described in Section 5.3. The third section does the off-line processing of the collected data. All the DOA estimation algorithms are coded in MATLAB and runs on the host PC attached to the system. All MATLAB codes are also available on the Sun Workstations.

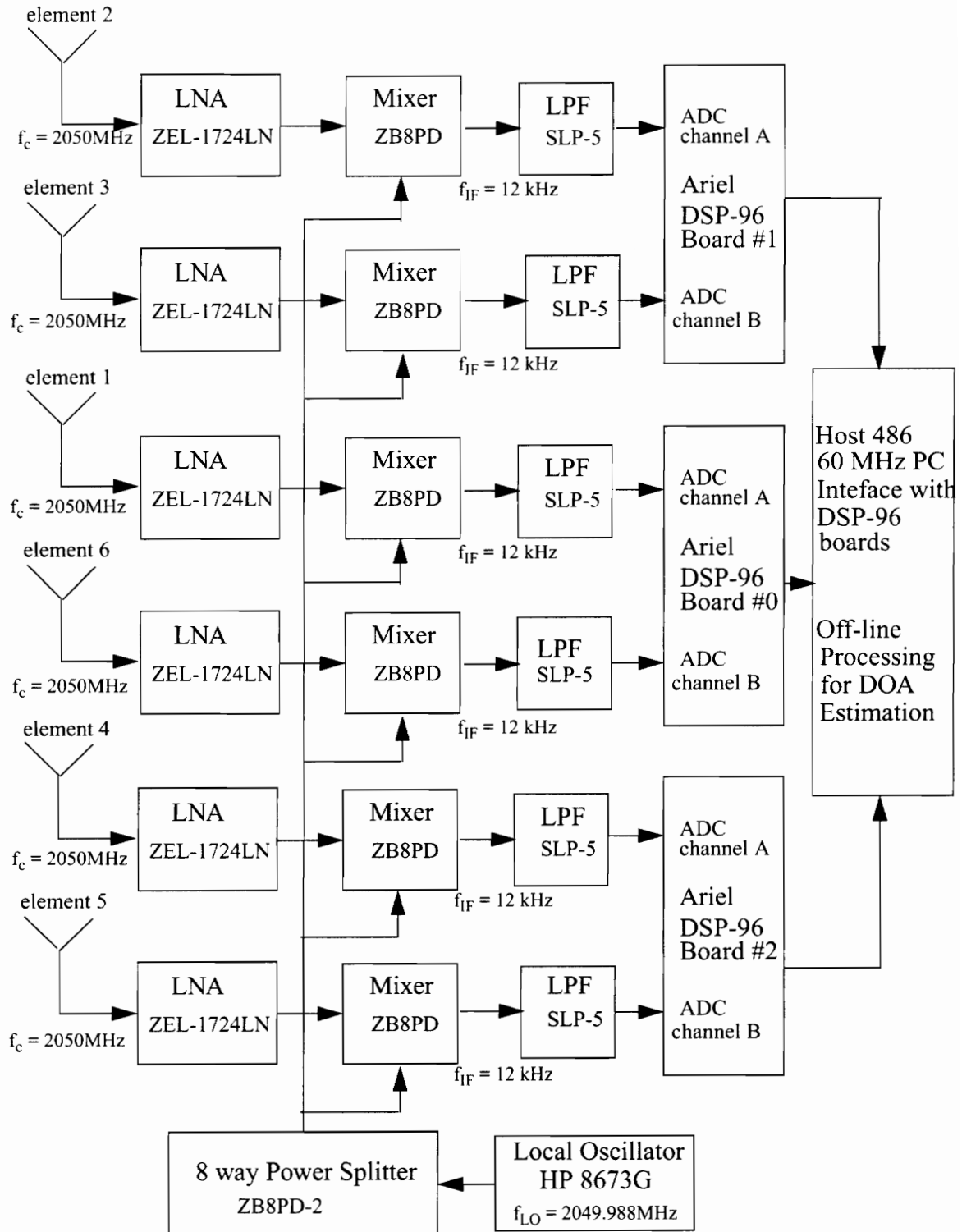


Figure 5.1: A block diagram of the DOA measurement system.

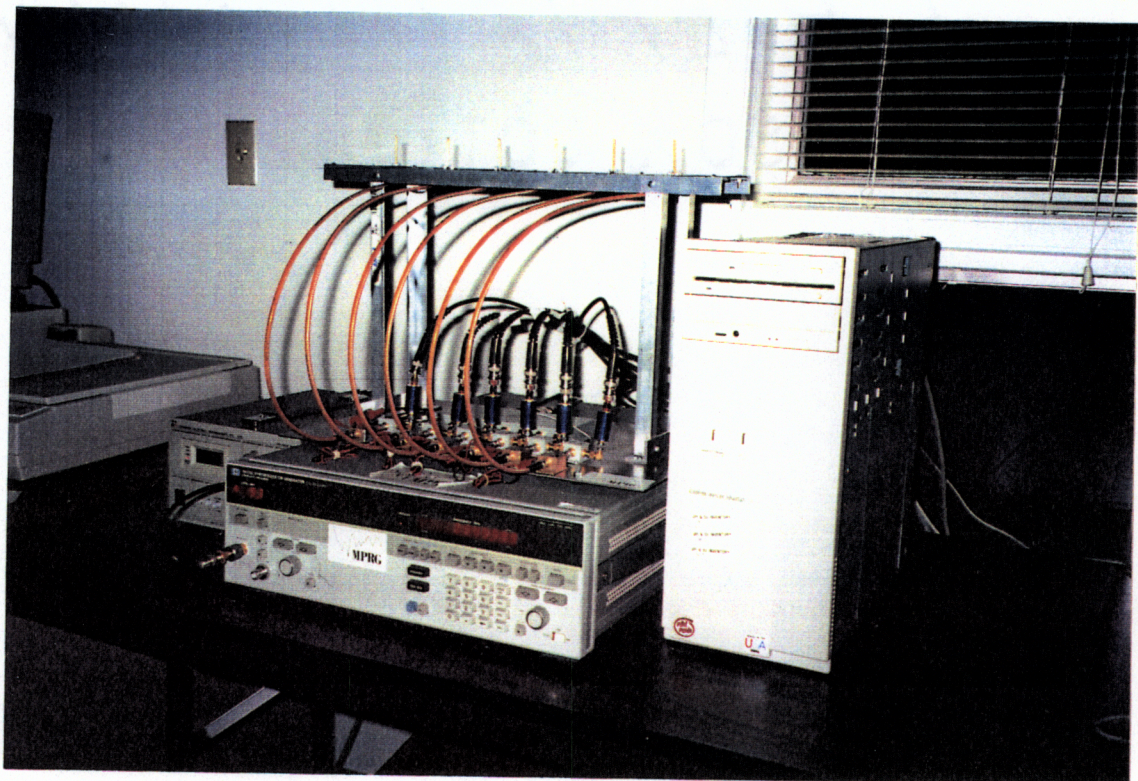


Figure 5.2: Photograph of the six element uniformly spaced linear array receiver used for DOA measurements.

5.2 Antenna Array and RF front-end

The antenna array is a six element uniformly spaced linear array. It consists of six quarterwave monopole elements spaced one half wavelength apart. Since the array is designed to operate at 2050 MHz, this corresponds to a spacing of 7.3 cms. Each quarterwave monopole element is built using a 3.7 cm long hollow brass tubing. Each brass tubing is soldered to the center conductor of a SMA jack chassis mount connector. The SMA connectors are bolted to a brass ground plane such that the connections to the antenna elements can be made from the bottom of the ground plane.

The RF section consists of a single downconversion stage built with no front-end filtering. The RF hardware is extremely simple and built using off-the-shelf components purchased

from Mini-Circuits, to reduce cost and complexity. Each monopole antenna element is connected to a Low Noise Amplifier (LNA) using a flexible SMA cable. The LNA's used are the Mini-Circuits ZEL-1724LN, which have a gain of 20 dB in the 1.7 to 2.4 GHz band, and a noise figure of 1.5 dB. The LNA's have a maximum power output rating of 10 dBm and a maximum input power rating of 13 dBm. The output of each amplifier is connected to the RF port of a Mini-Circuits ZEM-4300 mixer. The mixer has a conversion loss of 6.65 dB, making the overall gain in the RF chain equal to 13.35 dB. The local oscillator port of each mixer is connected to a 2049.988 MHz carrier which is generated by the Hewlett Packard Synthesized Signal Generator HP 8673G. The same local oscillator signal is connected to all the six mixers through an 8 way power splitter which has two of its output ports terminated with a 50 ohm load. The LO signal power is set at 13 dBm and the power splitter contributes a loss of 10 dB, which makes the LO signal power at the LO port of each mixer equal to 3 dBm. The mixer downconverts the input RF signal to a very low IF at 12 kHz. The IF output of each mixer is connected to a Mini Circuit SLP-5 Low Pass Filter (0 -5 MHz). The output of the IF filters are connected using BNC cables to the input of the A/D convertors on the DSP-96 boards. All the RF hardware is mounted on a heavy gauge steel plate. The monopole elements with the ground plane is mounted at a height of 31 cms above the plate using aluminum angle stock.

5.3 Sampling and Data Collection

Three Motorola DSP96002 based Ariel DSP-96 boards are used to sample the data from all the six channels synchronously, store them in a buffer and save them back to a file on the host PC. The software developed to set up the DSP-96 boards along with the host PC to collect data from the six channels of the antenna array receiver consists of many parts. One is the C code which runs on the host PC and the others run on the DSP-96 boards.

The host program [65] is a C-program which is developed and compiled using Borland C. The program downloads the DSP codes on to the DSP-96 boards, and uses the m96bcs

library supplied by Ariel Corp. to interact with the DSP-96 boards. The code which runs on the DSP-96 boards are written in two parts. The higher level functions such as host interface, and other less speed sensitive functions are written in C and compiled using the Intermetrics C compiler for DSP-96. Through function calls, the C code [68][69] accesses macros written in a separate file [66][67] in the MOTOROLA DSP 96002 assembly language. The assembled object modules and C compiled object module are linked along with the required libraries and locator files to obtain a single object module [72][73]. The locator file [70][71] specifies exactly where different segments of code need to be located on the DSP-96 board memory. The locator file gives us the flexibility to locate different sections of the code in internal, external, SRAM, DRAM, X,Y,L,P memory according to the speed and ease of access requirements. For more information on these topics, refer to the Ariel DSP-96 users manual [Are93].

One of the three DSP-96 boards, designated board #0, is set up as the master board, and the other two DSP-96 boards, designated board #1 and #2, are set up as slave boards. The master board handles all the communication with the host PC, controls the DSPNet, and co-ordinates the sampling on all the three boards. As shown in Figure 5.1, the IF signals obtained at the output of the RF chain from elements 1 and 6 are connected to the A/D convertors on the master board #0, and the IF signals from elements 2,3 and 4,5 are connected to the slave board #1 and #2 respectively. This rather strange assignment of DSP boards to the different antenna elements is made to maintain compatibility with the 4 element adaptive array program that runs on the same hardware.

The analog daughter card on each of the DSP-96 boards is programmed to generate a hardware interrupt (IRQA) every time a dual channel sample is available at the analog-to-digital convertor output. Samples are latched simultaneously on the A and B channels. Whenever this hardware interrupt occurs, the processor jumps to program memory location \$8 (the IRQA ISR vector). An instruction at \$8 instructs the processor to jump to the location that handles the interrupt (ISR). The ISR fetches the two 32 bit samples from the

two A/D convertor outputs on each board and stores them in a buffer.

Once the buffer is full, the data is transferred to the host PC on request. While data in the master board buffer is send directly to the host, data from the slave boards are transferred to the master board via DMA which in turn sends it to the host.

It is required that all the A/D convertors on the three DSP-96 boards sample at the same time. Failure to do so, will produce a frequency dependent phase shift between each element due to the delay. Therefore it is required that the sampling on all the three boards be synchronized. This requires that the sampling clocks be tied together, and that all the three boards start sampling (collecting data) at the same time instant. Section 5.3.1 details how the sampling on the three boards (six channels) are synchronized.

5.3.1 Configuring Multiple DSP-96 boards for Synchronous Sampling

When multiple DSP-96 boards are installed in the same PC, it is required to adhere to the following guidelines:

1. Each DSP-96 board must be set at a different I/O base address.
2. There must be a record in the configuration file M96.CFG corresponding to each board and its particular I/O address.
3. Multiple DSP-96 boards may not be set to share the same DMA channel.
4. A DSP-96 board may not be set to share the same AT-bus interrupt with another DSP-96 board.
5. When using DSPnet, each board must have a unique DSPnet setting (0 to 9).

To achieve synchronous sampling of data from all the three boards, it is required to ensure the following:

1. Tie up the sample clocks of all the three boards.
2. Ensure that the corresponding samples from each board were picked at the same sampling instants. That is, the sampling and data collection process on all three boards should begin at the same sampling instant (Frame synchronization).

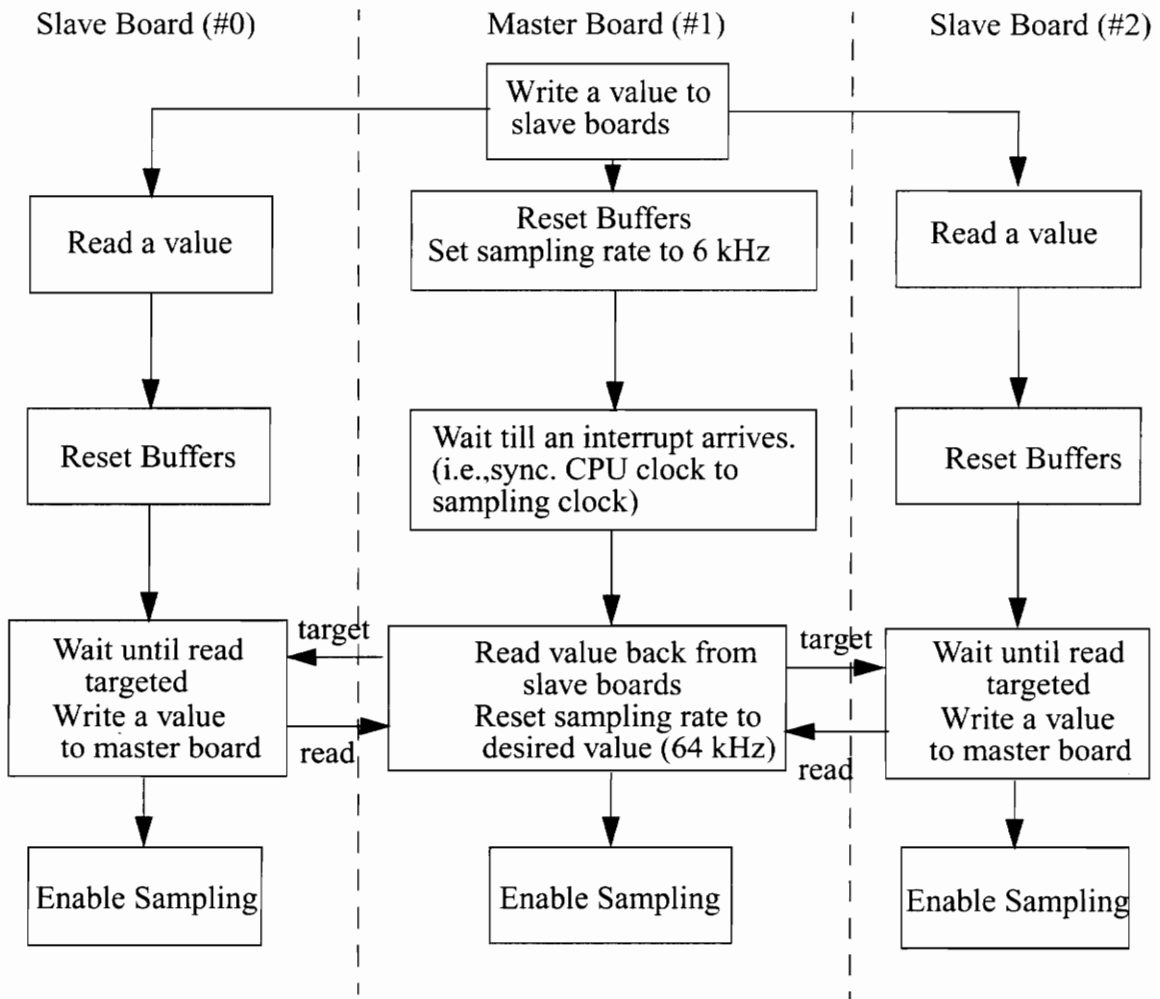


Figure 5.3: Flowchart illustrating the frame synchronization process

Two headers on each board provide access to the master clock and sample clock. The master clock header, P3, has three pins. The first pin of P3 is the programmable master clock

signal generated by each board by setting the sampling rate in software. The second pin accepts an external master clock. Under normal operation, the programmable master clock from each board is fed to its own A/D convertor by placing a jumper between the two points. This clock is 256 times higher than the desired sample rate. A second header, P2, allows similar access to the sample clock which is 1/256 of the master clock. Under normal operation, the programmable sample clock on pin 1 of P2 is fed to the sample clock input on pin 2 of P2. To tie up the sampling clocks of the slave boards to that of the master board, the following hardware connections need to be made. Short pins 1 and 2 on header P3 on master board (see Ariel manual [Are93] for P3 location). Connect a wire from P3 pins 1 and 2 on the master board to P3 pin 2 on the slave board. Short pins 1 and 2 on header P2 on master board (see Ariel manual [Are93] for P2 location). Connect a wire from P2 pins 1 and 2 on the master board to P2 pin 2 on the slave board. For both connections a shielded cable type with the shield connected to pin 3 of the particular header need to be used.

A proper handshaking protocol is used to ensure that the sampling and data collection process on all three boards begin at the same sampling instant, and hence have the data frame from all the six A/D convertors synchronized. As mentioned earlier, one of the boards is configured as the master board and the other two as slave boards. The master board writes a value to each of the slave boards, and that value is read by the slave boards. The slave boards then write back a return value to the master board which is read only at a known precise time. After writing a value to the slave boards the master board reduces its sampling rate to the lowest possible value, i.e. 6 kHz. Since the sampling clocks of all the boards are tied together, this implies that all the boards are now operating on a 6 kHz sampling clock. The sampling clock is reduced to this low rate to ensure that there is sufficient time to execute many instructions between sampling instants. Having done this, the sampling is momentarily enabled on the master board. The master board now waits for the first sampling interrupt (IRQA) to arrive. Once the first interrupt arrives we know that we are now at the beginning of a sample clock and have time to execute plenty of instructions

before the arrival of the next interrupt. We actually have 167 μ s (2755 instruction cycles) before the next interrupt arrives. At this time, sampling is disabled on the master board, and the returned values from the slave boards are quickly read. Once the returned values from the slave boards are read, sampling is enabled on all the three boards at the desired rate. This ensures that the first ADC interrupt on all the three boards occur at the same time and hence the data collected from all three boards correspond to the same time instants. This procedure is shown to work for sampling frequencies upto 64 kHz.

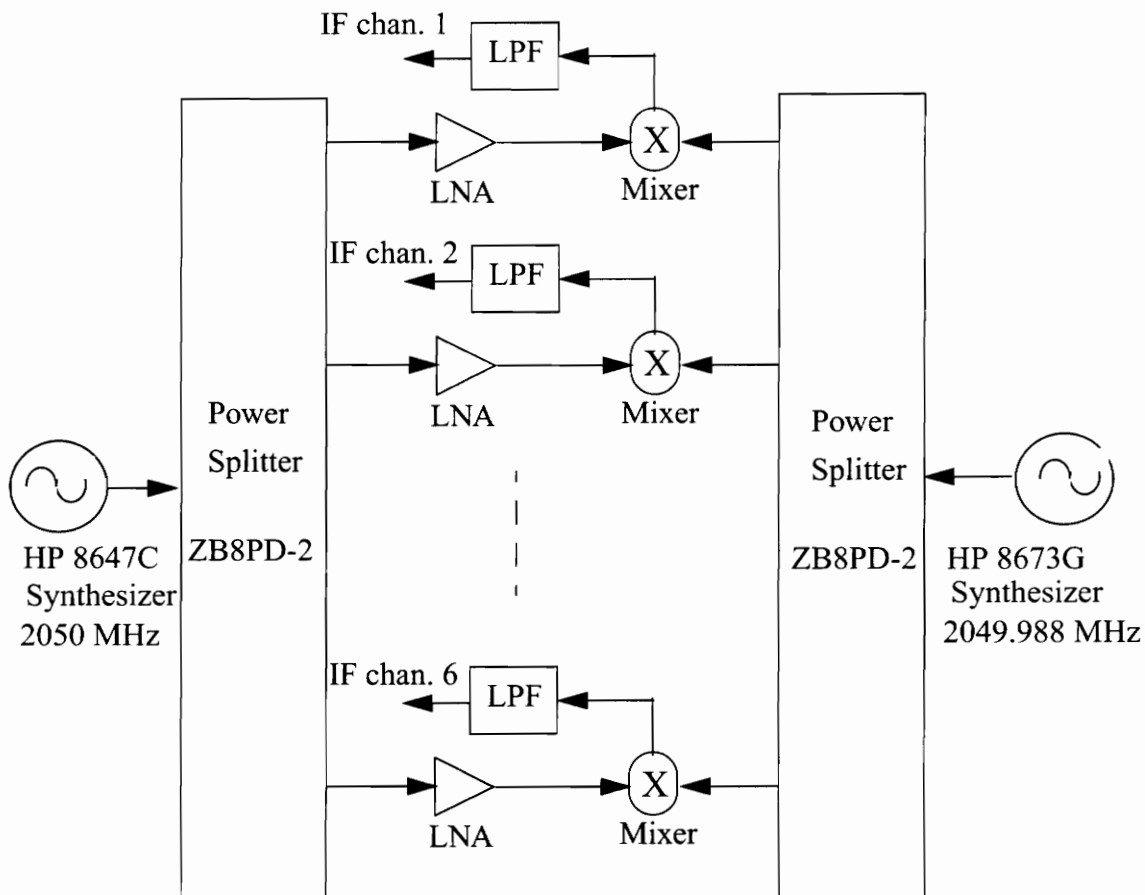
The boards were checked for proper synchronization by simultaneously feeding a square wave from a single source to all six ADC inputs (two on each board). By looking at the zero-crossings, one can decide if all the channels are synchronized or not. Presence of any offset between channels will clearly indicate mis-synchronization. Figure 5.3 shows a flowchart detailing the entire frame synchronization process.

5.4 RF Chain Phase Calibration

Since all the direction of arrival estimation techniques rely on the phase difference between the signals on the individual antenna elements to estimate the angle of arrival, it is necessary that the RF chain connected to each of the element does not introduce different phase shifts. In other words, the phase difference between the signals at each element should be solely due to the spatial separation of the antenna elements and a function of the angle of arrival. Therefore, any phase difference between the signals on each element caused by the RF chain has to be corrected using a calibration procedure.

The basic idea behind phase calibration is to determine the phase correction factors θ_i to compensate for phase differences in the RF chain of the six channels. The phase correction factor θ_i , is the phase shift which must be applied to channel i so that when a signal at 2050 MHz is introduced at the monopole element, the signals measured at the output of the RF chain 1 and RF chain i have equal phase. The calibration procedure uses the setup

shown in Figure 5.4. A 2050 MHz input signal is fed to all the six RF chains through an 8 way power splitter which has two of its unused output ports terminated with a 50 ohm load. It was found that the power splitter introduces identical phase shifts from the input port to each of its output port, and hence it is ensured that the signal fed to each of the RF chain has identical phase. Once this is ensured, the phase difference between the IF signals at the end of each RF chain is solely due to the phase differences caused in the RF chain.



LNA : Mini Circuits ZEL-1724LN
 Mixer: Mini Circuits ZEM-4300
 LPF : Mini Circuits SLP-5

Figure 5.4: Hardware setup for the RF chain phase calibration

Using sampled data obtained from the calibration set up, the phase difference between

each element is determined by finding the arctangent between the complex samples from each channel. The real samples from each channel can be converted to complex samples by performing I-Q IF to baseband downconversion on the 12 kHz IF signal. The MATLAB program calib.m [74] determines the phase difference of each channel with respect to the channel corresponding to the first antenna element, and stores the phase correction factors, θ_i , to a calibration file. This calibration file is read by the DOA estimation programs and the necessary phase corrections are applied to all data collected before performing DOA estimation using them. Phase corrections are applied by multiplying the i th channel complex baseband signal by $e^{-j\theta_i}$.

5.5 Receiver Sensitivity and Dynamic Range

The sensitivity and dynamic range of the receiver is determined by the dynamic range of the analog-to-digital convertors, the operating range of the front-end amplifiers and mixers, the IF amplification obtained at the amplifier in front of the ADC on the DSP-96 analog daughter card.

The ADC's on the DSP-96 board are 16 bit ADC's and hence the signal-to-quantization ratio is 96 dB when operated at full scale. Since we do not have an automatic gain control circuit (AGC) to ensure that the ADC's always operate at full scale, we are not be able to guarantee the full dynamic range of the ADC. Depending on the input signal level relative to the full scale level, the actual number of bits used for representing the sampled signal will vary, and hence the signal-to-quantization noise ratio also varies.

The useful dynamic range of the ADC is determined by the signal-to-quantization noise ratio that can be tolerated. In other words, it depends on how many bits of resolution we need to be able to successfully process the sampled data. A simple experiment was conducted to determine how many bits of resolution is required. A transmitter antenna was

placed at a known angle and the DOA estimation algorithms were ran to determine the direction-of-arrival. The experiment was repeated with lower and lower transmitter power until the DOA estimation algorithm began to produce large errors (i.e the DOA estimate varied by greater than 2 degrees from the estimate made when the received signal was large enough to use the full dynamic range of the ADC). It was found that, if the received signal was large enough to swing over at least the 7 least significant bits of the ADC the DOA estimation errors were within +/- 2 degrees.

The ADC's on the DSP-96 board have a full scale input equal to 4V peak-to-peak. An adjustable gain amplifier in front of the ADC can vary the sensitivity of the analog-to-digital convertors. Adjusted to maximum sensitivity, an input of 500 mV peak-to-peak will give a full scale reading on the ADC. This corresponds to obtaining a voltage gain of 8. At this level of sensitivity, the step size of the A/D convertor is equal to $\Delta = \frac{500mV}{2^{16} - 1} = 7.62\mu V$, and for a signal to swing over a 7 bit range it should have a

peak-to-peak voltage equal to $\Delta \times (2^7 - 1) = 0.96774mV$. Therefore, the minimum signal level at the input of the A/D convertor board (i.e., minimum IF signal out of the LPF in the RF chain) to do useful processing is equal to 0.9677mV peak-to-peak.

Therefore, from the point of view of the A/D convertor, the maximum IF signal out of the LPF is equal to 500 mV peak-to-peak (i.e equal to -8 dBm) and the minimum signal level is equal to 0.9677 mV peak-to-peak (i.e equal to -62 dBm). Now, in order to find the dynamic range and sensitivity of the overall receiver, we need to compute the input RF signal power levels that will fall within the above computed maximum and minimum IF signal levels at the ADC input.

The front-end LNA has a 20 dB gain, the mixer has a 6.65 dB conversion loss and the LPF has a loss which is less than 1 dB, making the overall front-end gain equal to $20 - 6.65 - 1 = 12.35$ dB. Therefore an RF signal power of $-8 - 12.35 = -20.35$ dBm will produce a full

scale reading on the ADC, and the minimum required RF input signal power is equal to $-62 - 12.35 = -74.35$ dBm. This corresponds to an overall dynamic range of $-20.35 - (-74.35) = 54$ dB.

5.6 Processing for DOA Estimation

The sampled data from the six element linear array receiver is processed off-line for DOA estimation. The DOA estimation algorithms were coded in MATLAB and runs on the PC attached to the measurement system, as well as on the Sun workstations. Figure 5.5 shows a flow chart illustrating the off-line processing steps. The processing program [75][76] reads the user specified file which contains sampled data from the six element linear array. The file also contains any comments which may be entered by the user during data collection. Data samples corresponding to the six different channels are separated and each channel data is passed through an 8-16 kHz band pass filter to remove any harmonics or spurious signals. The BPF used is anFIR filter of order 20.

The filtered signal is then downconverted to base band using I-Q demodulation. Downconversion is achieved by multiplying the IF signal with a complex exponential at 12 kHz. Downconversion is followed by low pass filtering to remove the harmonics. The low pass filter is an FIR filter of order 20. The output of the low pass filter is the complex baseband equivalent of the sampled IF signal.

The phase calibration correction factors are read from the file containing it, and the complex baseband signals are phase shifted by the amount specified in the file. After applying these phase corrections, the complex baseband data matrix, X , is formed. The direction-of-arrival estimation algorithms can now be applied on the complex baseband data matrix. For the DOA algorithms to work under coherent signal conditions, forward and conjugate backward averaging is used as a spatial smoothing technique to decorrelate the coherent signals. ESPRIT and the integrated ILSP-CMA with ESPRIT algorithms are used for esti-

mating the directions of arrival from the data matrix. Figure 5.6 and 5.7 illustrates the Total Least Squares ESPRIT (TLS-ESPRIT) and the integrated ILSP-CMA with TLS-ESPRIT algorithms For more details on these algorithms see Chapter 3.

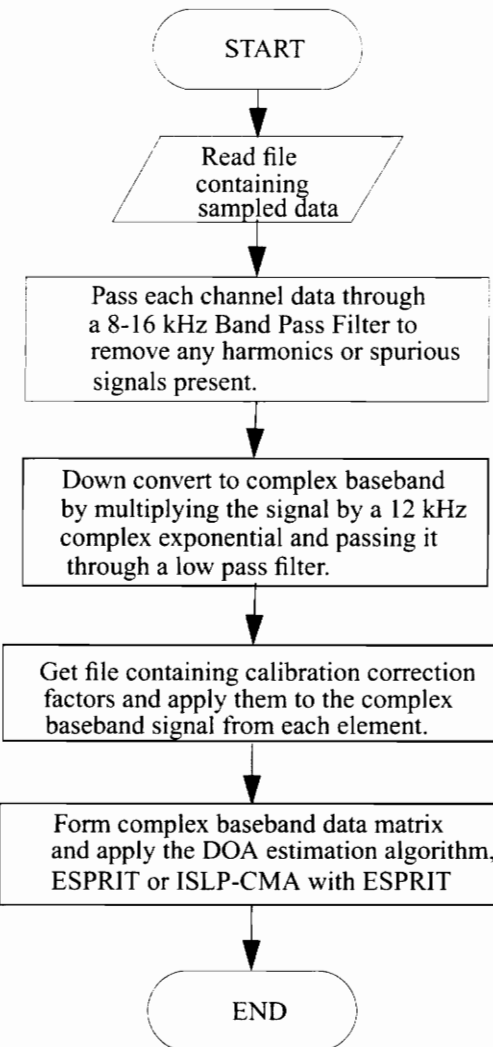


Figure 5.5: Flowchart illustrating the off-line processing steps

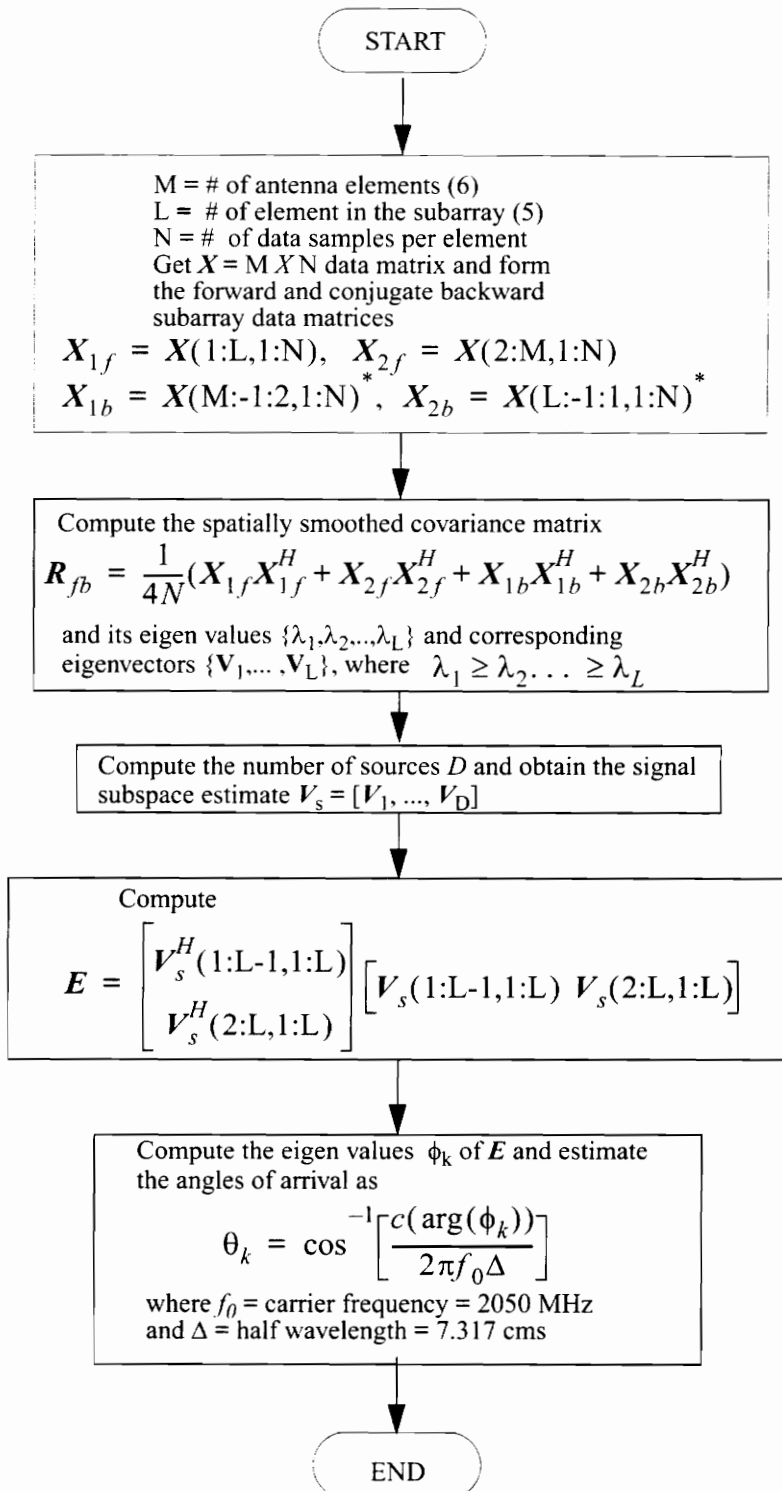


Figure 5.6: Flowchart illustrating the TLS-ESPRIT algorithm for DOA estimation. This is implemented in Program [76].

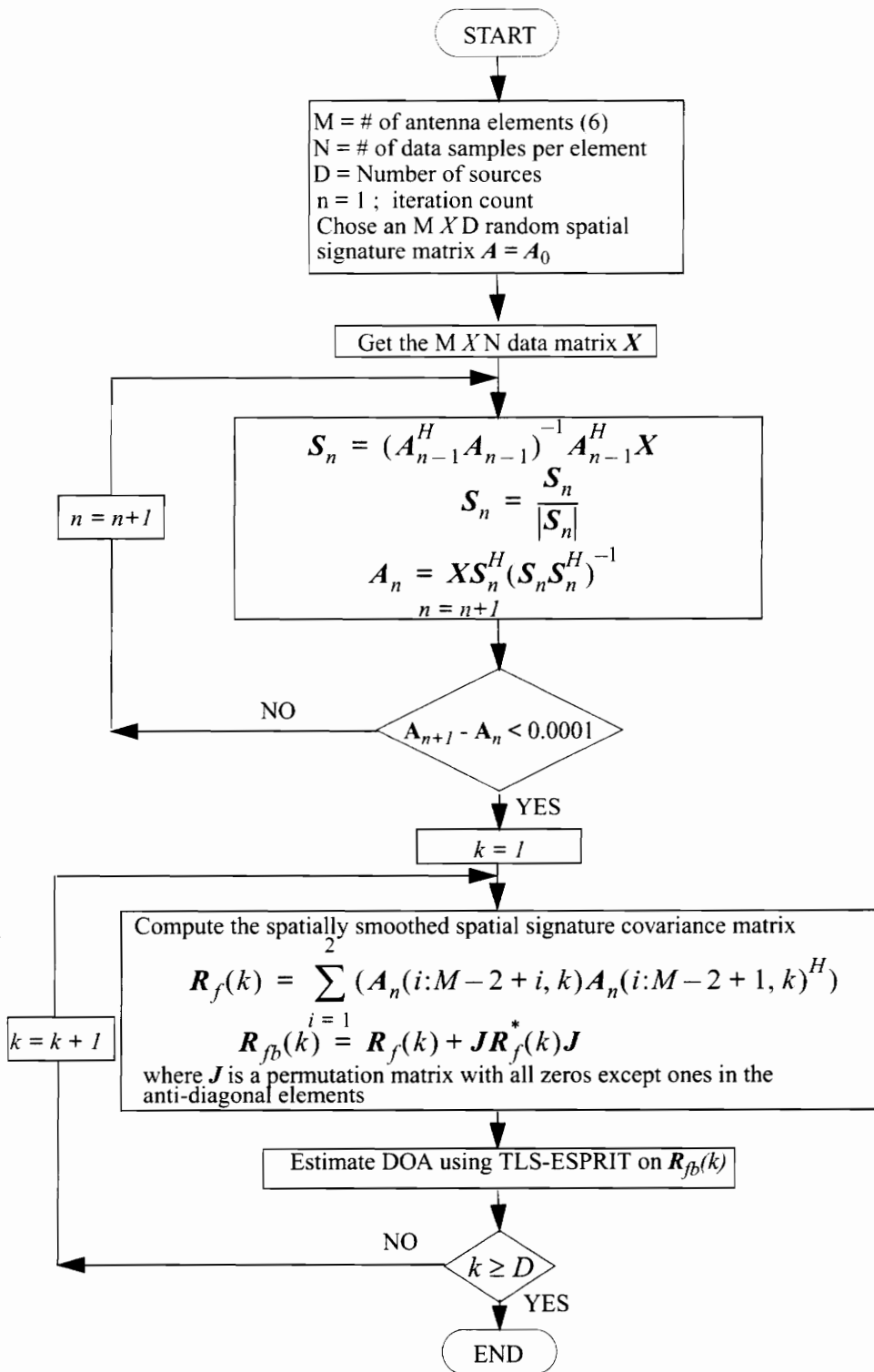


Figure 5.7: Flow chart illustrating the integrated ILSP-CMA with TLS-ESPRIT algorithm for DOA estimation. This is implemented in Program [75].

Chapter 6

DOA Measurement Experiments and Results

6.1 Introduction

This chapter describes the direction-of-arrival measurement experiments conducted using the six element linear array operating at 2050 MHz. The objective of the experiments was to test the functioning of the measurement system and verify the performance of DOA estimation algorithms. The two algorithms whose performance is studied are the TLS-ESPRIT and the integrated ILSP-CMA with TLS-ESPRIT algorithms. The experiments were designed such that the DOA estimation accuracy of these algorithms under different signal conditions are studied. Tests were conducted with multiple uncorrelated signals as well as coherent multipath signals. This chapter also presents the results of the measurements along with an analysis of the errors in measurement, and simulations which corroborate the measurements and verify the most significant error sources.

6.2 Description of the DOA Measurements

Since the objective is to verify the functioning of the system, DOA measurements were made under known signal conditions. That is, multiple transmitter antennas were placed at

known locations such that the direction of arrival of the plane waves at the receiver antenna is known beforehand. According to the number and type of signals transmitted, the experiments can be grouped into three different categories.

1. A single antenna positioned at locations with known angles with respect to the receiver array, and transmitting a CW tone signal at 2050 MHz. Under this set up, in the absence of multipath, at the receiver array we have a single signal (ray) incident at a known direction-of-arrival.
2. Multiple (up to three) antennas located at different locations at known angles with respect to the receiver array, and connected to different signal sources transmitting CW tone signals at 2050.000, 2049.999 and 2050.001 MHz respectively. Under this set up, at the receiver array, we have multiple uncorrelated signals (rays) incident at known directions-of -arrival.
3. Multiple (up to three) antennas located at different positions at known angles with respect to the receiver array, and connected to the same source transmitting a CW tone signal at 2050 MHz. Under this set up, at the receiver array, we have multiple signals (rays) that are perfectly correlated incident on the array at known directions-of-arrival. This is identical to a coherent multipath situation where the multiple rays incident on the receiver array are attenuated and phase shifted versions of the same signal.

The DOA experiments were conducted in the Western Sizzling parking lot near the MPRG building. The antenna array receiver was placed approximately half way along one edge of the parking lot. At a distance of 60 feet from the receiver array location, using a protractor and a rope, points were marked out every five degrees along a semicircle on the field. The angles were measured with respect to the receiver array axis. These marking were made so that we can position the transmitter antennas at known angles with respect to the receiver array axis.

A transmitter receiver (T-R) separation of 60 feet was chosen as a compromise between various factors. First, to keep the transmit power to a minimum it is required to reduce the T-R separation distance. Also, since spatially separated antennas need to be fed from the same source via coaxial cables (for the case of coherent signals), keeping a large T-R separation distance implies that we will need longer cables to obtain the required angular separation between multiple transmitter antennas. At the same time, we cannot keep the T-R separation to be very small, as this will invalidate the plane wave assumptions.

The DOA estimation algorithms described in chapter 3 are based on modeling the incident signals as plane waves, and assumes that the propagation conditions do not change as the ray traverses the extent of the array. If the incident wave is a spherical wave instead of a plane wave, the direction of arrival of the wave with respect to each individual receiver antenna element will be different from one another, and the difference is directly proportional to the physical dimension of the array and inversely proportional to the radius of the spherical wave (which is equal to the T-R separation distance). A good rule of thumb to ensure the validity of the plane wave assumption is to have the transmitting source at a distance of at least 50 times the maximum dimension of the receiver array [Don93]. Under such conditions, the difference between the DOA's relative to the closest and most distant antenna elements is less than about 1 degree.

Since the array operates at 2050 MHz ($\lambda = 0.14634 \text{ m}$) and has six elements, each spaced one half wavelength apart, the total extent of the array is equal to $\frac{5\lambda}{2} = 0.36585 \text{ m}$.

Therefore, the T-R separation should be at least $50 \times 0.36585 = 18.2925 \text{ m}$, which is approximately equal to 60 feet.

As discussed in section 5.5, the minimum required received power for the antenna array receiver is approximately -75 dBm. Assuming free space propagation, the minimum required transmitter power can be calculated using the Friis free space formula [Rap95].

$$P_r = \frac{P_t G_t G_r \lambda^2}{(4\pi)^2 d^2} \quad (6.1)$$

For a T-R separation distance of 60 feet, using equation (6.1), at 2050 MHz the minimum required transmitter power level is equal to -10 dBm. For all the experiments, the transmitter signal generator power was kept at 10 or 15 dBm. With the cable connecting the source to the antenna having a loss of 10 dB, the effective transmitted power was equal to 0 or 5 dBm.

Quarterwave monopoles were used as transmitting antennas. The quarter wave monopoles were constructed using 3.7 cm long hollow brass tubing soldered to an SMA jack which was bolted to a brass ground plane. The monopole antennas were mounted on PVC pipes at a height of 1.37 m (4.5 ft.). The receiver array was kept on a trolley such that the array was 1.37 m above the ground.

6.2.1 Measurements with a Single Transmitter Antenna

A CW tone signal at 2050 MHz was generated using the HP83620 signal generator. The signal generator output power was set to 15 dBm, and the RF signal was fed to a monopole antenna using a flexible SMA cable which has a 10 dB loss. The transmitter antenna was placed at different positions such that the receiver array has a line-of-sight wave impinging on it at known angles. Measurements were made at every five degrees, beginning with 0 degrees up to 180 degrees. For each DOA measurement, 2048 (2 K) samples of the signal was collected from each antenna element at a sampling rate of 64 kHz[65].

Figure 6.1 shows the results of the DOA measurements made with a single transmitter antenna. The RMS error is plotted as a function of the angle of arrival. The RMS error for the single plane wave case is simply the difference between the estimated and actual DOA. The actual DOA is taken as what is measured using a protractor and rope and marked on the field. It should be noted that inaccuracies in the measurement of actual DOA will also

manifest as DOA estimation error in all the plots presented. Since angle marking were made at a distance of 60 feet from the receiver array, one degree corresponds to a distance of approximately one foot. Therefore, if the marked positions are in error by one foot, it will correspond to an error in actual DOA measurement of approximately one degree.

As seen from Figure 6.1, for the case of a single transmitter, the DOA estimated by the two algorithms (TLS-ESPRIT and ILSP-CMA with TLS-ESPRIT), are within ± 5 degrees of the actual DOA, except for the case when the angle of arrival is 0 or 180 degrees (endfire), where the error is within 10 degrees.

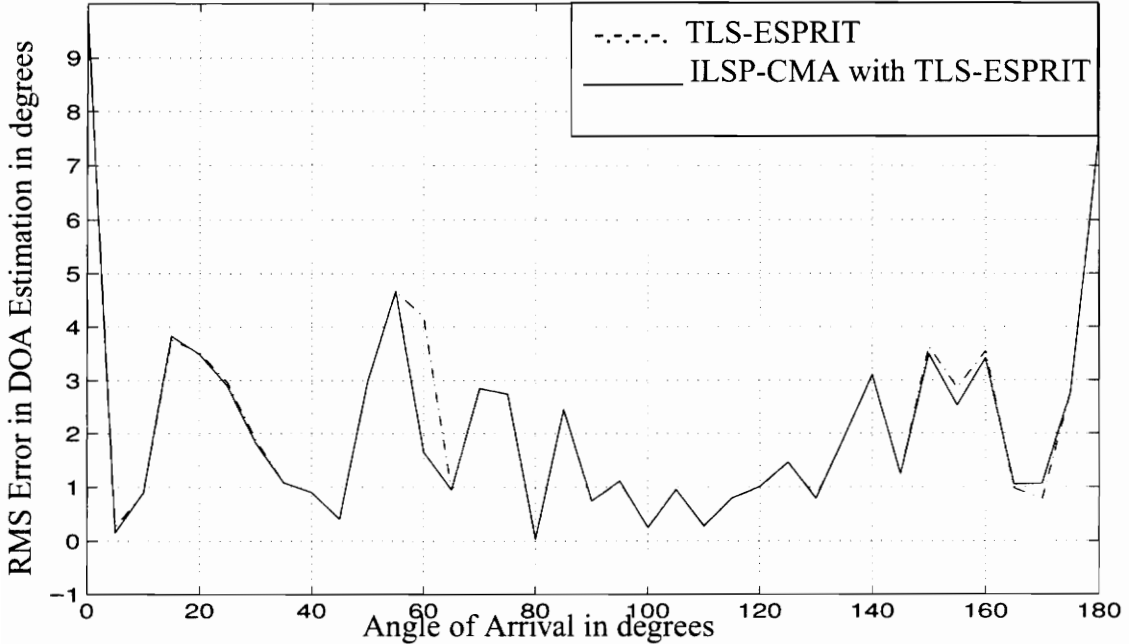


Figure 6.1: DOA Measurement Results - RMS Error in DOA Estimation as a function of the angle of arrival. RMS error is computed as the absolute difference between the estimated and actual angle of arrival.

6.2.2 Measurements With Multiple Transmitter Antennas Fed From Uncorrelated Sources

These measurements were set up to test the performance of the DOA estimation

algorithms under uncorrelated signal conditions. This is similar to having signals from multiple users impinging on the array. DOA measurements were made using two and three transmitters, with each of them spatially separated by different angles. As shown in Chapter 4, the accuracy of the DOA estimation algorithms is a function of the angular separation between the multiple signals and also the angle of arrival itself (broadside giving better performance than endfire). The DOA measurement experiments were designed such that the performance of the DOA estimation algorithms could be studied as a function of the angular separation between multiple (two or three) signals and also the angle of arrival itself.

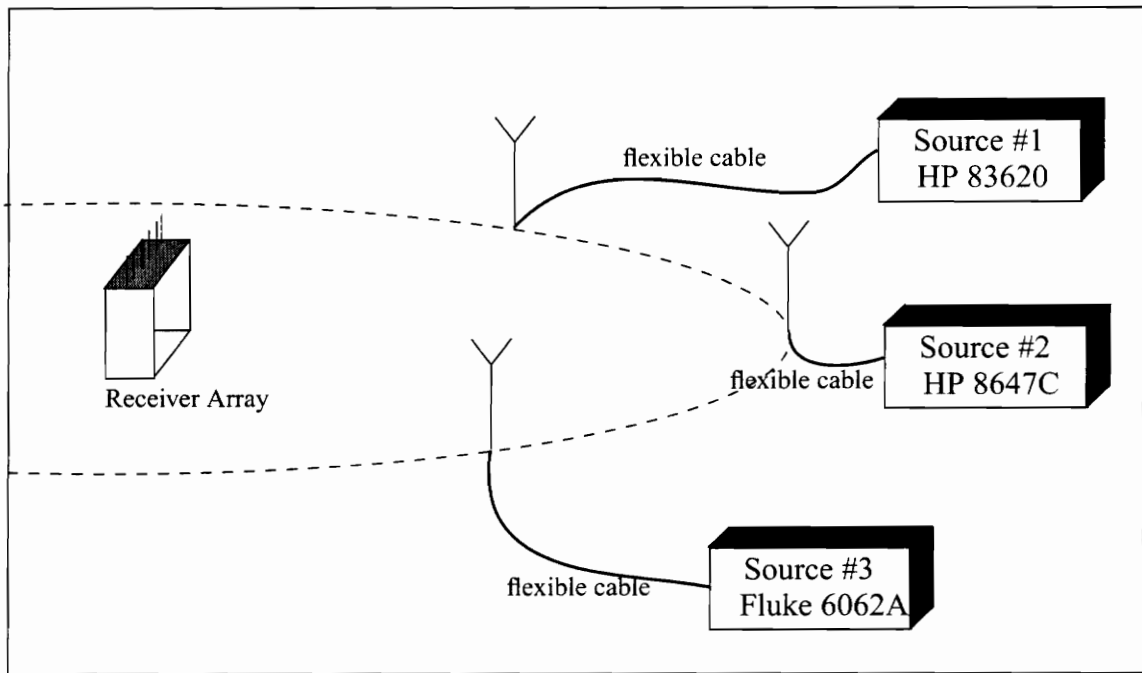


Figure 6.2: Illustration of a the DOA measurement setup with three uncorrelated signals being transmitted at different angles with respect to the receiver array location.

The three uncorrelated signals were generated using separate signal sources at different frequencies. The first signal is a CW tone at 2050 MHz generated by the HP83620 signal generator. The second signal is a CW tone at 2049.999 MHz generated by the HP8648C signal generator, and the third signal is a CW tone at 2050.001 MHz generated by the

Fluke 6062 signal generator. All the signal generators were set up for a power output of 10 dBm (the maximum power output that can be obtained from the Fluke 6062 is 10 dBm). Since all the sources were connected to their antennas using a cable of 10 dB loss, the effective transmitter power was equal to 0 dBm (1mW). Figure 6.2 illustrates the experimental setup for the case of three uncorrelated signals.

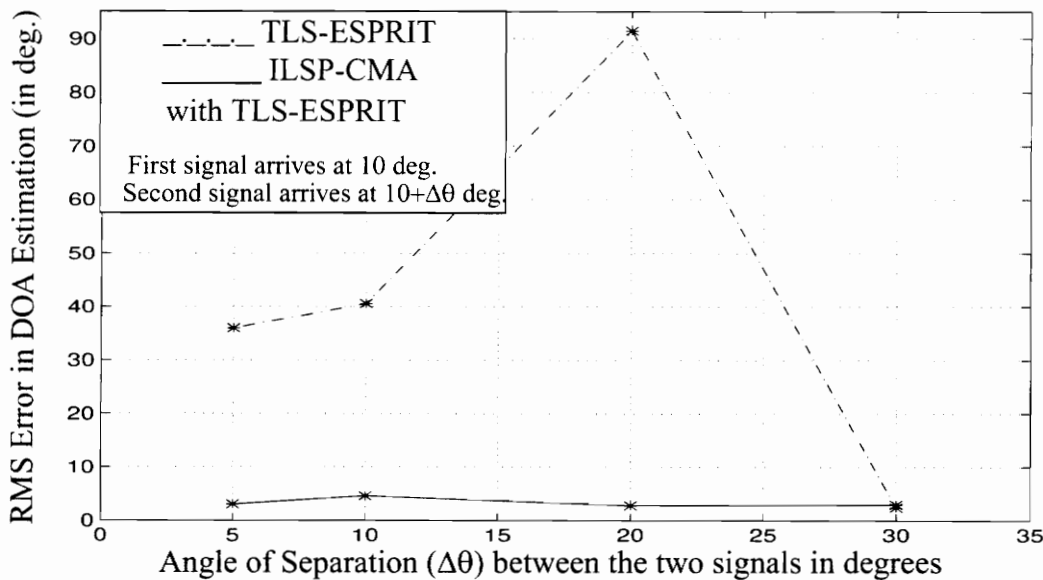


Figure 6.3: DOA Measurement Results - RMS Error in DOA estimation as a function of angle of separation between the two uncorrelated sources. The first signal arrives at 10 degrees and the second signal arrives at $10+\Delta\theta$ degrees.

Figures 6.3 to 6.9 show the results of the DOA measurements performed with multiple uncorrelated signals. In all the figures, the RMS error in DOA estimation is plotted as a function of the angular separation between adjacent signals. If $\theta_1, \dots, \theta_D$ are the actual measured angles of arrival of the D signals, and $\hat{\theta}_1, \dots, \hat{\theta}_N$ are the angles estimated by the algorithms, the RMS error (RMSE) in DOA estimation is defined as

$$RMSE = \sqrt{\frac{1}{D} \sum_{d=1}^D (\theta_d - \hat{\theta}_d)^2} \quad (6.2)$$

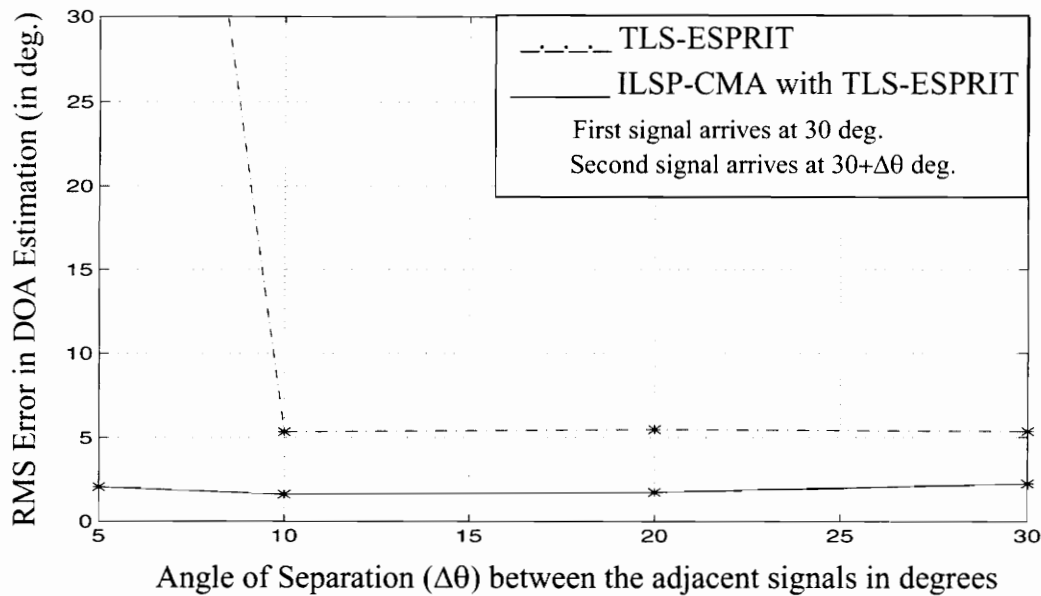


Figure 6.4: DOA Measurement Results - RMS Error in DOA estimation as a function of angle of separation between the two uncorrelated signals. The first signal arrives at 30 degrees and the second signal arrives at $30+\Delta\theta$ degrees.

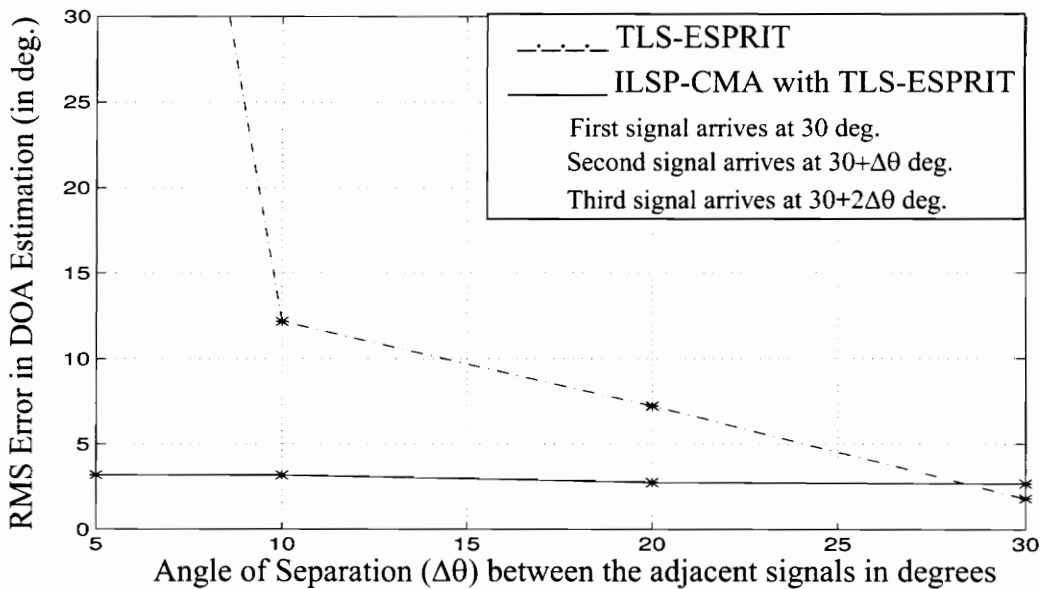


Figure 6.5: DOA Measurement Results - RMS Error in DOA estimation as a function of angle of separation between adjacent uncorrelated signals. The first signal arrives at 30 degrees, the second signal arrives at $30+\Delta\theta$ degrees and the third signal arrives at $30+2\Delta\theta$ degrees.

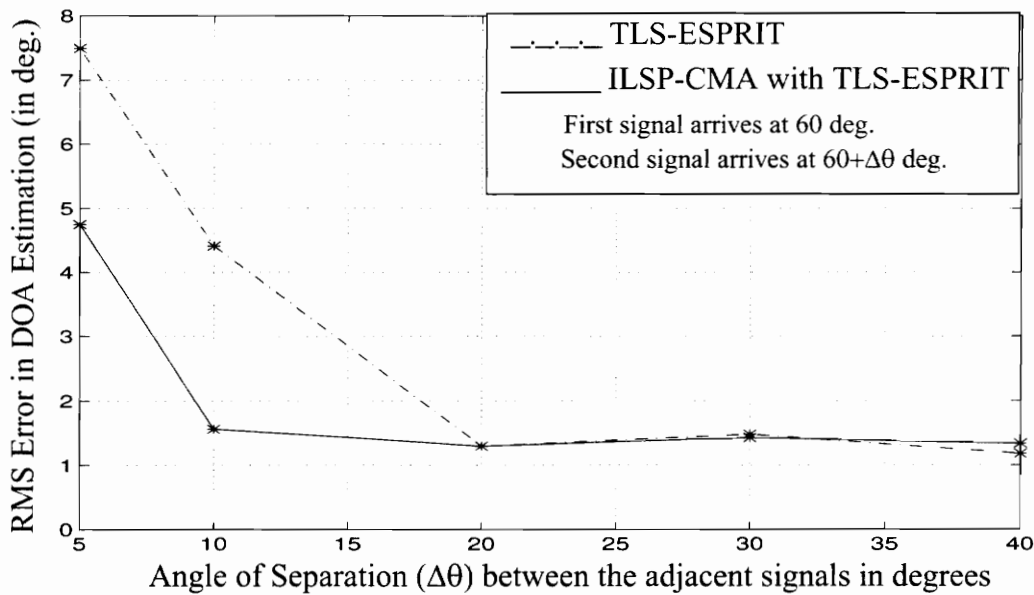


Figure 6.6: DOA Measurement Results - RMS Error in DOA estimation as a function of angle of separation between the two uncorrelated signals. The first signal arrives at 60 degrees and the second signal arrives at $60+\Delta\theta$ degrees.

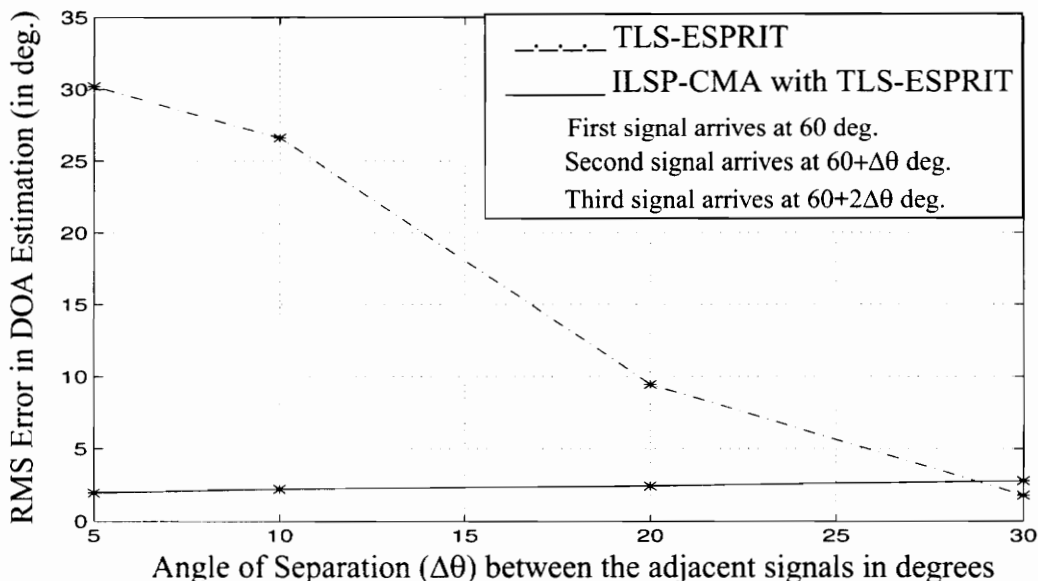


Figure 6.7: DOA Measurement Results - RMS Error in DOA estimation as a function of angle of separation between adjacent uncorrelated signals. The first signal arrives at 60 degrees, the second signal arrives at $60+\Delta\theta$ degrees, and the third signal arrives at $60+2\Delta\theta$ degrees.

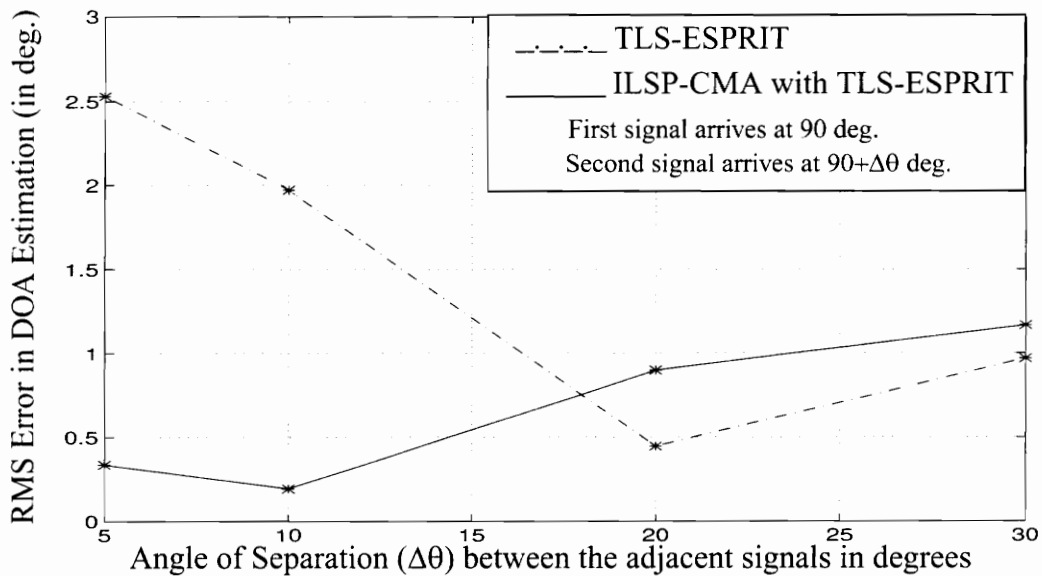


Figure 6.8: DOA Measurement Results - RMS Error in DOA estimation as a function of angle of separation between the two uncorrelated signals. The first signal arrives at 90 degrees and the second signal arrives at $90+\Delta\theta$ degrees.

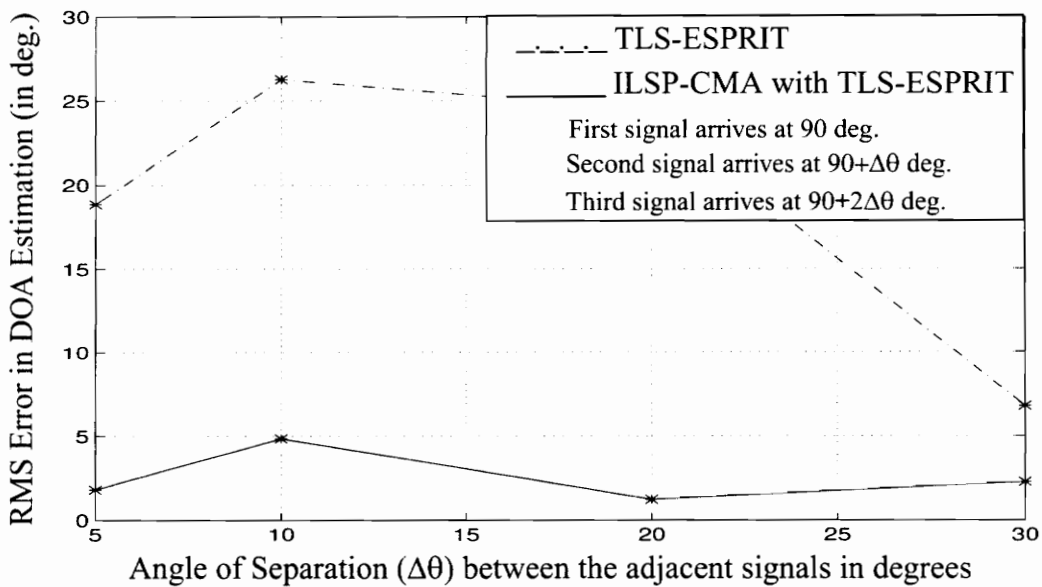


Figure 6.9: DOA Measurement Results - RMS Error in DOA estimation as a function of angle of separation between adjacent uncorrelated signals. The first signal arrives at 90 degrees, the second signal arrives at $90+\Delta\theta$ degrees, and the third signal arrives at $90+2\Delta\theta$ degrees.

For all the test situations, the angular separation between all the adjacent transmitter antennas were kept equal. Figure 6.3 shows the RMS error in DOA estimation as a function of angular separation $\Delta\theta$, with the first signal arriving at 10 degrees and the second signal arriving at $10 + \Delta\theta$ degrees. Figures 6.4, 6.6, and 6.8 show the same with the first signal arriving at 30, 60, and 90 degrees respectively. Figures 6.5, 6.7, and 6.9 show the RMS error in DOA estimation error for the case of three uncorrelated signals.

As seen from Figures 6.3 to 6.9, the integrated ILSP-CMA with TLS-ESPRIT algorithm is able to estimate the directions-of-arrival for the case of two signals within less than ± 5 degrees for most of the angles and angular separations at which the measurements were made. The TLS-ESPRIT algorithm produced large errors when there are two uncorrelated signals, one arriving at 10 degrees and the other arriving at angle separated from the first signal by less than 30 degrees (see Figure 6.3). The TLS-ESPRIT algorithm also produced large errors when there are three uncorrelated signals (see Figures 6.5., 6.7, and 6.9). Section 6.3 provides an analysis of these errors.

6.2.3 Measurements With Multiple Transmitter Antennas Fed From a Single Source

These measurements were set up to test the performance of the DOA estimation algorithms under correlated signal conditions. This is similar to having multipath signals from a single user incident on the receiver array. DOA measurements were made with two, three, and four signals, with each of them separated from one another by different angles. As mentioned in Section 6.2.2, the experiments are designed to verify the performance of the DOA algorithms as a function of angle of arrival and the angular separation between adjacent sources.

All the required signals were generated by a single source. The HP 83620 signal generator was set up to generate a CW tone at 2050 MHz at an output power level of 15 dBm. This

signal was fed to multiple transmitter antennas via power splitters and cables. Equal loss cables were used such that the power transmitted by all the antennas are approximately equal. With the splitter and the cables providing an attenuation of approximately 13 dB, the power transmitted by the antennas was approximately equal to 2 dBm.

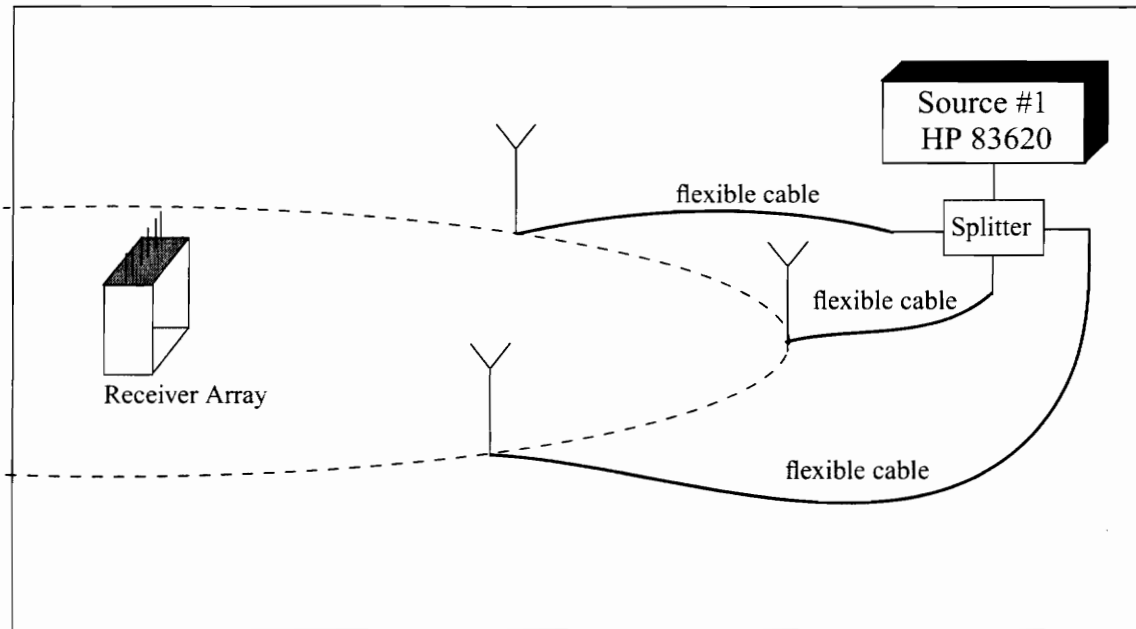


Figure 6.10: Illustration of a the DOA measurement setup with three correlated (fully coherent) signals being transmitted at different angles with respect to the receiver array location.

Figures 6.11 to 6.15 show plots of the RMS error in DOA estimation as a function of angle of separation for various angles of arrival. It is seen that the performance of the TLS-ESPRIT and the integrated ILSP-CMA with TLS-ESPRIT is more or less the same. For the case of two coherent signals being transmitted, both the algorithms estimate the angle of arrivals within an RMS error of 5 degrees for most cases (see Figures 6.11, 6.12, and 6.14). When the angle of separation between the coherent signals is only five degrees, the rms error is greater than 5 degrees. For the case of three coherent signals being transmitted, both the algorithms produce large errors except when the signals are separated by more than 30 degrees (see Figures 6.13 and 6.15). Section 6.3 provides a detailed analysis of the errors in DOA measurement.

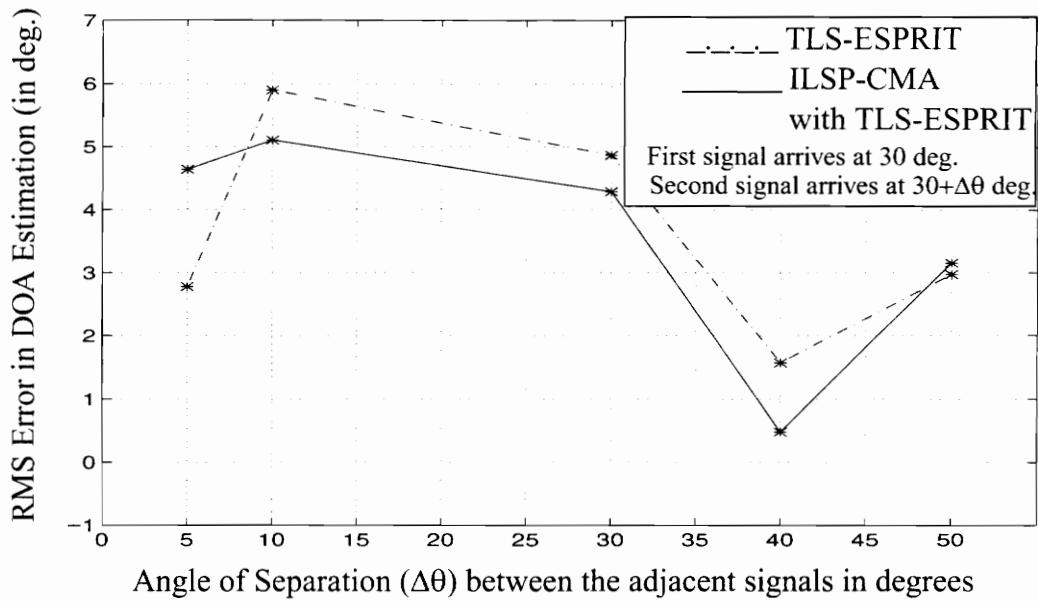


Figure 6.11: DOA Measurement Results - RMS Error in DOA estimation as a function of angle of separation between the two fully correlated (coherent) signals. The first signal arrives at 30 degrees and the second signal arrives at $30+\Delta\theta$ degrees.

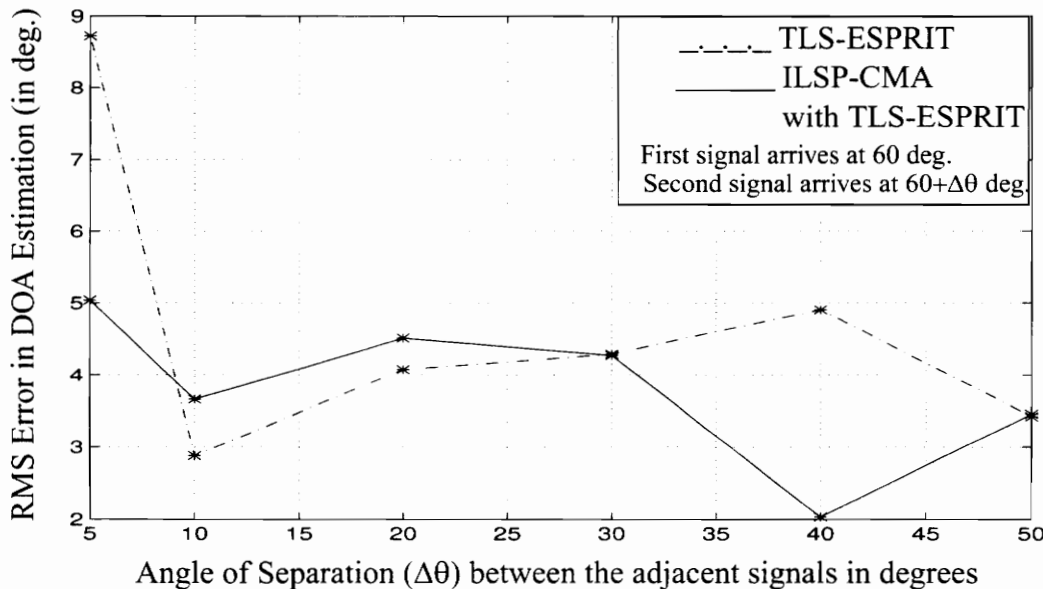


Figure 6.12: DOA Measurement Results - RMS Error in DOA estimation as a function of angle of separation between the two fully correlated (coherent) signals. The first signal arrives at 60 degrees and the second signal arrives at $60+\Delta\theta$ degrees.

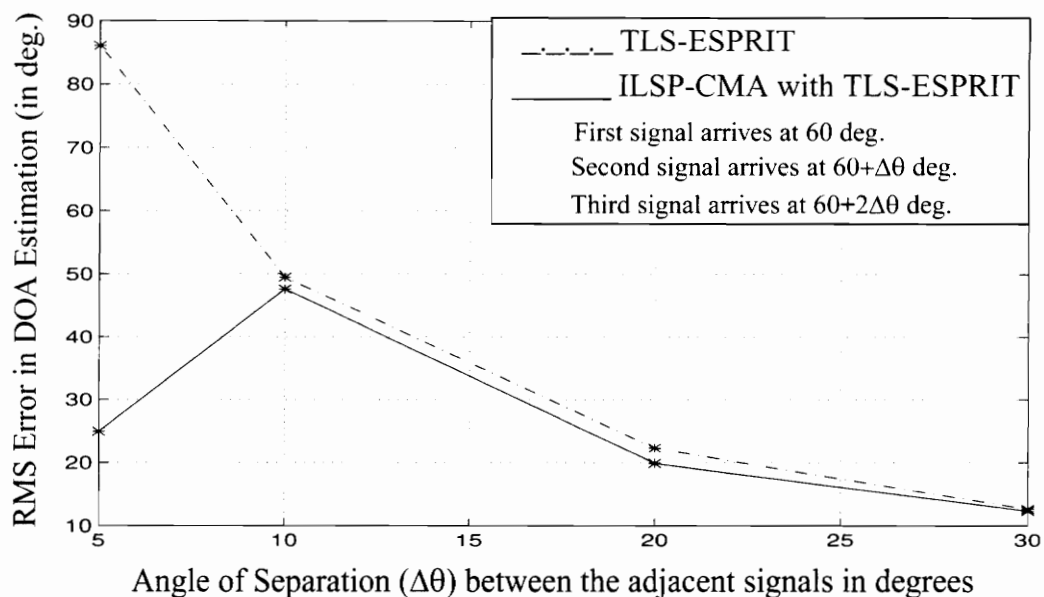


Figure 6.13: DOA Measurement Results - RMS Error in DOA estimation as a function of angle of separation between the two fully correlated (coherent) signals. The first signal arrives at 60 degrees, the second signal arrives at $60+\Delta\theta$ degrees, and the third signal arrives at $60+2\Delta\theta$ degrees.

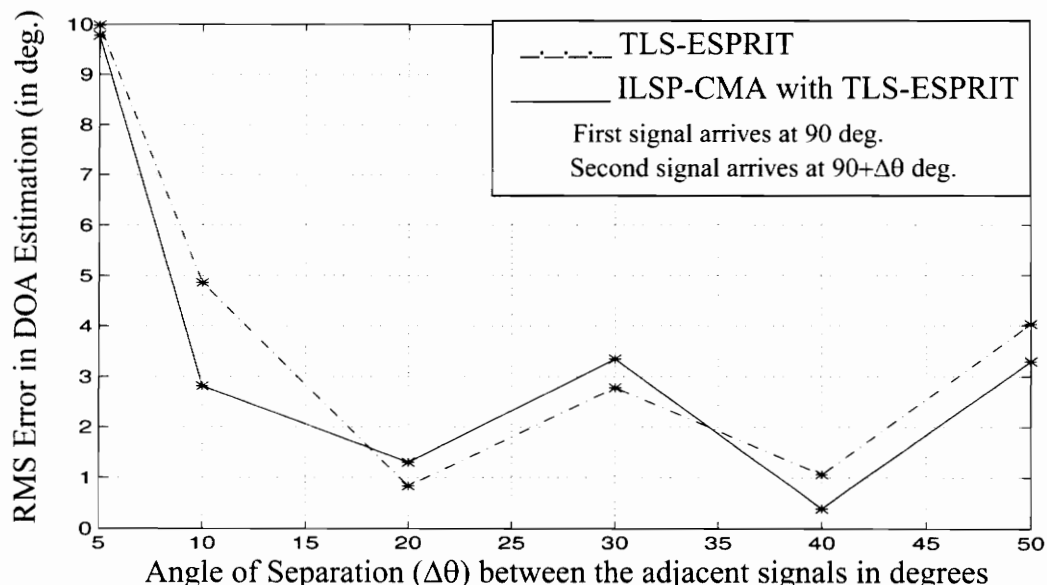


Figure 6.14: DOA Measurement Results - RMS Error in DOA estimation as a function of angle of separation between the two fully correlated (coherent) signals. The first signal arrives at 90 degrees and the second signal arrives at $90+\Delta\theta$ degrees.

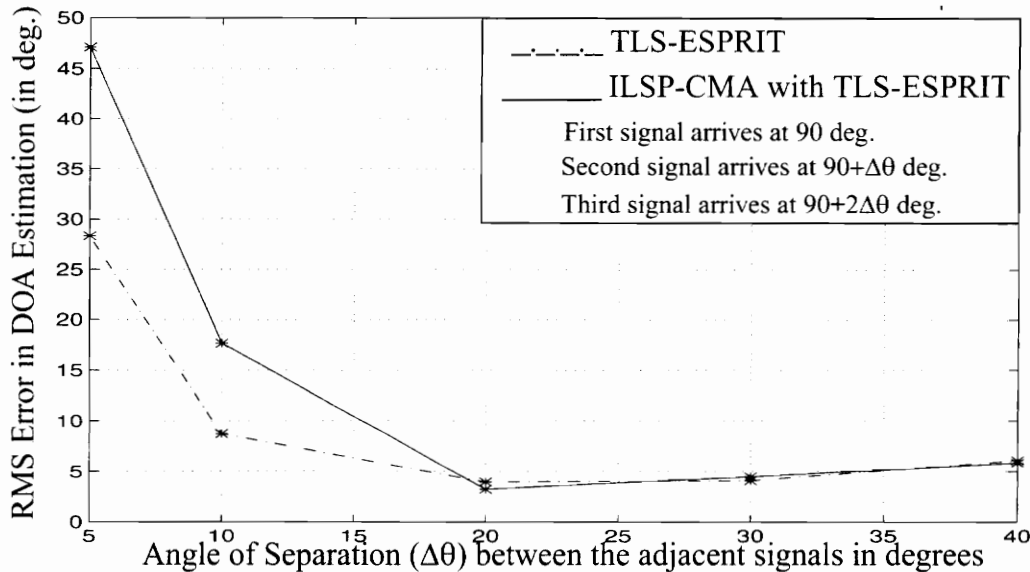


Figure 6.15: DOA Measurement Results - RMS Error in DOA estimation as a function of angle of separation between the two fully correlated (coherent) signals. The first signal arrives at 90 degrees, the second signal arrives at $90+\Delta\theta$ degrees, and the third signal arrives at $90+2\Delta\theta$ degrees.

6.3 Sources of Error in DOA Estimation

The DOA measurement results presented in section 6.2 show that both the TLS-ESPRIT and the integrated ILSP-CMA with TLS-ESPRIT algorithm were able to estimate the directions-of-arrival in most cases within an accuracy of ± 5 degrees. For the case of coherent signals, the algorithm produced large errors when more than two transmitter antennas were used. It was also found that the TLS-ESPRIT algorithm performed worse than the integrated approach in the case of multiple uncorrelated signals. This was true, especially when the signals arrived close to the endfire angles. For coherent signals, the performance of both the algorithms was more or less equal.

As seen from the simulation results presented in Chapter 4, under ideal conditions, the TLS-ESPRIT algorithm and the integrated ILSP-CMA with TLS-ESPRIT algorithm

should perform significantly better than it did in the DOA experiments. The poorer performance of these DOA estimation algorithms may be attributed to several causes. First, the ESPRIT approach requires that the array be comprised of two identical overlapping subarrays. Therefore, if the two subarrays are not identical due to physical perturbations of the array geometry, the performance of the algorithm can be significantly degraded [Sch93]. Second, any phase difference induced in the RF chains of the six channels can cause errors in the DOA estimate. Though the phase differences between the individual RF chains are compensated for through the RF chain calibration procedure (see Section 5.4), phase variations with time due to component drift can degrade the performance of the system. Third, multipath that already exists in the measurement area may overload the array, and lead to the failure of the DOA estimation algorithms. That is, for every transmitter antenna positioned at a known angle, multipath reflections in the channel would produce multiple rays that will arrive at the array at unknown angles, and this would cause errors in the estimate of the direction-of-arrival of the known signal. Further, mutual coupling between the array elements may also cause errors.

Simulations were conducted to investigate the effect of these error sources on the DOA estimation algorithms for all the signal scenarios under which the measurements were conducted. The goal was to understand the reasons for the failure of the algorithms under those situations where large errors were produced. Separate simulations were run to study the effect of (1) perturbation in antenna element locations (2) RF phase calibration errors and (3) multipath existing in the channel.

Simulation of Perturbation in Antenna Element Locations: Ideally, the antenna elements are each supposed to be spaced a half wavelength apart. Therefore, if the first element location is taken as the origin of the coordinate axis, and the array is aligned along a straight line, the individual element locations may be expressed in vector form as $\frac{\lambda}{2} [0 \ 1 \ 2 \ 3 \ 4 \ 5]^T$. In order to study the effect of perturbation of element locations, simulations were ran using a randomly perturbed location vector,

$$\frac{\lambda}{2} \begin{bmatrix} 0 \\ 1 + 0.002(\text{rand} - 0.5) \\ 2 + 0.024(\text{rand} - 0.5) \\ 3 + 0.054(\text{rand} - 0.5) \\ 4 + 0.008(\text{rand} - 0.5) \\ 5 + 0.065(\text{rand} - 0.5) \end{bmatrix} \quad (6.3)$$

instead of the ideal location vector (“rand” is a uniform random number between 0 and 1, and hence rand-0.5 is a uniform random number between -0.5 and 0.5). Notice that the random perturbations on individual elements are weighted by different coefficients. These weighting coefficients are proportional to the actual perturbation on the array element locations, so that the simulations would duplicate as closely as possible, the actual perturbations present in the array. For example, in the actual array, it was found that the fourth and sixth element were displaced the most from their ideal location, whereas the second and fifth were the least perturbed. Hence the fourth and sixth element in (6.3) have larger coefficients than the second and fifth element. After incorporating these perturbations into the simulation, the DOA estimation algorithms were tested to determine the error in DOA estimation for each of the different scenarios at which the actual measurements were made. Section 6.4 presents the results obtained through 100 Monte Carlo runs of these simulations.

Simulation of RF Chain Phase Calibration Errors: Though the phase difference between the six RF channels in the DOA measurement system may be measured and compensated for, it was found that the phase difference varies with time. The time varying phase difference between the RF channels, and the errors in the measurement of the phase difference may lead to performance degradation of the DOA measurement system. Phase differences between the RF channels were measured several times over a period of four hours to observe the amount of phase drift in each channel. Phase difference measurements were made using the RF chain phase calibration procedure detailed in Section 5.4. To simulate the random phase variations in the RF chain, the complex baseband array input data vector X was multiplied by a random phase shift vector

$\exp(j\Phi_{rand})$, where

$$\Phi_{rand} = \begin{bmatrix} 0 \\ 0.0497(rand - 0.5) \\ 0.0279(rand - 0.5) \\ 0.0458(rand - 0.5) \\ 0.0835(rand - 0.5) \\ 0.0590(rand - 0.5) \end{bmatrix} \quad (6.4)$$

The coefficients in (6.4) were chosen as the difference between the minimum and maximum phase value obtained during the four hour observation period. Since the phase drifts observed in the six RF channels were different from one another, the coefficients in (6.4) are not all equal. Notice that some RF channels have larger phase drifts than the others. Therefore, using the random phase drift given by (6.4), the simulations can duplicate the actual phase drift observed in the measurement system. After incorporating these perturbations into the simulations, the DOA estimation algorithms were tested to determine the error in DOA estimation for each of the different scenarios at which the actual measurements were made. Section 6.4 presents the results obtained through 100 Monte Carlo runs of these simulations.

Simulation of Multipath due to Reflections in Channel: When a transmitter antenna is placed at a known angle with respect to the receiver array, apart from the line of sight ray, reflected rays from the surrounding buildings will also be incident on the array. The presence of these reflected rays can cause errors in the estimation of the direction of the desired line-of-sight component. The errors caused by the existence of these multiple rays will depend on the number of multipath rays, their angles-of-arrival, and relative power levels.

In order to investigate if the multipath that exists at the DOA measurement site was a cause for the large errors seen in some of the DOA measurements, we made a study of the multipath structure of the measurement site. The multipath structure of the measurement

site was characterized through power delay profile measurements and ray tracing.

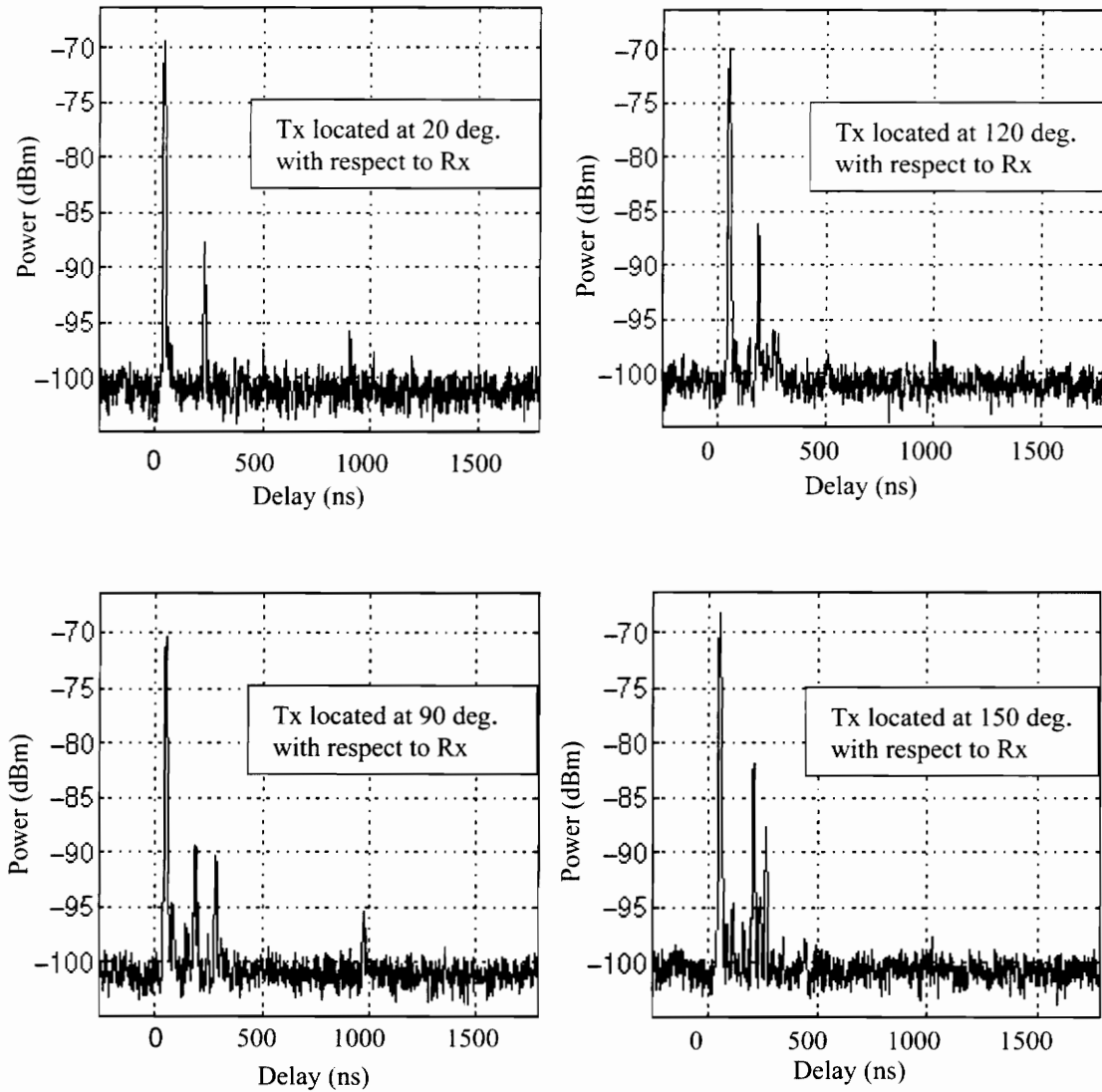


Figure 6.16: Figure showing sample power delay profiles corresponding to four transmitter locations. The first profile was measured when the transmitter was located at 20 degrees with respect to the receiver, and the subsequent ones were measured when it was located at 120, 90, and 150 degrees respectively.

Power delay profile measurements using the MPRG channel sounder [New96] were conducted at the measurement site to check for the existence of multipath components. The channel sounder receiver was positioned at the same point at which the antenna array receiver was placed for DOA measurements. The channel sounder transmitter was kept at different angles with respect to the receiver, and power delay profiles were measured at every 10 degrees. It was found that for each of the transmitter locations, there were at least one multipath component, arriving with a delay of approximately 200 ns, which was about 10 to 20 dB below the line-of-sight component. For many locations, there were additional multipaths too. Figure 6.16 shows the measured power delay profiles for some of the transmitter antenna locations.

As described above, the power delay profile measurements show that multipath does exist at the measurement site. In order to study the effect of these multipath rays on DOA estimation algorithms, we also need to know the angle of arrival of each of these multipath rays. We used ray tracing to determine the angle of arrival of the multipath rays. To facilitate ray tracing, the measurement site was modeled using MPRG's site specific propagation prediction software [Kau95]. The dimensions of the four buildings around the measurement area were measured, and the buildings were modeled as four rectangular concrete boxes. The terrain was assumed to be flat.

For each transmitter antenna location, the number of multipath reflected rays incident on the array, their angles of arrival and the relative power levels were determined using ray tracing techniques. It was found that for each of the transmitter antenna locations at which measurements were made, apart from the line of sight (LOS) ray and a ground reflected ray, there were at least three other significant (about 15 to 20 dB below the line-of-sight ray) multipath rays, arriving at the receiver. For example, Figure 6.17 shows that when a single transmitter antenna is placed at an angle of 20 degrees with respect to the receiver array axis, there is an LOS ray, a ground reflected ray, and three single bounce multipath rays at 76.9, 177 and -77 degrees arriving at the receiver array. It was also predicted that

there are many more multipath components due to multiple bounces, but all of them were at least 30 dB below the LOS component.

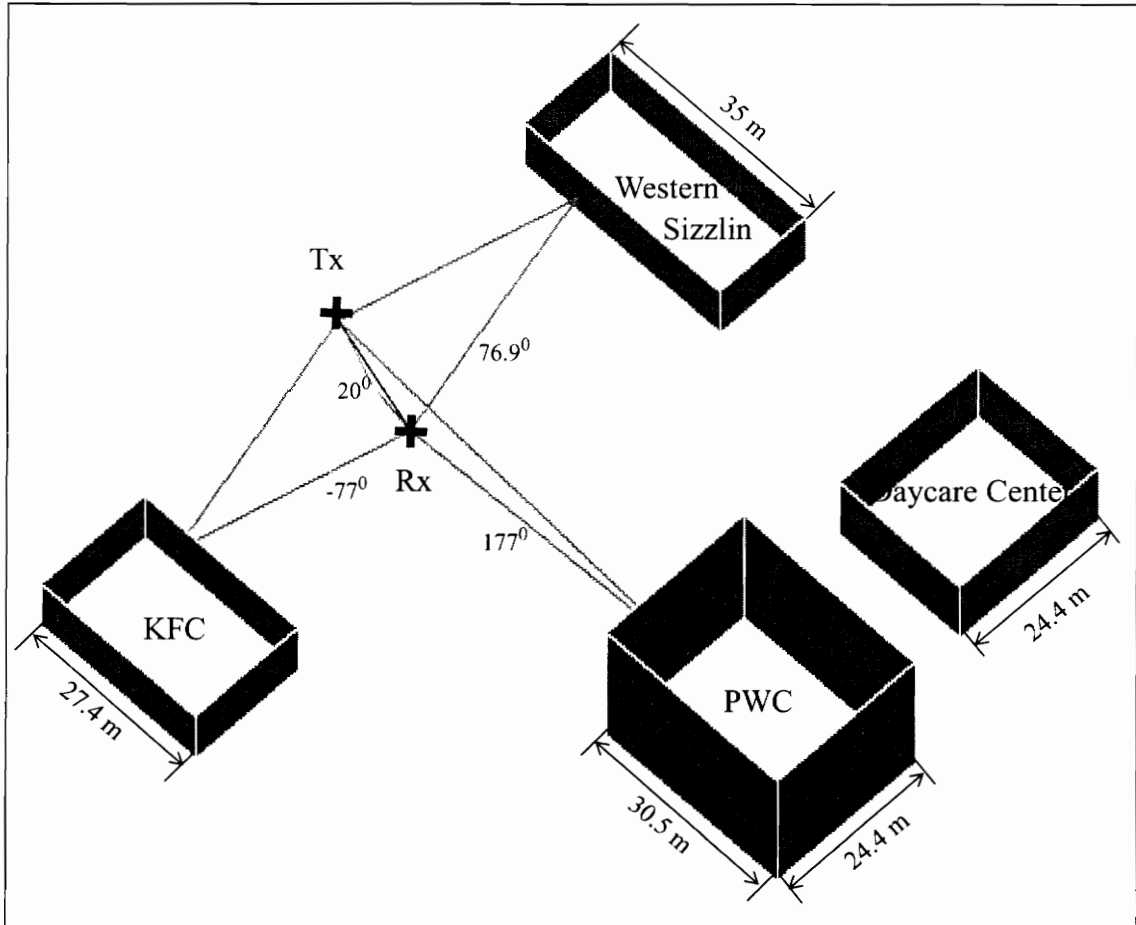


Figure 6.17: Figure showing the single bounce multipath rays incident on the array when a single transmitter antenna is located at 20 degrees with respect to the receiver array axis. Using ray tracing it was found that for all transmitter locations, there were at least three multipath components that were about 15 to 20 dB below the line-of-sight component.

Through ray tracing and power delay profile measurements, it is seen that multipath does exist at the DOA measurement site. Simulations were conducted incorporating three additional multipath components for each LOS ray that is incident on the array (the number of LOS rays is equal to the number of transmitter antennas used). Each of these

components were set up to have a power level 15 dB below the LOS component and angles of arrival as predicted by the ray tracing software. After incorporating these multipath rays into the simulation, the DOA estimation algorithms were tested to determine the error in DOA estimation for each of the different scenarios at which the actual measurements were made. Section 6.4 presents the results of the simulations.

6.4 Results of the Simulation Based Study

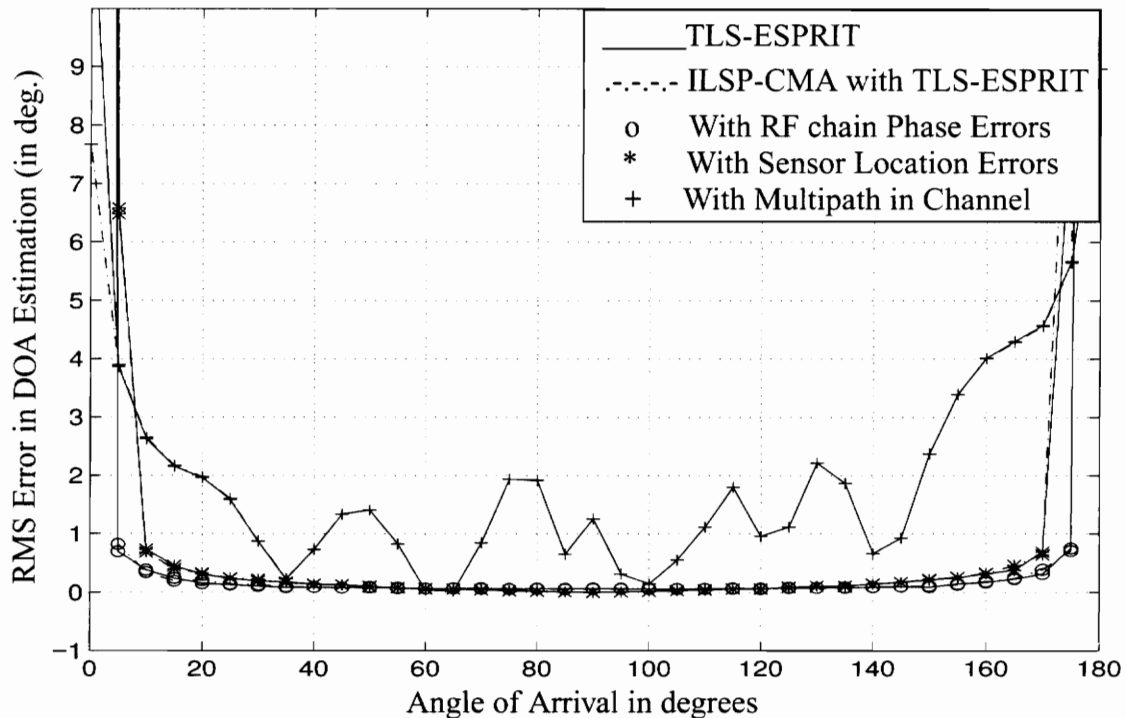


Figure 6.18: Simulation Results - Figure illustrates the RMS error in estimating the DOA of a single source under RF chain phase errors, sensor location errors, and multipath in channel. (The plots were generated by Programs [79][81][83][85][87][89][90])

In Section 6.2, we presented the results of the DOA measurements that were conducted. This section presents the results of simulations that recreated the measurement scenarios incorporating the possible sources of error. Separate simulations were run for each of the three possible sources of error, and DOA estimation error due to each of the three possible

sources of error are presented separately. Figures 6.18 to 6.30 present simulation results corresponding to each of the measurement results presented in Section 6.2 (Figures 6.1, 6.3 through 6.9, 6.11 through 6.15).

Figure 6.18 shows the RMS error in DOA estimation for the case of a single transmitting antenna. It is clearly seen that perturbation in antenna element location, RF chain phase drift, as well as the existence of multiple reflected rays produce large errors at the end-fire angles (0 and 180 deg.). It is also seen that RF chain phase drift and perturbation in antenna element location does not cause any significant errors in the estimated DOA at angles other than the endfire angles. The existing multipath in the channel is the most prominent source of error.

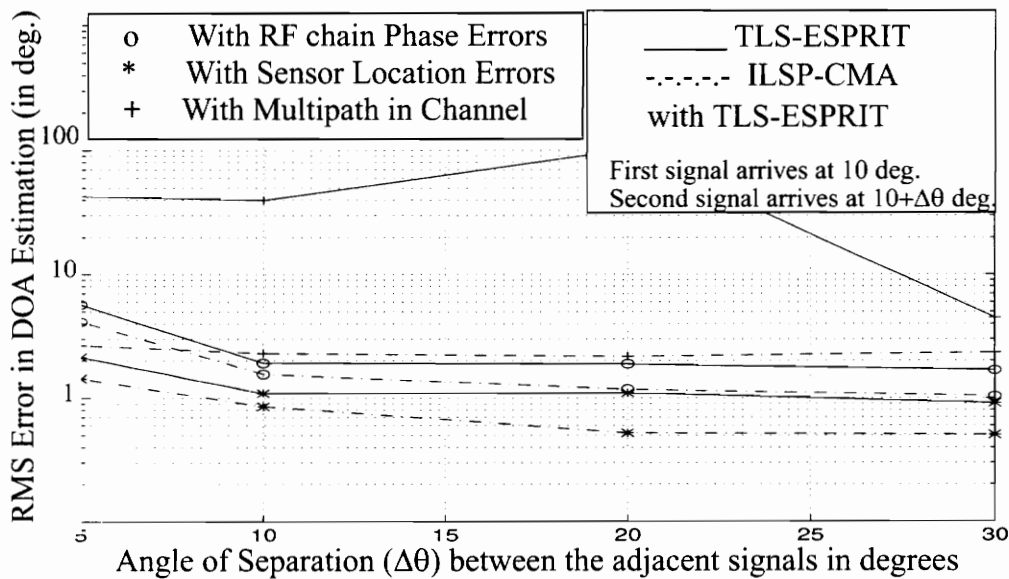


Figure 6.19: Simulation Results - Figure illustrates the RMS error in estimating the DOA of two uncorrelated signals arriving at 10 and $10+\Delta\theta$ degrees respectively, under RF chain phase errors, sensor location errors, and multipath in channel. (The plots were generated by Programs [78][80][82][84][86][88][90])

Figures 6.19 through 6.25 shows the results for the case of two or three transmitting antennas fed from uncorrelated sources, and located at different angles and angular

separations. The results show that the dominant source of error is the multipath existing in the channel. It is seen that the TLS-ESPRIT algorithm produces much larger errors than the integrated ILSP-CMA with TLS-ESPRIT algorithm. While the integrated approach is able to estimate the DOA within ± 5 degrees, the TLS-ESPRIT algorithm fails completely for many cases. This is also true with the actual measurement results shown in Figures 6.3 through 6.9. Therefore, for the DOA measurements using uncorrelated signals, we can conclude that the errors observed with the TLS-ESPRIT algorithm was due to the existence of multipath in the channel.

The performance advantage obtained through the integrated approach may be explained as follows. Since the integrated approach is signal selective, it is able to separate the two uncorrelated signals and determine the directions of arrival of each signal separately. While the TLS-ESPRIT algorithm determines the DOA of both the signals by performing eigen decomposition on a single covariance matrix (i.e. the input covariance matrix), the integrated approach forms two separate covariance matrices (i.e two spatial signature covariance matrices) for each of the signals. Therefore, for example when there are two antennas transmitting uncorrelated signals, and each signal giving raise to three reflected rays and a line-of-sight ray, there are a total of 8 rays incident on the array. These 8 rays overload the 6 element array and hence produces large errors. On the other hand the integrated approach first separates the two uncorrelated signals, and hence has to handle only 4 rays at a time. This does not lead to overloading problems and hence the integrated approach is able to estimate the DOA's more accurately. In other word, the integrated approach is able to perform better than the conventional TLS-ESPRIT since it operates on a more restricted signal subspace.

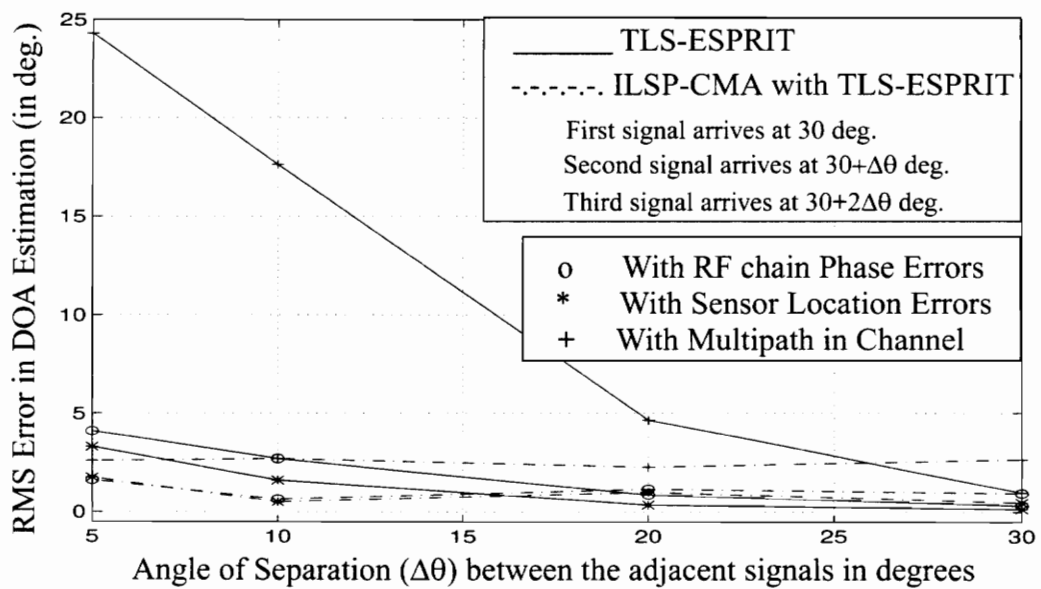
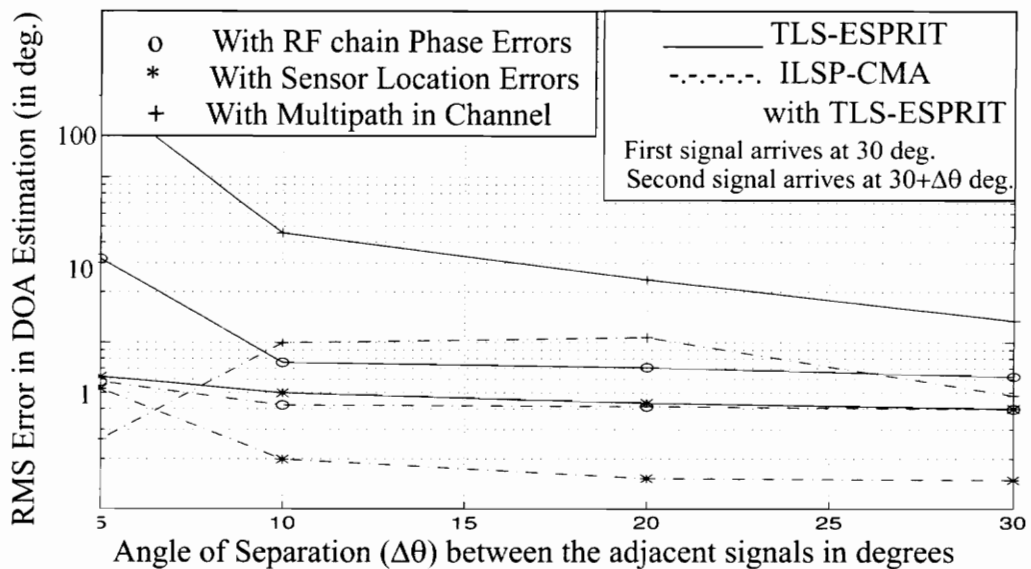


Figure 6.21: Simulation Results - Figure illustrates the RMS error in estimating the DOA of three uncorrelated signals arriving at 30, $30+\Delta\theta$, and $30+2\Delta\theta$ degrees respectively, under RF chain phase errors, sensor location errors, and multipath in channel.

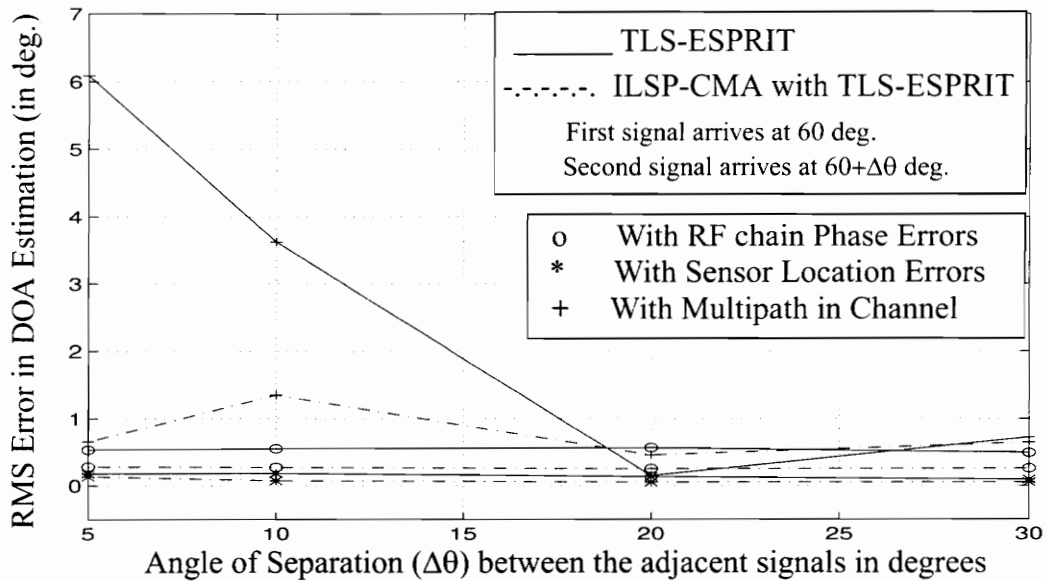


Figure 6.22: Simulation Results - Figure illustrates the RMS error in estimating the DOA of two uncorrelated signals arriving at 60 and $60+\Delta\theta$ degrees respectively, under RF chain phase errors, sensor location errors, and multipath in channel.

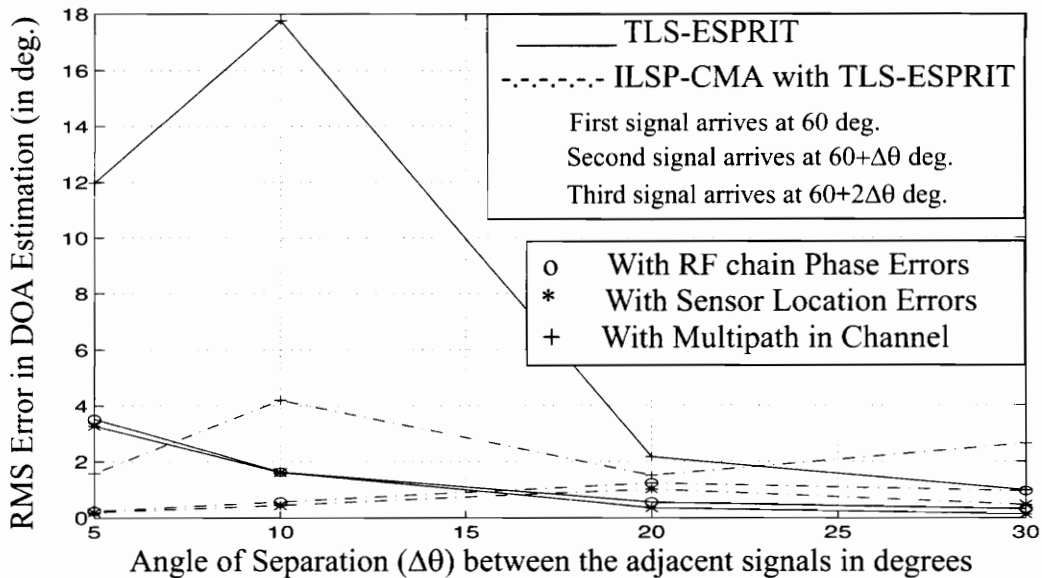


Figure 6.23: Simulation Results - Figure illustrates the RMS error in estimating the DOA of three uncorrelated signals arriving at 60, $60+\Delta\theta$, and $60+2\Delta\theta$ degrees respectively, under RF chain phase errors, sensor location errors, and multipath in channel.

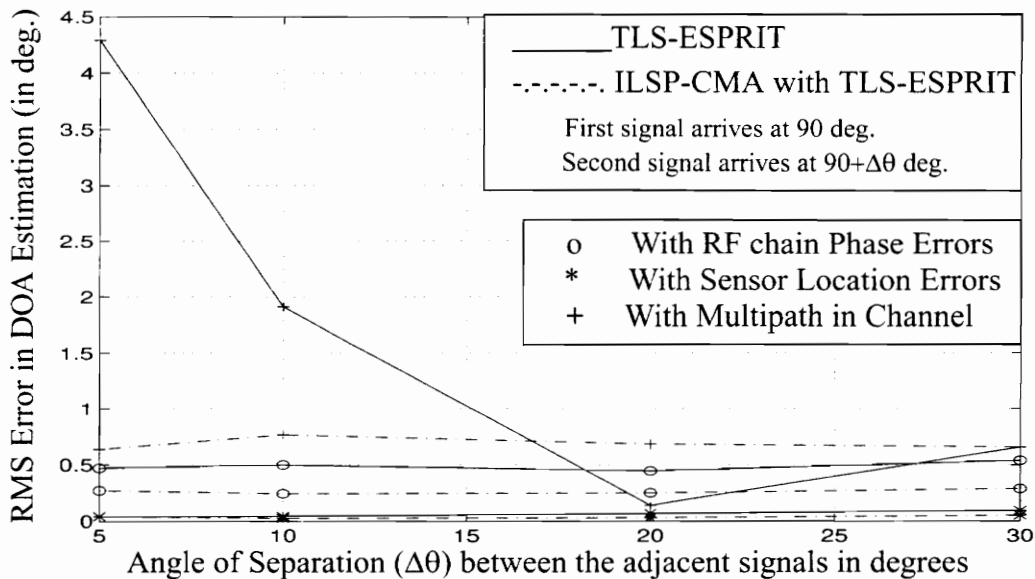


Figure 6.24: Simulation Results - Figure illustrates the RMS error in estimating the DOA of two uncorrelated signals arriving at 90 and $90+\Delta\theta$ degrees respectively, under RF chain phase errors, sensor location errors, and multipath in channel.

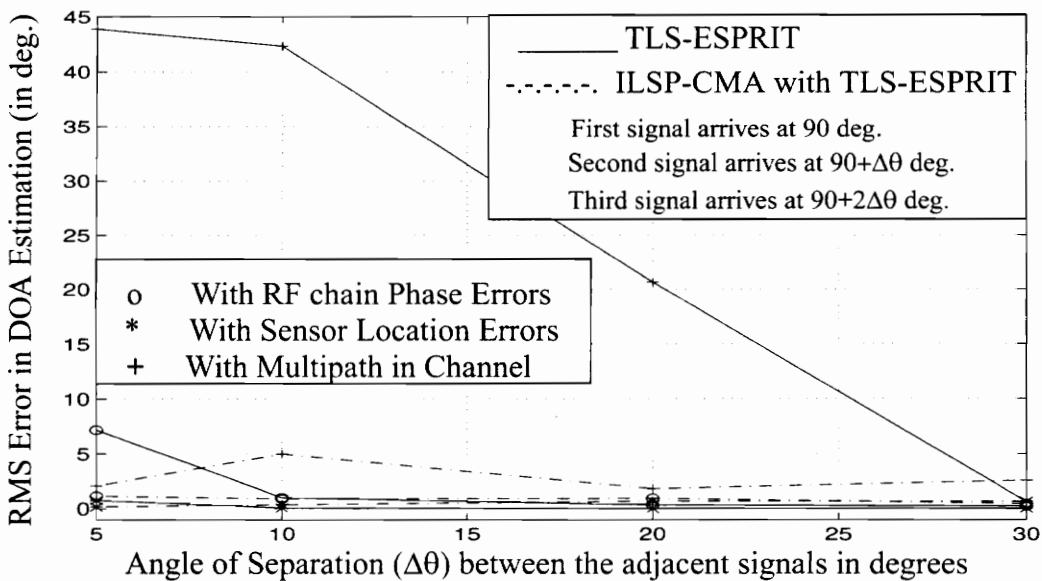


Figure 6.25: Simulation Results - Figure illustrates the RMS error in estimating the DOA of three uncorrelated signals arriving at 90, $90+\Delta\theta$, and $90+2\Delta\theta$ degrees respectively, under RF chain phase errors, sensor location errors, and multipath in channel.

Figures 6.26 through 6.30 show the simulation results for the case of two or three transmitter antennas fed from the same source (correlated signals). Here again, it is seen that the most prominent source of error is the existing multipath in the channel. It is also seen that the RF chain phase drift and perturbations in antenna element location lead to larger errors in DOA estimation when the incident signals are coherent than when the incident signals are uncorrelated. It is also seen that the performance of both the TLS-ESPRIT and the integrated ILSP-CMA with TLS-ESPRIT algorithms are more or less the same. This is due to the fact, that since the incident signals are coherent (same source), they cannot be separated. Therefore, both the algorithms will have to estimate the DOA's by performing eigen decomposition on a single matrix. Since there is only one source, there is only a single spatial signature. The performance of both the algorithms as seen through actual measurement is in agreement with the results of the simulation.

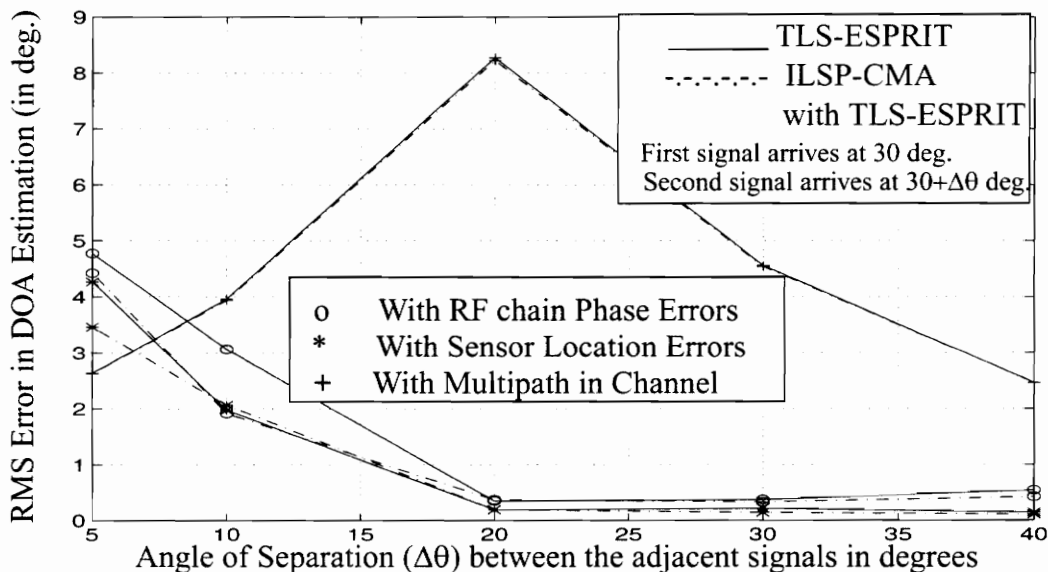


Figure 6.26: Simulation Results - Figure illustrates the RMS error in estimating the DOA of two coherent signals arriving at 30 and $30+\Delta\theta$ degrees respectively, under RF chain phase errors, sensor location errors, and multipath in channel. (The plots were generated by Programs [79][81][83][85][87][89][90])

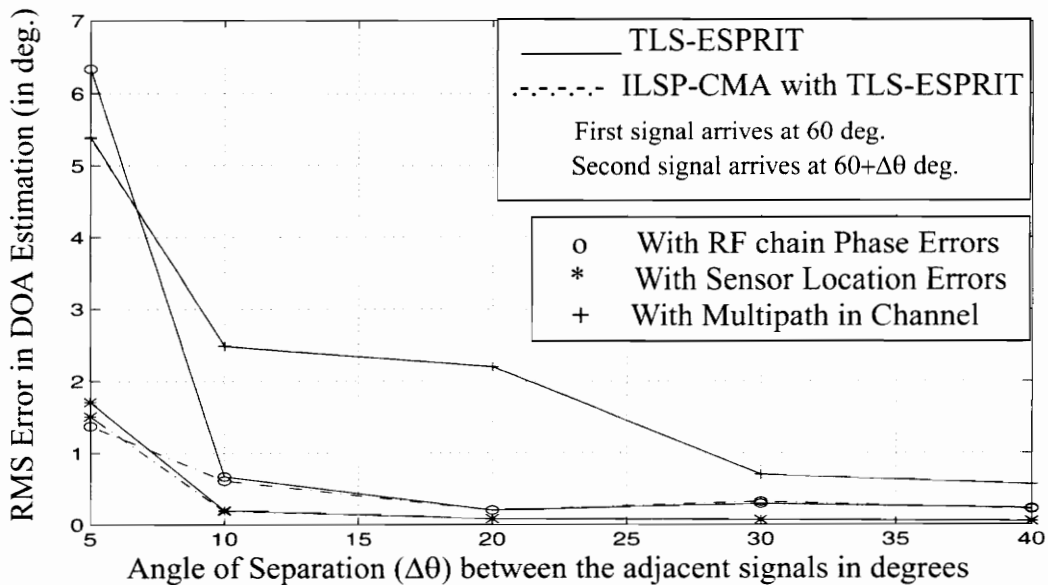


Figure 6.27: Simulation Results - Figure illustrates the RMS error in estimating the DOA of two coherent signals arriving at 60 and $60+\Delta\theta$ degrees respectively, under RF chain phase errors, sensor location errors, and multipath in channel.

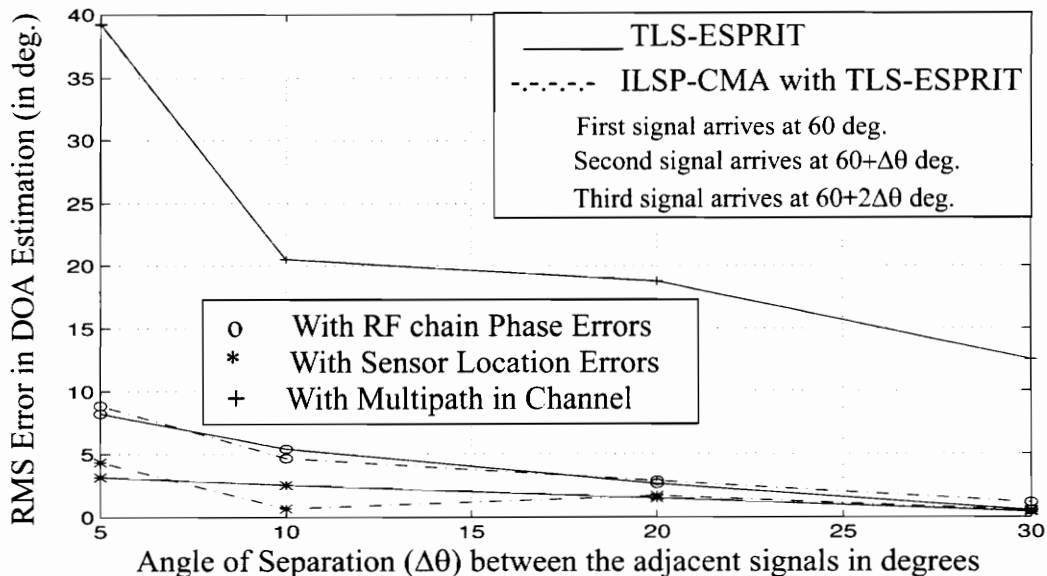


Figure 6.28: Simulation Results - Figure illustrates the RMS error in estimating the DOA of three coherent signals arriving at 60, $60+\Delta\theta$, and $60+2\Delta\theta$ degrees respectively, under RF chain phase errors, sensor location errors, and multipath in channel.

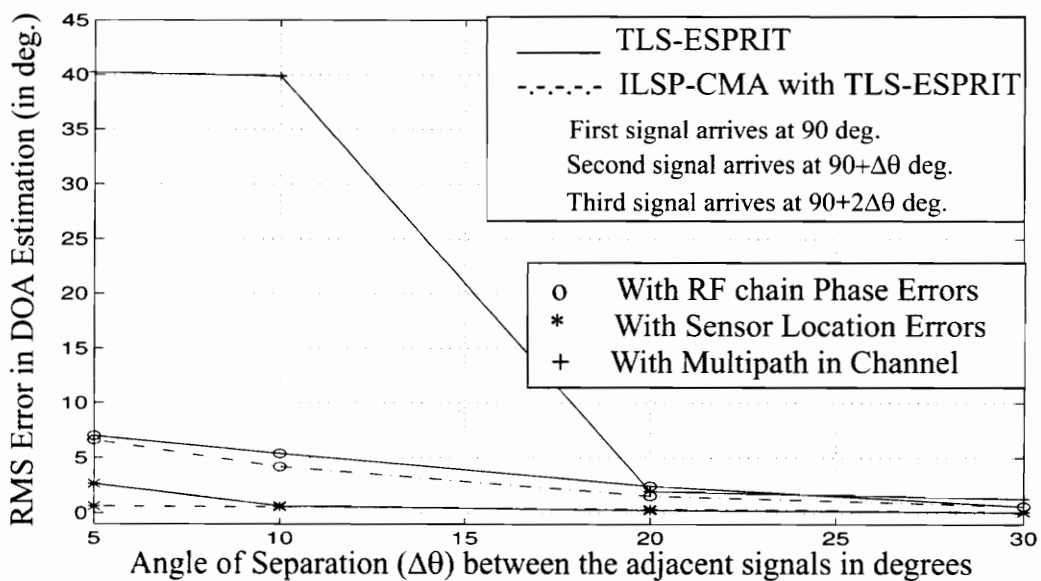
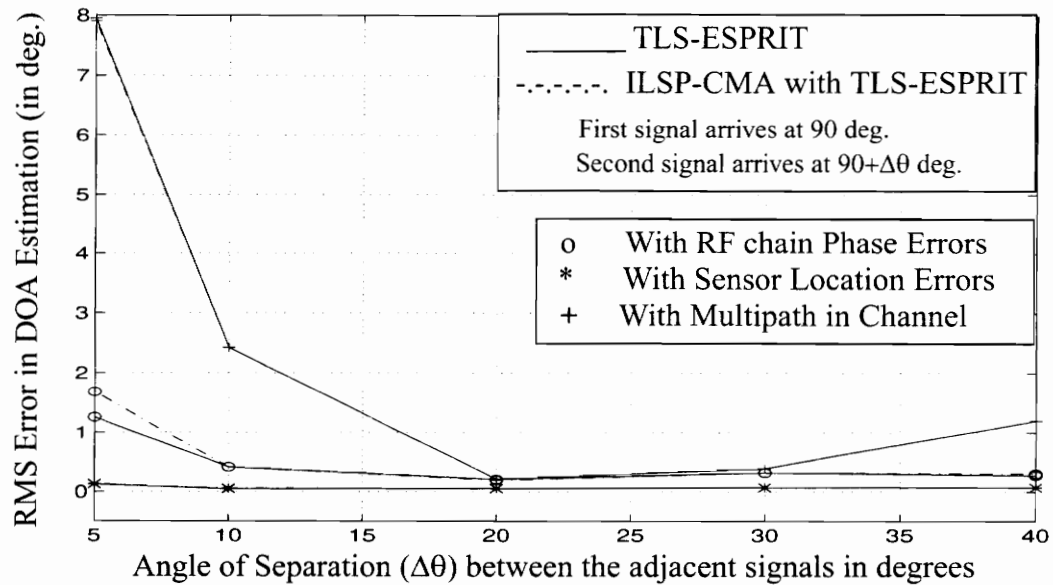


Figure 6.30: Simulation Results - Figure illustrates the RMS error in estimating the DOA of three coherent signals arriving at 90, $90+\Delta\theta$, and $90+2\Delta\theta$ degrees respectively, under RF chain phase errors, sensor location errors, and multipath in channel.

6.5 Conclusion

In this chapter, we described the DOA measurement experiments conducted to evaluate the performance of the DOA measurement system. The results of the measurements were also presented. For most cases, the estimated direction of arrival was within ± 5 degrees of the actual DOA. For the case of uncorrelated signals, it was found that the integrated approach performed significantly better than the conventional TLS-ESPRIT approach. The measurement results indicated that both the algorithms produced large errors when there were three transmitters fed from a single source (coherent signals). We also presented a detailed analysis of the errors in DOA estimation. It was found through simulations, that the excess multipath that existed at the measurement site was the leading cause for the failure of the DOA estimation algorithms when there were three or more transmitting antennas fed from a single source. Multipath in the channel was also the cause for the poor performance of TLS-ESPRIT under uncorrelated signal conditions.

Chapter 7

Conclusion and Future Work

7.1 Conclusion

In this thesis, we developed a direction-of-arrival measurement system using a six element uniformly spaced linear antenna array testbed operating at 2050 MHz. In the first phase of this project, an extensive simulation based comparison of various high resolution direction-of-arrival algorithms was made. A MATLAB testbed was created to test the performance of the DOA algorithms under different conditions. The algorithms studied are the subspace-based algorithms such as MUSIC and ESPRIT and the integrated algorithm which combines ILSP-CMA with subspace-based techniques. All the performance comparison were made for the case of a six element uniformly spaced linear array.

Simulation results demonstrated the superiority of the integrated approach over the conventional subspace approach. In Section 4.3, we showed that the integrated approach which combines ILSP-CMA with TLS-ESPRIT performs significantly better than the conventional approach especially when multiple signals are incident at closely spaced angles, low signal-to-noise ratio, and when a small number of data samples are used to

estimate the direction of arrival. It is also seen that the integrated approach is more robust to imperfections in building the array (see Figures 4.17 and 4.18).

Field experiments were conducted to verify the performance of the DOA estimation algorithms. It was shown that integrated ILSP-CMA with TLS-ESPRIT algorithm was able to estimate the directions-of -arrival in most cases within an accuracy of ± 5 degrees. For the case of coherent signals, the algorithms produced large errors when more than two transmitter antennas were used. In Section 6.2.2, it was also found that the TLS-ESPRIT algorithm performed significantly poorer than the integrated approach in the case of multiple uncorrelated signals. A detailed simulation-based study was made to investigate the reasons for the large errors in DOA estimation that was found in certain cases. Simulation results presented in Section 6.4 showed that the existence of coherent multipath in the channel (verified by power delay profile measurements and ray tracing) overloaded the array under many conditions and lead to the failure of the algorithms.

In order to prevent the failure of DOA estimation algorithms due to overloading, we need to know the maximum number of possible signals/components, and design the array with sufficient number of elements. This will ensure that the array can handle all the rays without getting overloaded. We could also design the array using directional elements so that the array has a more restricted field of view.

7.2 Suggestions For Future Work

Currently, the direction-of-arrival measurement system is not capable of doing real-time measurements. The DSP-96 boards are used only to sample and collect data, and the processing is done off-line on the host PC or the Sun Workstations. To make the system completely real-time, the DOA estimation algorithms may be coded directly on the DSP.

The quarter wave monopoles used to form the linear array may be replaced by microstrip

patch antennas which offer several advantages. Microstrip antennas are lightweight, low profile, easy to fabricate and can be made conformal [Bah80][Jam81][Jam89][Siw95].

The DOA measurement system may be used to do real world measurements which can be useful in understanding the multipath channel in terms of the angle spread. Such characterization is useful in the study of systems employing some form of spatial diversity. The measurement system may be used to verify channel models that incorporate angle of arrival statistics.

The DOA measurement system along with the ray tracing software may be used to develop a position location system. If the direction of arrival of multiple components of a signal at the receiver array are known, it is possible to trace back the rays to determine the location of the source as the point of intersection of the multiple rays.

Appendix 1

List of Abbreviations

AOA	Angle of Arrival
CMA	Constant Modulus Algorithm
DOA	Direction of Arrival
DF	Direction Finding
ESPRIT	Estimation of Signal Parameters via Rotational Invariance
ILSP-CMA	Iterative Least Squares Projection Based CMA
LS-ESPRIT	Least Squares ESPRIT
LMS	Least Mean Square algorithm
ML	Maximum Likelihood
MUSIC	MUltiple SIgnal Classification
RMSE	Root Mean Square Error
SCORE	Spectral COherence REstoral algorithm
TLS-ESPRIT	Total Least Squares ESPRIT
ULA	Uniformly spaced Linear Array

References

- [Age86A] Agee, B.G., "Fast Adaptive Polarization Control Using the Least Squares Constant Modulus Algorithm," *Proceedings of the Twentieth Asilomar Conference on Signals, Systems, and Computers*, pp. 590-595, 1986.
- [Age86B] Agee, B.G., "The Least-Squares CMA: A New Technique for Rapid Correction of Constant Modulus Signals," *Proceedings of the ICASSP-86*, pp. 953-956, 1986.
- [Age88] Agee, B.G., "Convergent Behavior of Modulus-Restoring Adaptive Arrays in Gaussian Interference Environments," *Proceedings of the Twenty-Second Asilomar Conference on Signals, Systems and Computers*, pp. 818-822, 1988.
- [Age89a] Agee, B.G., "Blind Separation and Capture of Communication Signals Using a Multitarget Constant Modulus Beamformer," *Proceedings of the IEEE MILCOM*, pp. 340-346, 1989.
- [Age89b] Agee, B.G., "The Property Restoral Approach to Blind Adaptive Signal Extraction," *Ph.D dissertation*, U.C. Davis, 1989.
- [Aka73] Akaike, H., "Information Theory and an Extension of the Maximum Likelihood Principle," *Proceedings of the 2nd International Symposium on Information Theory*, B.N. Petrov and F. Caski, Eds. pp. 267-281, 1973.
- [And63] Anderson, T.W., "Asymptotic Theory for Principal Component Analysis," *Annals of Mathematical Statistics*, vol. 34, pp. 122-148, 1963.
- [Are93] Ariel Corp. *User's Manual for the DSP-96 DSP96002 Floating Point Attached Processor Board with Dual-Channel Analog I/O*, Ariel Corp., Highland Park, NJ, Jan 1993.
- [Bah80] Bahl, I.J., Bhartia, P., *Microstrip Antennas*, Artech House Inc., 1980

- [Bar83] Barabell, A.J., "Improving the Resolution Performance of Eigenstructure-based Direction Finding Algorithms," *Proceedings of the ICASSP-83*, pp. 336-339, 1983.
- [Bar84] Barabell, A.J., Capon, J., Delong, D.F., Johnson, J.R., Senne, K., *Performance Comparison of Superresolution Array Processing Algorithms*, Technical Report TST-72, Lincoln Laboratory, M.I.T., 1984.
- [Bie79] Bienvenu, W.J., Kopp, "Principle de la goniometrie Passive adaptive," *Proc. 7'eme Colloque GRESIT*. Nice, France, 106/1-106/10, 1979.
- [Big95] Bigler, L., Lin H.P., Jeng, S.S., Xu, G, "Experimental Direction of Arrival and Spatial Signature Measurements at 900 MHz for Smart Antenna Systems," *Proceedings of the IEEE Vehicular Technology Conference*, vol. 1, pp. 55-58, 1995.
- [Bla94] Blaschka Jr., J, "911, Wireless and the Future," *APCO Bulletin*, pp. 12-28, July 1994
- [Bor79] Borgiotti, G.V., Kaplan, L.J., "Superresolution of Uncorrelated Interference Sources by Using Adaptive Array Techniques," *IEEE Transactions on Antennas and Propagation*, vol. AP-27, pp. 842-845, 1979.
- [Bur67] Burg, J.P., "Maximum Entropy Spectral Analysis," *Proceedings of the 37th Annual Meeting of the Society of Geophysicists*, pp. 34-41, 1967.
- [Cap69] Capon, J., "High Resolution Frequency-Wavenumber Spectral Analysis," *Proceedings of the IEEE*, vol. 57, no. 8, pp. 1408-1418, August 1969.
- [Cap79] Capon, J., "Maximum Likelihood Spectral Estimation," *Nonlinear Methods of Spectral Analysis*. ed. Haykin, S., Springer, New York, pp. 155-179, 1979.
- [Col69] Collin, R.E., Zucker, F.J., *Antenna Theory- Part I*, McGraw Hill Book Company, 1969.
- [Don93] Don E. Dudgeon, *Array Signal Processing - Concepts and Techniques*, Prentice Hall, 1993.
- [Eva82] Evans, J.E., Johnson, J.R., Sun, D.F., *High Resolution Angular Spectrum Estimation Techniques for Terrain Scattering Analysis and Angle of Arrival Estimation in ATC Navigation and Surveillance System*, M.I.T. Lincoln Lab., Lexington, MA, Rep. 582, 1982.
- [Fed88] Feder, M., Weinstein, E., "Parameter Estimation of Superimposed Signals Using the EM Algorithm," *IEEE Transactions on Acoustics, Speech, and Signal Processing*, vol. 36, pp. 477-489, April 1988.
- [Gab80] Gabriel, W.F., "Spectral Analysis and Adaptive Array Superresolution

- Techniques," *Proceeding of the IEEE*, vol. 68, no. 6, pp. 654-666, June 1980.
- [Gar87A] Gardner, W.A., "Spectral Correlation of Modulated Signals. Part I: Analog Modulation," *IEEE Transactions on Communications*, vol. COM-35, pp. 584-594, 1987.
- [Gar87B] Gardner, W.A., "Spectral Correlation of Modulated Signals. Part II: Digital Modulation," *IEEE Transactions on Communications*, vol. COM-35, pp. 595-601, 1987.
- [Gar88] Gardner, W.A., "Simplification of MUSIC and ESPRIT by exploitation of cyclostationarity," *Proceedings of the IEEE*, vol. 76, pp. 845-847, July 1988.
- [Gar91] Gardner, W.A., "Exploitation of Spectral Redundancy in Cyclostationary Signals," *IEEE Signal Processing Magazine*, pp. 14-36, April 1991.
- [Gar94] Gardner, W.A., ed., *Cyclostationarity in Communications and Signal Processing*, IEEE Press, 1994
- [Gol73] Golub, G.H., Pereyra, V., "The differentiation of Pseudo-inverses and Nonlinear Least Squares Problems Whose Variables Separate," *SIAM Journal of Numerical Analysis*, vol. 10, pp. 413-432, 1973.
- [Gol89] Golub, G.H., Van Loan, C.F., *Matrix Computations*, Second Edition, John Hopkins University Press, 1989.
- [Goo86] Gooch, R.P., Lundel, J., "The CM Array: An Adaptive Beamformer for Constant Modulus Signals," *Proceedings of the ICASSP-86*, pp. 953-956, 1986.
- [Gri83] Griffiths, J.W.R., "Adaptive Array Processing: A Tutorial," *IEE Proceedings*, vol. 130, Parts F and H, no. 1, pp. 3-10, February 1983.
- [Hab86] Haber, F., Zoltowski, M., "Spatial Spectrum Estimation in a Coherent Signal Environment Using an Array in Motion," *IEEE Transactions on Antennas and Propagation*, vol. AP-34, pp. 301-310, March 1986.
- [Hay85] Haykin, S. "Radar array Processing for Angle-of-Arrival Estimation," *Array Signal Processing*, Prentice Hall, NJ, ch. 4, pp. 194-292, 1985
- [Hay91] Haykin, S., *Adaptive Filter Theory*, Printice Hall, 1991.
- [Jam81] James, J.R., Hall, P.S., Wood, C., *Microstrip Antenna - Theory and Design*, Peter Peregrinus Ltd., 1981.
- [Jam89] James, J.R., Hall, P.S., ed. *Handbook of Microstrip Antennas*, Peter Peregrinus Ltd., 1989
- [Joh86] Johnson, R.L., "Eigenvector Matrix Partition and Radio Direction Finding

- Performance," *IEEE Transactions on Antennas and Propagation*, vol. AP-34, no. 8, pp. 985-991, August 1986.
- [Kau95] Kaushik, P., Rappaport, T.S., Ahamed, M., Zhang, N., "SISP - Software Tool for Propagation Prediction," *AGARD*, Greece 1995.
- [Ken95] Kennedy, J., Sullivan M.C., "Direction Finding and "Smart Antennas" Using Software Radio Architectures," *IEEE Communications Magazine*, pp. 62-68, May 1995.
- [Kik94] Kikuma, N., Hachitori, K., Saito, F., Inagaki, N., "CMA Adaptive Array Antenna Using Transversal Filters for Spatial and Temporal Adaptability in Mobile Communications," *Proceedings of the Virginia Tech's Fourth Symposium on Wireless Personal communications*, pp. 4.1-4.10, 1994
- [Kum83] Kumaresan, R., Tufts, D.W., "Estimating the Angles of Arrival of Multiple Plane Waves," *IEEE Transactions on Aerospace and Electronic Systems*, vol. AES-19, no. 1, pp. 134-139, January 1983.
- [Lar83] Larimore, M.G., Treichler, J.R., "Convergence Behavior of the Constant Modulus Algorithm," *Proceedings of the ICASSP*, pp. 13-16, Boston, 1983.
- [Lar85] Larimore, M.G., Treichler, J.R., "Noise Capture Properties of the Constant Modulus Algorithm," *Proceedings of the ICASSP-85*, pp. 1161-1164, April 1985.
- [Li93] Li, J., Compton, R.T., "Maximum Likelihood Angle Estimation for Signals with Known Waveforms," *IEEE Transactions on Signal Processing*, vol. 41, no. 9, pp. 2850-2861, September 1993.
- [Li94] Li, J., Compton, R.T., "Angle of Arrival Estimation of Coherent Signals Using an Array Doublet in Motion," *IEEE Transactions on Aerospace and Electronic Systems*, vol. 30, no. 1, pp. 126-133, January 1994.
- [Lib95] Liberti Jr., J.C., Analysis of CDMA Cellular Radio Systems Employing Adaptive Antennas, *Ph.D Dissertation*, Virginia Tech, 1995.
- [Lib96] Liberti Jr., J.C., Rappaport, T.S., A Geometrically-Based Model for Line-Of-Sight Multipath Radio Channels," *IEEE Vehicular Technology Conference*, 1996.
- [Lun88] Lundell, J., Widrow, B., "Application of the Constant Modulus Adaptive Beamformer to Constant and Non-Constant Modulus Signals," *Proceedings of the Twenty-First Asilomar Conference on signals, Systems, and Computers*, pp. 432-436, 1988.
- [Mat89] Mathews, P., Mohebbi, B., "Direction of Arrival Measurements at UHF," *Electronic Letters*, pp. 1069-1070, 1989.

- [New96] Newhall, B., Saldanha, K.J., Rappaport, T.S., "Propagation Time Delay Spread Measurements at 915 MHz in a Large Train Yard," *IEEE Vehicular Technology Conference*, 1996.
- [Nic88] Nicolau, E., Zaharia, D., *Adaptive Arrays*, Elsevier Publications, 1989.
- [Par95] Parra, I.P., *Improved Constant Modulus Algorithm for Smart Antenna Systems*, Masters Thesis, The University of Texas at Austin, May 1995.
- [Pau86A] Paulraj, A., Roy, R., Kailath, T., "A Subspace Rotation Approach to Signal Parameter Estimation," *Proceedings of the IEEE*, vol. 74, pp. 1044-1045, July 1986.
- [Pau86B] Paulraj, A., Roy, R., Kailath, T., "Estimation of Signal Parameters via Rotational Invariance Techniques - ESPRIT," *Proceedings of 19th Asilomar Conference on Circuits and Systems*, pp. 83-89, 1985.
- [Pau93] Paulraj, A., et. al., "Subspace Methods for Direction-of-Arrival Estimation," Chapter 16, *Handbook of Statistics 10 - Signal Processing and its Applications*, ed. Bose, N.K., and Rao, C.R., pp. 693-640, 1993.
- [Pil89A] Pillai, S.U., Kwon, B.H., "Forward/Backward Spatial Smoothing Techniques for Coherent Signal Identification," *IEEE Transactions on Acoustics, Speech, and Signal Processing*, vol. 37, no. 1, pp. 8-15, January 1989.
- [Pil89B] Pillai, S.U., Kwon, B.H., "Performance Analysis of MUSIC-Type High Resolution Estimators for Direction Finding in Correlated and Coherent Scenes," *IEEE Transactions on Acoustics, Speech, and Signal Processing*, vol. 37, no. 8, pp. 1176-1189, August 1989.
- [Por88] Porat, B., Friedlander, B., "Analysis of The Asymptotic Relative Efficiency of The MUSIC ALgorithm," *IEEE Transactions on Acoustics, Speech, and Signal processing*, pp. 532-544, 1988.
- [Ott91] Otterston, B., Viberg, M., Kailath, T., "Performance analysis of the Total Least Squares ESPRIT Algorithm," *IEEE Transactions on Signal Processing*, pp. 1122-1135, 1991.
- [Rap95] Rappaport, T.S., *Wireless Communications - Principles and Practice*, Prentice Hall, 1995.
- [Ris78] Rissanen, J., "Modeling by the Shortest Data Description," *Automatica*, vol. 14, pp. 465-471, 1978.
- [Roy89] Roy, R., Kailath, T., "ESPRIT-Estimation of Signal Parameters via Rotational Invariance Techniques," *IEEE Transactions on Acoustics, Speech, and Signal Processing*, vol. 29, no. 4, pp. 984-995, July 1989.

- [Roy90] Roy, R., Kailath, T., "ESPRIT-Estimation of Signal Parameters via Rotational Invariance Techniques," *Optical Engineering*, vol. 29, no. 4, pp. 296-313, April 1990.
- [Sch79] Schmidt, R.O., "Multiple Emitter Location and Signal Parameter Estimation," *Proceedings of RADC Spectrum Estimation Workshop*, Griffiss AFB, NY, 243-258, 1979.
- [Sch86A] Schmidt, R.O., "Multiple Emitter Location and Signal Parameter Estimation," *IEEE Transactions on Antennas and Propagation*, vol. AP-34, no. 3, pp. 276-280, March 1986.
- [Sch86B] Schmidt, R.O., Franks, R.E., "Multiple Source DF Signal Processing: An Experimental System," *IEEE Transactions on Antennas and Propagation*, vol. AP-34, no. 3, pp. 281-290, March 1986.
- [Sch89] Schell, S.V., Calabretta, Gardner, W.A., Agee, B.G., "Cyclic MUSIC algorithms for signal selective DOA estimation," *Proceedings of the ICASSP-89*, pp. 2278-2281, 1989.
- [Sch93] Schell, S.V., Gardner, W.A., "High Resolution Direction Finding," Chapter 17, *Handbook of Statistics 10 - Signal Processing and Applications*, ed. Bose, N.K., and Rao, C.R., pp. 755-817, 1993.
- [Sch94] Schell, S.V., "Performance Analysis of the Cyclic MUSIC Method of Direction Estimation for Cyclostationary Signals," *IEEE Transactions on Signal Processing*, vol. 42, no. 11, pp. 3043-3050, November 1994.
- [Sha85] Shan, T.J., Wax, M., Kailath, T., "On Spatial Smoothing for Estimation of Coherent Signals," *IEEE Transactions on Acoustics, Speech, and Signal Processing*, vol. ASSP-33, pp. 802-811, August 1985.
- [Sha87] Shan, T.J., Paulraj, A., Kailath, T., "On Smoothed Rank Profile Tests in Eigenstructure Methods for Directions-of-Arrival Estimation," *IEEE Transactions on Acoustics, Speech and Signal Processing*, vol. ASSP-35, no. 10, pp. 1377-1385, October 1987.
- [Shy94] Shynk J.J., Gooch R.P., "Performance Analysis of the Multistage CMA Adaptive Beamformer," *Proceedings of the IEEE MILCOM*, pp. 316-320, 1994.
- [Siw95] Siwiak, K., *Radiowave Propagation and Antennas for Personal communications*, Artech House, 1995.
- [Sto89] Stoica, P., Nehorai, A., "MUSIC, Maximum Likelihood, and Cramer-Rao Bound," *IEEE Transactions on Acoustics, Speech and Signal Processing*, vol. 37, no. 5, pp. 720-741, May 1989.

- [Stu81] Stutzman, W.L., Thiele, G.A. *Antenna Theory and Design*, John Wiley & Sons, 1981.
- [Sub89] Sublett, B.J., Gooch, R.P., Goldberg, S.H., "Separation and Bearing Estimation of Co-channel Signals," *Proceedings of the IEEE MILCOM*, pp. 629-634, 1989.
- [Tak87] Takao, K., Kikuma, N., "An Adaptive Array Utilizing an Adaptive Spatial Averaging Technique for Multipath Environments," *IEEE Transactions on Antennas and Propagation*, vol. AP-35, no. 12, pp. 1389-1396, December 1987.
- [Tal94] Talwar, S., Viberg, M., "Blind Estimation of Multiple Co-channel Digital Signals Using an Antenna Array," *IEEE Signal Processing Letters*, vol. 1, no. 2, pp. 29-31, February 1994.
- [TR45] TR-45 Committee, "Survey of Location Technologies to Support Mobile 9-1-1," *Telecommunications Industry Association Report WJEM(911)/94.10.11.011*, 1994
- [Tre83] Treichler, J.R., Agee, B.G., "A New Approach to Multipath Correction of Constant Modulus Signals," *IEEE Transactions on Acoustics, Speech, and Signal Processing*, vol. ASSP-31, no. 2, April 1983.
- [Tre84] Treichler, J.R., Larimore, M.G., "A Real-Arithmetic Implementation of the Constant Modulus Algorithm," *Proceedings of IEEE*, pp. 3.2.1-3.2.4, 1984.
- [Tre85A] Treichler, J.R., Larimore, M.G., "The Tone Capture Properties of CMA-Based Interference Suppressors," *IEEE Transactions on Acoustics, Speech and Signal Processing*, vol. ASSP-33, no. 4, pp. 946-958, August 1985.
- [Tre85B] Treichler, J.R., Larimore, M.G., "New Processing Techniques Based on the Constant Modulus Adaptive Algorithm," *IEEE Transactions on Acoustics, Speech, and Signal Processing*, vol. ASSP-33, no. 2, pp. 420-431, 1985.
- [Van88] Van Veen, B.D., Buckley, K.M., "Beamforming: A Versatile Approach to Spatial Filtering," *IEEE ASSP Magazine*, pp. 4-24, April 1988.
- [Vib91] Viberg, M., Otterston, Bjorn, "Sensor Array Processing Based on Subspace Fitting," *IEEE Transactions on Signal Processing*, vol. 39, no. 5, pp. 1110-1120, May 1991.
- [Wax85] Wax, M., Kailath, T., "Detection of Signals by Information Theoretic Criteria," *IEEE Transactions on Acoustics, Speech and Signal Processing*, vol. ASSP-33, no. 2, pp. 387-392, April 1985.
- [Wax89] Wax, M., Ziskind, I., "Detection of the Number of Coherent Signals by the MDL Principle," *IEEE Transactions on Acoustics, Speech, and Signal*

- Processing*, vol. 37, no. 8, pp. 1190-1196, August 1989.
- [Wid67] Widrow, B., et.al., “Adaptive Antenna Systems,” *Proceedings of the IEEE*, vol. 55, no. 12, pp. 2143-2159, Dec. 1967.
- [Wid89] Widrow, B., Stearns, *Adaptive Signal Processing*, Prentice Hall, 1989.
- [Wu95] Wu, H.T., Yang, J.F., Chen, F.K., “Source Number Estimators Using Transformed Gershgorin Radii,” *IEEE Transactions on Signal Processing*, vol. 43, no. 6, pp. 1325-1333, June 1995.
- [Xu94A] Xu, G., Roy, R.H., Kailath, T., “Detection of Number of Sources via Exploitation of Centro-Symmetry Property,” *IEEE Transactions on Signal Processing*, vol. 42, no. 1, pp. 102-111, January 1994.
- [Xu94B] Xu, G., Kailath, T., “Fast Subspace Decomposition,” *IEEE Transactions on Signal Processing*, vol. 42, no. 3, pp. 539-550, March 1994.
- [Xu94C] G. Xu, et. al., Experimental Studies of Space-Division-Multiple-Access Schemes for Spectral Efficient Wireless Communications,” *Proceedings of the IEEE Asilomar Conference on Signal Processing*, pp. 800-804, 1994.
- [Xu95] Xu, G., Liu, H., “An Effective Transmission Beamforming Scheme for Frequency-Division-Duplex Digital Wireless Communication systems,” *Proceedings of the ICASSP*, pp. 1729-1732, 1995.
- [Zis88] Ziskind, I., Wax, M., “Maximum Likelihood Localization of Multiple Sources by Alternating Projection,” *IEEE Transactions on Acoustics, Speech, and Signal Processing*, vol. 36, no. 10, pp. 1553-1560, October 1988.
- [Zol86] Zoltowski, M., Haber, F., “A Vector Space Approach to Direction Finding in a Coherent Multipath Environment,” *IEEE Transactions on Antennas and Propagation*, vol. AP-34, no. 9, pp. 1069-1079, September 1986.

Programs

The following programs were used in the preparation of this thesis. All these programs may be found at `~riasis/thesis/programs` on the MPRG workstation network

- [1] res_ns_SNR.m
- [2] MUSIC_pert.m
- [3] MUSIC_ns.m
- [4] MUSIC_SNR.m
- [5] MUSIC_fb_ns.m
- [6] MUSIC_fb_SNR.m
- [7] LS_ESPRIT_ns.m
- [8] LS_ESPRIT_SNR.m
- [9] LSESPRIT_fb_ns.m
- [10] LSESPRIT_fb_SNR.m
- [11] TLS_ESPRIT_ns.m
- [12] TLS_ESPRIT_SNR.m
- [13] TLSESPRIT_fb_ns.m
- [14] TLSESPRIT_fb_SNR.m
- [15] ILSP_MUSIC_ns.m
- [16] ILSP_MUSIC_SNR.m
- [17] ILSP_fbMUSIC_ns.m
- [18] ILSP_fbMUSIC_SNR.m
- [19] ILSP_ML_ns.m
- [20] ILSP_ML_SNR.m
- [21] ILSP_LSESPRIT_ns.m
- [22] ILSP_LSESPRIT_SNR.m
- [23] ILSP_fbLSESPRIT_ns.m
- [24] ILSP_fbLSESPRIT_SNR.m
- [25] ILSP_TLSESPRIT_ns.m
- [26] ILSP_TLSESPRIT_SNR.m

- [27] ILSP_fbTESPRIT_ns.m
- [28] ILSP_fbTESPRIT_SNR.m
- [29] Perf_ns.m
- [30] Perf_SNR.m
- [31] TLS_ESPRIT_ang.m
- [32] TLSESPRIT_fb_ang.m
- [33] ILSP_TLSESPRIT_ang.m
- [34] ILSP_fbTESPRIT_ang.m
- [35] Perf_angle.m
- [36] TLS_ESPRIT_as.m
- [37] TLSESPRIT_fb_as.m
- [38] ILSP_TESPRIT_as.m
- [39] ILSP_fbTESPRIT_as.m
- [40] Perf_as.m
- [41] TLS_ESPRIT_pow.m
- [42] TLSESPRIT_fb_pow.m
- [43] ILSP_TESPRIT_pow.m
- [44] ILSP_fbTESPRIT_pow.m
- [45] Perf_pow.m
- [46] TLS_ESPRIT_cal.m
- [47] TLSESPRIT_fb_cal.m
- [48] ILSP_TLSESPRIT_cal.m
- [49] ILSP_fbTESPRIT_cal.m
- [50] Perf_cal.m
- [51] AIC_numsamp.m
- [52] MDL_numsamp.m
- [53] GAIC_numsamp.m
- [54] GMDL_numsamp.m
- [55] AIC_SNR.m
- [56] MDL_SNR.m
- [57] GAIC_SNR.m
- [58] GMDL_SNR.m
- [59] AIC_fb_numsamp.m
- [60] MDL_fb_numsamp.m
- [61] AIC_fb_SNR.m
- [62] MDL_fb_SNR.m
- [63] Or_est_numsamp.m
- [64] Or_est_SNR.m
- [65] DOAEXP2.C*
- [66] MASTER2A.ASM*
- [67] SLAVE2A.ASM*
- [68] MASTER2C.C96*
- [69] SLAVE2C.C96*

- [70] MASTER2A.LOC*
- [71] SLAVE2A.LOC*
- [72] DOAEXP2.LDD*
- [73] SLAVE2.LDD8
- [74] CALIB.M*
- [75] ILSPfbTESPRIT_real.m
- [76] TLSESPRIT_fb_real.m
- [77] measure_plots.m
- [78] ILSP_ph.m
- [79] ILSP_mult_ph.m
- [80] ILSP_pert.m
- [81] ILSP_mult_pert.m
- [82] ILSP_mp.m
- [83] ILSP_mult_mp.m
- [84] TLS_ph.m
- [85] TLS_mult_ph.m
- [86] TLS_pert.m
- [87] TLS_mult_pert.m
- [88] TLS_mp.m
- [89] TLS_mult_mp.m
- [90] ErrorPlots.m

* Also available on the PC at c:\m96\dev\rias\array1

Vita

Rias Muhamed was born on July 21, 1969 in Mahe, India. He received his Bachelor of Technology Degree in Electronics and Communications Engineering in May 1990 from Pondicherry University, Pondicherry. He joined the Electrical Engineering Department of Virginia Tech in Fall 1993 to pursue his M.S. Since February'94, he has been working with Dr. T. S. Rappaport at the Mobile and Portable Radio Research Group in the area of direction-of-arrival estimation using antenna arrays. Prior to joining Virginia Tech, Rias worked with Hewlett-Packard India, Bangalore from July 1991 to July 1993, and with International Data Management Ltd., Bangalore from June1990 to June1991.

A handwritten signature in black ink, appearing to read "Rias Muhamed".